
Comprehensive study of photoinduced processes:
*From an optimized quantum yield determination setup and
methodology to molecular dynamics*

Henrieta Derondeau



Dissertation

München 2023

Comprehensive study of photoinduced processes:
*From an optimized quantum yield determination setup and
methodology to molecular dynamics*

Henrieta Derondeau

Dissertation
an der Fakultät für Physik
der Ludwig-Maximilians-Universität
München

vorgelegt von
Henrieta Derondeau (née Volfová)
aus Nové Zámky, Slowakei

München, im Mai 2023

Erstgutachter: Prof. Dr. Eberhard Riedle
Zweitgutachter: Prof. Dr. Jürgen Hauer

Tag der Abgabe: 24.05.2023
Tag der mündlichen Prüfung: 19.07.2023

Kurzfassung

Die nachhaltige Synthese von Materialien durch Photochemie und Photokatalyse ist ein aktueller und äußerst wichtiger Bereich der Forschung. Ein tieferes Verständnis der Photoreaktionen ist unerlässlich, um die Strategie, die Reaktionsbedingungen und die chemischen Ausbeuten sowie die Reaktionsquantenausbeuten zu optimieren. Diese Arbeit konzentriert sich auf die Entwicklung neuartiger Geräte, die für diesen Zweck geeignet sind, und auf die Anwendung neuartiger und etablierter Aufbauten und Methoden zur Beschreibung der molekularen Dynamik molekularer Schalter, photochemischer und photokatalytischer Reaktionen.

Die Kosten eines lichtinduzierten Prozesses werden durch die Reaktionsquantenausbeute (RQY) angegeben. Derzeit ist die Aktinometrie immer noch die gängige Technik zur Bestimmung der RQY. Sie weist jedoch erhebliche Einschränkungen und Mängel auf. In dieser Arbeit wurde ein alternativer optischer Aufbau mit der Bezeichnung Quantum Yield Determination Setup (QYDS) entwickelt, der einen relativen Fehler von weniger als 5 % aufweist. Er kann unter Standard-Laborbedingungen verwendet werden. Außerdem wurde er für alle Reaktionstypen einzeln validiert, auch von verschiedenen Benutzern in verschiedenen Städten. Somit kann das QYDS die chemische Aktinometrie problemlos ersetzen.

Das QYDS ist modular aufgebaut und kann an die Bedürfnisse der Anwender angepasst werden. Durch den Einsatz neuartiger Komponenten (z.B. elektronischer Shutter, I/U-Wandler und Solarzellendetektor) konnte die Messgenauigkeit erhöht werden. Das QYDS deckt den Anregungsbereich von 255 nm - 1050 nm vollständig ab. Die Leistungserfassung reicht von etwa 20 μ W bis 1 W. Die GUI steuert den Aufbau und speichert die Daten. Das MathCad-Paket führt den Benutzer durch den gesamten Prozess und die Auswertung. Im Gegensatz zur Aktinometrie kann QYDS recht komplexe Reaktionsmodelle mit mehr als zwei Zuständen vorschlagen und differenzieren. Dies war der Fall bei der photochemischen Reaktion decarboxylative Photomakrozyklisierung von N-phthaloylierten GABA-Derivaten. Der QYDS-Ansatz zeigte die Korrelation zwischen der Menge an K_2CO_3 in der Lösung und der Bildung des Nebenprodukts.

Die typische Zeitskala für intermolekulare Prozesse und langlebige Intermediate liegt im μ s-Bereich und darüber. Zu diesem Zweck wurde das LED-basierte Pump-Repump-Probe-Setup entwickelt. Die Verwendung von preiswerten gepulsten Hochleistungs-LEDs anstelle von aufwendigen Kurzpuls-Lasern ermöglicht die Akkumulation der Spezies und die Verbesserung des Messsignals. Das Gerät wurde für den Nachweis des Zwischenzustands im photokatalytischen Prozess mit Rutheniumtrisbipyridyl verwendet.

Für weitere Experimente wurde ein von uns entwickeltes Transienten-Absorptionsspektrometer verwendet. Typische Interpretationsmethoden wurden um die spektrale Parametrisierung erweitert, die für die Analyse des Phänomens der Bandenverschiebung sehr nützlich ist. Dies wurde auf Betaine auf Pyridiniumbasis angewandt, und die extrahierten Zeitkonstanten ergaben eine gute Übereinstimmung mit dem Solvatationsprozess.

Die Untersuchung von Fotoschaltern auf der Basis von Diarylethen (DAE) ergab eine vergleichbare Dynamik wie bei der DAE-Familie, die eine Lösungsmittelabhängigkeit aufweist. Interessanterweise sind die ultraschnellen Reaktionen nicht automatisch mit hocheffizienten Prozessen verbunden. Obwohl die Bindungsspaltung hier auf einer sub-ps Zeitskala stattfindet, liegt die RQY immer noch unter 1 %. Die RQY unter 1 % für beide Reaktionsrichtungen wurde auch für den ersten photochromen Koordinationskomplex von DAE und den Polyoxometallat-Koordinationskomplex beobachtet.

Als photokatalytische Reaktion wurden die photoinduzierten Eigenschaften von **Ni-** und **Zn-Mabiq** untersucht und verglichen. Obwohl nach dem dynamischen Mechanismus zu erwarten war, dass **Zn-Mabiq** ein besserer Photokatalysator ist als **Ni-Mabiq**, behindert die Instabilität der reduzierten Form die erfolgreiche Reaktion. Es ist der Teilmittelcharakter von **Ni-Mabiq**, der es robuster gegenüber der Photodegradation macht.

Short summary

The sustainable synthesis of materials by photochemistry and photocatalysis is a timely and extremely important area. A deeper understanding of photoreactions is essential to optimize the strategy, reaction conditions, and chemical yields as well as reaction quantum yields. This work focuses on the development of novel devices suitable for this purpose and the application of these, combined with established setups and methods to describe the molecular dynamics of molecular switches, photochemical and photocatalytic reactions.

The cost of a light-induced process is provided by the reaction quantum yield (RQY). Currently, actinometry is still the accepted technique for determining the RQY. However, it has severe limitations and shortcomings. In this work, an alternative optical setup called Quantum Yield Determination Setup (QYDS) was developed having a relative error of less than 5%. It can be used under standard lab conditions. Moreover, it has been validated for all reaction types individually, including measurements by different users in different cities. Thus, QYDS can easily replace chemical actinometry.

The QYDS is modular and can be adapted to user needs. By using novel components (e.g., electronic shutter, I/U converter and solar cell detector) the measurement accuracy was increased. The QYDS fully covers the excitation range of 255 nm - 1050 nm. The power detection ranges from about 20 μ W - 1 W. The GUI controls the setup and stores the data. The MathCad package guides the user through the entire process and evaluation. Unlike actinometry, QYDS can suggest and differentiate quite complex reaction models with more than two states. This was the case for photochemical reaction decarboxylative photomacrocyclization of N-phthaloylated GABA derivatives. The QYDS approach revealed the correlation between the amount of K_2CO_3 in the solution and the formation of the side product.

The typical time scale for intermolecular processes and long-lived intermediates is in the μ s regime and beyond. For this purpose, the LED-based Pump-Repump-Probe instrument was developed. The use of a moderate price high power pulsed LED instead of a complex short pulse laser enables to accumulate the species and enhance the measurement signal. The device was used for the detection of the intermediate state in the photocatalytic process with ruthenium trisbipyridyl.

For further experiments a transient absorption spectrometer of our own design was used. Typical interpretation methods were extended to include spectral parameterization, which is very useful for analyzing the band shift phenomenon. This was applied to pyridinium-based betaines, and the extracted time constants gave good agreement with the solvation process.

The study of diarylethene (DAE)-based photoswitches revealed comparable dynamics to the DAE family, which exhibits solvent dependence. Interestingly, the ultrafast reactions are not automatically associated with highly efficient processes. Although the bond cleavage here occurs on a sup-ps time scale, the RQY is still below 1%. The RQY below 1% for both reaction directions was also observed for the first photochromic coordination complex of DAE and polyoxometalate coordination complex.

As a photocatalytic reaction, the photoinduced properties of **Ni-** and **Zn-Mabiq** were investigated and compared. Although according to the dynamic mechanism, **Zn-Mabiq** was expected to be a better photocatalyst than **Ni-Mabiq**, the instability of the reduced form hinders the successful reaction. It is the partial metal character of **Ni-Mabiq** that makes it more robust against photodegradation.

Publications

Publications in Journals:

- The central role of the metal ion for photoactivity: Zn- vs. Ni-Mabiq
R. Lauenstein, S. L. Mader, H. Derondeau, O. Z. Esezobor, M. Block, A. J. Römer, C. Jandl, E. Riedle, V. R. I. Kaila, J. Hauer, E. Thyrrhaug and C. R. Hess
Chem. Sci. 12, 7521-7532 (2021).
- Determination of reaction quantum yields: LED Based Setup with better 5% precision
H. Volfova, Q. Hu and E. Riedle
EPA Newsletter, 51 (2019).
- Visible Light Driven "on" / "off" Photochromism of a Polyoxometalate Diarylethene Coordination Complex
J. Xu, H. Volfova, R. J. Mulder, L. Goerigk, G. Bryant, E. Riedle and C. Ritchie
J. Am. Chem. Soc. 140, 10482 - 10487 (2018).

To be submitted:

- Photodecarboxylative ring annulation of α - and β -functionalized phthaloyl-GABA derivatives: a concise route to bioactive pyrroloiso-indolinones with high quantum efficiency
W. Schulze, A. Zimmer, J.-M. Neudörfl, F. M. Dato, M. Pietsch, H. Derondeau, F. Gaida, E. Riedle and A. G. Griesbeck
In preparation for ChemPhotoChem
- Optimized reaction quantum yield determination setup with better than 5% relative error
H. Derondeau, R. Wilcken, Q. Hu and E. Riedle
In preparation for ChemPhotoChem
- Addressing the Complexity of the Dynamic Photophysics of Pyridinium Betaines
P. McDonald, J. Xu, H. Derondeau, C. Guerrin, D. Lonsdale, L. Goerigk, S. Aloïse, E. Riedle and C. Ritchie
In preparation for Chemical Science

Contents

Kurzfassung	i
Short summary	iii
Publications	v
1. Introduction and historical notes	1
2. Experimental and interpretation methods	5
2.1 Broadband transient absorption spectroscopy	5
2.2 Optimal use of a spectral photometer	27
2.3 High end fluorescence setup with improved sensitivity	31
Appendix for Chapter 2	33
3. Optimized reaction quantum yield determination setup with better than 5% relative error	47
3.1 Introduction	47
3.2 Reaction quantum yield and its measurement methods.....	48
3.3 Concept of the Quantum Yield Determination Setup.....	50
3.4 Basic components of QYDS.....	53
3.4.1 LED as a light source	53
3.4.2 Optics and imaging – because every photon counts.....	56
3.4.3 Stirring in a cuvette	59
3.4.4 Detection of the incident and transmitted light	62
3.4.4.1 Calibration of the solar cell.....	66
3.4.5 Shutter.....	68
3.4.6 Automatized QYDS.....	68
3.5 Measurement	70
3.5.1 Measurement preparation	70
3.5.1.1 Characterization of molar absorptivity spectra for reactant and product(s).....	71
3.5.1.2 Choice of the excitation light – its wavelength and illumination power	76
3.5.2 Measurement procedure	81
3.6 Evaluation.....	82

3.6.1	Introduction of an uniform header for the UV/vis files	82
3.6.2	Baseline correction.....	82
3.6.3	Time evolution of the concentration	84
3.6.4	RQY calculation.....	84
3.7	Validation.....	87
3.7.1	Photochemical reaction of o-nitrobenzaldehyde.....	87
3.7.2	Molecular photoswitches	89
3.7.3	Reaction quantum yield of azobenzene	91
3.8	Application of the Fisher method for extraction of the product spectrum to azobenzene as a model system.	94
3.9	Reaction quantum yield - more than just one number	97
3.10	Conclusion and Outlook.....	99
	Appendix for Chapter 3.....	100
4.	Ultrafast switching of diarylethene based molecular photoswitches	113
4.1	Introduction	113
4.2	Photochemical properties and reaction quantum yield	114
4.3	Transient absorption for the cyclization (ring closing) process.....	119
4.4	Transient absorption for the cycloreversion (ring opening) process.....	129
4.5	The first polyoxometalate diarylethene coordination complex.....	135
	Appendix for Chapter 4.....	138
5.	Decarboxylative photomacrocyclization of N-phthaloylated GABA derivatives	155
5.1	Introduction	155
5.2	UV/vis spectroscopy and RQY	156
5.3	Transient absorption measurements	165
	Appendix for Chapter 5.....	168
6.	Comprehensive study of photo-induced properties of Ni- and Zn-Mabiq	177
6.1	Introduction	177
6.2	Molecular and electronic structure.....	178
6.3	Electronic properties (UV/vis spectra).....	178
6.4	Reaction quantum yield of the photoreduction	180
6.5	Ni- and Zn-Mabiq as photocatalyst.....	188
6.6	Transient absorption.....	194
	Appendix for Chapter 6.....	202

7.	LED based pump-repump-probe instrument for μs dynamics	215
7.1	Introduction	215
7.2	Setup	215
7.2.1	Measurement principle	218
7.2.2	Detection of the one electron reduced intermediate	221
7.3	Outlook	227
	Appendix for Chapter 7	229
8.	Summary and Outlook	233
9.	References	239
	Acknowledgments	257

1. Introduction and historical notes

“One has to do something new in order to be able to see something new.”

Georg Christoph Lichtenberg

The interaction of light and matter is the main focus of photochemistry and photocatalysis. This important branch of science studies the chemical reactions that occur upon illumination with light. The deeper understanding of photoinduced reactions can be used for applications in solar energy conversion [Sza22, Gon19], synthesis and design of new chemical species and drugs [Bri12a, Bug22, Ma21], water decontamination [Pai16, Tim15], and many other applications [Can22], including the study of the origin of life [Gre21].

Photochemistry is governed by two basic laws. The second law is known as the Stark-Einstein law. The second law states that light is absorbed in a quantized form as photons, with one photon activating one molecule. This is the case for light and medium illumination intensities. However, when excited by a focused high-power laser, two-photon absorption can occur, leading to excitation to higher energy levels [Göp31].

The first law finds its origin already in the early 19th century. The first report on this phenomenon comes from Grotthuss in 1819 [Gro19]. In his experiment, red iron thiocyanate was exposed to light dispersed by a prism. The results showed that a chemical reaction was possible only with illumination in the blue-green range. However, he incorrectly assumed that absorption was a physical property and did not depend on chemical structure. This statement was later corrected by Draper in 1841 [Dra41]. Absorption is a chemical property and correlates with the chemical structure of the molecule. Based on the observations of Grotthuss and Draper, the first law of photochemistry was established.

The first law of photochemistry states that the absorption of light by the target molecule is mandatory to enable the photoinduced chemical reaction. Or in other words:

When it does not absorb, it does not react.

However, in our experience over many years, there are still chemical communities that do not put enough emphasis to this simple principle. There are various reasons for such actions. In some cases, the chemical reaction is deliberately taken to its limits. In other cases, it is due to the lack of proper lighting equipment.

This work is intended to provide an incentive to think about the controlled and targeted

illumination for the photoactive species. For this purpose, our group has developed a versatile setup (**Quantum Yield Determination Setup, QYDS**) that covers the full range of illumination for typical photochemical as well as photocatalytic species and hence, the illumination wavelength can be simply and straightforward optimized to particular photo-absorbing conditions (see Chapter 3).

One of the most important topics in photochemistry is the quantification of light-induced reactions in terms of their efficiency. This involves investigating how many photons per molecule are required for a successful reaction. This information is provided by the reaction quantum yield (RQY).

Determination of the number of created product molecules can be considered as rather straightforward. Various analytical methods can be used for this purpose (UV/vis, GC, NMR). However, quantifying the number of absorbed photons was a major challenge for almost two centuries. In the following the historical view on the quantification of absorbed light is summarized.

The first known instrument for measuring light intensity was published by Sir John Herschel [Ame84]. This "first actinometer" was based on the calibrated measurement of the expansion of a liquid solution. The liquid expansion resulted from the absorption of light in the dark liquid with very high optical density due to its heating. For this purpose, a very highly concentrated copper sulfate solution was used as the dark solution [Her34, Her40, Rab21, Vos97]. In essence, the instrument is just an extension of the well-known expansion thermometer, where the expansion of mercury or alcohol is measured quantitatively.

The next generation of measuring instruments for determining the amount of light was based on thermopiles. Four years after the discovery of the Seebeck effect in 1826, Melloni introduced the first thermopile in which several bismuth-copper thermocouples were connected in series. The absorbed light was converted into a voltage output signal [Bar62, Rog12].

In the 1950s, calibrated thermopiles were replaced by chemical actinometry. The actinometric standards have to be determined by measuring both the chemical yield and the amount of absorbed light – most times through the use of a thermopile. According to the IUPAC definition, the chemical actinometer is a chemical system with known RQY that undergoes a chemical photoreaction when irradiated with light. In 2004, the "IUPAC Technical Report" was published [Kuh04], defining chemical actinometry as the state of the

art. This publication summarizes the standardized procedure for correct actinometric measurement. It also lists all relevant and recommended chemical actinometers.

A closer look at this list of chemical actinometers leads to an unexpected finding, namely that the user is severely limited in its application. Of the 67 liquid actinometers, only 41 are commercially available. The synthesis of an optically pure substance with impurities below 0.01% can be considered quite difficult in terms of workload and time. Additional analytical methods such as CG or NMR are often required to verify the chemical purity. Such analytical methods are quite expensive and require additional expert personnel. Therefore, it is easier to buy a highly pure substance that is immediately ready for spectroscopic measurement.

UV/vis is a spectroscopic method that is easy to perform nowadays and is available in every spectroscopic laboratory. However, out of 41 substances, only 19 are suitable for UV/vis analysis. In addition, six of these 19 actinometers are no longer recommended by IUPAC, either because more suitable systems are available for the respective wavelength range or because a concentration, pH or oxygen dependence of the RQY has been found [Kuh04].

Of the 13 actinometers recommended as reliable, 10 are suitable for excitation in the UV range between 200-400 nm and only three for excitation between 400-500 nm. Excitation above 500 nm is completely missing. Yet, it is particularly the range above 500 nm that is interesting and relevant for the study of photochemical processes that utilize excitation by sunlight. Furthermore, many photochemical substances and photoswitches require the excitation light above 500 nm. A large impetus for the synthesis of such systems is the intended use in biology based applications in the deep red window of blood absorption.

It is worth noting that many of the actinometers recommended by IUPAC were measured in the 50-70ties using old-fashioned thermopiles (e.g., Cambridge 18-junction thermopile calibrated by the National Physical Laboratory [Hat56] for the measurement of the potassium ferrioxalate actinometer) with an active area of only 0.4 cm². Although there are efforts to redetermine the RQYs for some of the actinometric substances [Lad17, Gal10, Sta18, Wri21], there has been no official update or reassessment of the RQYs for actinometers by the IUPAC.

If one regards the current progress in the optical powermeter detectors based on thermopiles, it is doubtful whether there still is a need for chemical actinometry. A common commercially available powermeter can quantify the illumination power in a range of less

than a mW to well above 1 W with an accuracy of better than 3%. Additionally, the good optical powermeters are calibrated by the manufacturer in accordance to NIST standards. Thus, it is reasonable to take advantage of such devices and dispense with unnecessary and time consuming actinometric measurements.

Determination of the RQY can provide a deeper understanding of the photochemical or photocatalytic systems. Additional information about the molecular dynamics can be obtained by measuring ultrafast time-resolved spectroscopy. Together, this information provides an overall picture of the photoinduced reaction that can be used for further design optimization or additional industrial applications.

In this thesis, the revised design and the implementation of a highly flexible QYDS is reported (Chapter 3). A number of test measurements are performed for the validation of the setup. The molecular dynamics as well as the RQY of photochemical systems (Chapter 5), photocatalytic systems (Chapter 6), and photoswitches (Chapter 4) were investigated and analyzed by ultrafast time-resolved spectroscopy. In addition, a novel and low-cost LED-based pump-pump-probe instrument for μ s-dynamics has been developed (Chapter 7) to study rather slow processes in the μ s-range, e.g., intermolecular processes [Zew00a], processes in biological systems [Hau14, Kut17], or long-lived intermediates.

The motivation and goal of this work was not to excite molecules with random light, but to excite the researchers to think more deeply about light and photochemical processes and to show them that it is possible, with very reasonable effort, to develop various devices that can simplify daily laboratory routines.

2. Experimental and evaluation methods

2.1 Broadband transient absorption spectroscopy

Ultrafast time resolved spectroscopy is one of the key methods to provide a clear picture of excited state molecular dynamics. A detailed analysis of the resulting measurement enables to understand processes such as internal conversion and intersystem crossing present in all investigated systems, photoinduced electron, proton or general charge transfer [Sch08, Let18], and the isomerization of photoswitches [Wil18, Sot20] or it may help to detect short lived intermediate states [Ish09] of a photoreaction.

A standard method to study such photoinduced phenomena is the broadband transient absorption (pump-probe) spectroscopy [Meg09, Rie13, Bra14, Lan18]. The general principle is based on an excitation of the molecules by an ultrashort pump pulse typically within tens of femtoseconds. The subsequent probing with a spectrally broad probe pulse at different delays results in a spectro-temporal evolution of the signatures of the excited and product states.

The timescale of a typical molecular process ranges from fs to μ s and hence the spectroscopy in the femtosecond [Zew00b, Meg09, Mat13] and nanosecond regime [Lan13, Rie13] is most suitable. The excitation wavelength of such photoinduced processes varies between the UV and visible range, sporadically in the NIR. The typical wavelength region to trace the absorption changes is in the region between 250 nm and 700 nm, in some cases up to the NIR. These requirements and far beyond are fulfilled by the transient absorption measurement system developed by Riedle and coworkers [Meg09, Mat13, Rie13, Bra14], which is demonstrated in Fig. 2-1.

The Ti:sapphire amplifier (CPA2001; Clark-MXR, Inc.) with kHz repetition rate and central wavelength of 778 nm produces 150 fs pulses with an energy of nearly 1 mJ. A noncollinear optical parametric amplifier (NOPA) provides tunable pulses from 450 nm to 740 nm or even in the near infrared (NIR) [Wil97, Rie00, Cer03]. The wavelength of the pump pulse can be extended down to 220 nm if the frequency doubling with a β -barium borate (BBO, type-I) crystal is applied. The fused silica prism compressor is used to compress the output from the NOPA by compensating the pulse chirp. The autocorrelator of own design enables to measure the pulse duration [Koz04, Hom11]. The typical pulse duration used in experiments is approximately 30 fs or below from the deep UV out to 1200 nm.

The time delay between the pump and the probe pulse is controlled by a linear delay stage with sub-10 fs accuracy (M-531 PD; Physik Instrumente GmbH). The maximal tunable time delay is about 2 ns. The $\lambda/2$ plate positioned before the sample enables to control the polarization of the light. The polarization angle between pump and probe pulse is adjusted to the magic angle of 54.7° to suppress contributions from rotational diffusion [Fle76]. The laser beam is focused into the sample with a round profile and size of approximately $100 \mu\text{m}$.

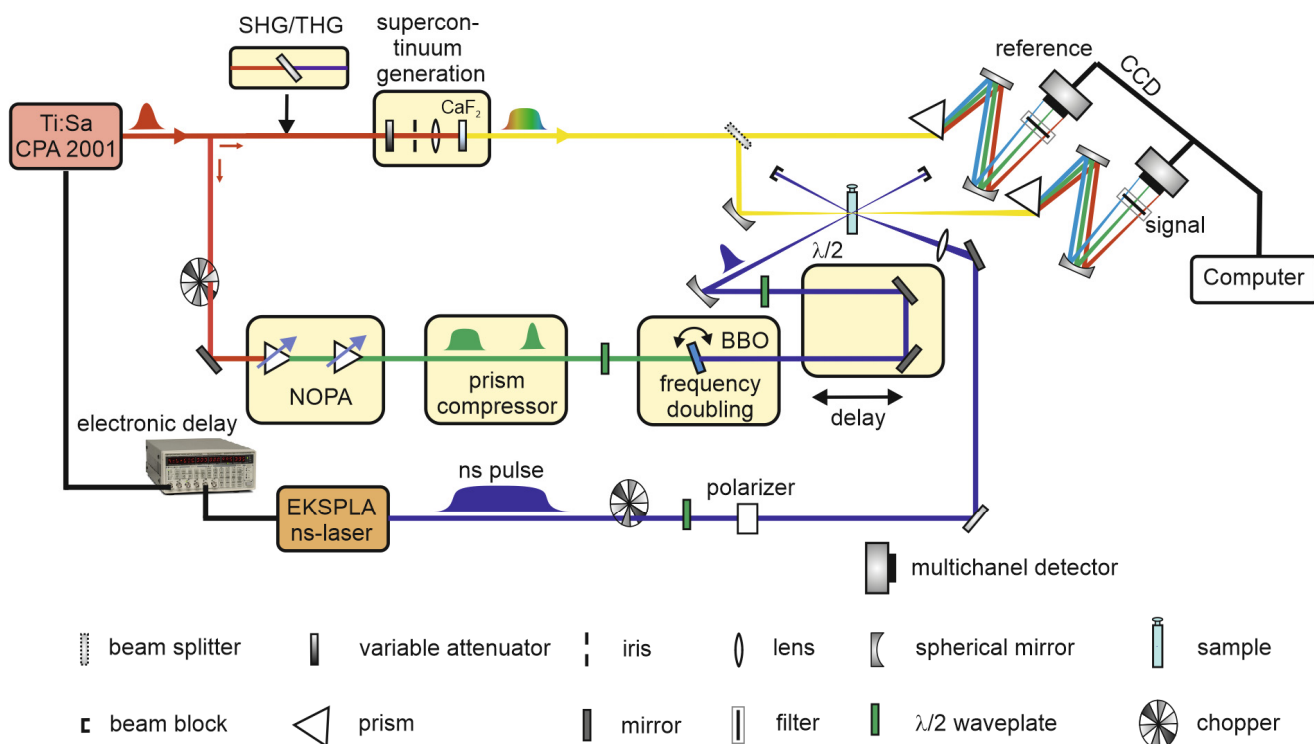


Figure 2-1 Schematic representation of the broadband transient absorption spectrometer from fs to μs regime. CPA: chirped pulsed amplification, SHG/THG: second/third harmonic generation, NOPA: noncollinear parametric amplifier, BBO: β -barium borate crystal.

The time delays above 2 ns cannot readily be provided by a mechanical delay stage due to its size limitation. Thus, for experiments in the ns and μs regime a wavelength tunable optical parametric oscillator (OPO) (NT-242-PFG0035, EKSPLA) with 1 kHz repetition rate is used. Laser pulses in the wavelength region between 210 nm and 2600 nm can be easily adjusted with a pulse duration of ≈ 2.5 ns. The nanosecond pulses are synchronized electronically by a TTL-pulse from the Ti:sapphire. The time delay between pump and probe is electronically controlled by an electronic delay generator (DG645, Stanford Research

Systems Inc.). The maximal adjustable time delay is 790 μs with a temporal accuracy of better than 100 ps [Koe13]. The typical spot size of the pump light is approximately 200 μm . The stable broadband probe pulse is generated by supercontinuum generation (SCG) [Bra09, Meg09] by focusing a small fraction of the Ti:sapphire beam into 5 mm calcium fluoride (CaF_2) crystal. The constant circular translation movement of the crystal within the focal plane avoids accumulative damage and increases its lifetime. The probe spectrum covers the wavelength region from 285 nm to 720 nm [Meg09, Bra09, Hub01]. If desired, the wavelength range can be extended to 225-1700 nm by using a second harmonic or third harmonic generation (SHG/THG) before the SCG [Rie13]. The fundamental of the CPA is suppressed with an appropriate filter so, thus the spectral phase quality of the probe beam is as much as possible preserved. The transmitted light behind the sample is spectrally dispersed in the fused silica prism and detected with a CCD camera with single-shot readout (Entwicklungsbüro Stresing). In order to increase the signal to noise ratio and to avoid pseudo-structures in the TA spectra that are due to spectral correlations, the probe beam is split into the beam passing through the sample (signal) and the reference beam focused onto a second identical CCD chip (reference camera) [Dob10, Bra14]. Hereby the reference arm does not cross the sample cell. The wavelength calibration is performed before the measurement with the aid of well-known spectral features of colored glass filters (BG36, Schott AG and short pass filters, Asahi Spectra Inc.) and dielectric coated mirrors (HR355-HT532, Laser Components GmbH). The probe beam is focused into the sample with a spot size of about 35 μm .

The basic idea of the pump probe spectroscopy is to compare the transmitted spectrum with and without the excitation pump pulse. This can be achieved by blocking of every second pump pulse by chopping. The spectral changes are measured in the optical density (OD):

$$\Delta\text{OD}(\lambda, \Delta t) = -\log\left(\frac{I^*(\lambda, \Delta t)}{I_0(\lambda)}\right) \quad (2.1)$$

where I^* and I_0 correspond to transmitted light of the excited and non-excited sample. Introducing the second reference CCD camera enables suppression of spectral correlations and it enhances the signal to noise ratio [Bra14]. The difference in the transmittance reference signal ΔT_{ref} on the reference detector is given as:

$$\Delta T_{\text{ref}}(\lambda, \Delta t) = \frac{R^*(\lambda, \Delta t)}{R_0} \quad (2.2)$$

where R^* is the pumped signal and R_0 is the unpumped signal. Consequently, the relation for transmittance of the sample signal corresponds to:

$$\Delta T_{\text{sample}}(\lambda, \Delta t) = \frac{S^*(\lambda, \Delta t)}{S_0} \quad (2.3)$$

with the pumped sample signal S^* and sample signal without excitation S_0 . The recorded transient absorbance signal in OD is calculated according to reference [Bra14]:

$$\Delta OD(\lambda, \Delta t) = -\log\left(\frac{S^*(\lambda, \Delta t)}{S_0} \cdot \frac{R_0(\lambda)}{R^*(\lambda, \Delta t)}\right) \quad (2.4)$$

In order to ensure proper exchange of the sample and avoid accumulation of the photoproducts or photodegraded species, custom made flow cells [Bre03, Meg09] are applied instead of conventional cuvettes. The flow cell consists of two fused silica 200 μm thick glass windows and an optical pathlength down to 100 μm which enables to reduce the coherent artifact and the group velocity mismatch. The optical pathlength can be adjusted by a teflon spacer with various thickness of 100 μm , 250 μm or 1mm.

Interpretation and modelling of the transient absorption data

The transient absorption signal has typically the following contributions:

- a) **ground state bleach** (GSB): $\Delta OD < 0$, the negative signal results from the depopulation of the ground state into the excited state.
- b) **stimulated emission** (SE): $\Delta OD < 0$, the excited molecule interacts with the incoming photon under relaxation to the ground state. This process is accompanied by emission of a second photon and hence the intensity of the probe light is increased due to the stimulated emission. Typically found in region, where fluorescence is expected.
- c) **excited state absorption** (ESA): $\Delta OD > 0$, positive signal resulting from the population of the excited state.
- d) **product absorption** (PA): $\Delta OD > 0$, after relaxation of the excited state into the product ground or excited state a positive signal with an infinite lifetime (if the product stable) is observed.

The signal of about or less than hundred femtosecond length found around $\Delta t = 0$ ps is known as coherent artifact (CA) and it results from the temporal overlap of the pump and

probe pulse in a material [Kov99, Lor02]. This overlap leads to nonlinear interaction of the pump and probe pulses in which the main contributions originate from two photon absorption (TPA) and cross phase modulation (XPM) [Bau18]. As a reference, the CA is measured in the pure solvent before the actual photoreactive experiment. The CA signal can be modeled empirically by a Gaussian and/or its first and second derivative [Meg09, Kov99] and so it can be disentangled from the molecular TA signal. The CA also helps to evaluate the time zero and it is used to correct the measurement data from the probe chirp.

In the following, various modeling methods for the evaluation of the transient absorption data are discussed. The evaluation method of the transient data is based on the following assumption: the rate of change in the population N_i (for state i) per unit time is proportional to the decay rate k_i and the population of N_i :

$$\frac{dN_i}{dt} = -k_i \cdot N_i \quad (2.5)$$

This corresponds to the assumption that the decay is purely statistical – justified in many situations but not all. Diffusional processes for example are governed by slightly differing rules leading to a stretched exponential decay. The inverse of the decay rate defines the lifetime τ_i in which the population decreases to $1/e$ of the initial value:

$$\tau_i = \frac{1}{k_i} \quad (2.6)$$

The solution of the differential equation defined in Eq. 2.5 is given as:

$$N_i(t) = N_i(0) \cdot \exp(-k_i t) = N_i(0) \cdot \exp\left(-\frac{t}{\tau_i}\right) \quad (2.7)$$

with the population at time zero $N_i(0)$. Assuming a system with n different states, the time evolution of the signal is related to the sum of n exponential functions with different amplitudes A_i and n time constants τ_i , [Meg09]:

$$F(t) = \text{IRF}(t) \otimes \left\{ \theta(t) \left[\sum_i^n A_i \cdot \exp\left(-\frac{t}{\tau_i}\right) \right] \right\} + \text{const.} + \text{CA} \quad (2.8)$$

The instrument response function IRF limits the time resolution and is typically defined by a Gaussian function. The IRF is convoluted with the Heaviside step function $\theta(t)$. This approach also known as "single line analysis" is suitable for a single wavelength. This

method can be applied preferably on a system without a noticeable spectral shift of the particular band which typically originates from solvation or vibrational cooling [Meg11a]. In other cases, the decay constants may become strongly wavelength dependent.

Global analysis methods

The evaluation of the whole data set enables the "global analysis" [Sto04, Van04, Fit06, Ruc12, Sla15]. Hereby, the whole dataset is fitted simultaneously with a defined set of time constants. Strictly speaking, a bilinear model is assumed where the "transient spectra" are time-independent and the time constants are independent of the spectral position. Even though this assumption cannot be derived rigorously, it is quite convenient mathematically and applies in many practical cases. The global analysis provides as a result the decay associated difference spectra DADS for each extracted time constant. The negative band in the DADS relates to an increase of ESA band and recovery of the GSB or SE. The positive DADS is related to intensity increase of the GSB signal and reduction of the signal in ESA. Due to the fact, that the DADS represent the difference in the species spectra, the interpretation of such data cannot be regarded as straightforward. However, if the kinetic model of the system is known and it is implemented into the evaluation, the species associated difference spectra (SADS) can be extracted [Sto04]. The subsequent subtraction of the GSB leads to species associated spectra (SAS) which can be interpreted as conventional molar absorptivity $\varepsilon_i(\lambda)$ [Koe13].

An additional powerful method how to extract SAS from the TA data is based on the spectral reconstruction. The TA spectra can be considered as a linear combination of the intermediate species spectra and GSB spectrum with a certain scaling factor: The scaling factor is directly related to the concentration of the excited molecules. The analysis of the second derivative of certain vibronic feature of the spectrum is considered as very beneficial to obtain the correct scaling factor. Since a positive signal at all wavelengths for the extracted spectrum is required, the analysis can be straightforwardly performed. This spectral analysis also known as the TEM method that was originally described by Thulstrup, Eggers and Michl in the 1970s [Mic87, Mic70a, Mic70b] and it is widely used in the realm of spectroscopy [Vet17, Sai15, Wid13, Gaw98].

A few illustrative cases

An exemplary dataset for the fs-ps measurement is demonstrated in Fig. 2-2. Hereby the molecular switch from the diarylethene (DAE) family in the closed form (**c-DAE**) in toluene is excited with 390 nm pump pulses. The photoreaction results in a bond cleavage and the open isomer is formed. The reactive bond participating in the ring cleavage is designated with red circles in the upper part of Fig. 2-2. The molar absorptivity spectra of the pure open and closed form in toluene are demonstrated in Appendix 2-A1.

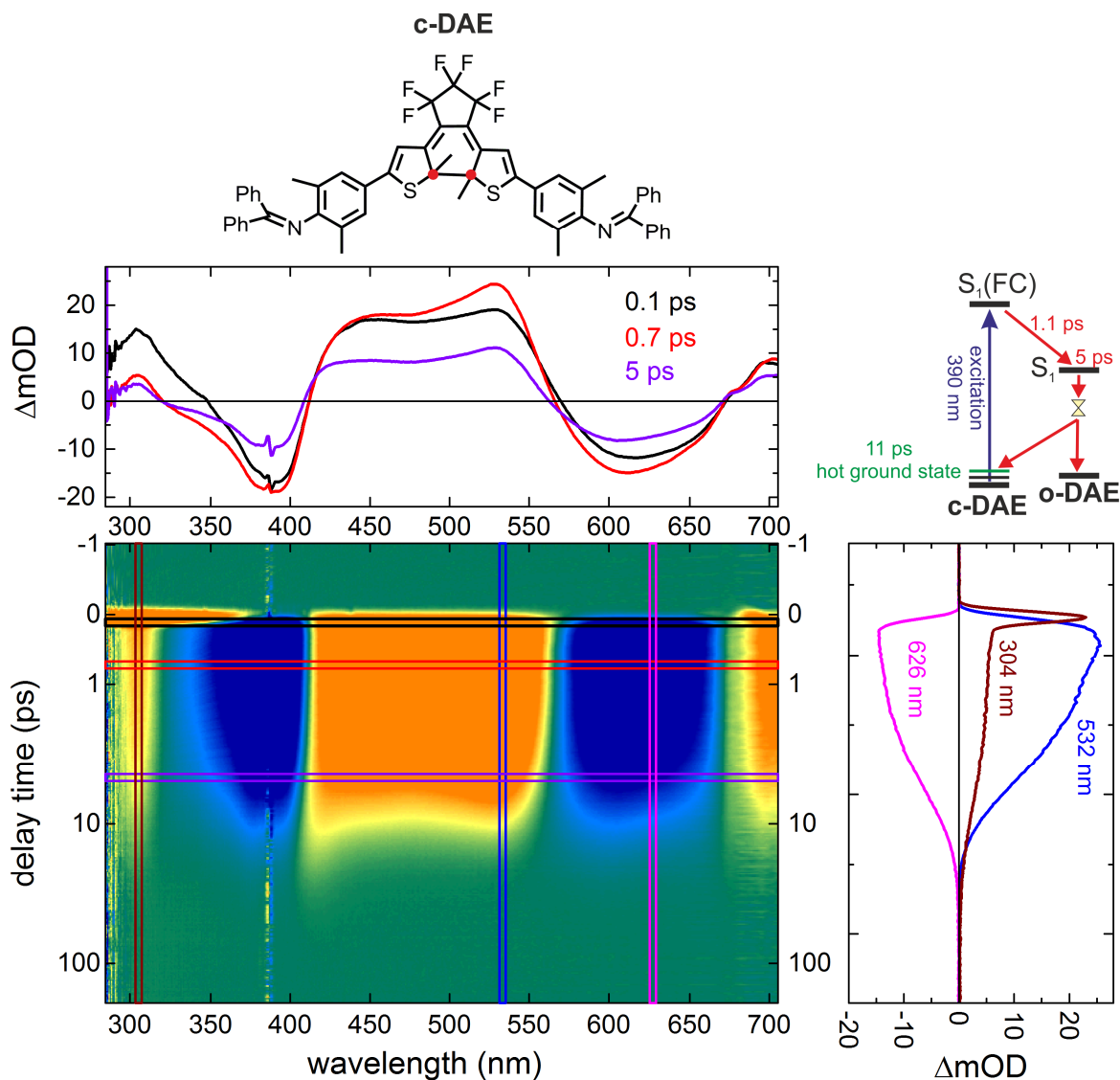


Figure 2-2 Example of a transient absorption measurement for the closed form of a molecular switch from the DAE family (**c-DAE**) in toluene upon 390 nm excitation measured in 100 μm thick flow cell after excitation with 180 fs pulses centered at 390 nm with a pulse energy of 100 nJ.

The false color map demonstrates various contributions of the signal. The green color corresponds to $\Delta OD = 0$, blue color is related to a negative signal $\Delta OD < 0$ and orange to a positive signal $\Delta OD > 0$. The top panel demonstrates spectra at chosen time delays. In the right panel the temporal decay at certain wavelength can be found.

The very broad ESA signal around 500 nm overlaps with two GSB bands positioned around 390 nm and 630 nm. The further ESA signals are detected at 300 nm and 700 nm. All spectral features decay within several tens of picoseconds, whereas no residual negative GSB signal is to observe. This absence of the product formation can be explained with a very low RQY (reaction quantum yield) of 0.1%, which is a typical order of the magnitude for the ring opening [Iri88, Iri95, Sum14].

According to the analysis of the measurement a three state kinetic model is required for the characterization of the excited state dynamics. Hereby, the time decay constants of 1.1 ps, 5 ps and 11 ps are found.

In various DAE systems, a fast structural evolution combined with vibrational cooling between 0.5 ps and 3 ps is reported [Hon20, Sot17]. The group of Elles [War12] assigns this time constant to the time required to overcome the activation barrier. Within this time range of a few picoseconds lies also the measured 1.1 ps and hence it is reasonable to assume, that this time constant is related to either vibrational energy transfer to the solvent or overcoming of the activation barrier.

The main contribution has the time constant of 4.8 ps and it is found mostly through the whole spectral region. The reported lifetimes of the excited state from which the ring opening may occur is in the range between 0.7 ps and 9 ps. The measured 5 ps are in close agreement with the literature values [Sot20, Hon20, Ham16].

The phenomenon of the vibrational cooling of the hot ground state is particularly expected for molecular switches, in which the major fraction of the excited population relaxes back to the ground state without successful ring opening [Hon20]. As the RQY is 0.1% and the spectral distribution of the 11 ps DADS is in close agreement with those reported in ref. [Hon20], the 11 ps is attributed to the vibrational cooling of the hot ground state.

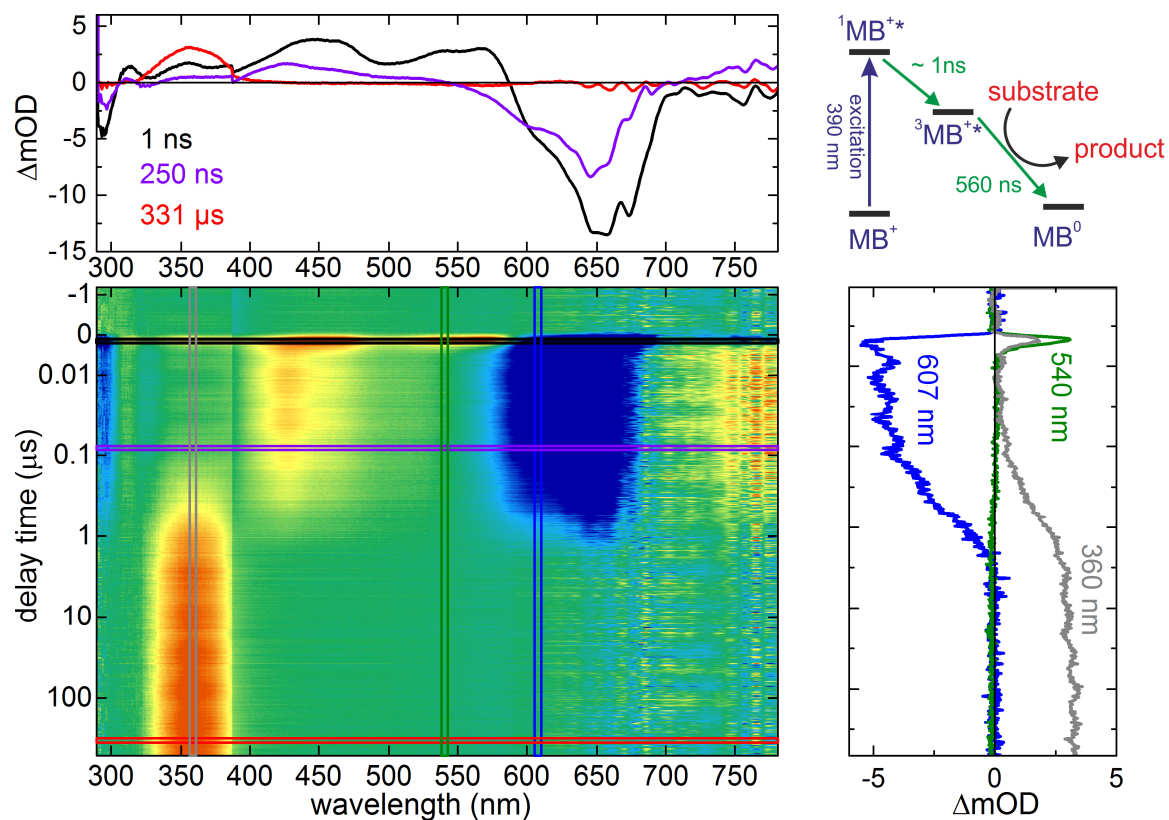


Figure 2-3 Example of transient absorption measurement in ns and μ s regime for photocatalytic isomerization of **Z-AB** (0.94 mM) with the aid of photosensitizer **MB** (45 μ M) in acetonitrile.

An exemplary measurement in the ns and μ s regime is demonstrated in Figure 2-3. Here (Z)-bis(methoxy) azobenzene (**Z-AB**) undergoes oxidative radical-cation-catalyzed isomerization in presence of the photosensitizer methylene blue PF₆ (**MB**).

The transient absorption data are demonstrated in Fig. 2-3. The **MB** molecules are excited with a 660 nm pump pulse, whereby firstly the singlet state of **MB** is populated. The lifetime of this singlet state is according to the measurement below 1 ns, which gives a good agreement with the literature value of 630 ps measured in methanol [Han18]. The depopulation of the singlet state is demonstrated by a green color in the right panel. Additionally, due to the ESA of the singlet state a distinct shift of the GSB towards blue at 600 nm is to observe.

After the subsequent intersystem crossing, the triplet state is populated with a corresponding triplet yield of about $QY_{IC} = 30\%$ [Han18]. The ESA band of the triplet state is demonstrated with the violet curve in the top panel in the region between 325 nm and 575 nm. The ESA band of the triplet state decays simultaneously with the GSB recovery with a time constant

of 560 ns. The reaction is completed after 24 μ s since the product has been created (see PA demonstrated with vertical grey line).

The reaction quantum yield can be extracted from the transient absorption data by a modified TEM method described above. The reaction quantum yield is given as a relation between the number of the created product molecules ($\#_{\text{product}}$) and the number of the **MB** molecules in the triplet state ($\#^3\text{MB}$):

$$\text{RQY} = \frac{\#_{\text{product}}}{\#^3\text{MB}} \quad (2.9)$$

The number of the **MB** in the triplet state can be extracted from the GSB at 140 ns, where all **MB** molecules have already populated the triplet state. The GSB spectrum is the inverse of the steady state absorption and therefore it can be straightforwardly subtracted from the TA data. The product absorption spectrum is also well known from the steady state absorption of the **E-AB** and it is analyzed at the delay time of 25 μ s. The resulting RQY of this reaction is 82% - in excellent agreement with the value of 83% reported by the group of Hecht considering the solvent and the concentration of the substrate and photosensitizer [Han18].

The suggested reaction mechanism of the reaction reported in the literature [Han18] is based on the excitation of the **MB**, which is subsequently reduced by an electron transfer. This electron originates from the neutral **Z-AB** molecule, which figures now as radical cation **Z-AB \cdot^+** . The Z-configured radical cation isomerizes rapidly into the E-form radical cation. The radical cation **E-AB \cdot^+** is subsequently reduced by a neutral **Z-AB** which results in the desired product of **E-AB** and a new radical cation **Z-AB \cdot^+** (see Fig. 2-B1 in Appendix) [Han18]. This type of mechanism is also known as radical chain reaction for which a RQY above unity is typical. However, as reported previously by the group of Hecht and coworkers, the RQY for the system varies from 0.63 to 1.99 depending on the solvent, concentration and ratio of **Z-AB** to **MB** [Han18]. In this work they argue, that the above mentioned RQY exceeds the QY of the intersystem crossing ($\text{QY}_{\text{IC}} = 30\%$) and therefore it is reasonable to assume that the reaction mechanism takes place through the photoinduced electron transfer rather than triplet energy transfer.

Maximum entropy analysis and spectral parameterization

In the following, two further analytical methods - maximum entropy analysis and spectral parameterization - are described. Analog to the global fit analysis, both abovementioned methods are suitable for the evaluation and interpretation of ultrafast transient absorption measurements with underlying complex dynamics. However, in contrast to the commonly termed “global fit”, they are model free and in combination they provide additional information that cannot be extracted from a global fit analysis straightforwardly.

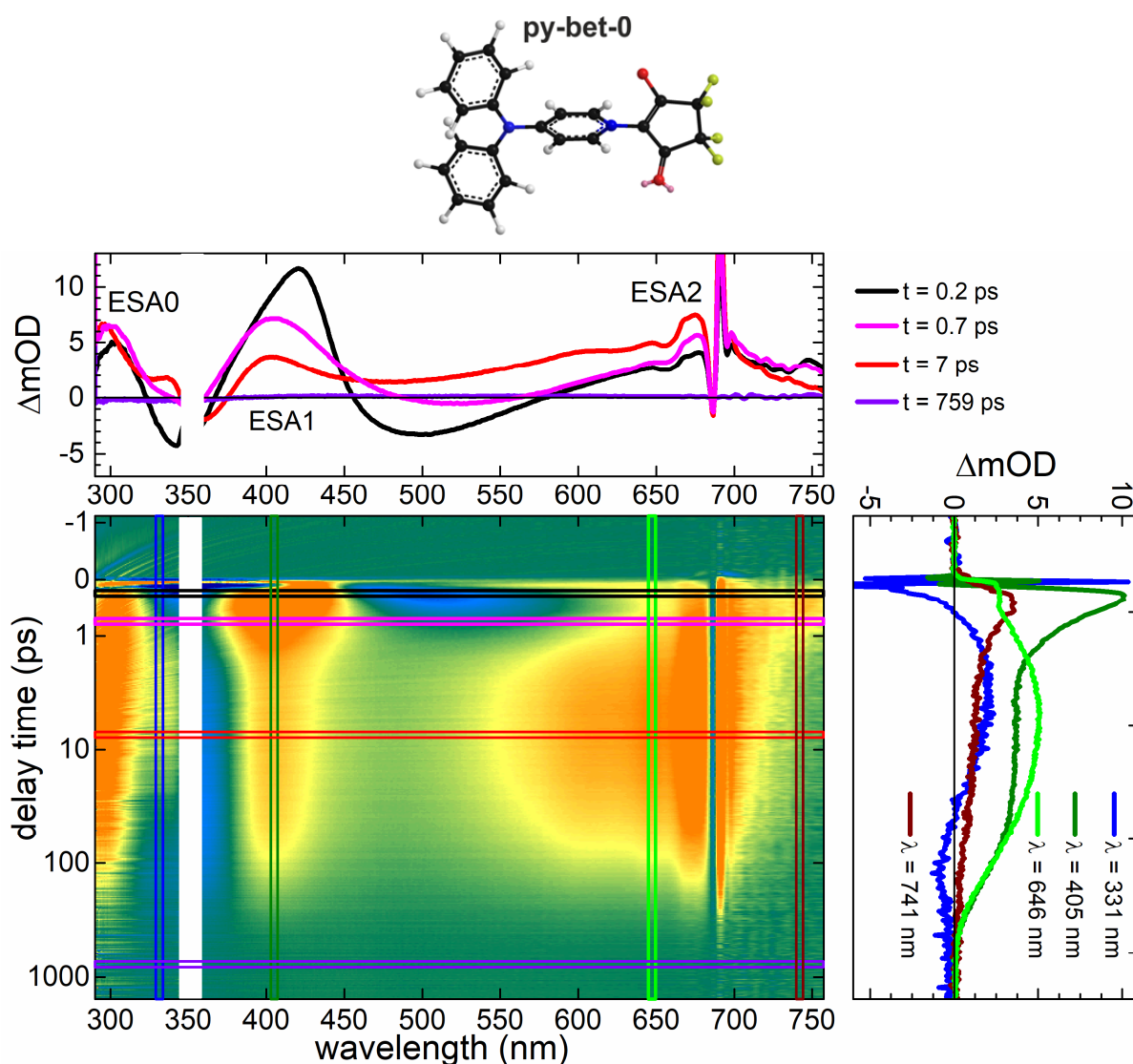


Figure 2-4 Transient absorption of **py-bet-0** in acetonitrile under standard conditions measured in 100 μm thick flow cell after excitation with 45 fs pulses centered at 348 nm with pulse energy of 140 nJ.

To explain the basic principle of the maximum entropy analysis and the spectral parameterization, two model systems in four different solvents are presented. The model systems, labeled **py-bet-0** and **py-bet-CH₃**, are shown in Fig. 2-C2 to Fig. 2-C16 in the Appendix.

Py-bet-0 and **py-bet-CH₃** were synthesized by group of Chris Ritchie, Monash University in Melbourne [Xu17]. Both species were measured and analyzed in cooperation with this group.

An example transient absorption measurement of the **py-bet-0** in acetonitrile upon 348 nm excitation is shown in Fig. 2-4. The negative band around 360 nm corresponds to ground state bleach (GSB). The positive signals around 280 nm, 425 nm and 680 nm are related to excited state absorption (ESA).

For further discussion, a specific nomenclature for the ESA bands is introduced. ESA0 is related to ESA around 300 nm, ESA1 around 410 nm and ESA2 around 675 nm (see Fig. 2-4 top). The negative stimulated emission (SE) band at 480 nm shifts by 45 nm towards red. The ESA1 signal shows in the first two picoseconds a slight blue shift (see later Fig. 2-9). The molecules in the excited state decay within 130 ps completely back to the ground state.

The set of all TA-measurements for **py-bet-0** as well as for **py-bet-CH₃** in methanol, acetonitrile, dichloromethane (DCM) and toluene can be found in Appendix 2-C.

Maximum entropy analysis

Maximum entropy analysis is a suitable evaluation approach even in cases, in which there is very limited information about the expected molecular dynamics. This approach is based on entropy inversion of the Laplace transform. It provides a probability density map $p(k)$ that a certain decay constant is present in the data set [Lor06, Kut13, Koe15]. For a fixed wavelength the fit function is given as:

$$F(t) = \int_0^{\infty} f(t, k) p(k) dk \quad (2.10)$$

$$f(t, k) = \int_{-\infty}^t \exp(-k(t-t')) \cdot \text{IRF}(t') dt' \quad (2.11)$$

Where k is defined as:

$$k = \frac{1}{\tau} \quad (2.12)$$

The entropy of the distribution is maximized in order to obtain the probability map $p(k)$ that does not contain more information than necessary to fit the data [Kut13]:

$$S = - \sum_{i=1}^m p(k_i) \cdot \ln(p(k_i)) \quad (2.13)$$

The spectral dependencies of the probability provide similar information as the DADS spectra of a global analysis, but ME is a model hypothesis free analysis since it originates from a transformation of the data. A positive signal signalizes the decrease of excited state absorption, whereas a negative one is related to a decrease of ground state bleach or stimulated emission. The width of the bands correlates to the uncertainty in the time constant.

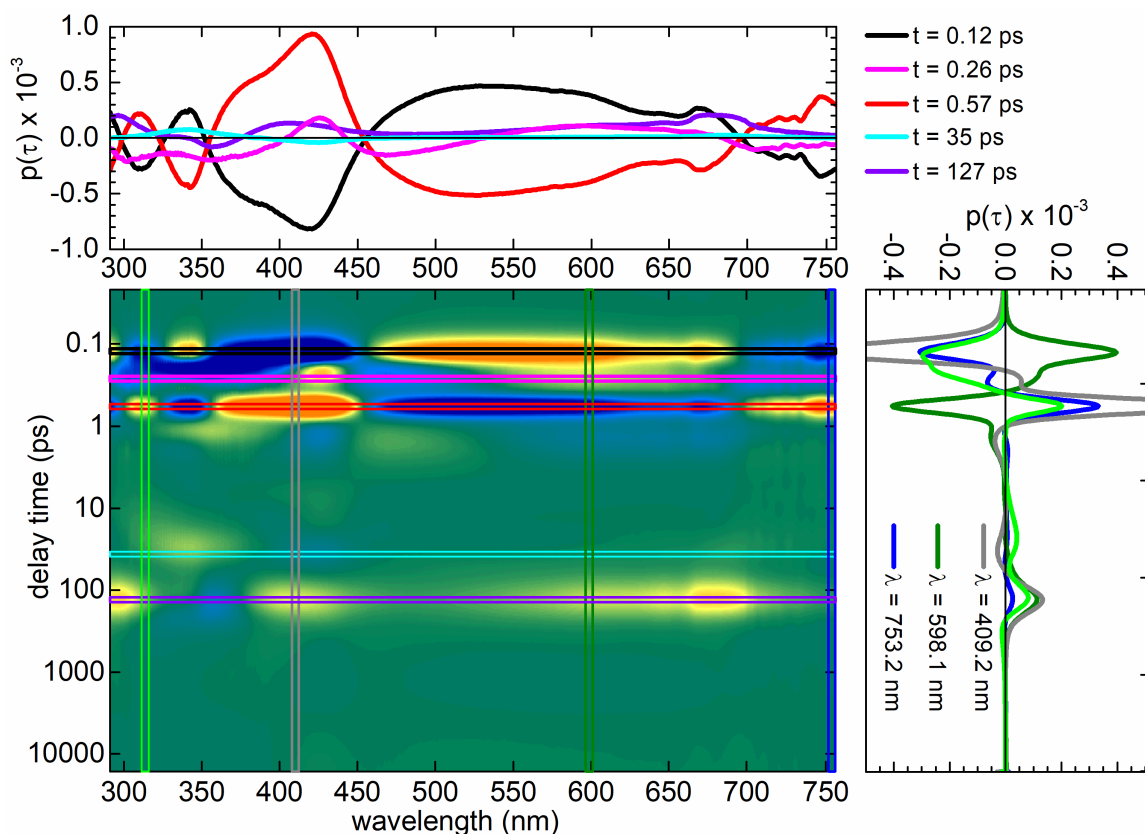


Figure 2-5 Maximum entropy analysis of **py-bet-0** in acetonitrile from Fig. 2-4.

This approach is not based on any model. It provides an information about the number of expected decay constants. In case of **py-bet-0** in acetonitrile (see Fig. 2-5) five different time

constant are found (see Tab. 2-1). The set of all maximum entropy analyses for **py-bet-0** as well as for **py-bet-CH₃** in methanol, acetonitrile, dichloromethane (DCM) and toluene can be found in Appendix 2-C.

Table 2-1 Resulting decay times obtained from the maximum entropy analysis.

	py-bet-0				py-bet-CH₃			
	MeOH	MeCN	DCM	toluene	MeOH	MeCN	DCM	toluene
decay 1 (ps)	-	-	-	-	< 0.1	0.08	0.19	0.21
decay 2 (ps)	-	0.12	0.15	0.31	0.14	0.21	0.43	0.52
decay 3 (ps)	-	-	-	2.8	-	-	-	1.5
decay 4 (ps)	0.11	0.25	0.35	10	0.52	0.73	0.84	5.0
decay 5 (ps)	0.46	0.55	0.81	-	2.35	1.9	3.5	776
decay 6 (ps)	6	31	64	82	11	45	-	-
decay 7 (ps)	58	130	>1500	>1500	121	221	>1500	>1500

The phenomenon of the band shifting due to the solvation process [Wil18] can be partly observed also in the maximum entropy analysis. The band shifting is mirrored in the first few picoseconds, in which the states are not perfectly separated, but rather smeared out. This can be clearly seen in the negative band around 400 nm, which smoothly spreads from 0.1 ps to 0.26 ps.

The decay times obtained from the maximum entropy analysis can be used as an initial guess for further evaluation approaches. The results of the maximum entropy analysis are summarized in Tab. 2-1.

Spectral parametrization

The transient absorption data are commonly evaluated by global fit analysis. This approach to disentangle the kinetics is typically used for rather predictable simple systems without any substantial spectral shifts of the bands. The method termed “global fit” by Stokkum and coworkers [Sto04] is based on a bilinear approach. This means that the TA data are considered as time independent DADS or species spectra and spectrally constant decay times. However, in the discussed case of a pronounced band shift in the SE as well as in the ESA around 400 nm is observed. This spectral shift contains valuable information about the dynamic processes, e.g., solvation [Wil18]. The application of the global fit analysis is in such cases not the approach of first choice [Mar14]. Consequently, an alternative method called spectral parametrization is used, which enables to extract the information about the dynamic process.

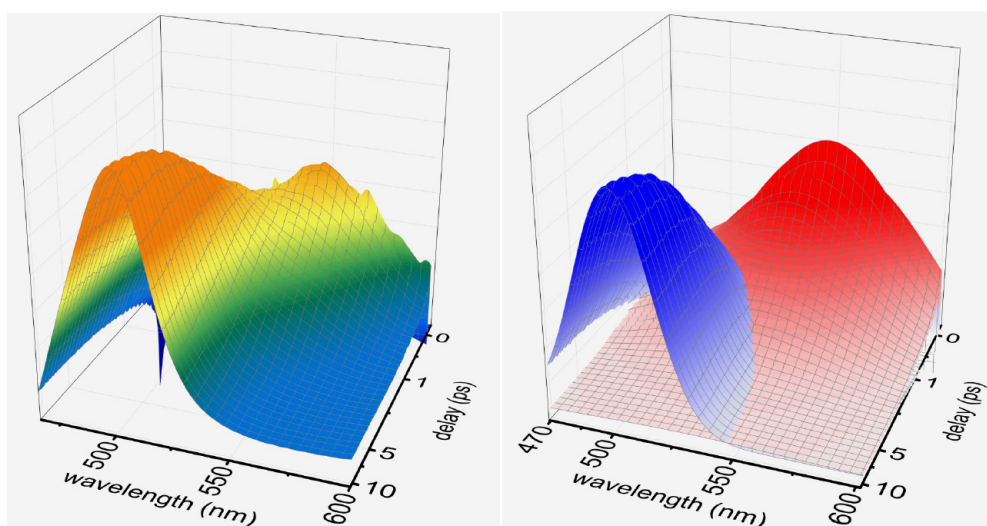


Figure 2-6 Example of the experimental TA data (left) that matches the result of spectral parametrization (right). In this case two Gaussian functions are used [Wil23].

The spectral parametrization uses a suitable set of functions in order to fit the spectral features. Hereby any set of functions that does indeed describe the spectra locally with as few parameters as possible can be used. Typically, a sum of Gaussian functions is used (see Fig. 2-6):

$$A(\lambda, \Delta t) = y_0(\Delta t) + \sum_{i=1}^n A_i(\Delta t) \cdot \exp\left(\frac{(\lambda - \lambda_{0,i}(\Delta t))^2}{(w_i(\Delta t))^2}\right) \quad (2.14)$$

where A is the amplitude, λ_0 the central wavelength, w is the width of the Gaussian function

and y_0 is the offset. An example experimental transient absorption data and the corresponding parametrization in 3D plot from reference [Wil23] is shown in Fig. 2-6. In this simple example, two Gaussians are used, in which the first function (red surface in Fig. 2-6 right) disappears and at the same time the second Gaussian (blue surface in Fig. 2-6 right) increases with the identical time constant. Consequently, the careful evaluation of the Gaussian's parameters, e.g., amplitude A or central wavelength λ_0 , provides more information about the dynamic process [Wil23]. If needed, skewed or asymmetric Gaussians like the functions *Asym2Sig*, *Bigaussian* or *LogNormal* can be well used.

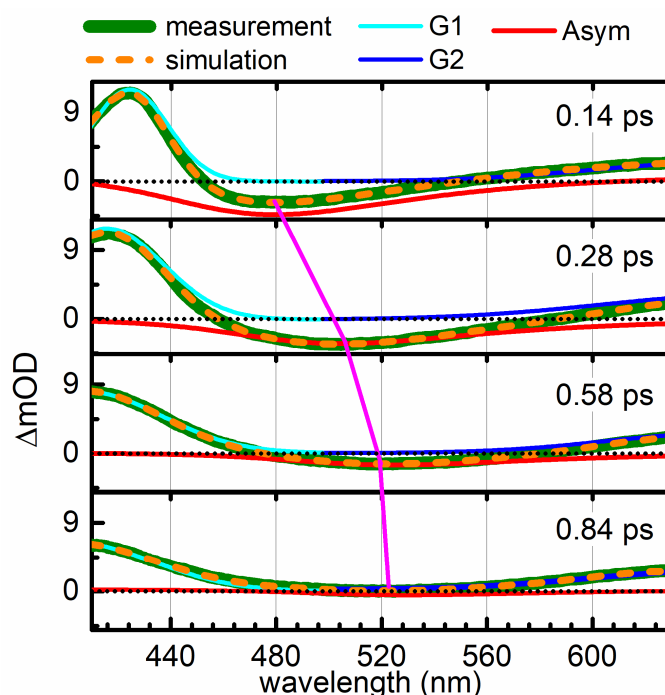


Figure 2-7 Spectral parametrization for the measurement data of **py-bet-0** in MeCN. Magenta line as guide to the eye indicates the red shift of the SE signal.

The spectral parameterization approach was used here for the evaluation of the ultrafast transient absorption data for **py-bet-0** and **py-bet-CH₃**. As shown in Fig. 2-7, the simulation with two Gaussian functions and one double sigmoidal asymmetric function gives a good agreement with the experimental data.

As demonstrated by a magenta line in Fig. 2-7, the central wavelength of the SE band shifts toward the red. This phenomenon can be straightforwardly evaluated by analyzing the central wavelength λ_0 of the correspondent function from the parametrization process. The time dependent change of the fitted Gaussian peak is shown in the top part of Fig. 2-8. In order to

elucidate the origin of this shift, the following correlation function is introduced:

$$C(t) = \frac{v(\infty) - v(t)}{v(\infty) - v(0)} \quad (2.15)$$

where $v(t)$ is the wavenumber at delay time t after excitation, and $v(0)$ and $v(\infty)$ corresponds to initial and final position of the peak. The correlation function is fitted with the aid of an exponential function. The corresponding plot is shown in Fig. 2-8 and the resulting fitting parameters are summarized in Tab. 2-2.

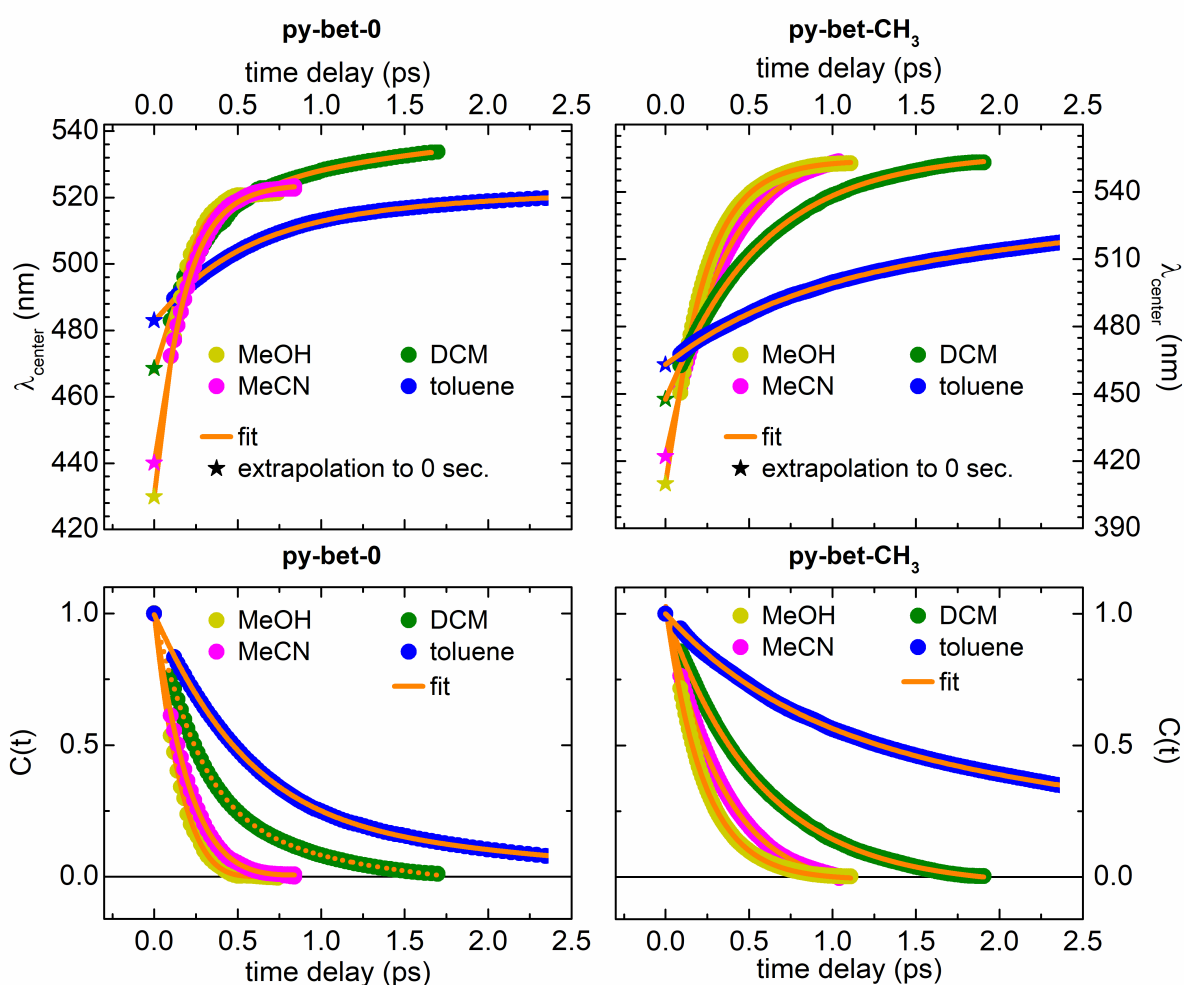


Figure 2-8 Dynamics of the peak shift in the SE signal together with the Gaussian fit.

Table 2-2 Fitting parameters obtained from spectral parametrization for the band shift in the SE signal.

		MeOH	MeCN	DCM	toluene
py-bet-0	λ_{shift} (nm)	95.5	83.0	63.5	61.0
py-bet-CH₃	λ_{shift} (nm)	143.0	132.0	106.0	83.5
py-bet-0	decay (ps)	0.14	0.18	0.35	0.6, 12.6, 155.0
py-bet-CH₃	decay (ps)	0.21	0.33	0.57	0.75 4.70
	solvation time (ps) [Hor95]	0.21	0.12	0.25	0.65, 3.0, 120 ps [‡]
	F(ϵ_0, n) *	0.71	0.71	0.47	0.02

[†]solvation time τ_{1e} from [Hor95], *dielectric measure of solvent polarity [Hor95], [‡] from reference [Lar99].

Analogous to the red shift analysis of the SE, the investigation of the blue shift of the ESA signal was performed (see Fig. 2-9). In the case of methanol, acetonitrile and DCM only one exponential function was used in order to fit the data. A multiexponential fit was required for evaluation of the band shift for **py-bet-0** and **py-bet-CH₃** dissolved in toluene. The extracted time constants are comparable to the solvation times reported by Maroncelli *et al.* (see Table 2-2). Consequently, it is reasonable to assume that the band shift originates predominantly from the solvation.

For both **py-bet-0** and **py-bet-CH₃**, the ESA decreases with the peak around 420 nm (**py-bet-0**) and 390 nm (**py-bet-CH₃**) within the first picosecond. This decay is accompanied by a blue shift of the ESA in the same picosecond. This phenomenon has been reported to be related to the rotation of the enolate moiety [Zha20, Iag17, Der17].

The blue shift of ESA is more pronounced in polar solvents such as methanol and acetonitrile. In both polar solvents, a blue shift of about 30 nm is observed for **py-bet-0**. When nonpolar toluene is used as solvent for **py-bet-0**, the blue shift decreases to 10 nm. Tab. 2.3 summarizes the absolute values of the blue shift in different solvents with the corresponding decay constants.

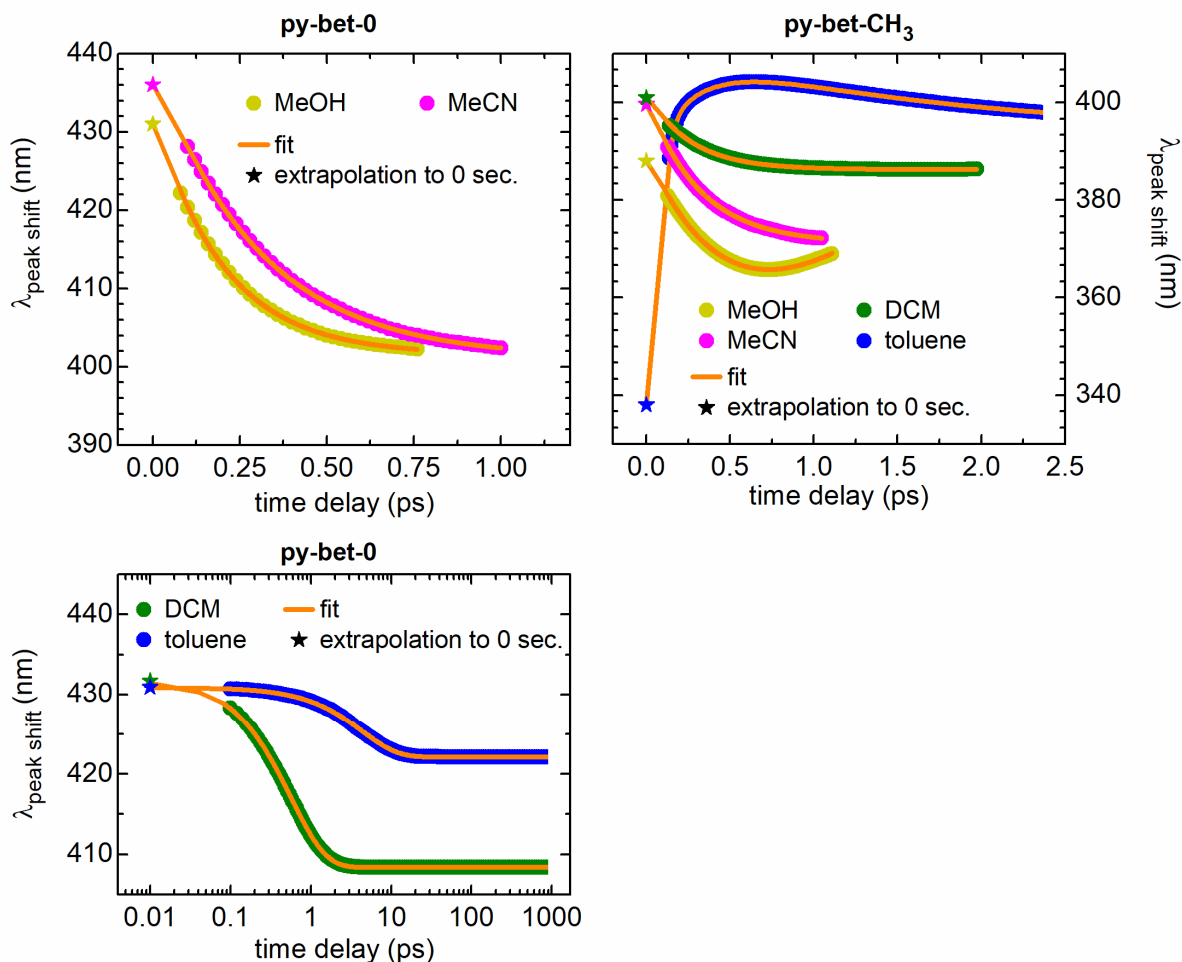


Figure 2-9 Shift dynamics of the ESA band for **py-bet-0** (left) and **py-bet-CH₃** (right) in various solvents.

Table 2-3 Fitting parameters obtained from spectral parametrization for the band shift in ESA.

		MeOH	MeCN	DCM	toluene
py-bet-0	λ_{shift} (nm)	28	33	23.4	10
py-bet-CH₃	λ_{shift} (nm)	22.7	27.6	14.8	59
py-bet-0	decay (ps)	0.20	0.30	0.56	4.40
py-bet-CH₃	decay (ps)	0.21	0.31	0.26	0.03, 0.25, 1.5
	solvation time (ps) [Hor95]	0.21	0.12	0.25	0.65, 3.0, 120 ps [†]
	$F(\epsilon_{0,n})$ *	0.71	0.71	0.47	0.02

[†]solvation time τ_{1e} from [Hor95], *dielectric measure of solvent polarity [Hor95], [‡] from reference [Lar99].

The spectral parametrization enables also to determine the time constants related to the (de-)population of various states. For this purpose, the area of the corresponding Gaussian fit function from the parametrization analysis is evaluated (see Fig. 2-10 and Fig. 2-11). The results give a good agreement with the time constants obtained from the maximum entropy analysis. The results are summarized in Tab. 2-4 and Tab. 2-5.

As demonstrated, the spectral parametrization is an elegant tool for the evaluation of the dynamics which includes such phenomena as peak shifting. Additionally, the spectral parametrization also provides an information about the real state population since this is proportional to the integral of the associated Gaussian.

Table 2-4 Fitting parameters from the spectral parametrization for the ESA obtained from the integral of the corresponding fitting function for **py-bet-0** in various solvents.

py-bet-0 MeOH				py-bet-0 MeCN				py-bet-0 DCM				py-bet-0 toluene			
ESA1		ESA2		ESA1		ESA2		ESA1		ESA2		ESA1		ESA2	
-	-	-	-	-	-	-	-	A>0	1.1 ps	A<0	1.1 ps	A>0	0.14 ps	A<0	0.22 ps
A>0	0.7 ps	A<0	0.9 ps	A>0	0.5 ps	A<0	0.7 ps	A>0	3.2 ps	A<0	3.2 ps	A>0	33 ps	A<0	4.7 ps
A<0	13 ps	A>0	13 ps	A<0	54 ps	A>0	54 ps	A<0	64 ps	A>0	64 ps	A<0	33 ps	A>0	62 ps
A>0	71 ps	A>0	71 ps	A>0	130 ps	A>0	131 ps	A>0	1350 ps	A>0	1350 ps	A>0	1250 ps	A>0	1250 ps

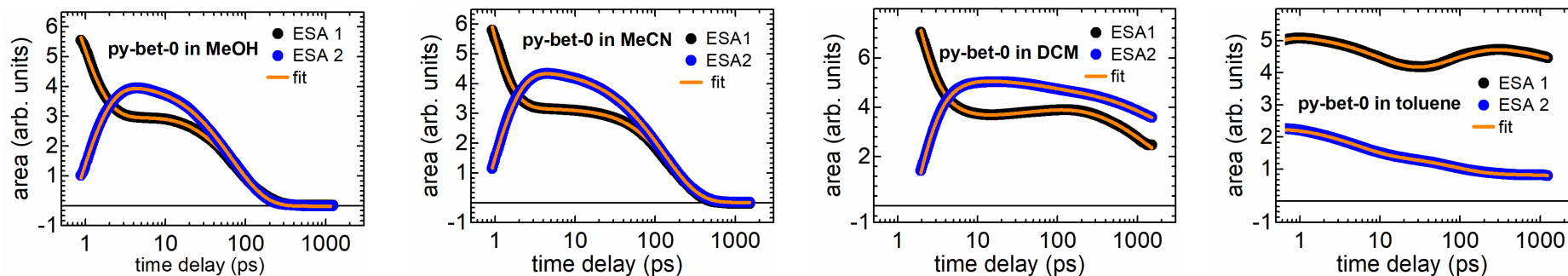


Figure 2-10 Time evolution of the area obtained from the parametrization for the ESA1 and ESA2 for **py-bet-0**.

Table 2-5 Fitting parameters from spectral parametrization for ESA obtained from the integral of the corresponding fitting function for **py-bet-CH₃** in various solvents.

py-bet-CH ₃ MeOH				py-bet-CH ₃ MeCN				py-bet-CH ₃ DCM				py-bet-CH ₃ toluene			
ESA1		ESA2		ESA1		ESA2		ESA1		ESA2		ESA1		ESA2	
-	-	-	-	-	-	-	-	-	-	-	-	A>0	0.3 ps	A<0	0.4 ps
A>0	0.4 ps	A<0	0.7 ps	A>0	0.7 ps	A<0	0.8 ps	A>0	0.8 ps	A<0	0.8 ps	A>0	1.5 ps	A<0	1.5 ps
A<0	8.4 ps	A>0	8.4 ps	A<0	72 ps	A>0	72 ps	A>0	4.0 ps	A<0	4.0 ps	A<0	20 ps	A>0	20 ps
A>0	122 ps	A>0	122.0 ps	A>0	210 ps	A>0	210 ps	A>0	1840 ps	A>0	1840 ps	A>0	1530 ps	A>0	1530 ps

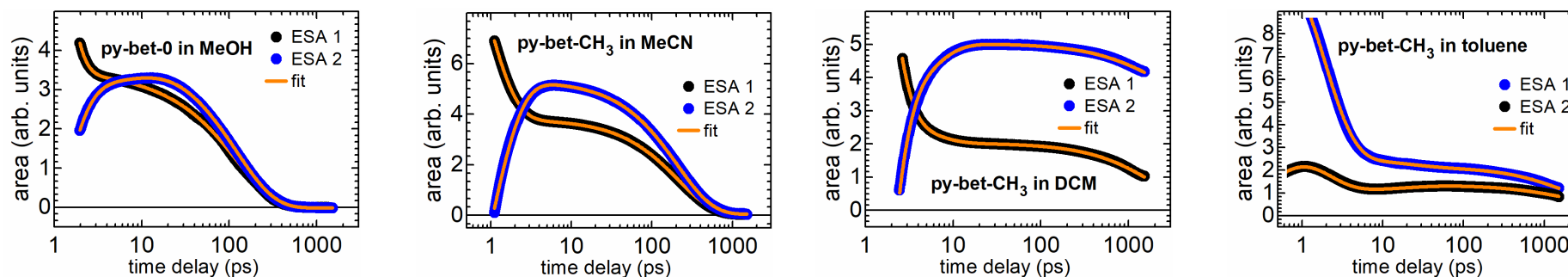


Figure 2-11 Time evolution of area obtained from the parametrization for the ESA1 and ESA2 for **py-bet-CH₃**.

2.2 Optimal use of a spectral photometer

Conditions for a measurement of an optimal baseline for UV/vis spectra

A possible source of systematic error in a detailed analysis of an UV/vis absorption spectrum is the diminished quality of the baseline of the photometric measurement. The form of the baseline is directly connected with the measurement of the reference. Since the correct baseline correction is critical for the accurate determination of molar absorptivity and thus for the determination of photospecies concentration, it is important to address the measurement of an optimal baseline for UV/vis spectra. The optimal baseline corresponds to $OD = 0$ over the entire spectral range when non-absorbing substrate is measured. The recommended procedure and the reasons for it are explained in detail below.

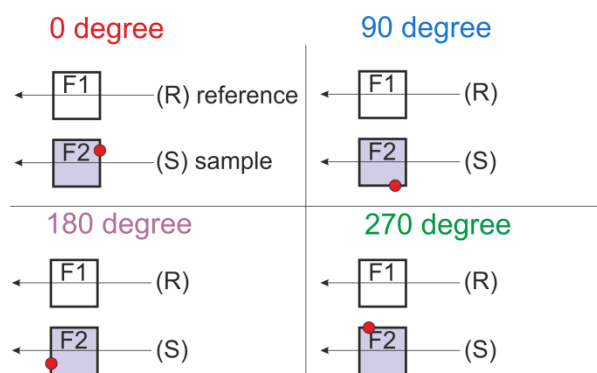


Figure 2-12 Schematic representation of the various orientations in the double beam spectrophotometer. The reference cuvette remains unchanged. The sample cuvette F2 was rotated by 90 degrees. The red dot is demonstrated only as a guide to the eye. Finally, the cuvette F2 was replaced by another cuvette F3. The experiment was performed analogously with absorption cuvettes A1, A2 and A3, however using rotation of 180°.

A double beam UV/vis spectrophotometer utilizes two beams, one passing the reference cuvette (R) and one passing the sample cuvette (S) (see Fig. 2-12). The baseline is measured before the first real measurement of the absorbing substance. It was observed that the individual differences of cuvettes as well as their orientations have a severe impact on the baseline. The observed deviations originate from the deviations in the parallelism of the cuvette windows and/or variations in the optical pathway.

In order to understand this effect, the following experiment was performed (see. Fig. 2-12). Three fluorescence (F1-F3, four polished sides) and three absorption cuvette (A1-A3, two polished sides) having an optical pathway of 10 mm, (Hellma) were filled with 2 mL of ethanol. A baseline scan was performed first. Then the baseline was measured using the cuvettes 1 (R) and 2 (S), thereafter the orientation of the cuvette 2 (S) was varied (see Fig, 2-12). In addition, the effect of the new cuvette 3 (S) measured under the previous baseline conditions was examined. The results are demonstrated in Figure 2-13 and Fig. 2-14.

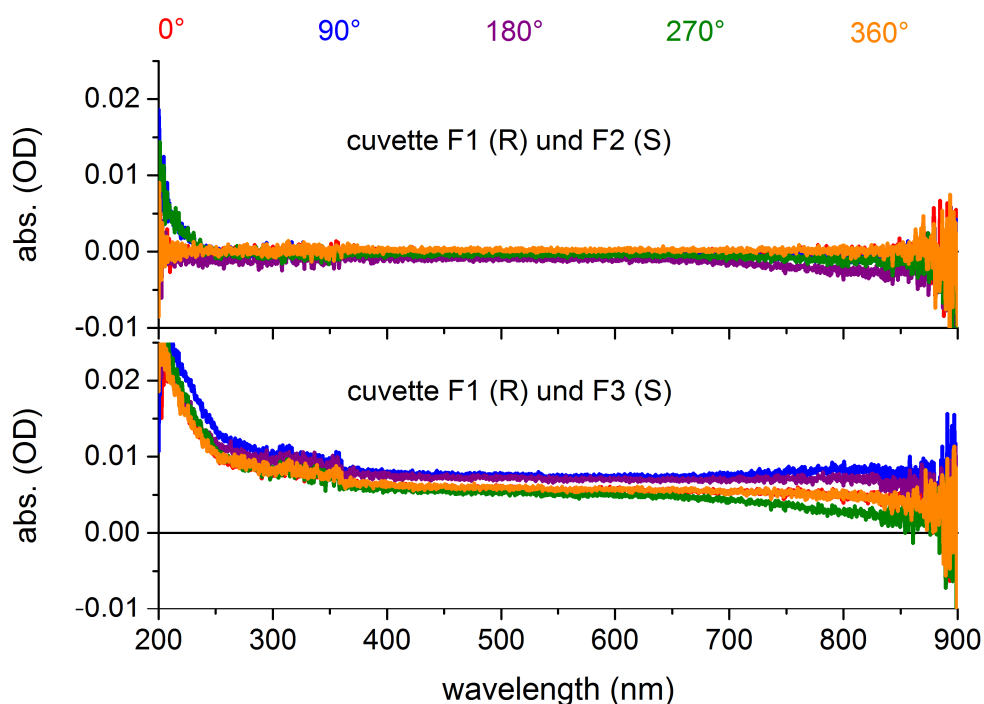


Figure 2-13 Impact of the fluorescence cuvette orientation on the baseline in an UV/vis spectrophotometer (SHIMADZU UV-2600).

Two fluorescence cuvettes F1 and F2 were filled with 2 mL ethanol. First, a baseline scan was performed with cuvettes F1 and F2 in the 0° orientation. Then the UV/vis spectra were measured in the different orientations 0° - 360° of F2 (top) with 0° orientation of F1. In addition, the measurement was repeated using a different fluorescence cuvette F3 instead of F2 (bottom). Any change of orientation or introduction of a new cuvette leads to noticeable deviations in the baseline.

According to the resulting deviations in the absorption spectra, it is recommended to consider following points for a double beam spectrometer:

- a. measure the baseline with two cuvettes filled with a solvent
- b. subsequently, empty and dry the signal cuvette and fill it with the sample
- c. preserve the orientation of the cuvette during the measurement

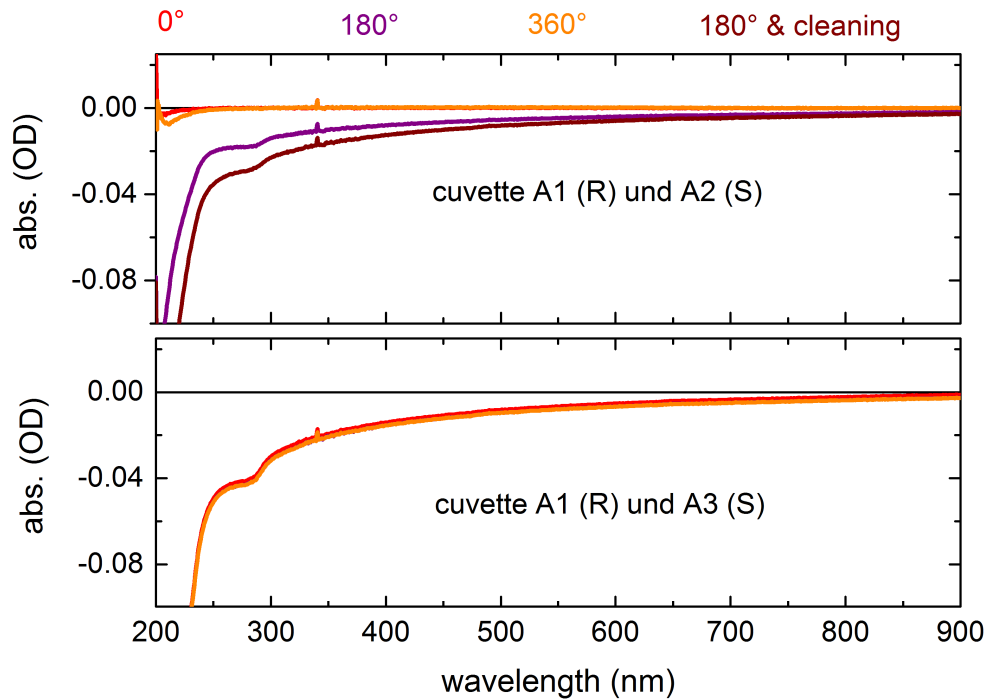


Figure 2-14 Analog to Figure 2-13, measured with absorption cuvettes.

Two absorption cuvettes A1 and A2 were filled with 2 mL ethanol. First, a baseline scan was performed with cuvettes A1 and A2 in the 0° orientation. Then the UV/vis spectra were measured in the different orientations 0° - 360° of F2 (top) with 0° orientation of A1. In addition, the measurement was repeated using a different absorption cuvette A3 instead of A2 (bottom). Any change of orientation or introduction of a new cuvette leads to noticeable deviations in the baseline.

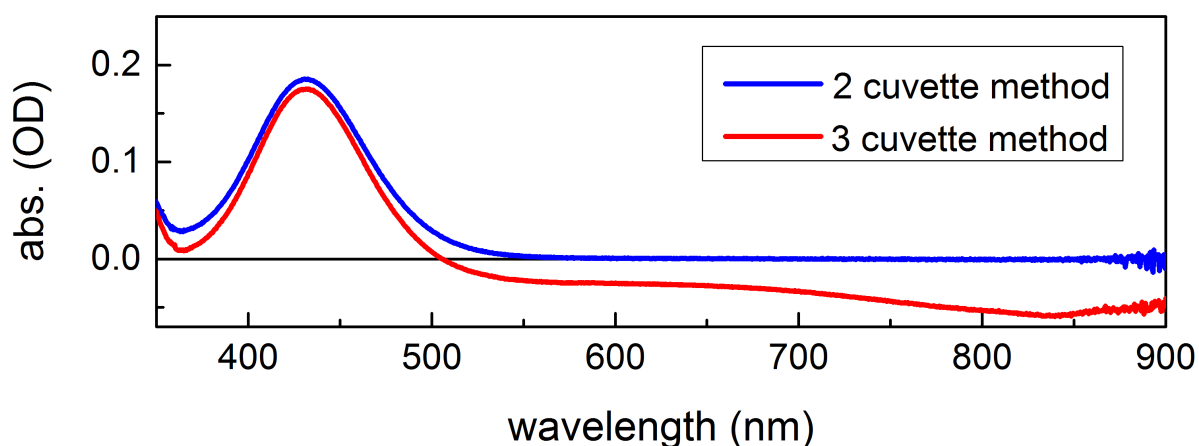


Figure 2-15 Impact of the measurement method on the spectrum/baseline of azobenzene in ethanol measured with the procedures described above.

In some cases of nearly constant shift of the baseline it is reasonable to try to clean the cuvette. On the other hand, assuming correct handling of the cuvette, the windows are not expected to be contaminated and no additional cleaning is required.

According to recent experience, the use of the third cuvette may be advantageous under these circumstances. The third cuvette serves as a reference after the baseline has been measured using the two-cuvette method mentioned above. In this way, an additional cuvette is spectroscopically defined and can be used at regular time steps to check the quality of the baseline.

In summary, it is recommended to use only two cuvettes for the whole UV/vis measurement ("2 cuvette method"). The application of an additional cuvette that is not concerned in the baseline correction may in extreme cases as demonstrated in Fig. 2-15 lead to extensive deviation in the baseline ("3 cuvette method").

In some special cases, a longer illumination period than 12 hours is required to follow the photochemical or photocatalytic reaction. In such cases, deviations in the baseline may occur (e.g., drift), which must be taken into account in the evaluation.

According to recent experience, the use of the third cuvette may be however advantageous under these circumstances. The third cuvette serves as a reference after the baseline has been measured using the two-cuvette method mentioned above. In this way, an additional cuvette is spectroscopically defined and can be used at regular time steps to check the quality of the baseline.

2.3 High end fluorescence setup with improved sensitivity

The information about the fluorescence (FL) properties of the species may provide a deeper understanding of the molecular dynamics upon irradiation with light. However, in some cases the commercially available fluorescence spectrometer cannot fulfill the measurement requirements such as detection of weak signals or detection in the NIR or IR region.

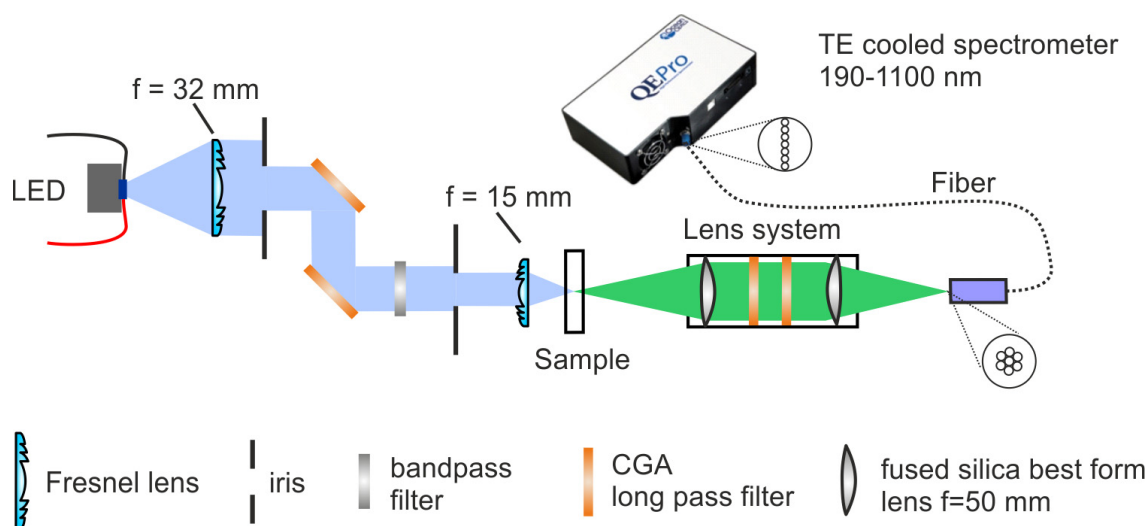


Figure 2-16 Schematic representation of the high-end fluorescence setup.

Therefore, a setup of our own design is introduced. An easily exchangeable LED is used as an excitation source. The light is imaged into the sample by a lens system consisting of two Fresnel lenses (UV acrylic material, Fresnel Technologies, Inc.). The first lens ($f = 32$ mm, $\text{Ø} = 2$ inch) collimates the light and the second lens ($f = 15$ mm, $\text{Ø} = 2$ inch) images the light into the sample. The SMD chip of the LED is typically 1 mm. Consequently, the spot size in the sample is about $500 \mu\text{m}$. In order to suppress undesired wavelengths above the nominal wavelength, a pair of long pass filters (Newport, color glass alternative (CGA) filter) is introduced after the first iris in a reflective geometry (see. Fig. 2-16). Optionally, a band pass filter can be used to control the spectral distribution of the excitation light.

The excitation power can be easily controlled by the current applied on the LED. The typical excitation power used is in the mW region or below. The sample is constantly stirred to prevent photodegradation. The fluorescence signal is collected by a pair of fused silica best form lenses ($f = 50$ mm, B. Halle) and imaged into the fibers. The “round-to-linear” fiber bundle (Thorlabs product # BFL200 S02) is used to enhance to collection efficiency. This fiber bundle consists of seven fibers ($200 \mu\text{m}$ each) arranged in a hexagonal shape on one

end that transitions to a linear arrangement on the other so that the match to the detector – actually the entrance slit - is optimized. Hereby, the fiber with a high hydroxyl ion content (high OH: 250 nm to 1200 nm) or a low hydroxyl ion count (low OD: 400 nm to 2400 nm) can be used. The high sensitivity spectrometer (Ocean Optics, QE Pro) with a CCD array is cooled by a Peltier element and covers the wavelength range from 190 to 1100 nm. The typical OD of the sample at the excitation wavelength is below 0.1 OD to avoid an inner filter effect. For a large Stokes shift of this fluorescence even a higher OD can be used.

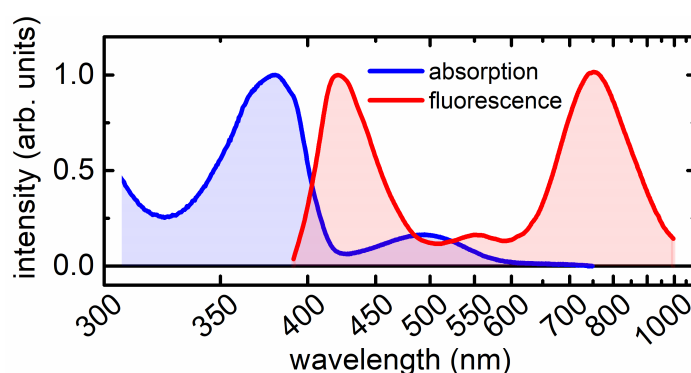


Figure 2-17 Absorption and fluorescence of the HTI photoswitch under excitation with 365 nm LED. The data originate from ref. [Wil23]. Lifetime of states S_2 and S_1 are 360 fs and 660 fs, respectively.

In addition to the optimized collection and detection of the FL signal, the setup benefits from the LED as an excitation light. In contrast to pulsed laser sources, the LED in cw-mode accumulates the molecules in the excited state. Consequently, the fluorescence signal is increased and even species with low fluorescence quantum yield or very short fluorescence lifetimes and weak fluorescence are well resolved, see Fig. 2-17. Since the lifetimes of the state S_2 ($\tau_2 = 360$ fs) and S_1 ($\tau_1 = 660$ fs) are rather short, the FL cannot be detected with a commercially available setup. However, our high-end fluorescence setup of own design can detect and resolve straightforwardly even weak FL signals. A typical overall recording time of just 1 s suffices due to the multi-channel detection.

For the detection of emission spectra in the range up to 1700 nm an InGaAs based spectrometer is used. Again, the detector in the Ibsen photonics, ROCK NIR RSM-445 Spectrometer, Wavelength range: 900 - 1700 nm, Resolution: 3.3 nm is Peltier-cooled. As a result, a comparatively low priced and extremely fast NIR emission spectrometer is obtained. The NIR range is gaining increasing interest for the investigation of solar harvesting devices.

Appendix for Chapter 2

Appendix 2-A

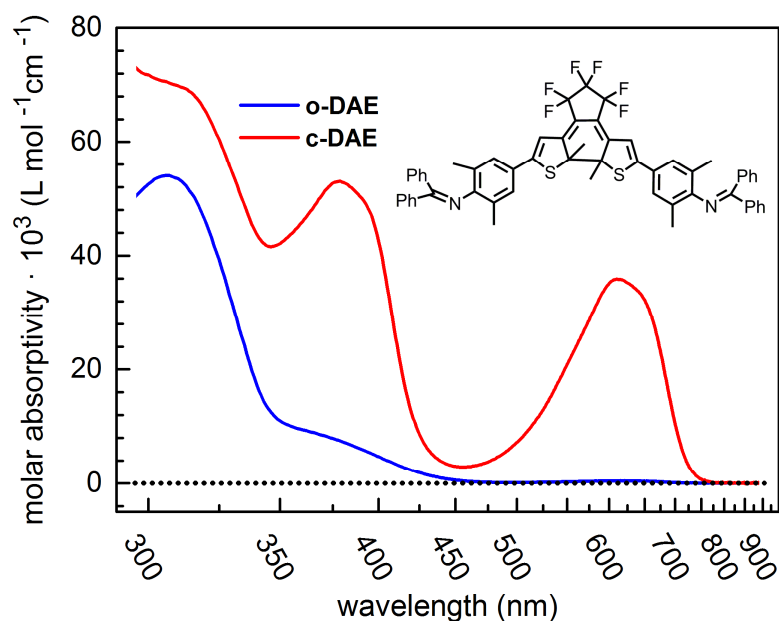


Figure 2-A1 Molar absorptivity spectra of the pure open and closed form of investigated diarylethene molecule in toluene.

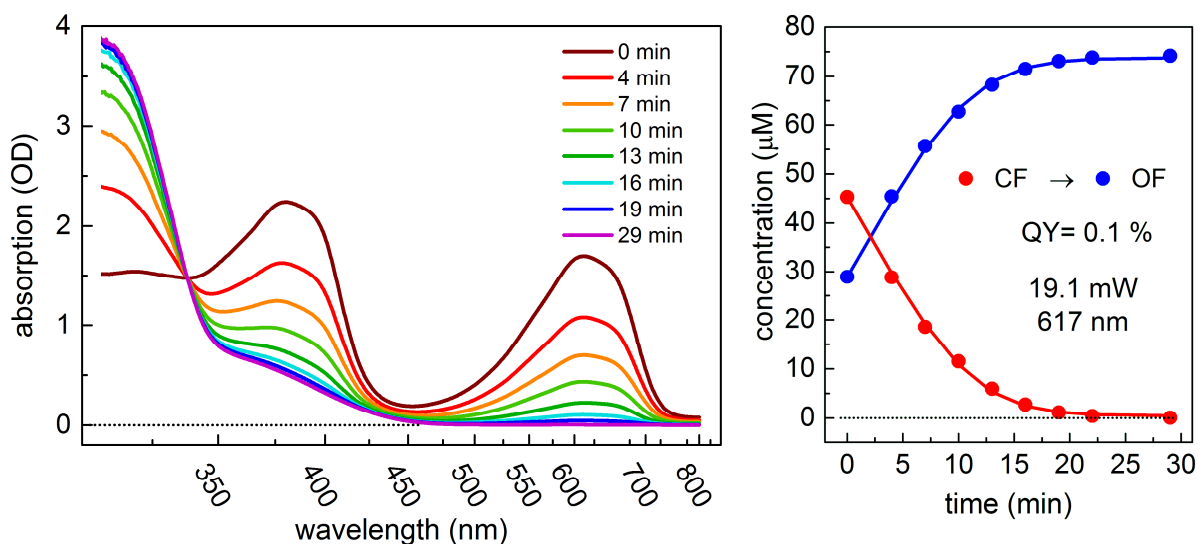


Figure 2-A2 (left) Spectral changes of the open form of **c-DAE** molecule upon illumination with a 617 nm LED with a power in the sample of 19.1 mW. A solution of 74 μM in a 10 mm absorption cuvette with volume of 2 mL was used. (right) Time evolution of concentrations during the illumination and numerical simulation (fit).

Appendix 2-B

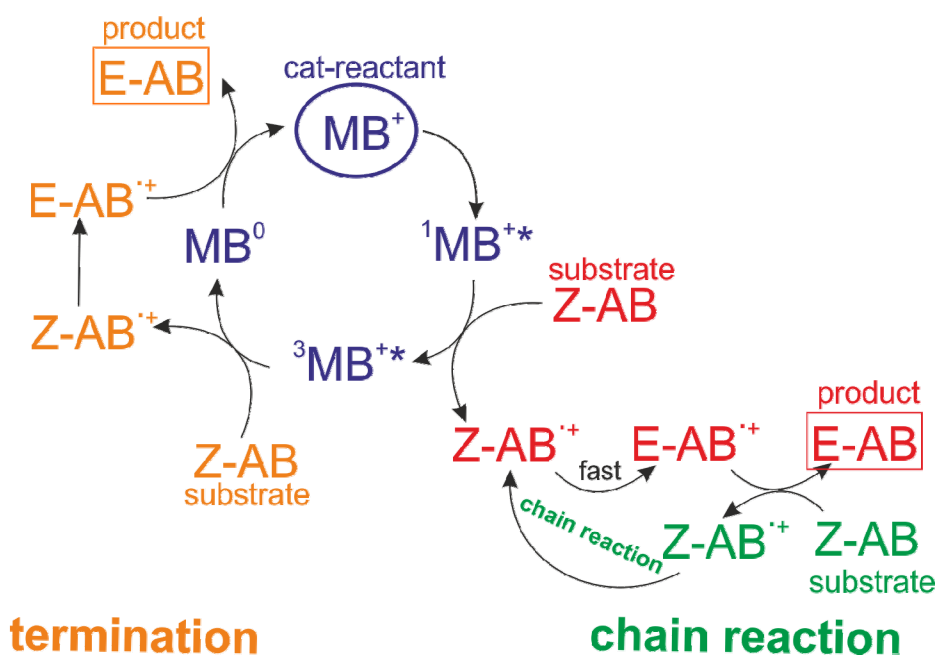


Figure 2-B1 Proposed reaction mechanism of the oxidative catalysis of **Z-AB** with photosensitizer **MB**.

The nanosecond transient absorption measurements on **MB** were performed under standard conditions as well as under nitrogen atmosphere. For the degassed conditions an integrated degasser (Kanuer Online Degasser) was used that continuously removes the oxygen from the solution. It enables to reach an oxygen concentration of about 20 times lower than under standard conditions. The results are summarized in Tab. 2-B.

Table 2-B Lifetime of the triplet state for MB τ_T in acetonitrile for various experimental conditions extracted from nanosecond transient absorption spectroscopy.

photosensitizer	substrate	measurement conditions	lifetime of MB triplet state τ_T (ns)
MB	-	with O ₂	270
MB	-	degassed with N ₂	3 500
MB	Z-AB	degassed with N ₂	560

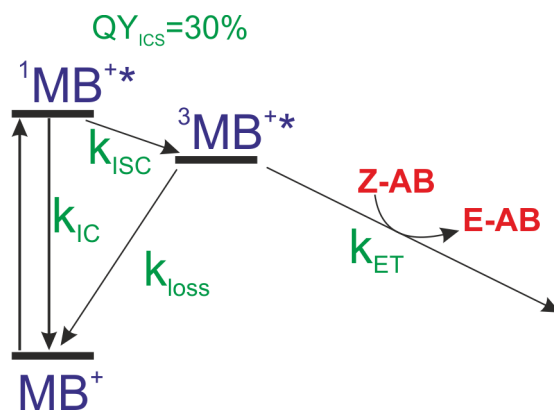


Figure 2-B2 Kinetic model of the oxidative radical-cation-catalyzed isomerization in presence of photosensitizer **MB**.

The reaction quantum yield can be also extracted from the rate constants that participate in the reaction. The rate constant of a successful reaction k_{SR} consists of the rate constant of the electron transfer k_{ET} and the rate constant for intersystem crossing back to the ground state k_{loss} :

$$k_{SR} = k_{ET} + k_{loss} \quad (B-1)$$

The lifetime of the triplet state under degassed conditions is $3.5 \mu s$, whereby this lifetime is reduced to 560 ns , if the substrate **Z-AB** is present. From this information the rate constant of the electron transfer k_{ET} can be extracted:

$$k_{ET} = 1.5 \cdot 10^6 \text{ s}^{-1} \quad (B-2)$$

The reaction quantum yield can be calculated according to:

$$RQY = \frac{k_{ET}}{k_{SR}} = 84 \% \quad (B-3)$$

This value gives a good agreement with the value of 82% obtained with the aid of the TEM method described in Section 2.1.

Appendix 2-C

The pyridinium based betaines are aromatic molecules with a zwitterionic donor acceptor moiety [Lev91, Mal12]. The majority of betaines have a dipolar electronic ground state that cannot be formally represented by a mesomeric chargeless structure [Mac14, Xu17].

The systems under study **py-bet-0** and **py-bet-CH₃** (see Fig. 2-C1) consist of three different groups: diphenylamine, pyridinium and enolate moiety. The pyridinium and enolate moieties are not in a co-planar arrangement but twisted with a torsion angle of about 30°. This breaking of co-planarity is even more pronounced, when a pyridinium is substituted with an additional methyl group (see Fig.2-C1 top right).

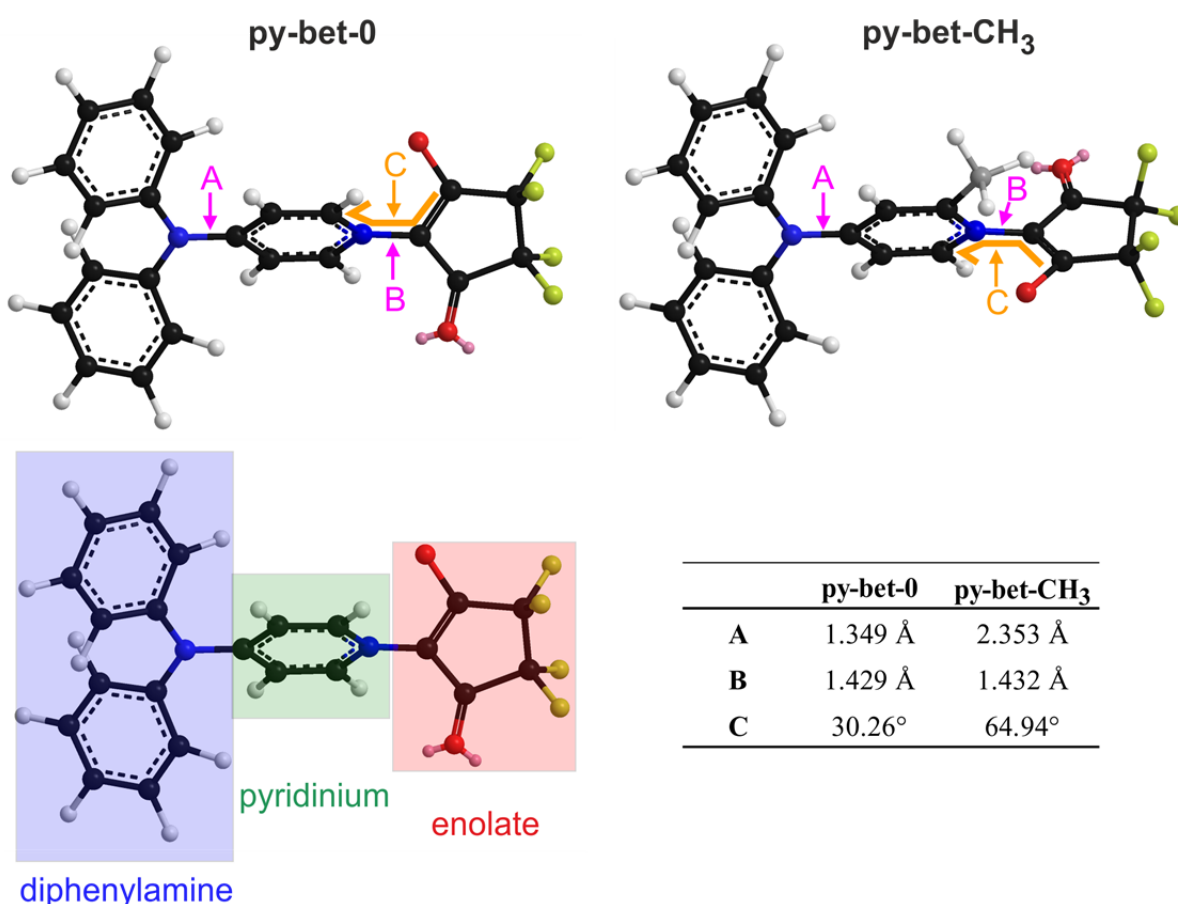


Figure 2-C1 Molecular structure of the pyridinium based betaines **py-bet-0** and **py-bet-CH₃** under study with corresponding bond lengths and angles summarized in table bottom right. Coloring of atoms: black = carbon, red = oxygen, grey = hydrogen, yellow = fluorine.

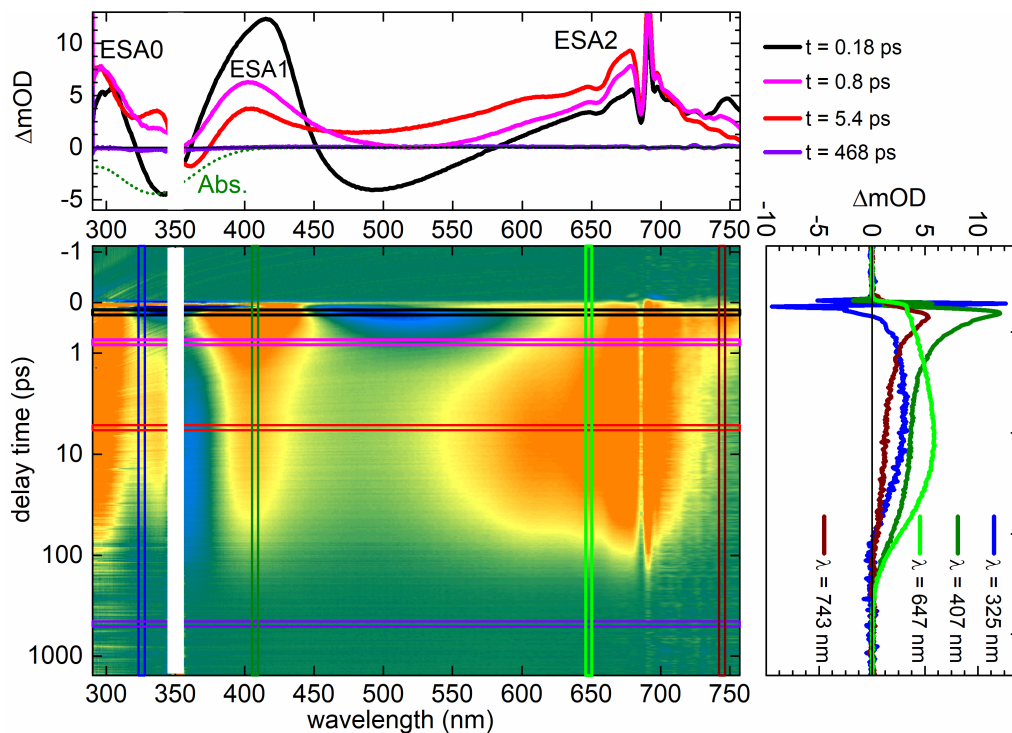


Figure 2-C2 Transient absorption data of a 1.4 mM solution of **py-bet-0** in methanol measured in a 100 μm thick flow cell after excitation with 45 fs pulses centered at 348 nm having a pulse energy of 150 nJ.

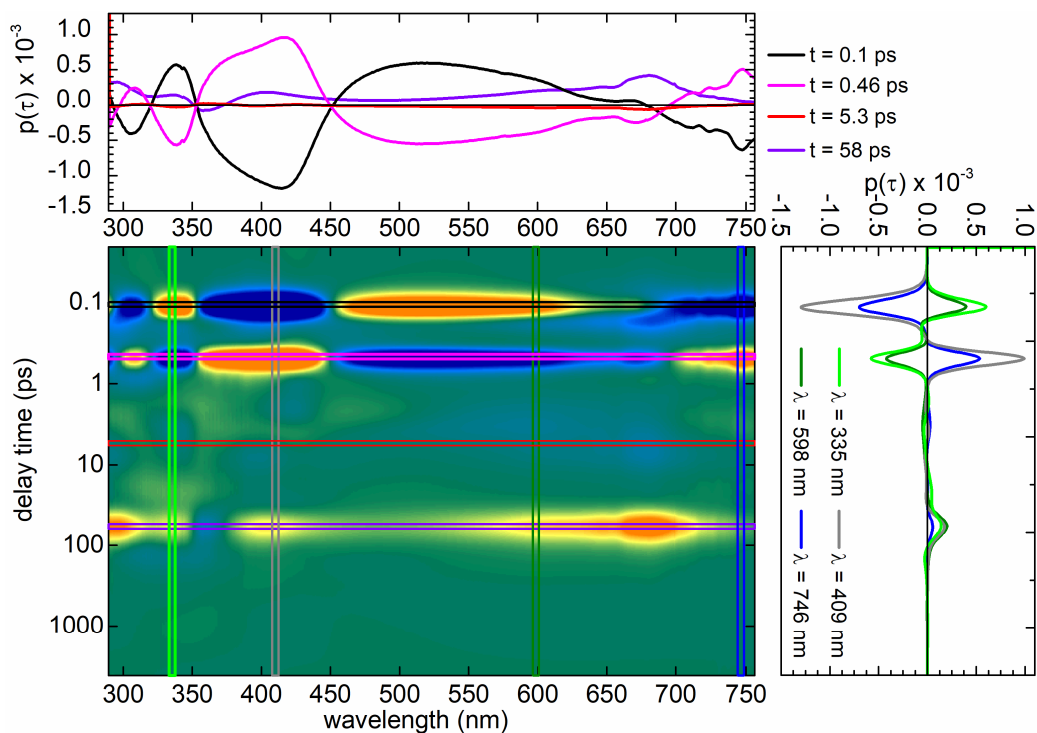


Figure 2-C3 Maximum entropy analysis for the fs/ps data set from Fig. 2-C2.

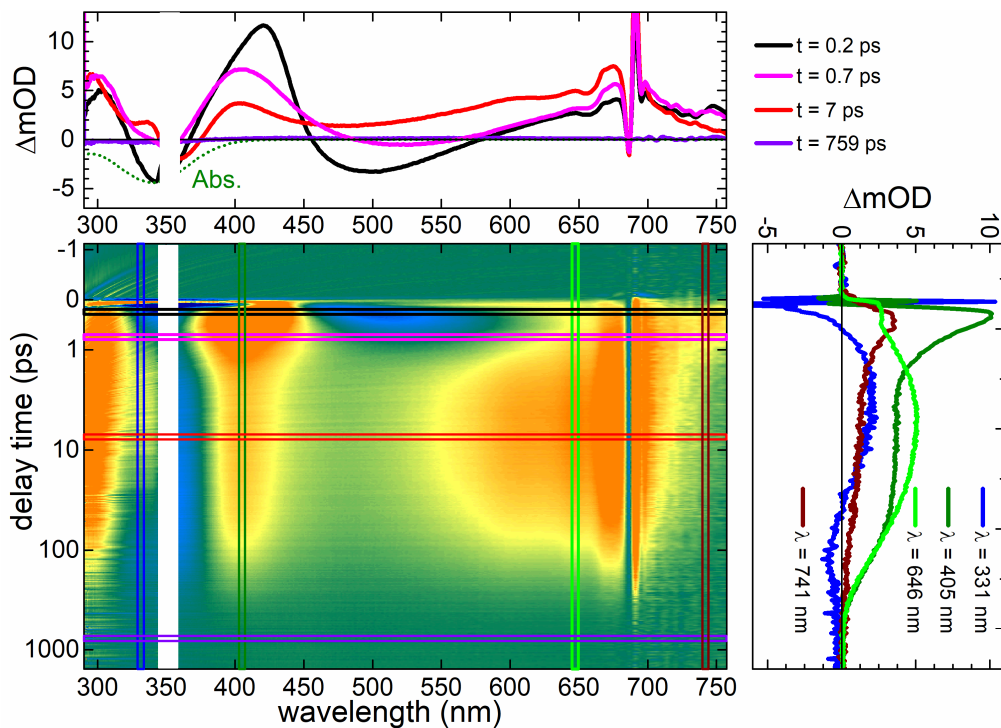


Figure 2-C4 Transient absorption data of a 1.2 mM solution of **py-bet-0** in acetonitrile measured in a 100 μm thick flow cell after excitation with 45 fs pulses centered at 348 nm having a pulse energy of 140 nJ.

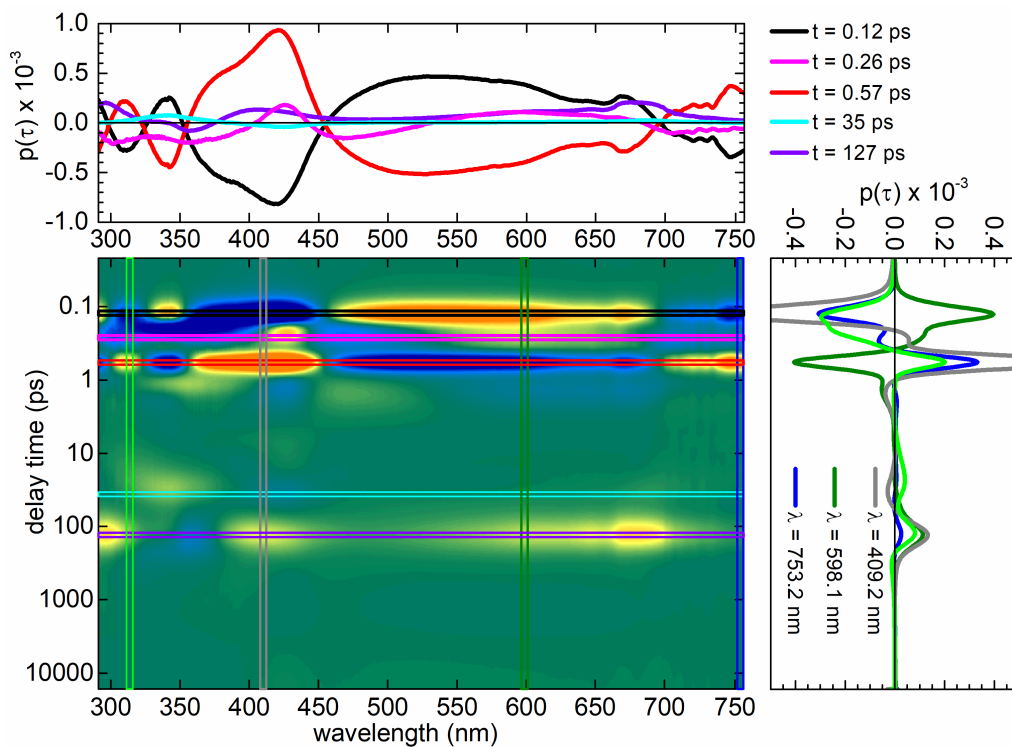


Figure 2-C5 Maximum entropy analysis for the fs/ps data set from Fig. 2-C4.

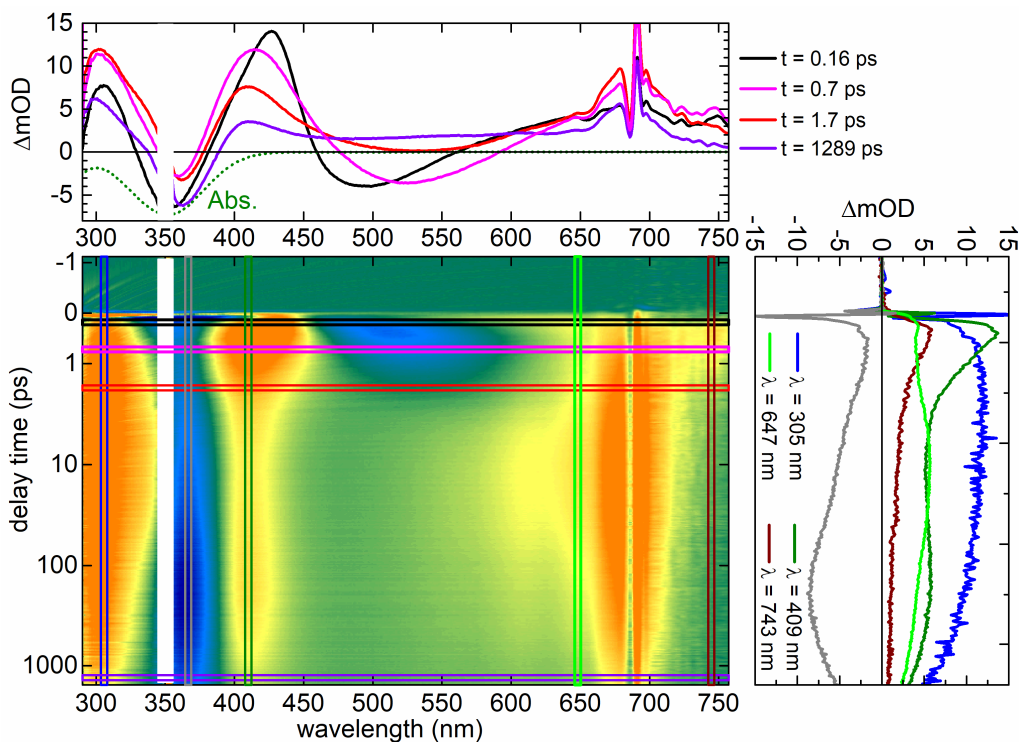


Figure 2-C6 Transient absorption data of a 1.6 mM solution of **py-bet-0** in DCM measured in a 100 μm thick flow cell after excitation with 45 fs pulses centered at 348 nm having a pulse energy of 150 nJ.

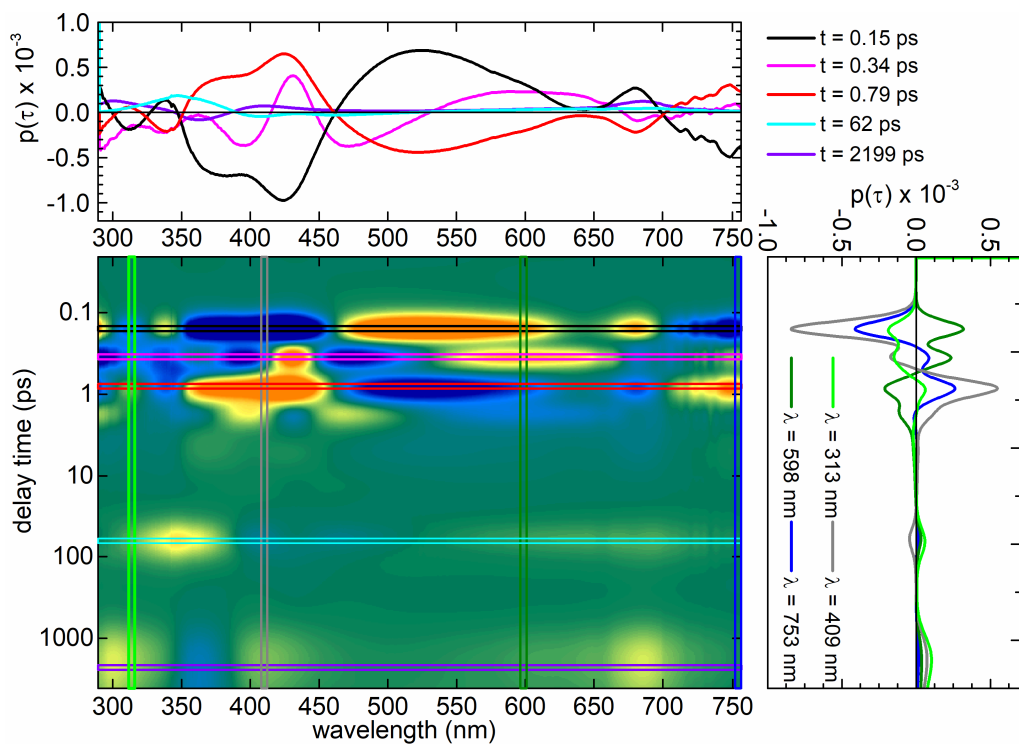


Figure 2-C7 Maximum entropy analysis for the fs/ps data set from Fig. 2-C6.

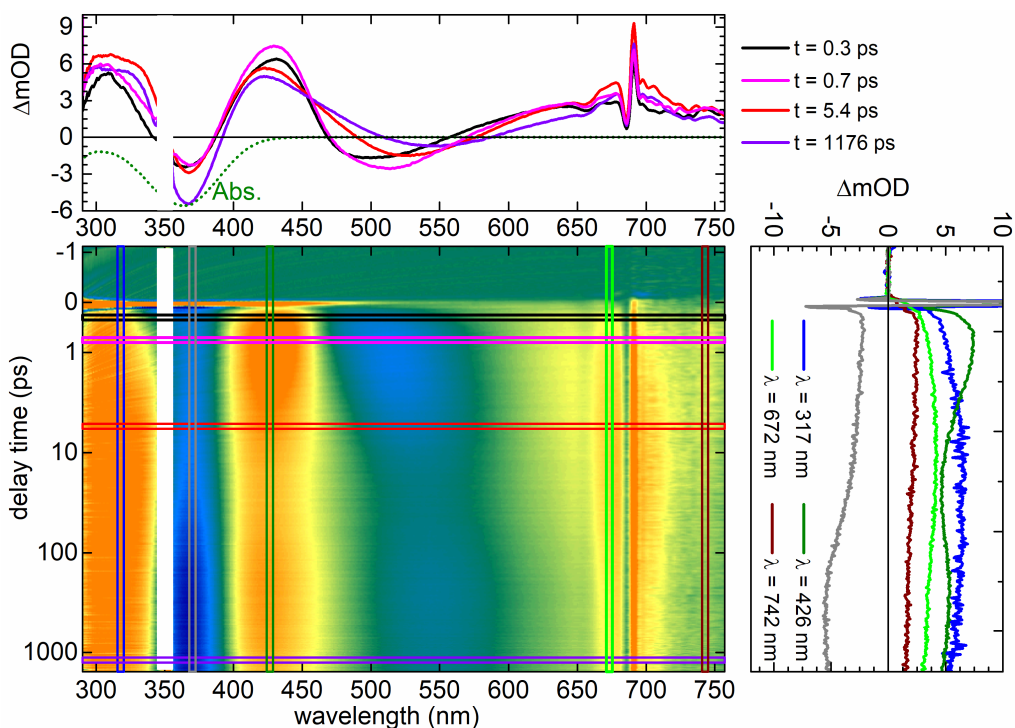


Figure 2-C8 Transient absorption data of a 1.1 mM solution of **py-bet-0** in toluene measured in a 100 μm thick flow cell after excitation with 45 fs pulses centered at 348 nm having a pulse energy of 150 nJ.

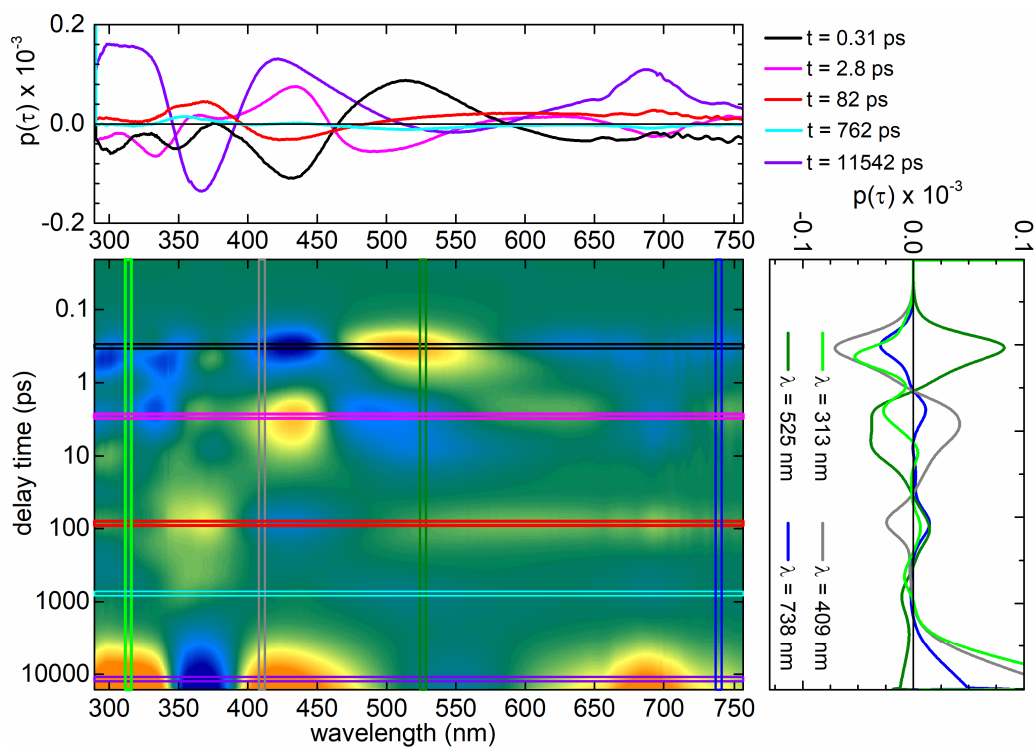


Figure 2-C9 Maximum entropy analysis for the fs/ps data set from Fig. 2-C8.

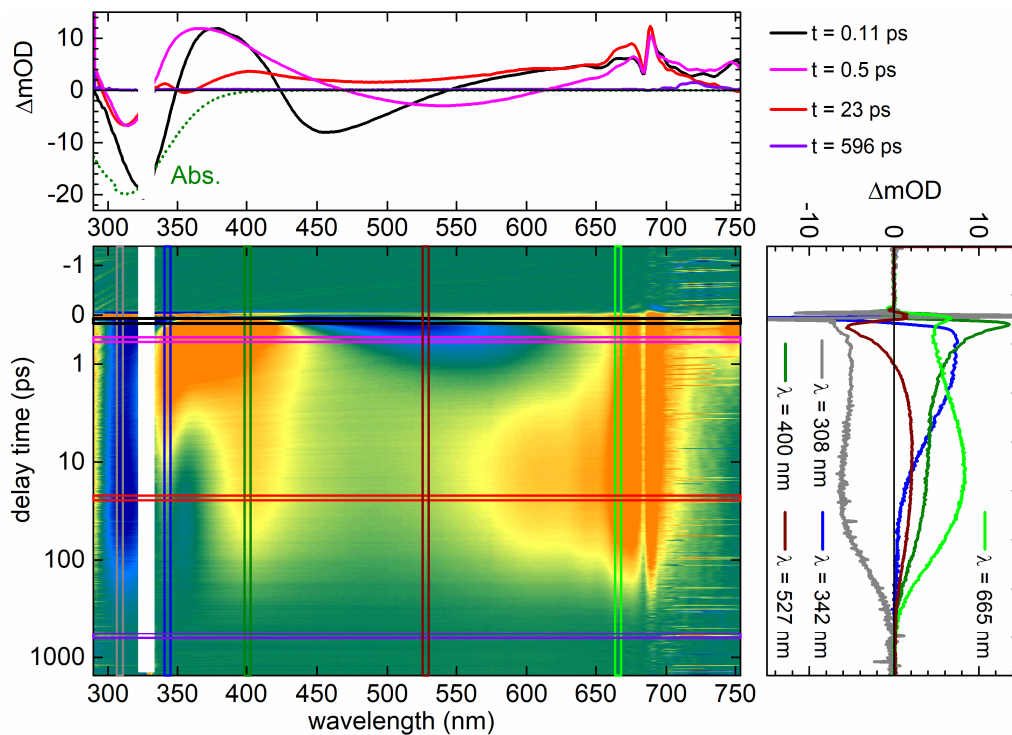


Figure 2-C10 Transient absorption data of a 2.2 mM solution of **py-bet-CH₃** in methanol measured in a 100 μm thick flow cell after excitation with 45 fs pulses centered at 330 nm having a pulse energy of 159 nJ.

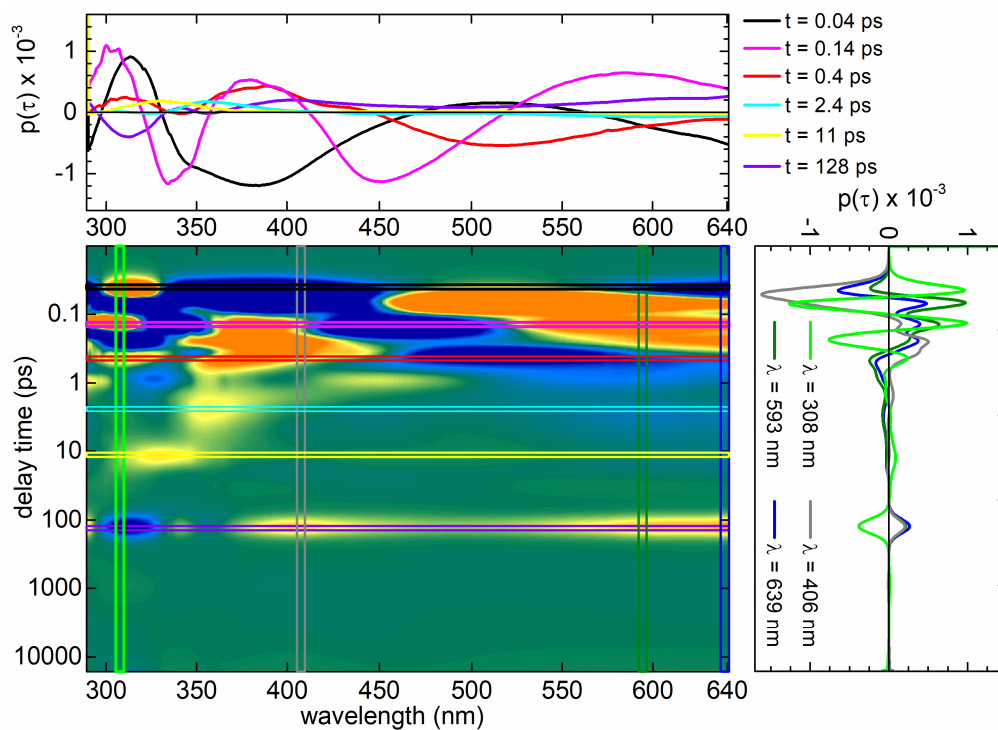


Figure 2-C11 Maximum entropy analysis for the fs/ps data set from Fig. 2-C10.

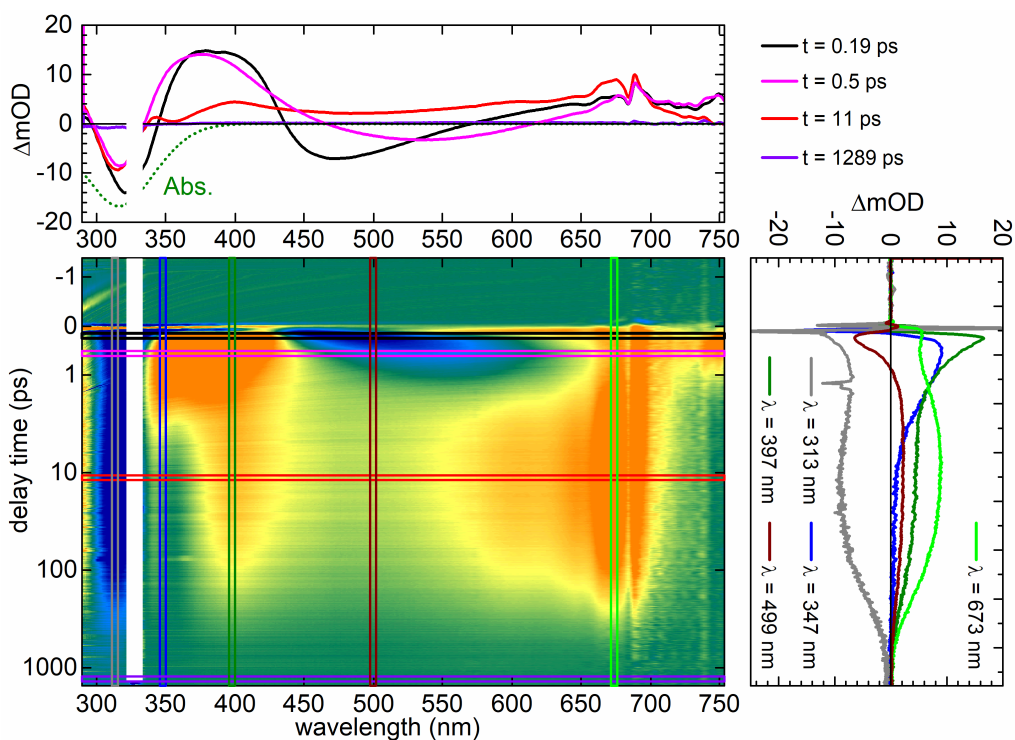


Figure 2-C12 Transient absorption data of a 1.7 mM solution of **py-bet-CH₃** in acetonitrile measured in a 100 μm thick flow cell after excitation with 45 fs pulses centered at 330 nm having a pulse energy of 166 nJ.

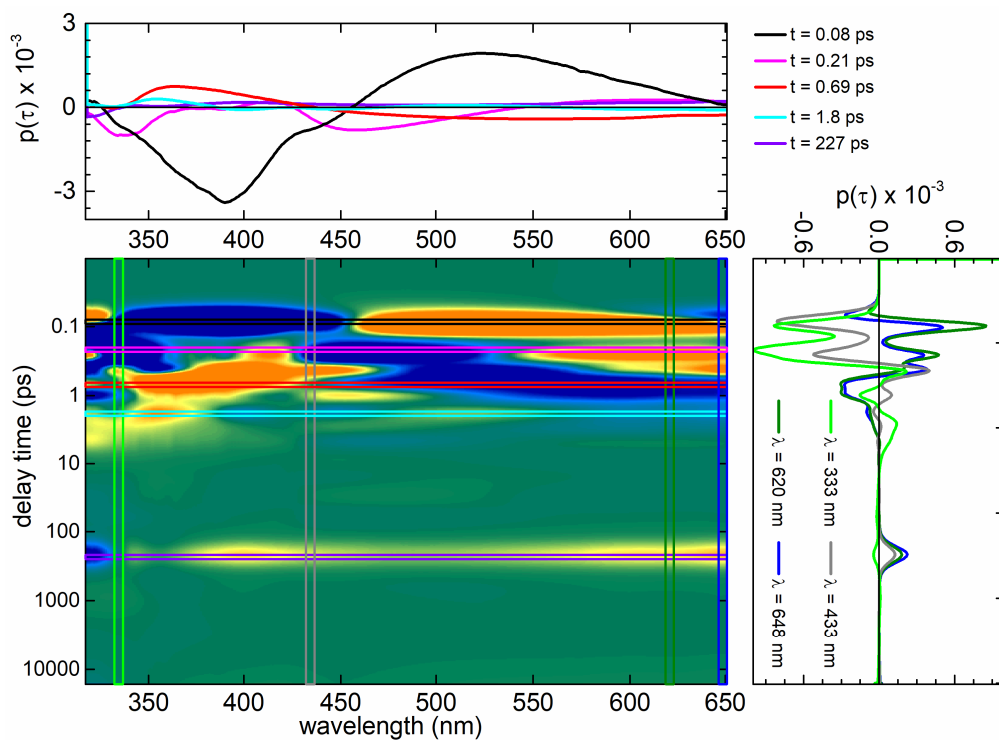


Figure 2-C13 Maximum entropy analysis for the fs/ps data set from Fig. 2-C12.

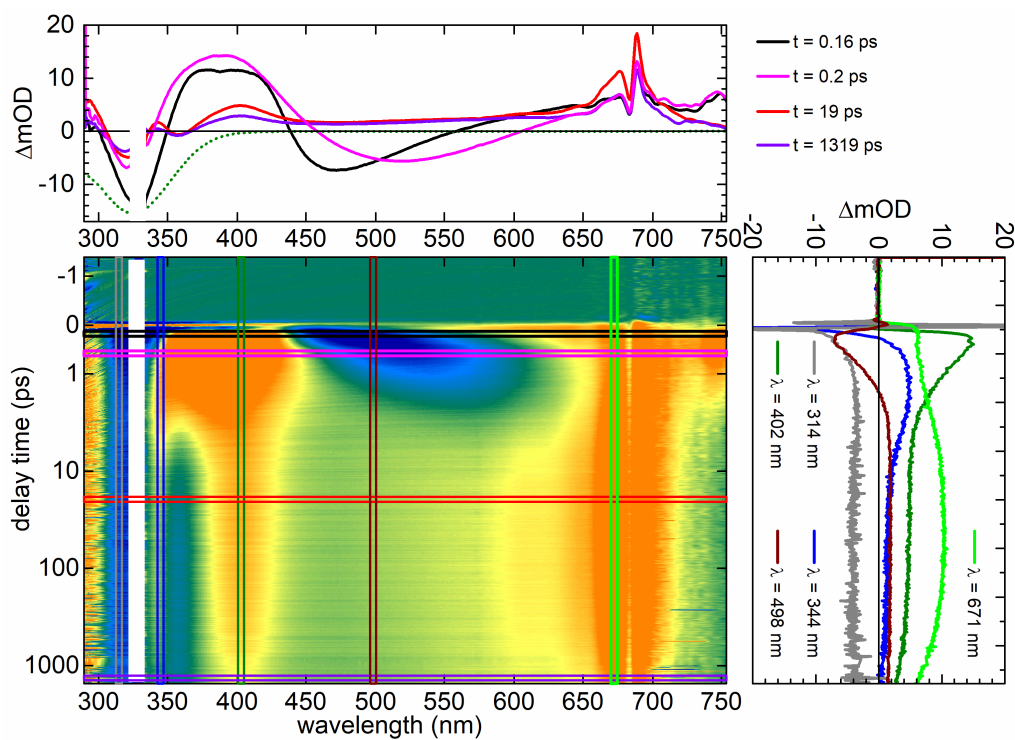


Figure 2-C14 Transient absorption data of a 2.3 mM solution of **py-bet-CH₃** in DCM measured in a 100 μm thick flow cell after excitation with 45 fs pulses centered at 330 nm having a pulse energy of 166 nJ.

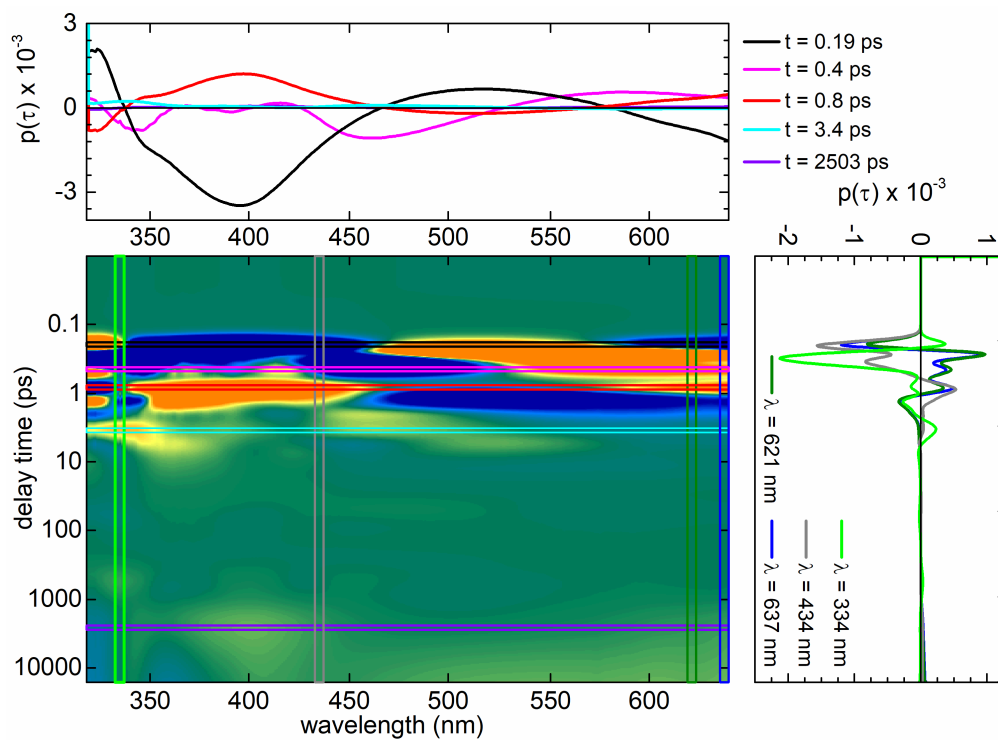


Figure 2-C15 Maximum entropy analysis for the fs/ps data set from Fig. 2-C14.

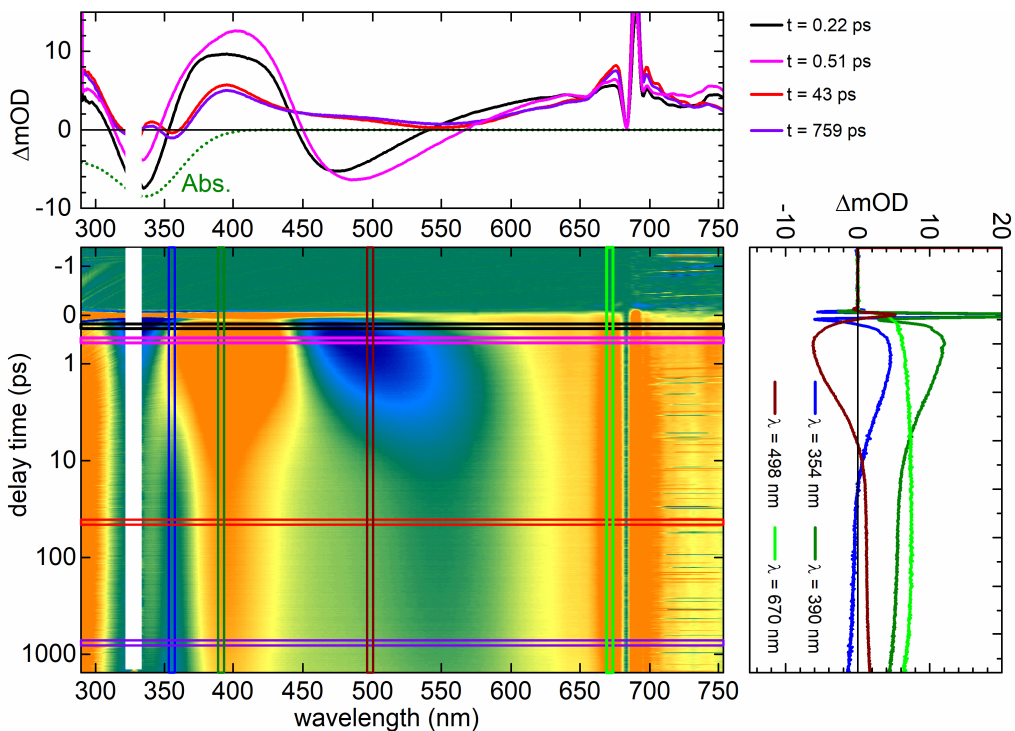


Figure 2-C16 Transient absorption data of a 2.9 mM solution of **py-bet-CH₃** in toluene measured in a 100 μm thick flow cell after excitation with 45 fs pulses centered at 330 nm having a pulse energy of 159 nJ.

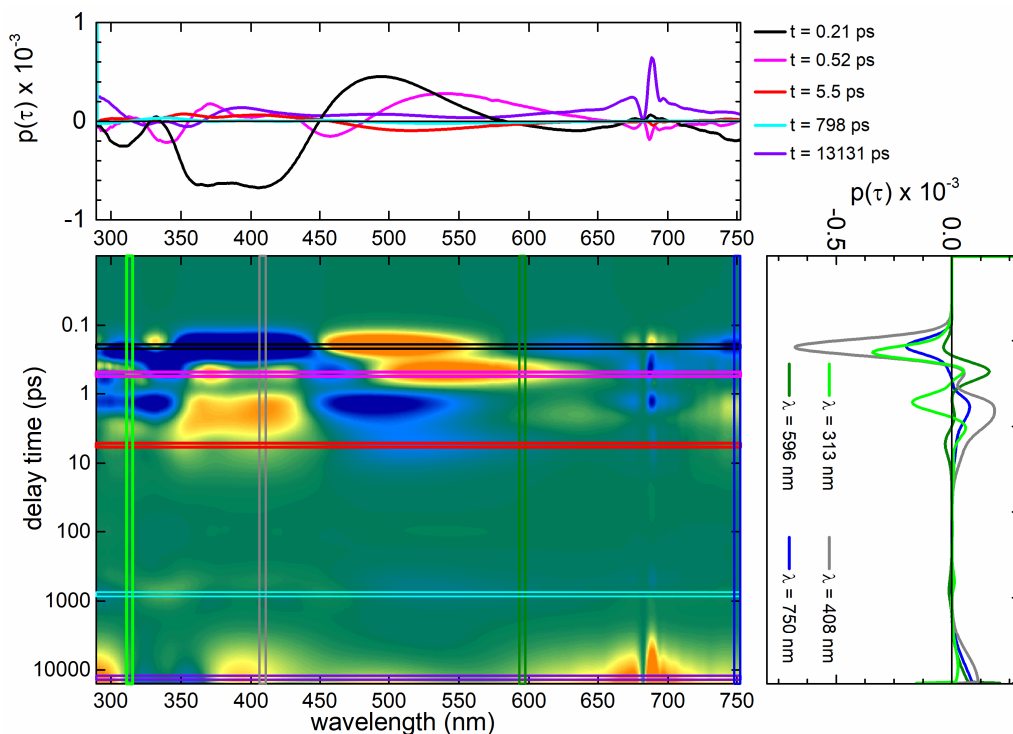


Figure 2-C17 Maximum entropy analysis for the fs/ps data set from Fig. 2-C16.

3. Optimized reaction quantum yield determination setup with better than 5% relative error

3.1 Introduction

To gain control over chemical processes is of significant interest in the realm of chemistry. Over a long period, chemical reactions were studied mainly within the scope of thermodynamic parameters such as reaction temperature or pressure. Subsequently, light became one of the most powerful tools to promote various reactions.

A notable improvement and progression were achieved with the invention of nowadays widely employed light emitting diodes (LED). These LEDs, providing high illumination power, introduced in an inexpensive and commercially easy accessible way narrow band light sources with several advantageous features [The14, Nar17, Sen17, Pat18].

One of the utmost interests in photochemistry concerns the cost of such a light induced process. The information about how many absorbed photons are required per one molecule for a successful reaction is described by the reaction quantum yield (RQY). In some special cases even the reaction mechanism can be predicated (e.g., the $RQY > 1$ points to a radical chain reaction [Lov19, Cis15]).

Although the first mention of RQY goes back to the 1910s [War13, War17, Rub10], it is still the paramount characteristic for photocatalysis [Cis15, Pit15, Mar18, Buz19, Lov19] and photochemistry [Iri14, Pri13, Pet18, Zho19, Dat20]. Since the actinometry [Kuh04] as the state-of-the-art for RQY determination has its well-known shortcomings and restrictions [Dem76, Bow76, Kir83, Wri20], it is important to approach the issue of measuring the RQY, concerning the overall concept, the accuracy and the cost.

In this chapter a totally rebuilt version of the Quantum Yield Determination Setup (QYDS) [Meg10] as a compact solution for rapid and facile determination of the RQY with better than 5% relative error is introduced. Due to the combination of controlled illumination and careful evaluation, which is applicable without restrictions for various photosystem categories, the QYDS method should replace chemical actinometry as a much more powerful alternative. Since the need for a simple and versatile setup to determine QY was reported [Mas10], it is in our interest to establish a measurement method that does not depend on experimental boundary conditions and provide robust RQY values within standard lab conditions.

QYDS is successfully used since 2010 by numerous groups worldwide (for complete list of users see Appendix 3-A) [Tuc12a, Maj16, Hof17, Ass18, Raw18, Xu18, Ger19, Lac19, Bue20]. Importantly, the QYDS is a modular setup that is applicable for any system in the field of photocatalysis, photochemistry and molecular switches.

3.2 Reaction quantum yield and its measurement methods

In the realm of photochemistry the RQY $\phi(\lambda)$ is defined as the number of a specific reaction product N_{prod} per number of absorbed photons of the photoactive species $N_{\text{ph,abs}}$ [McNau97, Bra07, Ser02]:

$$\phi(\lambda) = \frac{N_{\text{prod}}}{N_{\text{ph,abs}}} \quad (3.1)$$

However, this simple version of the formula does not consider that the newly formed product molecules may also absorb the excitation light. This product absorption can lead to wrong values within the experiment. For a precise determination of RQY a detailed analysis of the following two parameters is required: first, the number of absorbed photons by a reactant and second, the number of created product. The latter can be extracted from standard analytical methods like UV/vis, NMR spectroscopy or other spectroscopic methods. The number of photons can be nowadays straightforwardly determined by a commercially available calibrated thermopile power meter within a moderate price category. Overall the RQY has to be considered as a differential and time dependent quantity.

In the first half of 19th century, the thermopiles had too small an active detector area and were not common to find in a standard chemistry laboratory [Lei30]. In order to overcome this problem, the RQY of several photochemical reactions [Lei30, Lei34, Cal52, Par53, Hat56, Zim58] were characterized and defined as chemical actinometers. These chemical systems with known RQY allowed to determine the number of photons indirectly [McNau97] and thus the chemical actinometry became the state-of-the-art method for the quantification of light.

However, in the case of actinometry an additional spectroscopic measurement is required only for the quantification of the incident light. Furthermore, the chemical actinometer needs to absorb in the same wavelength range as the system under study. Considering all the actinometers suggested by IUPAC [Kuh04, Mon06], there is a notable limitation when choosing an appropriate actinometric system: from 67 actinometers only 41 are

commercially available. From these only 13 are reliable and possible to analyze with UV/vis. Ten of them are suitable for the UV range between 200 nm and 400 nm, while only three are applicable between 400 nm and 500 nm. Although there are still efforts to report novel actinometers, the wavelength range is always restricted to below 700 nm [Pit15, Rei19a, San09]. Additionally, the actinometer reactions are rather complex and require advanced laboratory conditions and skilled personal.

An additional disadvantage of the chemical actinometry is that the list of proposed actinometers widely accepted in the community relies on results which were measured within the technical scope of the fifties and sixties [Par53, Hat56]. The huge necessity to redetermine these values is still underestimated. For example, the reaction QY of the widespread actinometer azobenzene varies in the literature by a factor of two with respect to the solvent, the wavelength excitation and the isomerization direction (see Tab. 3.2) [Bir53, Bor79, Rau84, Mon06]. Recently, the group of Wirz [Lad17] redetermined RQYs of azobenzene in methanol. The highest difference in the absolute values of the RQY in comparison to published data in the 80-ties was in the range of 12%. It was suggested that the newly determined values should be considered for actinometry.

Actinometry dealt since decades with the topic of possible measurement errors and its challenges to eliminate all systematic errors [Dem76, Bow76, Kir83, Wri20]. However, the most critical point of numerous actinometers is the fact that the newly formed product also absorbs the excitation light. For this reason, the evaluation of such data is restricted to very low conversion rates of the substrate. Thus, only the initial slope of the photoconversion is evaluated and used for further calculation of the photon flux.

There are several groups that recently improved the method of data evaluation [Vol19, Gom12, Str17, Rei19a]. In these experiments a full illumination until a photostationary state (PSS) is performed. The experimental data is subsequently fitted to a kinetic model by solving the differential equations for temporal evolution of concentrations numerically. Reinfelds *et al.* [Rei19a] assigned this method to the global analysis of the whole spectra. This approach offers the flexibility to approach any photoinduced process – photocatalysis or photochemical system including molecular switches.

One of the crucial requirements for the precise determination of the quantum yield is the exact information about the molar absorptivities of substrate and product. This was already discussed in the work of Wirz and Heger [Lad17]. The molar absorptivities are not only

necessary to calculate the time evolution of the substrate and product concentrations from UV/vis, but also crucial in order to gain information about the fraction of absorbed photons by substrate and product. Thus, it is essential to calculate the exact value of the RQY.

There are several reports on self-built optical instruments to provide the RQY. However, most of them still use ferrioxalate actinometry to determine the photon flux [Gom12, Lad17, Str17, Rei19a]. Only in few cases, a calibrated photospectrometer, photodiode or power meter is used to quantify the emitted light [Sta18a, Jan17]. Although since 2015 there is a commercial optical system from SHIMADZU on the market "QYM-01 Photoreaction Quantum Yield Evaluation System" [QYM-01], this instrument has not been available for a long time in Europe and several other countries. Currently, SHIMADZU's PQY-01 Photoreaction Evaluation System is now available worldwide [PQY-01]. Nevertheless, the market for such devices can be described as relatively young and modest. However, the photochemical and photocatalytic community shows a great interest in smart, versatile and modular setups that can provide straightforward solutions.

The goal of this work is to introduce and discuss a straightforward concept for the RQY measurement. In this chapter the instrument, a detailed protocol of the measurement preparation and procedure, as well as the evaluation of the data based on a global analysis of the whole data set are summarized. The concept is validated for all known photoreaction types and discussed in detail. Notably, the entire optical instrument uses commercially available optics and is designed to make the entire measurement process simple and intuitive.

3.3 Concept of the Quantum Yield Determination Setup

In accordance with the preliminary investigations [Meg10], our focus is on a controlled illumination of the sample. In order to reach the optimum measurement accuracy of the RQY, novel components and features were introduced.

In the now introduced QYDS setup (see Fig. 3-1) we replaced the camera objective with fused silica best from lenses which image the excitation light into the sample. This replacement provides an applicability of high power LEDs down to the UV-C region without any significant transmission losses.

LEDs are the most favorable illumination source type. They are inexpensive, commercially easily available light sources and can cover the range from the UV-C to the NIR. LEDs are

spectrally well-defined, in addition their emission spectral band can be easily controlled by an optical filter. The illumination power can be readily adjusted by a corresponding driving current. This driving current is controlled by a precise power supply (320-KA3005P, RND Lab) within the range up to 1.4 A. If required, the sample can be irradiated intermittently with the aid of accessory electronics. Using pulsed light is favorable for a radical chain reaction, in which the excitation light is required only in the initiation phase of the reaction. In combination with a kinetic model, the length of the radical chain reaction can be estimated [Hu20].

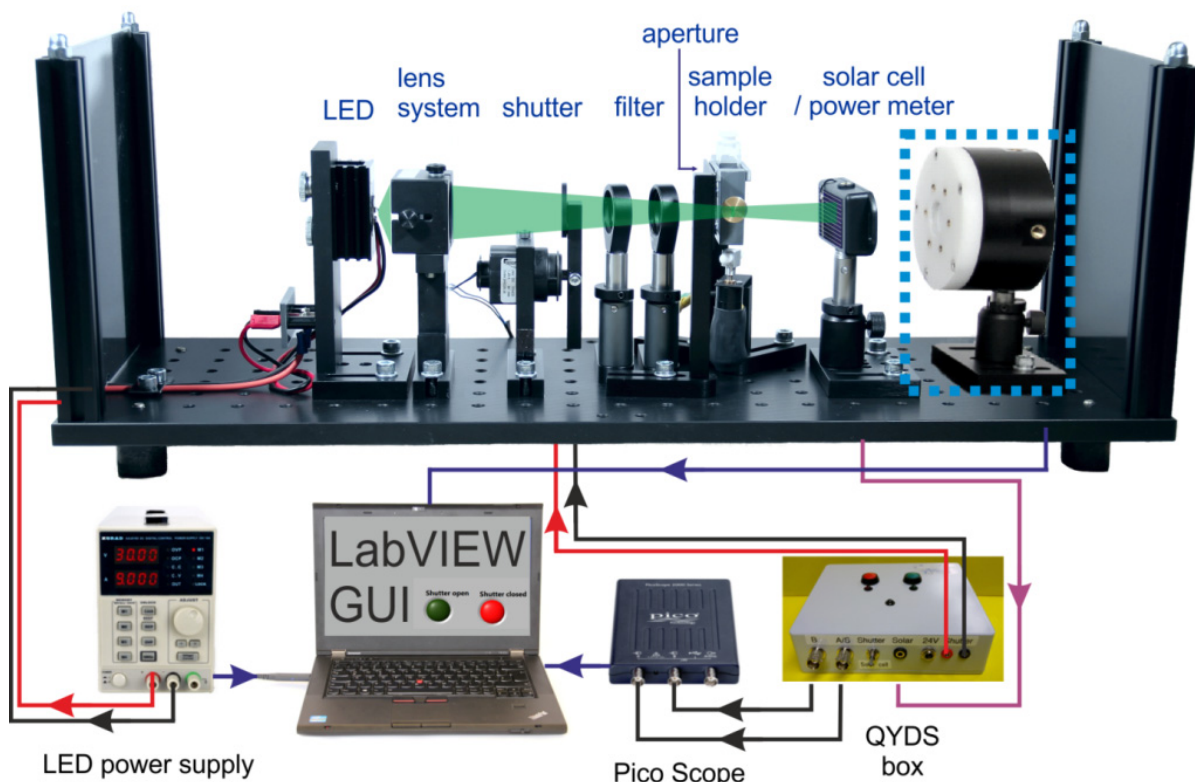


Figure 3-1 Quantum Yield Determination Setup. The LED light is imaged into the sample using fused silica best form lenses. The transmitted power is detected by a calibrated UV-sensitive solar cell or a powermeter. The QYDS box encloses all electronics for the shutter control and the I/U converter as a part of the radically improved detection system of the transmitted power.

In contrast to chemical actinometry, the number of absorbed photons is measured directly by a calibrated NIST (National Institute of Standards and Technology) traceable power meter or a calibrated UV sensitive solar cell detector (SCD). In order to convert the photocurrent into a voltage we designed a large dynamic range I/U converter according to ref. [Eck12].

A digital scope Picoscope tracks continuously the transmitted light. An electronically controlled mechanical shutter blocks the illumination light and thus continuously switching on and off of the LED is avoided. The necessary electronics of the I/U converter and shutter are part of the QYDS box.

For a measurement, the corresponding sample inside a cuvette is irradiated at least 1 minute. Thereafter, the light is blocked by the shutter and the time counter of the system stopped. In a log file, the illumination time and the transmitted power for each illumination step are automatically saved. In the next step, the sample is transferred into the UV/vis spectrometer and the absorption spectrum is measured. This procedure is repeated until no spectroscopic changes are observed. Typically, 15 - 25 UV/vis spectra are recorded in order to reach this equilibrium. The whole measurement process is controlled and continuously monitored by a LabVIEW GUI developed by Riedle's group. The entire instrument is enclosed in a black PVC box, to prevent a reaction of the sample from any ambient light source.

The measured raw data is subsequently post-processed and evaluated. Our evaluation method is not restricted to the linear regime and it considers the whole measurement data set up to the PSS. The time evolution of the substrate and product concentrations are extracted from the UV/vis by projection onto the basis spectra. Subsequently, the temporal evolution is modeled using the number of absorbed photons and the number of substrate and product molecules in the cuvette for each time interval. The resulting set of ordinary differential equations is solved numerically, whereby the only free parameters are the RQY for forward and if present for backward reactions. The evaluation method has also been extended to include possible side products.

The QYDS is a modular setup and can be easily adapted to the needs of the user. For example, in case of a degassed reaction or when using a flow cell these additional modules can be easily placed around the sample holder. If desired, it is possible to perform fatigue resistance measurements of molecular switches by introducing a second LED and shutter [But19].

3.4 Basic components of QYDS

3.4.1 LED as a light source

LEDs have gone through substantial progress over the last decades. Their advantages, having a long lifetime of several ten thousand hours and good luminous efficiency as well as photon flux stability make LEDs more favorable in comparison to halogen lamps, mercury lamps or xenon arc lamps. These broad band lamps would require additional suppression of undesired wavelengths. Such spectral filtering results in a huge inefficiency, because only a small percentage of the light can be used for the excitation process.

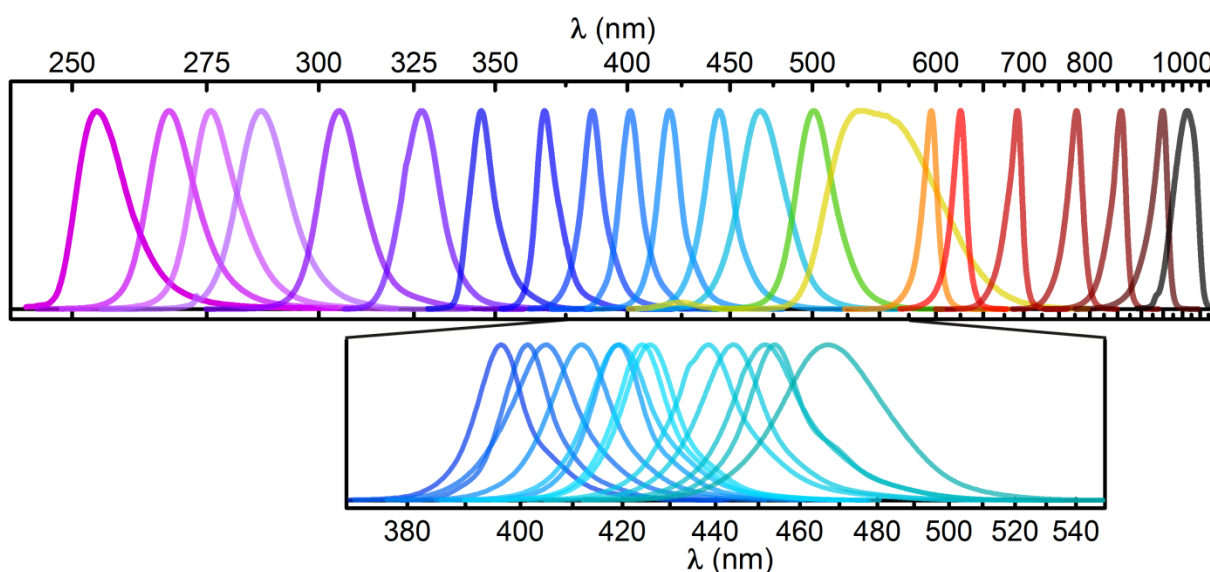


Figure 3-2 Selection of LEDs as an efficient light source for the excitation. The spectral range is fully covered from 255 nm to 1050 nm.

The commercially available high power LEDs are nowadays covering the full range between 255 nm and 1050 nm (Fig. 3-2 and their specifications in Appendix 3-B). Furthermore, the spectrally well-defined emission band of LEDs can be controlled by an optical filter. The illumination power can be easily regulated by the driving current. However, it is not recommended to decrease the driving current below 10% of the allowed maximum current due to possible instable photon flux of the LED. If further attenuation is required, a neutral density optical filter can be used. According to our observations, the LED should be warmed up for 30 minutes in order to avoid a thermal drift. After this initial warm-up phase, the illumination power remains constant.

The here used LEDs are glued on a heat sink 32 x 50 x 20 mm³ (SK 76 50; Fischer Elektronik GmbH & Co KG), with the needed heat dissipation ensured by a thermally conductive adhesive (WLK DK 10; Fischer Elektronik GmbH & Co KG). The excitation wavelength can be adjusted by a fast and easy exchange of the LED (see Fig. 3-3). In contrast to the preliminary QYDS version [Meg10], the translational stages for adjusting the LED position became obsolete by a precise positioning on a heat sink. This optimization of the LED position is possible due to an adjustment tool that was developed specifically for this purpose and is printed in a 3D printer.



Figure 3-3 LED mounted on the heat sink. Two screws are used to mount the unit onto the holder.

The illumination power can be easily controlled by a current applied on the LED chip. However, most LEDs show some spectral variations in dependence on the driving current. In order to understand this relationship between the emission spectrum of the LEDs and its driving current, the spectral distribution is investigated in 100 mA steps. A set of five Gauss functions is used to fit and smooth the measured emission LED spectra. Due to the fact, that the numerous LED spectra are rather asymmetrical in spectral distribution, a central wavelength λ_c is introduced and used for further analysis.

$$\lambda_c = \frac{\int \lambda \cdot I(\lambda) d\lambda}{\int I(\lambda) d\lambda} \quad (3.2)$$

where $I(\lambda)$ is the intensity at wavelength λ .

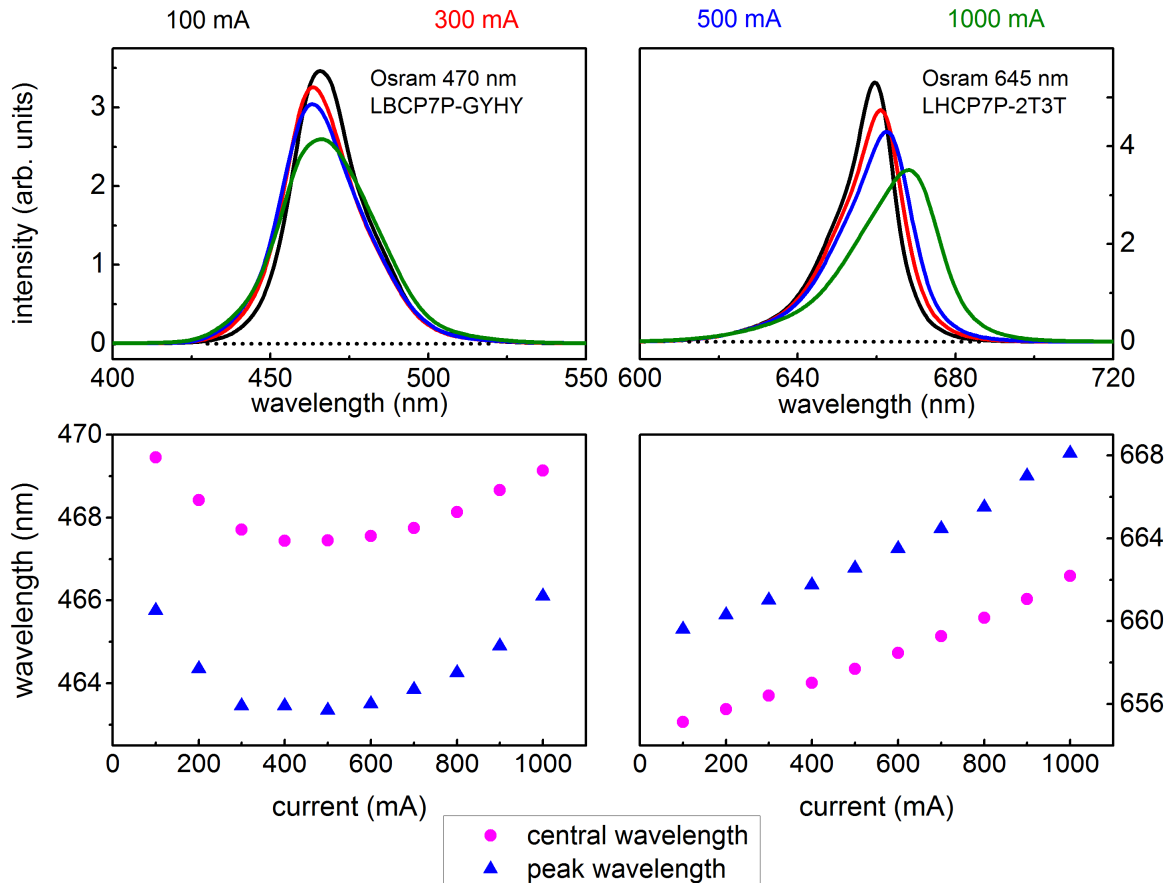


Figure 3-4 Variation of the spectral distribution in dependence on the LED driving current. In case of the red LED (right), the central wavelength shifts monotonously towards higher wavelengths up to 8.5 nm relative to the starting value. The blue LED revealed a non-linear trend, in which the central wavelength shows blue shift and then red shift by only 2 nm.

In Fig. 3-4 two examples of Osram LEDs (470 nm and 645 nm) are shown. In both cases, the spectral distribution gets broader with increasing current. An increase up to 11 nm in the FWHM is observed. In the case of the red LED the higher driving current shifts the central wavelength monotonously to higher wavelengths.

A difference in the position of the central wavelength up to 8.5 nm is measured between 100 mA and 1000 mA. This red shifting phenomenon can be explained by a variation in the semiconductor band gap due to the increasing temperature on the LED chip [Hui17]. On the other hand, the blue LED shows a non-linear trend with very modest blue shift of no more than 2 nm. This effect is attributed to the Stark effect and a band filling effect [Hui17, Pan20, Chi96].

According to the results summarized in Appendix 3-C (for LED specifications see

Appendix 3-B), only very modest spectral variations are observed for LEDs in the UV-C range up to 300 nm. Most of the LEDs reveal a monotonous red shift as shown in Fig. 3-4 right. The most pronounced red shifting effect (up to 11 nm red shift) is observed for yellow (590 nm), red (617 nm) and IR LED (850 nm). The most prominent broadening of the spectrum is detected in case of a far red LED at 730 nm. This spectrum gets 20 nm broader in FWHM. Consequently, it is highly recommended to measure the spectral distribution of the corresponding LED for the respectively applied current and use only the resulting spectrum for the final evaluation of the reaction quantum yield.

3.4.2 Optics and imaging – because every photon counts

The central idea of the QYDS is to image the LED light into the sample under study and to precisely quantify the amount of light. The selection of appropriate optics is one of the most important steps for controlling light. In the following, various optical designs applicable in the QYDS setup are introduced.

Since the light is emitted from a LED in a cone defined by a rather large opening angle, the optical system needs to collimate and image the light into the sample. In the initial version of the QYDS [Meg10] a photographic lens with a high f-number of 1.4 was chosen for this purpose (AF 50/1.4 D, $f = 50$ mm, Nikkor). Thus, an illumination power of several tens of mW in the visible range can be collected. The photographic lens is a good optic with excellent anti-reflective (AR) coating for the whole visible range. In addition, the focusing mechanics included easily allows setting the proper imaging. This lens transmits down to 400 nm, below the transmittance decreases quickly.

Replacing the photographic lens with fused silica best form lenses (B. Halle Nachfl. GmbH) the wavelength region can be extended into the deep UV-C region. The ratio of the lens curvatures is chosen to minimize the spherical aberration. Due to the extremely large spectral range, no AR coating is applied.

The focal lengths of the best form lenses were chosen with respect to the dimension of the emitting LED chip (SMD chip). The typical size of a square SMD chip is between 1 mm and 1.4 mm (see Fig. 3-5 left). By selecting focal lengths of $f = 25$ mm (the smallest value available for a lens with about 25 mm diameter) and $f = 150$ mm, a magnifying factor of 6 is achieved. Hence, the image has a dimension of 6 mm or 8.4 mm, respectively (see Fig. 3-5 right). This dimension is optimal for an $8 \times 8 \text{ mm}^2$ aperture that is positioned directly before the sample.

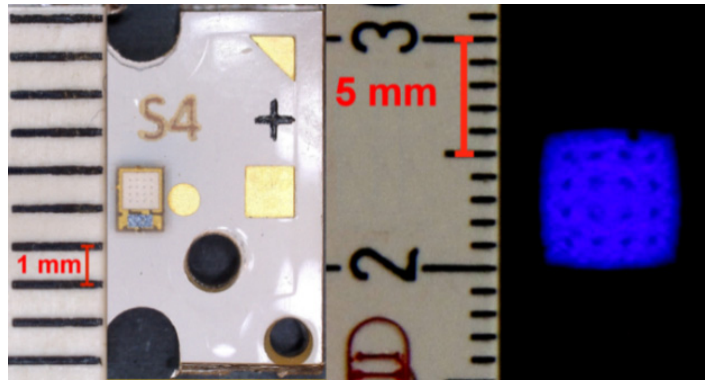


Figure 3-5 Detailed view of the 415 nm LED Luxeon LHUV-0415-0600 with 1 mm emitting area of the SMD chip (left). In case of correct imaging of the light, the pattern typical for a SMD chip can be clearly observed (right) at the sample position.

However, several LEDs have an additional silicone lens on top of the SMD to improve the collimation of the light. Such a lens enlarges the imaged light undesirably like a magnification glass (see Fig. 3-6 left) and the resulting spot size is magnified more than the calculated factor of 6 originating from the used best form lenses. Consequently, the imaged light is too large to pass through the $8 \times 8 \text{ mm}^2$ aperture and a substantial part of the light is clipped. In order to avoid this clipping, the $f = 150 \text{ mm}$ lens should be replaced by a lens with a focal length of $f = 100 \text{ mm}$ that results in an optimal imaging.

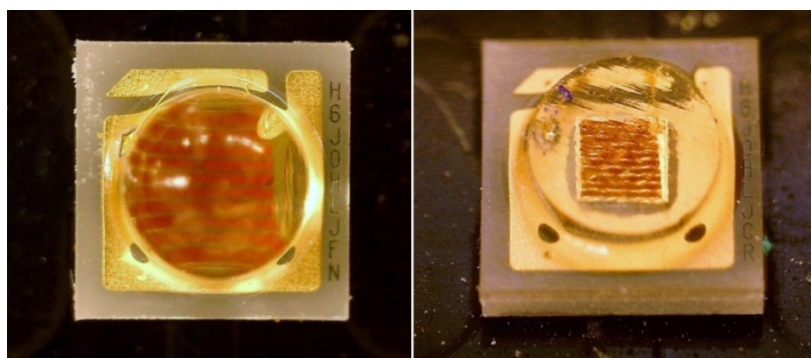


Figure 3-6 Demonstration of the Osram LED 645 nm (LHCP7P-2T3T) with a silicone lens on top of the emitting chip (left) and the same emitting chip after removal of the silicone lens (right) [Wie19].

The collection efficiency of the best form lens system is around 10% of the nominal power value of the LED. For photocatalytic or synthetic experiments extremely high irradiation powers are more preferred. For this purpose, we enhanced the optics to collect even more photons and image them into the cuvette.



Figure 3-7 Optics used in the QYDS. (left) one inch best form lenses; (middle) one inch Fresnel lens with a focal length of 15 mm; (right) two inch aspheric and plano-convex lens for highest collection efficiency.

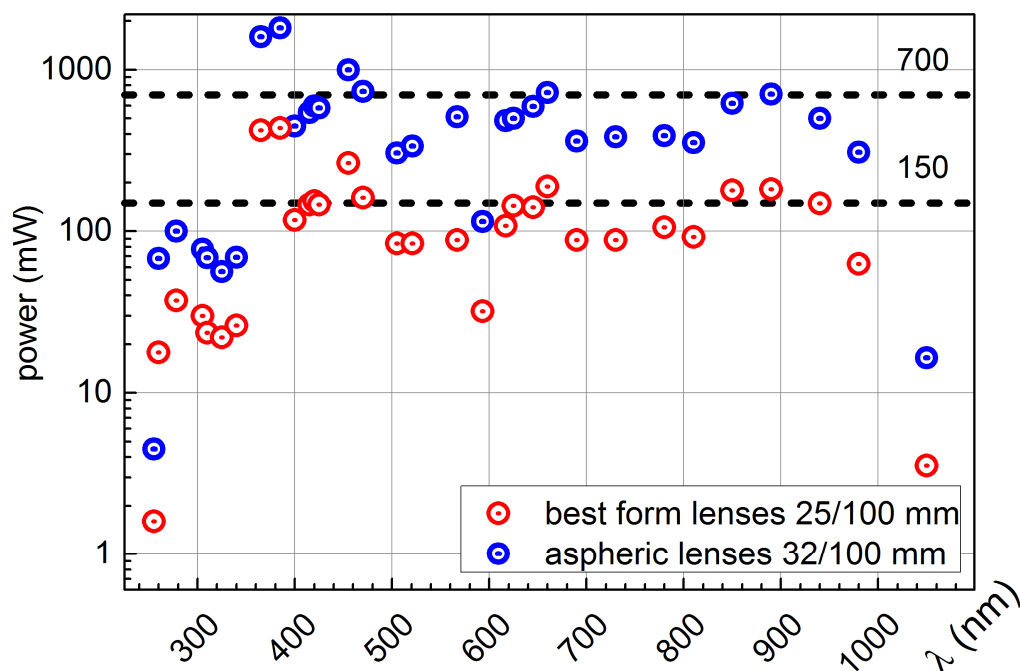


Figure 3-8 Graph showing the maximal illumination power in the sample using Ø1" fused silica best form lenses ($f = 25$ mm and 100 mm) or Ø2" aspheric ($f = 40$ mm for UV and $f = 32$ mm for VIS region) and plan-convex lens ($f = 100$ mm), depending on the wavelength.

A very high NA Fresnel lens (see Fig. 3-7 middle) can increase the power at the sample by roughly a factor of 4 ($f = 15$ mm, $NA = 0.64$ mm, UV acrylic, Fresnel Technologies, Inc.). This lens is then combined with a spherical lens to complete the imaging. The available Fresnel lenses transmit down to about 280 nm. They can therefore safely be used with LEDs of center wavelength 300 nm and above.

An enhanced illumination power up to 50% can be achieved by combining two inch aspheric and plano convex lens, see Fig. 3-7 right (for UV-region $f = 40$ mm, $NA = 0.63$, fused silica, UV coating (250-450 nm), Edmund Optics; for VIS region $f = 32$ mm $NA = 0.76$, B270, AR coating, Thorlabs; plano convex lens, $f = 100$ mm, fused silica, EK SMA). The results in Fig. 3-8 show that for several wavelengths more than one Watt of light can be provided in the sample. The 2" optics are used to obtain a large enough distance between the optics and the sample. Only this way the shutter and a possible filter can be integrated into the setup.

3.4.3 Stirring in a cuvette

Stirring of the solution is one of the crucial issues for an exact determination of the RQY. Thus, it is essential to consider typical spatial dimensions and reaction conditions of a photoinduced process.

In a regular photocatalytic reaction the concentration of the substrate is at least several mM and up to 0.5 M to increase product yield and also to facilitate diffusional processes. Depending on the sample and the chosen concentrations the whole photochemical process takes place within several hundred μm . A typical diffusion time for a 1 cm pathway is on the order of several hours depending on the solvent. Thus, a simple diffusion without external stimulus is not sufficient. The constant stirring of the solution warrants quasi-equilibrium conditions during the whole measurement process.

As a stirrer an external motor with a 14:1 gear (1524B024S R 15A 14:1 or 1524E024S R 155 11.8:1 for a reduced height; Faulhaber GmbH) is used as a stimulus. Its nominal operating voltage is 24 V for $9800/14 = 700 \text{ min}^{-1}$ rotations or 11.7 per second. To first order the rotation speed is linear in the voltage at low load and the driving voltage can therefore be used to control the amount of stirring. To actually stir inside the cuvette, a small but as large as possible teflon coated magnet is placed inside the cuvette and a larger one is mounted on the axle of the geared motor. As can be seen in Fig. 3-1 the motor assembly is placed directly under the cuvette mount.

In order to ensure proper sample exchange in the whole volume, the parameters for stirring

were consequently optimized. Hereby, several combinations of cuvettes and stirring bars were tested and analyzed using a video record. The results are summarized in Table 3-1.

According to the observations, it is not recommended to fill the cuvette completely (see Fig. 3-9 right). Even at the highest stirring speeds, some regions at the top of the cuvette are mixed very poorly or even not stirred at all. The optimal volumes summarized in Table 3-1 were chosen with respect to an adequate stirring and respecting the necessary fill level for a standard UV/vis spectrophotometer.

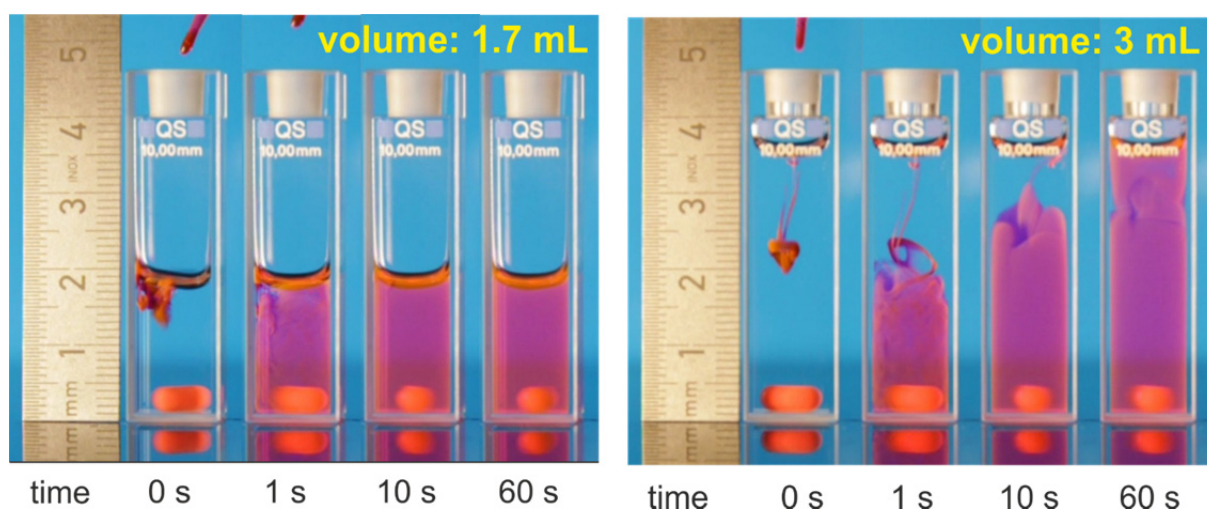


Figure 3-9 Comparison of the stirring of two solutions with different liquid levels. For this purpose, one drop of 100 mM rhodamine B dissolved in ethanol was added to the ethanol-filled cuvette with a volume of 1.7 mL (left) or 3 mL (right). Stirring was already in progress before the addition of the dye. The completely filled cuvette (3 mL) leads to non-homogenous mixing even after one minute of stirring at the highest stirring speed (1380 rpm).

Normally, a cuvette with an optical pathway of 10 mm is used. If possible, an absorption cuvette is to prefer because the manufacturer warrants better parallelism of the windows compared to fluorescence cuvettes and so the optical pathlength remains static over the entire cell window.

Semi-/micro fluorescence cuvettes are preferable if it is desired to work with an increased concentration at the same optical density or only a small amount of the sample is available. In contrast to 10 x 10 mm² cuvettes the position of the stirring bar is vertical.

In order to avoid the evaporation of the sample, the cuvettes are enclosed by an original PTFE stopper cap and wrapped with Parafilm®. Furthermore, the measurements can be also

performed under oxygen free conditions using a cuvette with a screw cap and a septum. The sample can be prepared directly in a glove box. Alternatively, the sample can be prepared under standard conditions and subsequently degassed by streaming the protective gas into the cuvette for around 15 minutes. During the measurement, the sample is under constant overpressure of the protective gas, which is provided by a balloon filled with nitrogen or argon. The balloon is injected directly into the cuvette having a crew cap with the septum via a syringe needle.

Table 3-1 Recommended cuvettes and associated parameters to reach the best quasi-equilibrium conditions.

Hellma cuvette type	light path (mm)	sample volume (mL)	stirring bar (mm)	operation voltage of the stirrer (V)
110-10-40	10	1.7 – 2	8 x 3	24
114F-10-40	4	0.7 - 0.8	8 x 3 7 x 2	18 20
115-F-10-40	2	0.37	8 x 1.5	18
for oxygen free conditions				
117-100-10-40 (with septum)	10	1.7 - 2	8 x 3	24
117104F-10-40 (with septum)	4	0.7 - 0.8	8 x 3 7 x 2	18 20
flow cell				
137-10-40	10	7.5*	-	-
137-1-40	1	7.5*	-	-

*depends on the own designed flow cycle.

In some cases, the repeated excitation of the substrate may lead to a degradation of the specimen. Additionally, at enhanced illumination powers, the increase of temperature in the reaction mixture becomes an issue. In such cases flow cells are preferred. For an enhanced exchange of the molecules, a cuvette with an optical pathway of 1 mm is recommended.

3.4.4 Detection of the incident and transmitted light

The detection of the incident and transmitted light is one of the most crucial parts of the RQY measurement. The difference is the absorbed power or the number of the absorbed photons when integrated over the whole illumination. The commercially available thermopile powermeter can measure the power in a range of less than a mW to 1 W with an accuracy of better than 3%. Good power meters are calibrated by the manufacturer in accordance to NIST standards.

In the QYDS setup a high sensitivity thermopile powermeter (PS19Q, Coherent, Inc.) is applied. The powermeter has a round sensor with diameter of 19 mm and it is suitable for applications from below 300 nm to 2000 nm. The sensor head is directly used for systems where several tens of mW are traced during the whole measurement, e.g., photocatalytic reactions.

However, in different systems like for instance molecular switches, the incident and transmitted power is rather low with typical values of a few hundred μW or even lower. There is no commercial powermeter, which could detect such small amount of light and at the same time would fulfill the requirement of a large active area ($> 10 \text{ mm}$) and calibrated sensitivity in the UV/C region.

A standard silicon solar cell introduces a suitable alternative providing the possibility of a very precise measurement of the illumination power. This might be surprising for a lot of researchers as pristine solar cells are rarely used for detecting light powers. However, considering the decades long use of solar cells in the harsh environment of building roofs, in retrospective our attempt with this technology is not too unreasonable. The number of photons is proportional to the number of free electrons and consequently the induced electrical current. Standard laboratory multimeters measure the current only indirectly by using a shunt resistor and measuring the voltage drop across it. This induces a voltage that counteracts the generation of photocharges and leads to a loss of linearity. More sophisticated devices are based on a transimpedance amplifier that converts the current into the desired voltage.

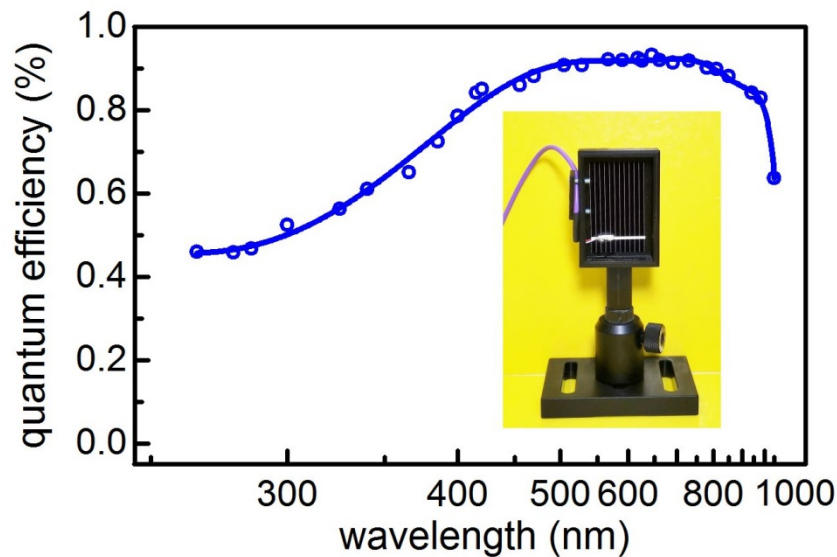


Figure 3-10 Quantum efficiency of the solar cell detector.

The SCDs used in the QYDS are provided by LEMO-SOLAR at a price of less than € 10.- per piece. They have a dimension of 27 x 45 mm² and an unobscured area of 27 x 36 mm². The surface is not covered by any additional protecting polymer layer and hence the SCD is sensitive down to at least 255 nm, with an external quantum efficiency of about 45% (see Fig. 3-10). So far, no remarkable aging of the SCD in the closed setup was observed. The aging is well below 1% per year and can be corrected by infrequent recalibration. Also we found that individual specimens do not differ by a significant amount.

In order to convert the current into a voltage, a I/U converter of own design according to the concept published by Eckel *et al.* [Eck12] is used. The I/U converter is based on a two stage feedback. The higher sensitivity stage is short circuited as the output voltage increases to more than about 80% of the positive supply voltage. The output voltage is read out by a digital oscilloscope Picoscope 2204A.

To get an outstanding signal to noise ratio of the amplified signal, it is crucial to establish a highly stable input voltage into the circuit. The Meanwell switching mode adapter provides 24 V with about ± 100 mV noise and spikes. In the first part of the board the voltage is reduced to +18 V and -18 V with sub-mV noise to +18 V and -18 V with high performance OpAmps (see upper part of Fig. 3-11). These voltages are used to supply the I/U converter which is based on the transimpedance amplifier using a junction field effect transistor (JFET 2N5460) as part of the feedback impedance (see lower part of Fig. 3-11). A bipolar transistor BC547BP is used in a Darlington scheme to boost the current capacity of the JFET. Depending on the magnitude of the solar cell current, the signal will be sent into different

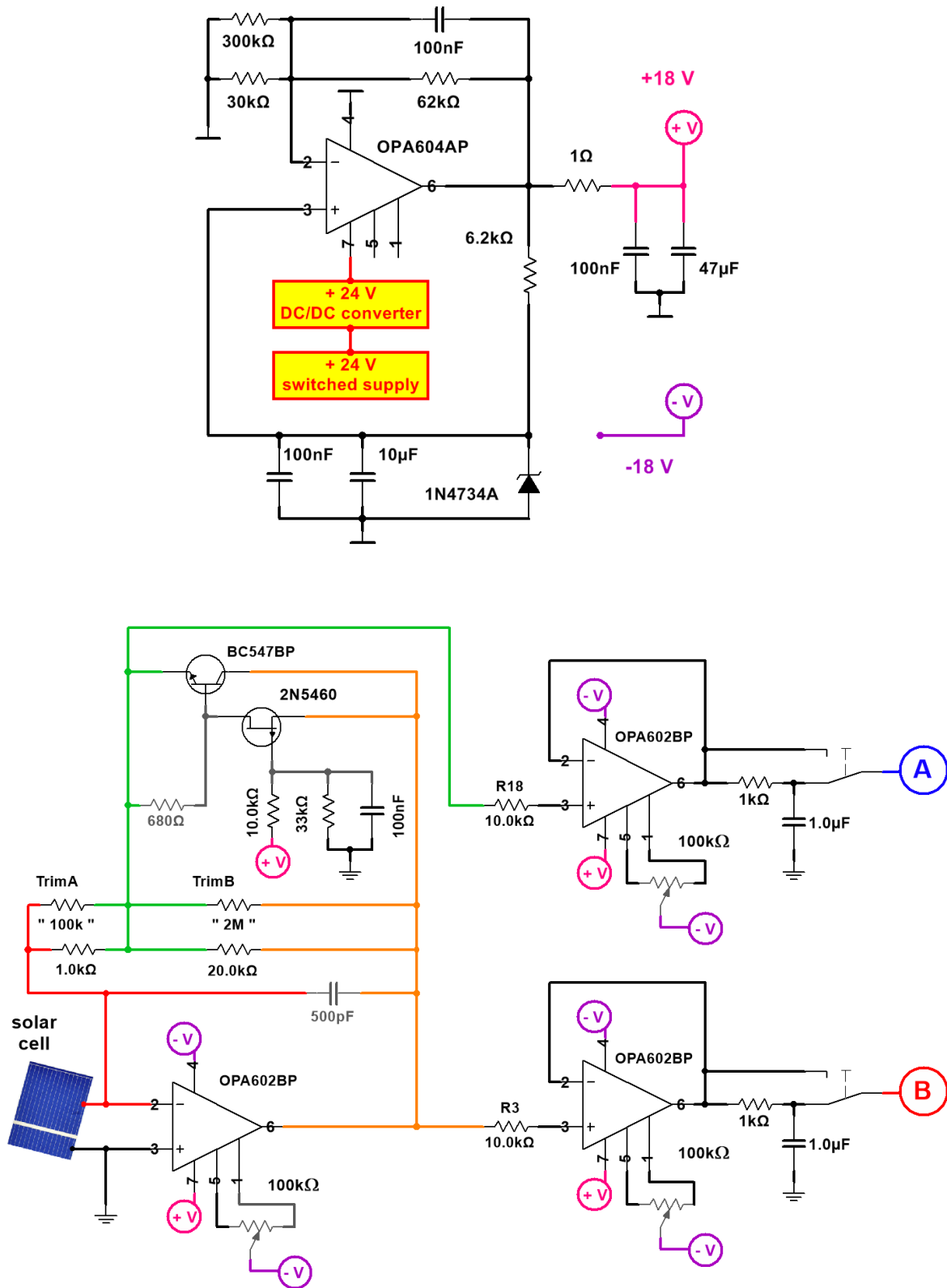


Figure 3-11 Schematic diagram for electronics of I/U converter. All OpAmps are "blocked" at the voltage supplies with a combination of a 100 nF ceramic and a 1 or 10 μF electrolytic capacitor.

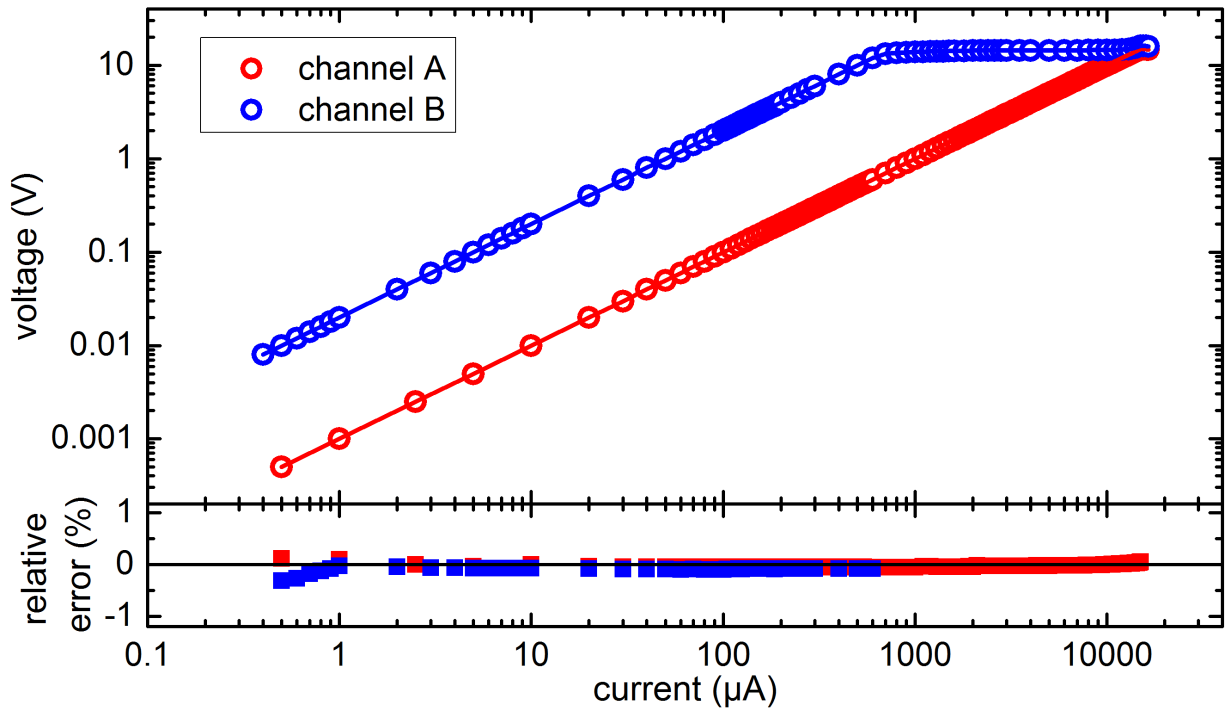


Figure 3-12 Linearity of the I/U converter between the applied current and the output voltage. The relative error to the expected value is below 0.01%.

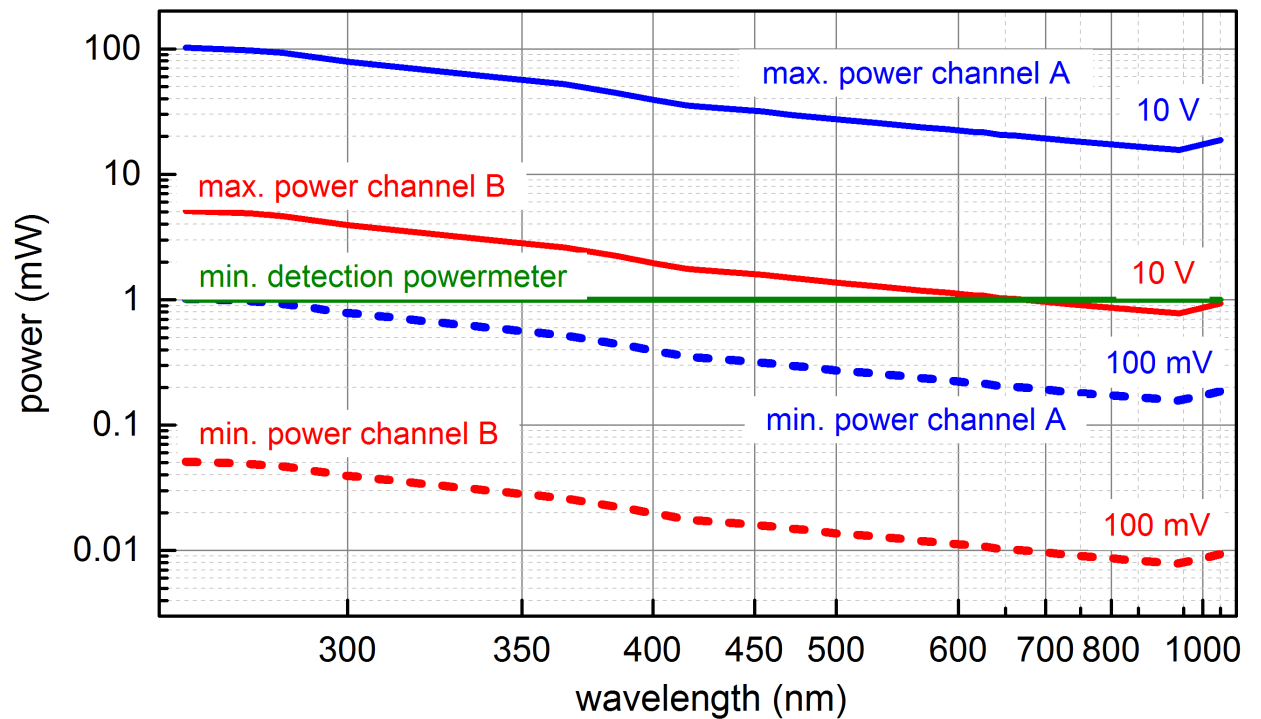


Figure 3-13 Measurable power range depending on the wavelength for channel A and B of the I/U converter.

outputs (see lower part of Fig. 3-11). The factor between the two output channels is set to 20 ± 0.001 . A residual noise of less than $100 \mu\text{V}$ at 0.1 to 10 V levels is achieved (see Appendix 3-D).

The SCD detector is calibrated using a powermeter under LED illumination with several mW light output. The SCD and I/U converter are highly linear over 5 orders of magnitude (see Fig. 3-12). To demonstrate the linearity, a current is applied on the I/U converter (Sourcemeter 2400, Tektronix, Inc.) and the output voltage is measured (Multimeter 8808A, Fluke Corporation). The relative error shown in the lower panel of Fig. 3-12 is well below per mill region. Due to the wavelength dependent quantum efficiency, the detectable illumination power of a SCD varies with the wavelength. Figure 3-13 shows the measurable ranges for both I/U output channels. In addition to the quantum yield also the energy $E = h \cdot \nu = h \cdot c / \lambda$ differs largely between 255 nm and 900 nm and leads to more power needed in the UV for an equal signal. For example, in case of the royal blue LED 455 nm the illumination range between $16 \mu\text{W}$ and 31 mW can be easily detected with the SCD. The green line corresponds to the lowest power that can be detected with a thermopile powermeter routinely with sub-5% accuracy. Hence, to measure illumination powers below 1 mW it is always recommended to use the SCD.

The SCD represents an elegant and inexpensive solution for a precise measurement of a low amount of light spread over a large area even in the deep UV/C region. The continuous tracing of the transmitted power enables to monitor the stability and feasible molecular degradation. Hence, it also may contribute to the optimization of the reaction conditions. Due to the high stability and sensitivity even for low amount of transmitted light, the SCD can be regarded as one of the most important instrument components that ensures the superb measurement precision of RQY.

3.4.4.1 Calibration of the solar cell

According to our experience, the calibration of the solar cell remains stable over several months. The aging of the SCD in an enclosed setup and under enhanced illumination was not observed.

The SCD is calibrated against the NIST traceable powermeter for the full range of wavelengths available from the set of high power LEDs. Users that are certain to only use a limited range can also restrict the calibration to that range.

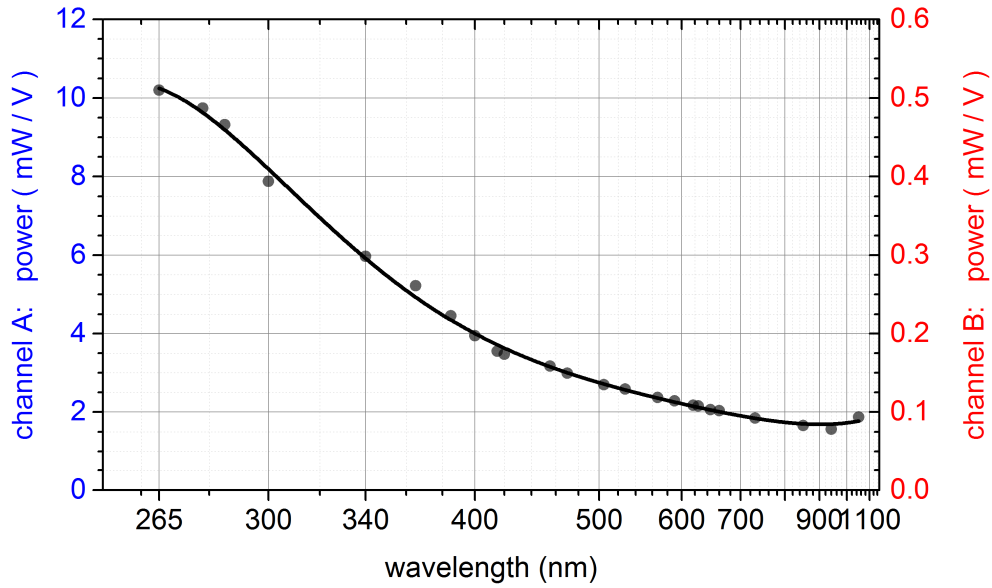


Figure 3-14 Wavelength dependence of solar cell calibration factor.

After the LED light in the QYDS is properly aligned and passes all optics including the $8 \times 8 \text{ mm}^2$ aperture cleanly, the dummy or sample cell is removed. The shutter as well as the housing of the setup is closed in order to avoid any detection of the LED and ambient light by the SCD. After the zero of the channel A and B is determined, the illumination power of the LED is adjusted to a reading on the channel A of about 8 V. Subsequently, the shutter is used to block the illumination light and the SCD is replaced by the power meter. It is recommended to avoid touching of the powermeter head because of the associated heating and baseline drift. Handling it by the mounting stub instead is more preferable. After the reaching the thermal equilibrium of the power meter the zero baseline is set. After opening of the shutter, the power values are read out. The calibration factor F_A is gives as:

$$F_A = \frac{P}{V_A(\text{illuminated}) - V_A(\text{dark})} \left[\frac{\text{mW}}{\text{V}} \right] \quad (3.3)$$

with illumination power P , V_A and V_B are the voltages measured in channel A and B. The factor between channel A and B is 20. Consequently, the calibration factor F_B in channel B can be calculated:

$$F_B = \frac{1}{20} \cdot F_A \left[\frac{\text{mW}}{\text{V}} \right] \quad (3.4)$$

The summary of calibration factors in dependence of wavelength is shown in Fig. 3-14.

3.4.5 Shutter

Repeated turning on and off the LED results in a thermal drift, during which the illumination power of the LED decreases by a few percent until a thermal equilibrium is reached. In order to avoid such occurrences an electronically controlled mechanical shutter is introduced that blocks the irradiation light. The shutter consists of a compact rotary solenoid (Drehmagnet CDR 030, Kendrion N. V.) and it can be opened and closed in 10 ms, whereby the delay of the electronic signal is about 40 ms. Consequently, the illumination time can be controlled with a millisecond precision providing an enhanced accuracy for the determination of the RQY.

The electrical control of the shutter is based on a H-bridge circuit consisting of four solid state relays (VO14642AT, Vishay Semiconductors) that are active after pushing the red or green button. The red and green control LEDs correspond to the opened or closed status of the shutter. This is accomplished by a RS Flip-Flop (Quad 3-State R-S Latches, HCC4043B, SGS-Thomson Microelectronics). The circuit schematic of the electronic circuit for the shutter can be found in Appendix 3-E.

3.4.6 Automatized QYDS

The measurement process of a typical QYDS experiment might be regarded as tedious. Indeed, pushing buttons on the QYDS box after pre-defined illumination time steps to open and close the shutter is a rather a monotonous work. After every illumination step the sample is transferred into the UV/vis spectrophotometer and an absorption spectrum is measured.

This whole measurement process can be automatized by the electrically controlled shutter and implementation of the photodiode array spectrometer (LAMBDA 265, PerkinElmer, Inc.), see Fig. 3-15. A fiber coupled Xe flash lamp of the spectrometer is used in an orthogonal geometry to the LED light. The Xe lamp light coupled into the fiber (FG600AEA, NA = 0.22, 600 μm core, 180-1200 nm, Thorlabs) is collimated and subsequently collected by the collimators (COL-UV/vis, lens diameter 6 mm, $f = 8.7$ mm, Avantes). The time required for a measurement of a UV/vis spectrum is now radically reduced from minutes to the sub-second regime.

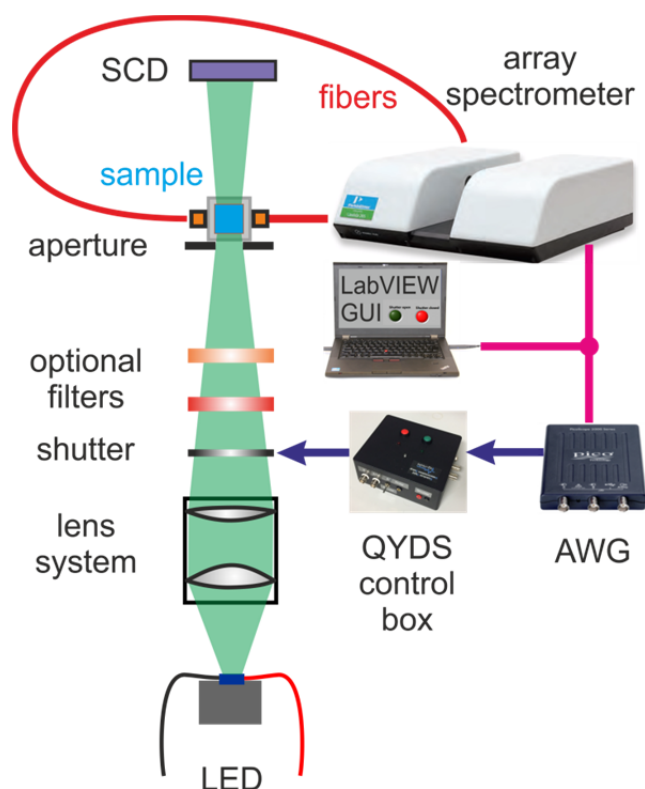


Figure 3-15 Overview of the automated QYDS setup coupled with an array photospectrometer. The AWG signal from Picoscope controls the shutter [Wil23].

The shutter is electronically controlled from a computer. The computer controls an arbitrary waveform generator (AWG) of a Picoscope to create short DC voltage signals that are transferred to the electronics within the QYDS box resulting in a controlled shutter. The reasonable illumination time steps are estimated by pre-measurement calculations from absorption spectra of the species.

As attractive this additional improvement sounds and indeed is for serious of many measurements, one has to be aware that the extra spectrometers is not available in most chemistry labs contrary to a standard spectral photometer. Its price tag of close to € 10K might cause some discussion with the leader of the group. In addition, the added complexity also needs a more careful optical alignment and testing of the linearity range of the setup. Last but not least, the maximum optical density and the sensitivity of the array spectrometer is considerably lower than a good scanning instrument.

3.5 Measurement

In this section, the process of planning and evaluating the experiment is discussed. The user benefits from our own programs developed in Mathcad Prime 5.0 and fully usable within the present version 8.0. Beside the post-processing and evaluation of the raw data, these programs help with planning of the suitable illumination. In this way one can largely avoid erroneous runs and waste of substance and time. Additionally, the most important aspects that affect the precision of the determination of RQY are discussed.

3.5.1 Measurement preparation

To avoid errors during the measurement, it is important to carefully consider the issue of measurement preparation. Measurement preparation addresses the individual steps that must be clarified before the actual measurement, as they provide us with important information about the photosystem under consideration.

There are two important points to consider in this context. The first point relates to spectral information of all species. This point can be further divided into two subgroups describing sample preparation in the chemistry laboratory, while the second subgroup refers to strategies for determining the molar absorptivity of the product spectrum:

1. Characterization of molar absorptivity spectra for reactant and product(s)
 - a. For reactant: Sample preparation – recommended weighing procedures to avoid errors in the initial concentration.
 - b. For product(s): Four different approaches for characterizing the molar absorptivity of the product spectrum.

Only when the molar absorptivity of all species is known is it possible to select an optimal illumination wavelength and power:

2. Choice of the excitation light – its wavelength and illumination power

In our experience, this issue is usually little addressed and often completely neglected. This can lead to abstruse constellations where the light is hardly absorbed by the reactant. This typically results in a long illumination time of several hours. On the other hand, too high illumination level leads to a completion of the reaction in less than 1 minute – way too short for a controlled experiment.

The goal of measurement preparation is to understand the photosystem and to choose the

measurement conditions optimally, since such careful selection can provide additional information about the photosystem and can simplify the further evaluation.

In following, the above-mentioned topics are discussed in detail and summarized below.

3.5.1.1 Characterization of molar absorptivity spectra for reactant and product(s)

Before starting the measurement, the system under study must be fully and quantitatively characterized by UV/vis spectroscopy. The molar absorptivities of substrate and product must be exactly known. This spectral information is required for an evaluation of the temporal evolution of the concentrations for substrate and product. In case that these spectra overlap, it provides an information about the fraction of photons absorbed by substrate and product and it helps the user to estimate the PSS (if present). Additionally, the spectral distribution of both substances is helpful to choose an appropriate excitation wavelength for the photoreaction.

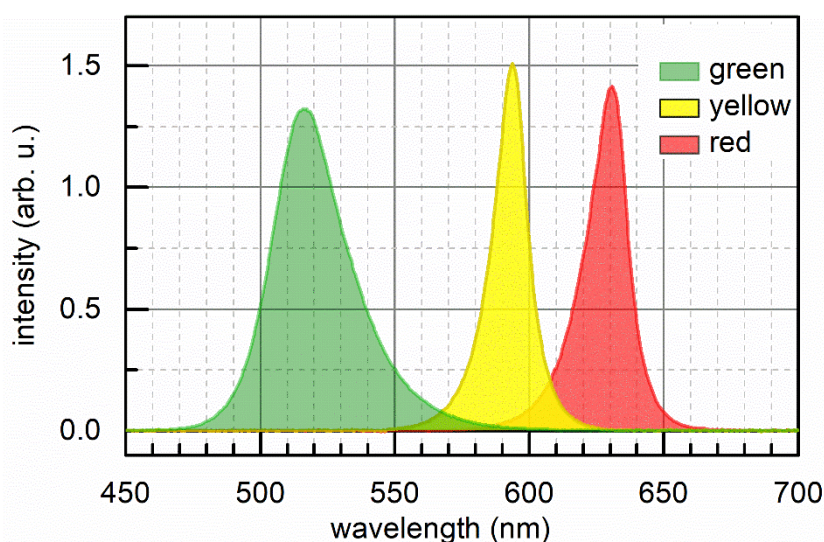


Figure 3-16 Spectral distribution of the LED based emitter that can be used during the preparation of the sample and the measurement instead of a standard ambient light source.

There are several issues, which are of utmost relevance for the precise characterization of the molar absorptivity. According to our experience, the measurement of the molar absorptivities can be regarded in some cases as rather challenging. In order to exclude possible errors from this preparation process, the most essential steps are discussed below.

If required, work in a dark room under controlled illumination of spectrally well-defined colored light to avoid undesired photoreactions. The LED based colored emitter (e.g., from

Synergy21) is an inexpensive light source with spectra available in various wavelength regions that can be used during the preparation process (see Fig. 3-16). Such LED spotlights are far superior to fluorescent lamps with a colored coating. However, some of the green spots are actually phosphor converted blue LEDs with a significant contribution at around 450 nm. These should be avoided.

In some photocatalytic reactions, the photocatalyst absorbs light only in the UV range. For such cases, dimmable white LED ceiling lights can be used, as they do not emit light below 400 nm (e.g., LED-Deckenleuchte, Aina-L rund, 3000 K, Blulaxa).

a) For reactant: Sample preparation – recommended weighing procedures to avoid errors in the initial concentration

The preparation of a stock solution can be regarded as the most important step to determine the molar absorptivity. It is recommended to weight around 5-10 mg of specimen to prepare a stock solution in a volumetric flask. A high quality balance in a suitable environment is needed for this step. If further dilution of the sample is required, reduce the number of dilution series to a minimum and work in the mL region to ensure the necessary dilution precision.

If possible, prefer absorption cuvettes to measure UV/vis spectra. In contrast to fluorescence cuvette, absorption cuvettes warrant a higher parallelism of the glass windows and thus lower deviations in the optical pathway.

The spectral resolution of UV/vis spectra is proportional to the square of the wavelength. This means, if the absorption bands under study are mainly in the UV region, the slit should be reduced to 0.5 nm and the sampling interval to 0.25 nm. For other specimen a slit width of 1 nm and a sampling interval of 0.5 nm are adequate.

The baseline of the UV/vis is fundamental for the correct determination of the molar absorptivity. According to our results and communicated experiences of collaborating groups, for a baseline measurement in a dual beam spectrophotometer it is recommended to use two absorption cuvettes filled with the pure solvent. For further measurements, the orientation of the cuvette must be preserved. The pure solvent in the sample cuvette is replaced with the substance under study. Applying an additional third cuvette leads to massive deviations in the baseline (for further details see Appendix 3-F).

The measurement region should be chosen in such a way, that at least 200 nm above the last

absorption band is additionally measured. This will be used later for a second baseline correction.

The molar absorptivity of the pure substrate $\epsilon_{\text{substrate}}(\lambda)$ is calculated from the UV/vis spectrum:

$$\epsilon_{\text{substrate}}(\lambda) = \frac{\text{OD}(\lambda)}{\text{concentration} \cdot \text{sample thickness}} \quad (3.5)$$

b) For product(s): Four different approaches for characterizing the molar absorptivity of the product spectrum.

According to our experience, the definition of the molar absorptivity of the product spectrum appears to be a rather challenging issue. However, this spectral information is crucial for exact evaluation and determination of the quantum yield. Therefore, four different approaches for determining the molar absorptivity of the product(s) are described below.

The **first approach** is to **chemically synthesize the product** and then measure UV/vis. However, this strategy, as simple as it sounds, is not always easy to manage. If the species is not available on the market in very high and pure quality, it must be synthesized in the laboratory. In many cases, chemical synthesis is not always straightforward. Such synthesis often requires complex and time-consuming procedures and purification steps to obtain spectroscopically pure species.

The **second approach** involves the use of an additional analytical method, e.g., **use of NMR or GC**. The procedure consists of the following steps:

i. Measurement of the absorption spectrum from the stable, pure isomer

In this step, the only uncertainty is the concentration. However, the uncertainty can be reduced if the following steps are carried out carefully. It is recommended to use the preparation procedure described above for the weighting.

For example, a typical hemithioindigo or diarylethene photoswitch is assumed. The molecular mass of hemithioindigo or diarylethene photoswitch is about 260 g/mol with a molar absorptivity of about $16 \times 10^4 \text{ L} \cdot \text{mol}^{-1} \cdot \text{cm}^{-1}$. In this case, a 2 mM solution can be prepared by dissolving 5.2 mg in 10 mL of solvent. Such a solution will give an OD of 32 if a 10 mm cuvette is used. However, the OD can be lowered to 3.2 by using a 1 mm cuvette instead. This is easily done since the molar absorptivity at the minimum between the first

and second absorption bands is usually 30% of the maximum of the first band. By using a thinner cuvette, the dilution chains can be completely avoided. Such procedure ensures higher measurement accuracy. The result of this first step is the molar absorptivity $\varepsilon(\lambda)$.

ii. Illumination of the sample with a defined light source - the LED - in the PSS and subsequent measurement of the NMR spectrum.

This step requires preparation of the sample in sufficient concentration for NMR analysis. Usually, a few tens of mM solutions are preferable. Since the OD is quite high, attention must be paid to two points: a) proper stirring and b) avoidance of unnecessarily long illumination time, which may lead to undesirable side reactions or degradation of the sample. Therefore, the recommended total illumination time for PSS is between 10 and 20 minutes. The illumination power must be selected accordingly.

Subsequently, the NMR spectra are measured and evaluated. Since the main uncertainty in this process is the evaluation of the NMR spectra, it is recommended to select the appropriate peaks/signals for comparison. According to our experience, it appears useful to export the NMR data as ASCII and perform true line fits instead of relying on the standard NMR programs [Wil22].

As a result of this step the ratio R of reactant and product in the PSS state is obtained.

$$R = \frac{c_{\text{react}}}{c_{\text{prod}}} \quad (3.6)$$

iii. Illumination of a diluted sample ($OD < \sim 2$) with the same light source into the PSS

Before starting the illumination, the initial spectrum is measured. This provides the information about the exact starting concentration. The ideal optical density of this diluted sample is around 2 OD. Subsequently, the illumination into the PSS with the same light source is repeated for this diluted sample. Hereby it should be ensured, that the cuvette is well sealed in order to avoid evaporation and subsequent change in the concentration. The final ratio in the PSS is expected to be identical with the PSS from above-mentioned point 2.

The molar absorptivity of the product $\varepsilon_{\text{prod}}(\lambda)$ can be calculated as following:

$$OD(\lambda) = d \cdot (c_{\text{react}} \cdot \varepsilon_{\text{react}}(\lambda) + c_{\text{prod}} \cdot \varepsilon_{\text{prod}}(\lambda)) \quad (3.7)$$

$$c_0 = c_{\text{react}} + c_{\text{prod}} \quad (3.8)$$

$$c_{\text{prod}} = \frac{R}{1+R} \cdot c_0 \quad c_{\text{react}} = \frac{1}{1+R} \cdot c_0 \quad (3.9)$$

By inserting Eq. 3.9 into Eq. 3.7 one obtains:

$$\frac{\text{OD}(\lambda)}{d} = \frac{R}{1+R} \cdot c_0 \cdot \varepsilon_{\text{react}}(\lambda) + \frac{1}{1+R} \cdot c_0 \cdot \varepsilon_{\text{prod}}(\lambda) \quad (3.10)$$

$$\varepsilon_{\text{prod}}(\lambda) = \frac{1+R}{d \cdot c_0} \cdot \text{OD}(\lambda) - R \cdot \varepsilon_{\text{react}}(\lambda) \quad (3.11)$$

The formula shown in Eq. 3.11 can be straightforward used to extract the molar absorptivity of the product spectrum.

The **third approach** uses the concept **described by Fischer** [Fis67]. This strategy is suitable for reversible two stage system ($A \rightleftharpoons B$). It is based on the commonly adapted assumption that the quantum yield remains constant while ensuring illumination in the same electronic band.

Therefore, two series of measurements are performed by illuminating the same absorption band with two different wavelengths, each up to the PSS. Then, the ratios of reactant and product in the final PSS are varied and different product spectra are extracted. These product spectra are used for the numerical integration of equations 3.20 and 3.21 in Chapter 3.6.4. As a result, a plot of RQY as a function of product fraction in the PSS is analyzed. At least one of the RQYs depends strongly on the assumed ratio and the values differ for the two illumination wavelengths. Only for the correct ratio they agree.

Using this approach, both the product spectrum as well as RQYs can be determined for the forward and reverse reactions. This method was successfully applied on the azobenzene as a model system. For further details and evaluation by using the Fisher method see Chapter 3.8.

The **fourth approach** is based on the spectral analysis, also known as **TEM method**. This approach was originally developed by Thulstrup, Eggers and Michl in 1970s [Mic87, Mic70a, Mic70b] and it is widely used in the realm of spectroscopy [Vet17, Sai15, Wid13, Gaw98]. This method uses the 2nd deviation during the spectral decomposition of the PSS in the specific spectral region with recognizable vibronic structure. The TEM method was successfully applied by the group of Wirtz [Vet17] for the extraction of (Z)-azobenzene in methanol using the spectral range between 300 nm and 380 nm. For further details on the TEM method, the reader is referred to Chapter 2.

Azobenzene as a model system

Azobenzene was chosen as a model system since it undergoes an isomerization from the initial and thermodynamically stable (E) to the (Z) isomer¹. Upon illumination with an appropriate light source, the isomerization process is promoted, resulting in a change of conformation. The thermally unstable (Z)-form undergoes thermal relaxation with a half-life of several days [Beh11, Nis76, Lad17].

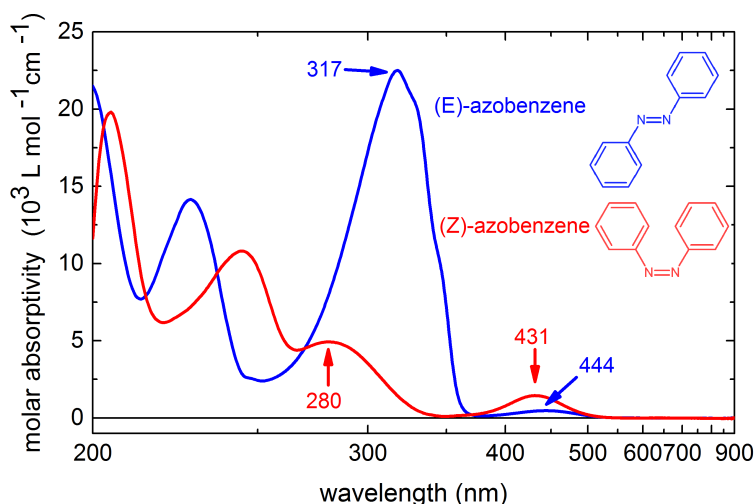


Figure 3-17 Molar absorptivities of azobenzene in ethanol.

Regarding the absorption spectra, shown in Fig. 3-17, the absorption between 280 nm and 320 nm corresponds to a π - π^* transition while the absorption around 430 nm corresponds to the n - π^* transition [Bir53]. Additionally, the quantum yields differ significantly between the two isomerization processes.

3.5.1.2 Choice of the excitation light – its wavelength and illumination power

a) Choice of the excitation wavelength

The motivation of this step is to consider more deeply the importance of the illumination light, as this is a very crucial part of photoreactions. For photocatalysis, it is strongly recommended that the illumination light is chosen so that the product generated absorbs a minimum of the incident light (if applicable). For molecular switches, on the other hand, the illumination should result in the PSS having the highest possible percentage of product. In order to obtain the mixtures with the highest percentage of the product (Z)-azobenzene,

¹ According to IUPAC, the widespread trans and cis nomenclature may be ambiguous in some special cases. Therefore, the E/Z nomenclature is in general more preferred and recommended [Cro76, Mos96].

exclusively the (E)-isomer has to be illuminated. However, due to the fact, that the absorption spectra of both isomers overlap, it is recommended to analyze the fraction of the light absorbed by both isomers at a chosen concentration and cuvette thickness.

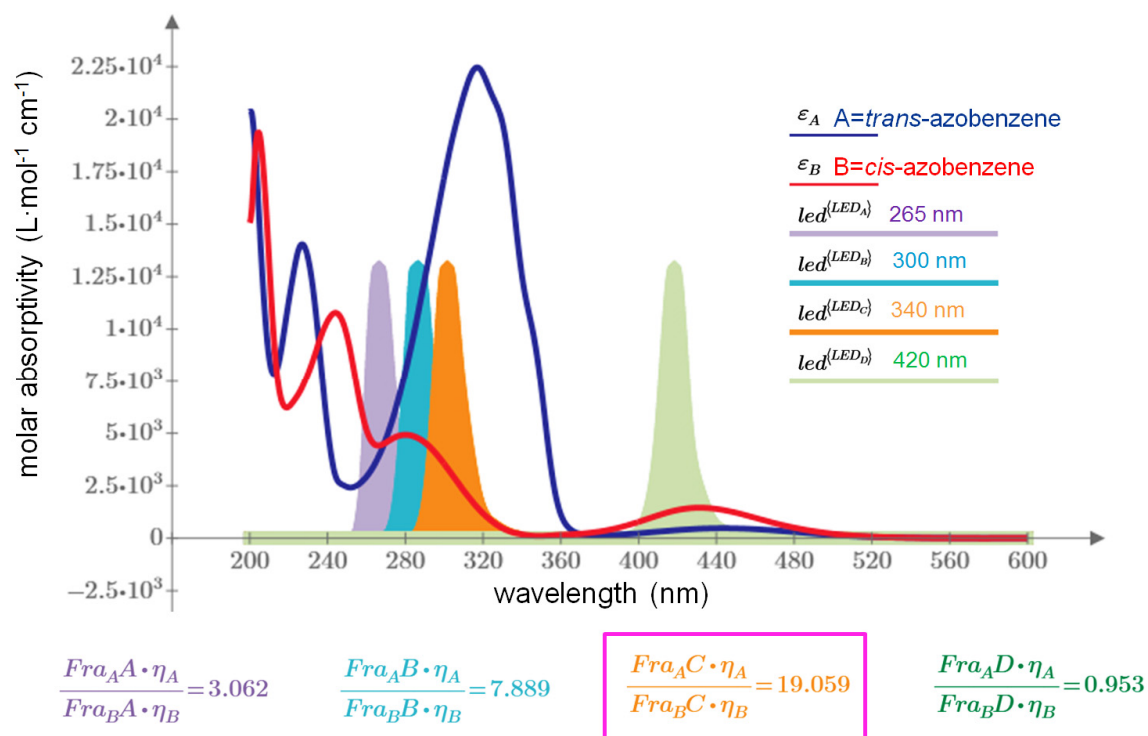


Figure 3-18 Screenshot of Mathcad program "01_pre-QYDS_LED_selection.mcdx" developed for choosing an optimal wavelength to achieve a PSS with the highest enrichment of the (Z)-azobenzene. The most suitable LED is 340 nm and it is highlighted by the magenta window

The formulas in the lower part of Fig. 3-18 refer to the fraction of absorbed photons for the reactant (Fra_A) and the product (Fra_B) for different selected LEDs, which are denoted by letters A, B, C and D. In addition, the initial estimated RQY for forward and reverse reaction (η_A and η_B) is considered. For further details on the evaluation with corresponding formulas, the reader is referred to Chapters 3.6.3 and 3.6.4 and the corresponding equations 3-12 to 3-18.

The fraction with the highest value reveals the optimal LED for the excitation to obtain as much (Z)-azobenzene as possible. In this case the LED with the nominal wavelength of 340 nm (Seoul Viosys, CUD4AF1B) was selected and used for further experiments (see Fig. 3-18).

The list of delivered LEDs is incorporated in the program. An interactive selection of the LED in the list enables to observe readily an impact on the ratio in PSS. The program can even consider filters that narrow the native LED spectrum.

b) Choice of the optimal illumination power

It is recommended to avoid the total illumination time until PSS to be too short in order to avoid not sufficient mixing, too short time steps and other disadvantages originating from too high optical power (e.g., decomposition of the specimen). On the other hand, too low an illumination power leads to enhanced time consumption of the measurements and possible thermal relaxation of the substance may occur. According to our observations, 45 minutes of

02_Illumination_Time photochem

- timing of illumination with QYDS

Vol := 2.0 *mL*

d := 10 *mm*

choose Vol in the range of 1.5 mL to 2 mL
take into account the minimum of volume that you need that the spektrometer light indeed passes through the sample and not empty space

$\epsilon_{mol} := 12.8 \cdot 10^3 \frac{L}{mol \cdot cm}$

conc_{mol} := 0.12 *mM*

OD := $conc_{mol} \cdot \epsilon_{mol} \cdot d = 1.536$

Abs := $1 - 10^{-OD} = 0.971$

penetration_depth := $\frac{1}{conc_{mol} \cdot \epsilon_{mol}} = 6.5 \text{ mm}$

λ := 340 *nm*

P := 0.2 *mW*

$N_{mol} := Vol \cdot conc_{mol} \cdot N_A = 1.445 \cdot 10^{17}$

$N_{photon} := \frac{P \cdot \lambda}{h \cdot c} = (3.423 \cdot 10^{14}) \frac{1}{s}$

QY := 14% estimated quantum yield

η := 50% desired chemical yield

$T_{illumination} := \frac{N_{mol}}{N_{photon} \cdot Abs} \cdot \frac{\eta}{QY} = 1553 \text{ s}$

T_{illumination} = 1553.1 *s*

+

minutes = 25

seconds = 53

Figure 3-19 Screenshot of the Mathcad program "02_pre-QYDS_illumination_time_choice photochem.mcdx" developed for the estimation of the optimum illumination power. The parameters in the blue windows characterize the sample.

total illumination appear to be optimal. The illumination time is divided into 15-25 steps. The RQY is guessed in the first step, or a very simple illumination experiment is performed to obtain the first estimation for the value of the RQY. As shown in Fig, 3-19, the illumination power P is varied so that the $T_{\text{illumination}}$ is about 25 minutes, when the desired chemical yield η is set to 50%.

Another approach assumes a conversion of 63%, since this corresponds to the function $1/e$. However, it is important to note that this is only an estimate if the spectra of reactant and product are spectroscopically different and well separated in wavelength. Unfortunately, this is usually not the case. In such cases - when the spectra of reactant and product overlap and the product consumes part of the incident photons - the total illumination time should be corrected by an additional 50%.

Time spacing in QYDS measurement

Basically, it is reasonable to collect the more detailed kinetics information at the beginning of the reaction. Therefore, the illumination times per step in this period are shorter in comparison to those close to the PSS. Due to the fact, that the changes of the concentration at the end of the reaction are relatively low the system requires elevated times to maintain the conversion effect. At this point it is obvious, that the equidistant time steps are not quite appropriate for a QYDS measurements.

The following semi-empirical formula is used to suggest suitable time intervals for each illumination step:

$$T_k = \frac{\tau}{2} \cdot 10^{-k/25} - \frac{\tau}{2} \quad (3.12)$$

whereby T is the vector of times for the $k = 0, 1 \dots 25$ point in time when UV/vis spectra should be taken. τ corresponds to the conversion rate. In case of molecular switches, the conversion rate of 20 min is proven to be a good starting value. Fig. 3-20 shows an example of an illumination cycle with 25 time steps and a total illumination time of about 1.5 hours.

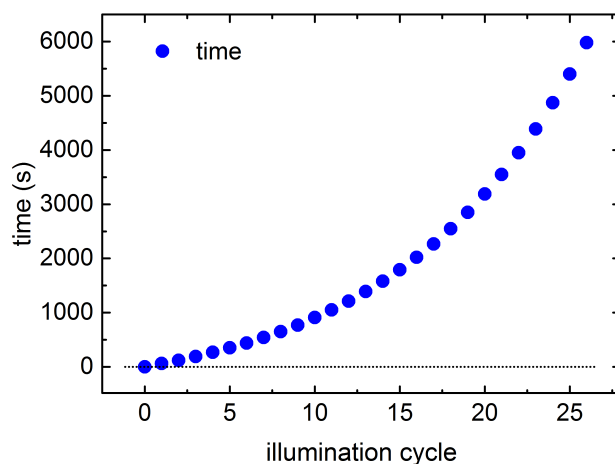


Figure 3-20 Plot of the exponential increase in the illumination time for each k -cycle.

Since the total illumination time is direct proportional to chemical yield η , it can be straightforward deviated the relation to conversion rate τ .

$$T_{\text{illum}} = \frac{N_{\text{prod}}}{N_{\text{photon}} \cdot \text{Abs}} \cdot \frac{\eta}{\phi} = \frac{\tau}{2} \cdot 10^{-k/25} - \frac{\tau}{2} \quad (3.13)$$

It is strongly recommended that the illumination power P_{illum} , chemical yield η , and conversion rate τ be selected to irradiate the sample for at least 1 minute.

3.5.2 Measurement procedure

The GUI of our own design is programmed in LabView 2016. It controls and reads out the power supply for the LED, the digital oscilloscope and the powermeter. The program is designed to control devices and to measure and document the illumination precisely.

The most relevant data are protocolled after each illumination step in a log file that is directly used by the Mathcad evaluation tools.

Before starting the actual illumination of the sample, the transmitted power behind a cuvette with pure solvent is measured and noted. For a correct protocol of the measurement, the most important parameters are centered in the middle of the GUI (see white windows in Fig. 3-21) and it is expected to fill them before starting the measurement. This information is saved in the header of the log file.

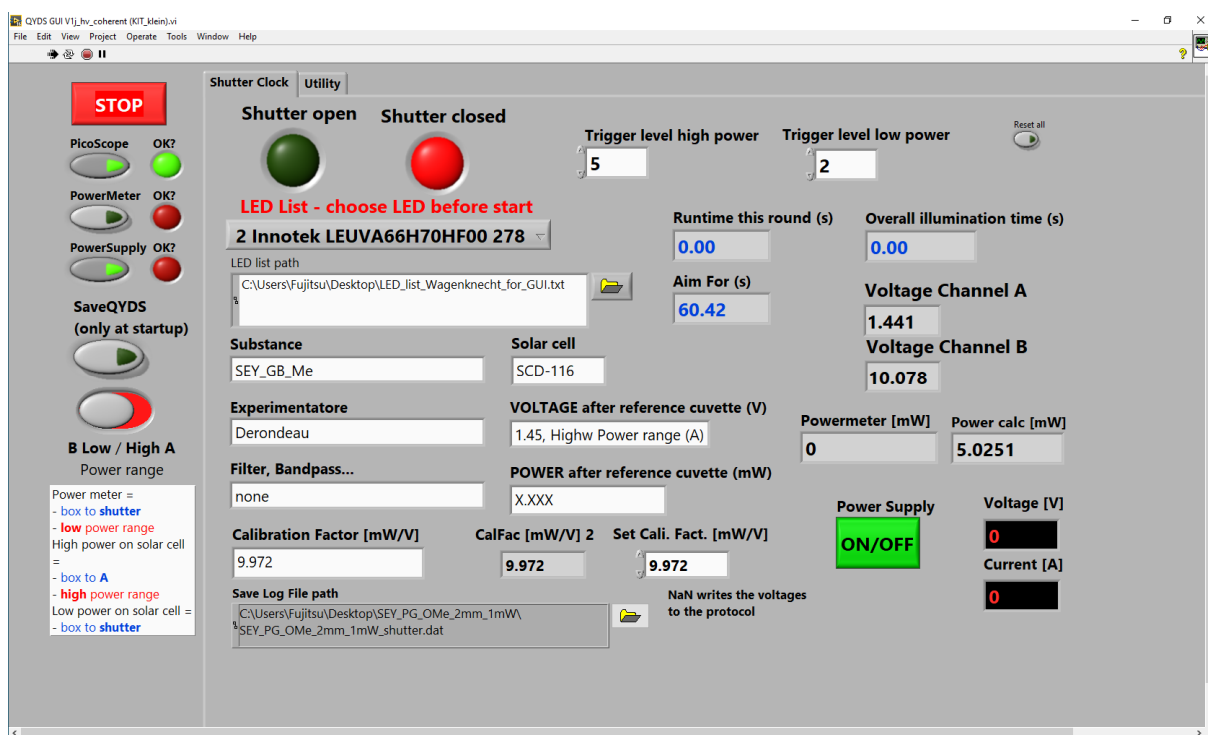


Figure 3-21 The LabView based GUI to control all electronic devices and the QYDS measurement. The set parameters as well as illumination and transmitted power are continuously saved in a log file that is subsequently directly read in by the Mathcad evaluation package.

At the beginning of the measurement, the UV/vis spectrum of the sample without an exposure to excitation light is measured. The sample is subsequently illuminated by the excitation light stepwise. The illumination steps are above one minute and increase

logarithmically. The user is referred to the "aim for (s)" window (see Fig. 3-21 right top), in which the next illumination time in seconds is recommended. After each irradiation step, the shutter is closed and an UV/vis spectrum is measured.

After no more spectral change in the sample is observed, the illumination process is finished and the data can be evaluated.

3.6 Evaluation

3.6.1 Introduction of an uniform header for the UV/vis files

The program of our own design converts the raw files obtained from a wide range of spectrophotometers and software into a valid uniform text format required for further evaluation. It implements a 37row header with all relevant information according to the JCAMP-DX format [McDon98]. The advantage of introduction of an uniform header is in preservation and gathering of all necessary information about the experimental parameters in one place.

3.6.2 Baseline correction

The correct baseline is crucial for the exact determination of the substrate and product concentrations. Despite a proper zeroing of the spectral photometer, some drifts or deviations in the baseline occur. These deviations may decrease the accuracy of the RQY value. In order to eliminate this effect, the program fits 4 Gauss functions to the longest wavelength spectral feature of each measured spectrum (see Fig. 3-22). The routine allows the precise determination of an optimum baseline value to be subtracted for each spectrum individually. The baseline corrected data are saved and used for further evaluation (see Fig. 3-23).

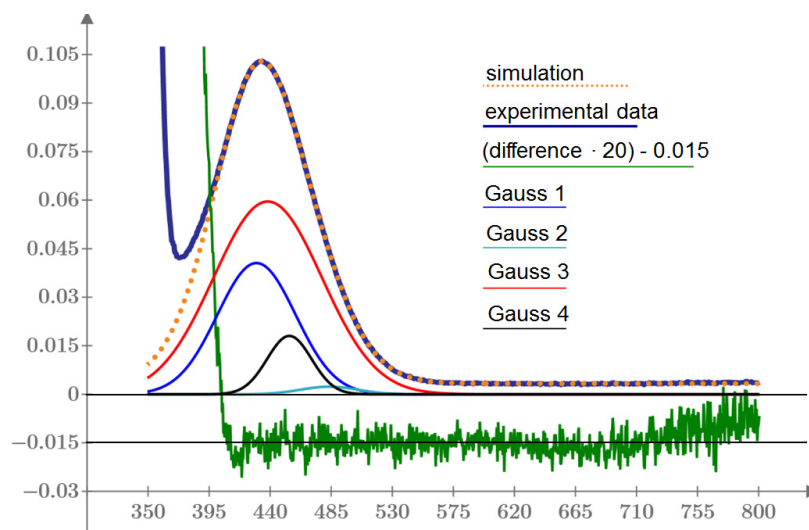


Figure 3-22 Screenshot of the "11_QYDS_spectra_baseline_correction.mcdx" Mathcad program. The baseline correction is based on the linear combination of four Gauss functions (orange dotted line). The green curve shows the difference between experimental and simulated values multiplied by a factor of 20. In this case, the baseline offset is corrected by a value of 3 mOD.

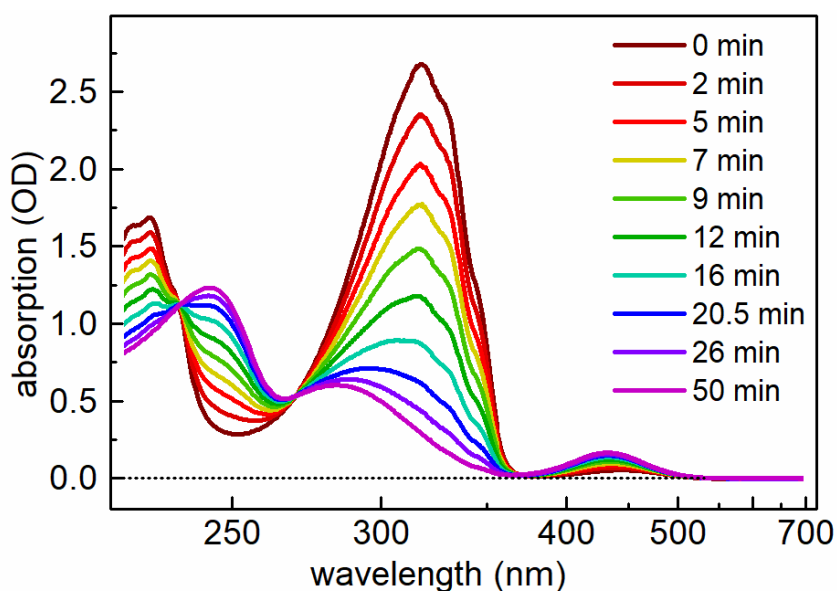


Figure 3-23 Selection of the baseline corrected UV/vis spectra for the isomerization process of (Z)-azobenzene in ethanol upon illumination with a 340 nm LED and a concentration of 119 $\mu\text{mol/L}$ in a 10 mm absorption cuvette and an illumination power of 601 μW .

3.6.3 Time evolution of the concentration

A widespread method to calculate the concentration is based on evaluation of the optical density at a single wavelength. This method leads to an unnecessary waste of the information in the measured data. In addition, in case of overlapping absorption spectra, the single wavelength analysis is impossible. Instead of this unnecessary waste of data points, a projection onto basis spectra is performed (see Eq. 3.14). Hereby, the molar absorptivities of both substances are explicitly used. The optical density is related to the molar absorptivity of the specimen $\epsilon_X(\lambda)$, the concentration of the specimen conc_X and the cuvette thickness d :

$$\text{OD}(\lambda, t) = \sum_{i=1}^n \epsilon_i(\lambda) \cdot \text{conc}_i(t) \cdot d \quad (3.14)$$

As an additional feature undesired slight changes of the sample can be immediately identified (e.g., creation of a side product, sample degradation etc.). The spectral decomposition of each UV/vis spectrum results in the time evolution of the concentration for substrate and product (see Fig. 3-24).

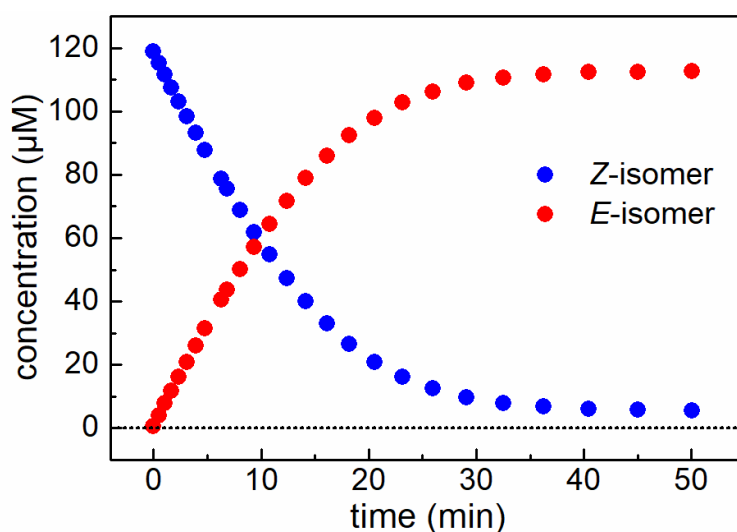


Figure 3-24 Time evolution of the isomerization from (Z)- to (E)-azobenzene in ethanol upon irradiation with a 340 nm LED and a concentration of 119 $\mu\text{mol/L}$ in a 10 mm absorption cuvette and an illumination power of 601 μW .

3.6.4 RQY calculation

A typical evaluation method widely used in the literature [Roi18] uses the initial slope of the increasing product concentration. This very simple approximation is only applicable on a system, in which the absorption spectra of substrate and product do not overlap at the

excitation wavelength. Besides the debatable issue of how far the process is still in the linear regime, the initial slope method is limited to rather low conversions that lead to a loss of precision and valuable information from the full conversion of the substance.

In the QYDS approach, the time evolution of both specimen concentrations is numerically simulated with the aid of the full information about the molar absorptivities and spectral distribution of the LED. The parameters used for the calculation of the simulated curve are fitted to the experimental data.

The whole evaluation procedure starts with the calculation of the number of photons:

$$N_{\text{Ph}}(t, \lambda) \left[\frac{1}{\text{s}} \right] = \frac{P_0 \cdot \text{LED}(\lambda) \cdot \lambda}{h \cdot c} \quad (3.15)$$

whereby $\text{LED}(\lambda)$ is the spectral distribution of the LED light, h is Planck's constant and c the speed of light. P_0 is the incoming illumination power. During the experiment, the transmitted power after the sample cuvette P_{sample} is continuously monitored. The reference power P_{ref} corresponds to the transmitted power after a cuvette filled with the pure solvent. However, the reference cuvette does not take into account, that part of the light is reflected back to the cuvette. Thus, a reflection correction for the power P_0 is introduced [Meg10]:

$$P_0(t) = (P_{\text{ref}}(t) - P_{\text{sample}}(t)) \cdot \frac{1 + R \cdot \frac{P_{\text{sample}}(t)}{P_{\text{ref}}(t)}}{1 - R} \quad (3.16)$$

where the reflection R is characterized by the Fresnel law regarding the refractive indices n_x of different media:

$$R = \frac{n_1 - n_2}{n_1 + n_2} \quad (3.17)$$

For example, the reflection at the fused silica cuvette and air boundary for 443 nm is $R_{\text{air/fus.sil.}} = 0.0357$. The contribution of the reflection of fused silica and ethanol is with $R_{\text{fus.sil./EtOH}} = 0.0014$ rather small.

The reference power P_{ref} is typically kept constant, but if it is desirable, the power can be decreased or enhanced according to experimental preferences even during the illumination. This has only to be considered properly in the evaluation.

The absorption $A(t, \lambda)$ is related to the time dependent concentration of the specimen i $c_i(t)$, molar absorptivity $\varepsilon_i(\lambda)$ and the cuvette thickness d :

$$A(t, \lambda) = 1 - 10^{-d \cdot \left(\sum_{i=1}^n c_i(t) \cdot \varepsilon_i(\lambda) \right)} \quad (3.18)$$

Using the spectral information of the substrate and product, one can calculate the number of absorbed photons for each isomer. For easier understanding an auxiliary quantity for the fraction of absorbed photons for species A is defined:

$$\text{Frac}_A = \frac{c_A(t) \cdot \varepsilon_A(\lambda)}{\sum_{i=1}^n c_i(t) \cdot \varepsilon_i(\lambda)} \quad (3.19)$$

Consequently, the change in the number of the isomer molecules per illumination time interval is given as:

$$\begin{aligned} \frac{dN_A(t)}{dt} &= \int \left[-\phi_{A \rightarrow B} \text{Frac}_A + \phi_{B \rightarrow A} \text{Frac}_B \right] N_{\text{Ph}}(\lambda) A(t, \lambda) d\lambda \\ \frac{dN_B(t)}{dt} &= \int \left[-\phi_{B \rightarrow A} \text{Frac}_B + \phi_{A \rightarrow B} \text{Frac}_A \right] N_{\text{Ph}}(\lambda) A(t, \lambda) d\lambda \end{aligned} \quad (3.20, 21)$$

This system of ordinary differential equations is integrated numerically and fitted to the experimentally determined concentrations with the forward and backward quantum yields ϕ_A and ϕ_B as fit parameters. Consequently, the quantum yield for both directions is determined within one experimental measurement (see Fig. 3-25).

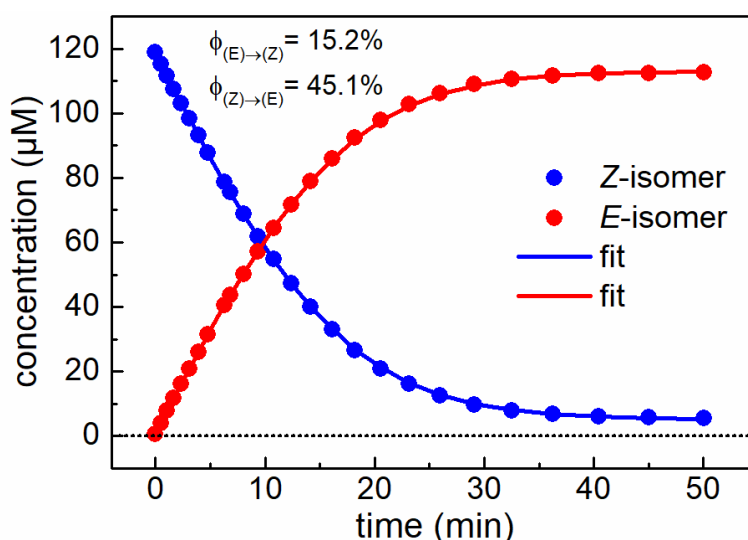


Figure 3-25 Results for isomerization of a 119 $\mu\text{mol/L}$ ethanolic solution of (Z)-azobenzene in a 10 mm cuvette upon illumination with a 340 nm LED and 601 μW illumination power. The RQY for both isomerization processes is readily extracted.

3.7 Validation

The comparison with standard chemical actinometry was used to validate the QYDS setup published in 2010 [Meg10]. The measured values were in superb agreement with published, well-established values. Another validation was based on the determination of quantum yields for reactions published by various groups and those analyzed in our laboratory [Meg10].

In this work, the QYDS method is validated by comparison with the well characterized systems from two different reaction type classes and compared with the values found in the literature. The first class is a classical photochemical reaction, where the reactant reacts upon illumination with light to the product. The photo-promoted backreaction or thermal backreaction is excluded. From this category the photoinduced reaction of *o*-nitrobenzaldehyde → *o*-nitrosobenzoic acid is investigated.

The second class is molecular photoswitches possessing high fatigue resistance that can be switched numerous times. For this purpose, a molecule from the diarylethene family (DAE) is studied - the molecular photoswitch 1,2-Bis(2,4-dimethyl-5-phenyl-3-thienyl)-3,3,4,4,5,5-hexa-fluoro-1-cyclopentene synthesized by Irie in 1995 [Iri95].

3.7.1 Photochemical reaction of *o*-nitrobenzaldehyde

The photoinduced transformation of *o*-nitrobenzaldehyde to *o*-nitrosobenzoic acid can be regarded as one of the widely spread actinometers [All00, Gal10, Ji18, Cru13]. The reaction proceeds intramolecularly [Geo80, Lai05] and can be easily monitored by the UV/vis spectroscopy.

The initial spectrum of the pure reactant is shown in Fig. 3-26 left as purple line. The absorption band in the UV-C region decreases upon illumination with UV-A light and a spectral feature around 300 nm appears. The created product starts to absorb the excitation light which may promote other additional reaction pathways. In our investigation we observed that the isosbestic point shifts slightly during the reaction (see Fig. 3-G in Appendix). This can be assigned to the decomposition of the product, as this has already been observed in ref. [Ji18].

The molar absorptivity of the pure product is not available in the literature and neither can it be purchased commercially. For this reason, a measurement with an excitation light of 340 nm was performed, in which the decomposition effect was much smaller. The product

spectrum was extracted from the last spectrum, at which the isosbestic point was preserved. The spectrum at this point consists of reactant and product. Subsequently, a variable percentage (5-10%) of the reactant spectrum is subtracted so, that no negative spectrum occurs. The value of 7% of the reactant in the mixture leads to a reaction quantum yield of 41.2% for 325 nm excitation light. Only minor changes were observed in the RQY value if the substrate concentration was varied by few percent.

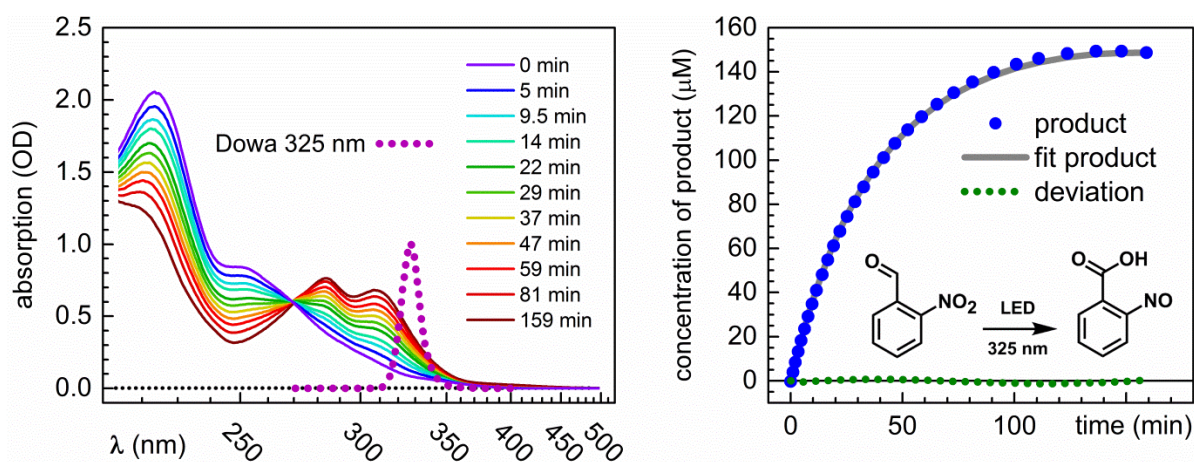


Figure 3-26 Photoinduced reaction of *o*-nitrobenzaldehyde to *o*-nitrosobenzoic in acetonitrile under standard conditions. The 153 μM solution in a 10 mm absorption cuvette is irradiated with a 325 nm LED and an illumination power of 500 μW . (left) Spectral changes upon illumination with excitation source. (right) Time evolution of the concentrations and numerical fit.

The right plot in Fig. 3-26 shows the time evolution of the product concentration and modeling fit (grey line). The residuum in dotted green line revealed minor deviation from zero, which can be attributed to the decomposition. The experimental values give a good agreement with a newer value of the RQY of $43 \pm 3\%$ reported by Galbavy *et al.* [Gal10] and Gescheidt and coworkers [Sta18a]. It is reasonable to support their suggestion to replace the established values of 50% [Kuh04, Lei34, Geo80].

3.7.2 Molecular photoswitches

The commercially available molecular switch used for the following validation was originally synthesized by Irie and coworkers [Iri95]. The high fatigues resistance without any noticeable side product and good thermal stability makes this system suitable for verification purposes. The colorless solution of the pure open form undergoes upon illumination with UV-B light a ring closing process in which additional absorption bands around 370 nm and 560 nm appear (see Fig. 3-27). Due to the fact, that both isomer forms overlap, it is reasonable to choose the excitation wavelength wisely to maximize the product partitioning in the PSS. Although 265 nm is the optimal illumination wavelength, only values for RQY at 300 nm have been published in the literature. For this reason, the LED with a central wavelength of 300 nm (Nikkiso, VPC1A1) was selected. The ring-opening reaction can be promoted by an excitation in the region of 480-620 nm. Thus, the LED with the nominal wavelength of 590 nm (Osram, LYCP7P-JRJT) was used. The measurements were performed in n-hexane solution.

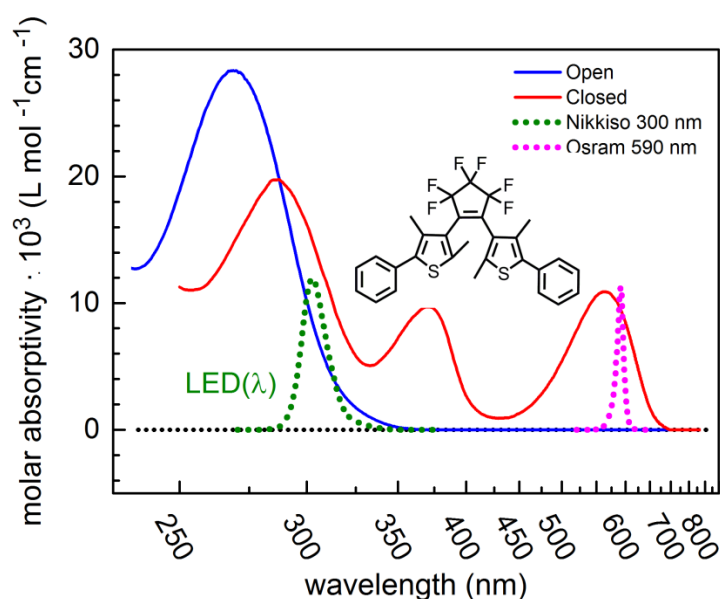


Figure 3-27 Molar absorptivities of the open and closed form of the DAE molecule in n-hexane used for the validation of the QYDS method. The excitation sources used for the photochemical reactions are shown in dotted lines.

The measured QY of 0.476 ± 0.024 for ring closing at 300 nm (see Fig. 3-28) and 0.0179 at 590 nm for ring opening (see Fig. 3-29) correspond within the experimental error to those reported by Irie *et al.* (0.45 ± 0.02 for cyclization at 313 nm and 0.017 at 590 nm for the cycloreversion process [Sum14]).

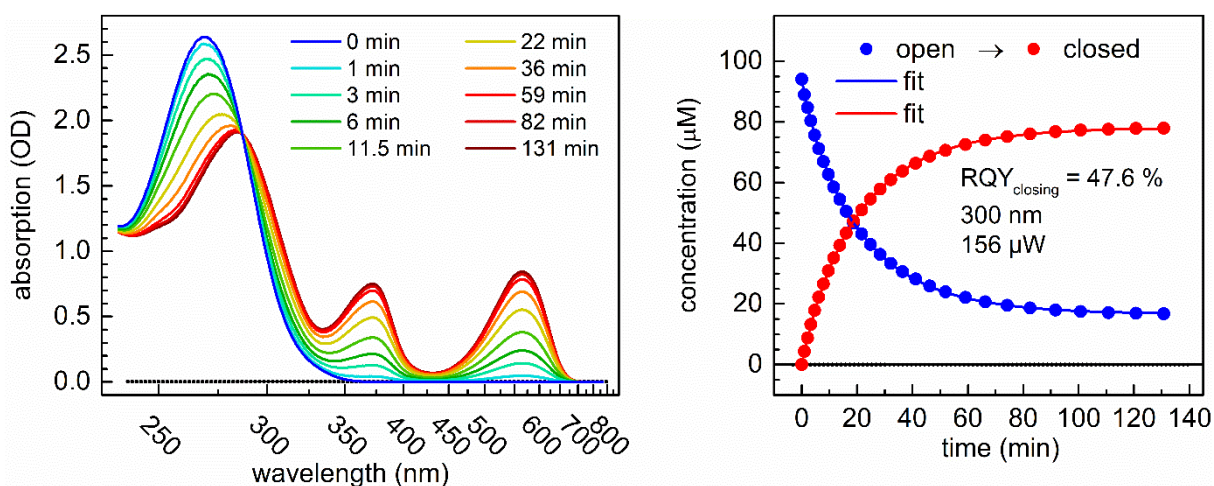


Figure 3-28 (left) Spectral changes of the open form of DAE molecule upon illumination with a 300 nm LED with the power in the sample of 156 μW . The solution was 95 μM in a 10 mm absorption cuvette with a volume of 2 mL. (right) Time evolution of concentrations during the illumination and numerical simulation (fit).

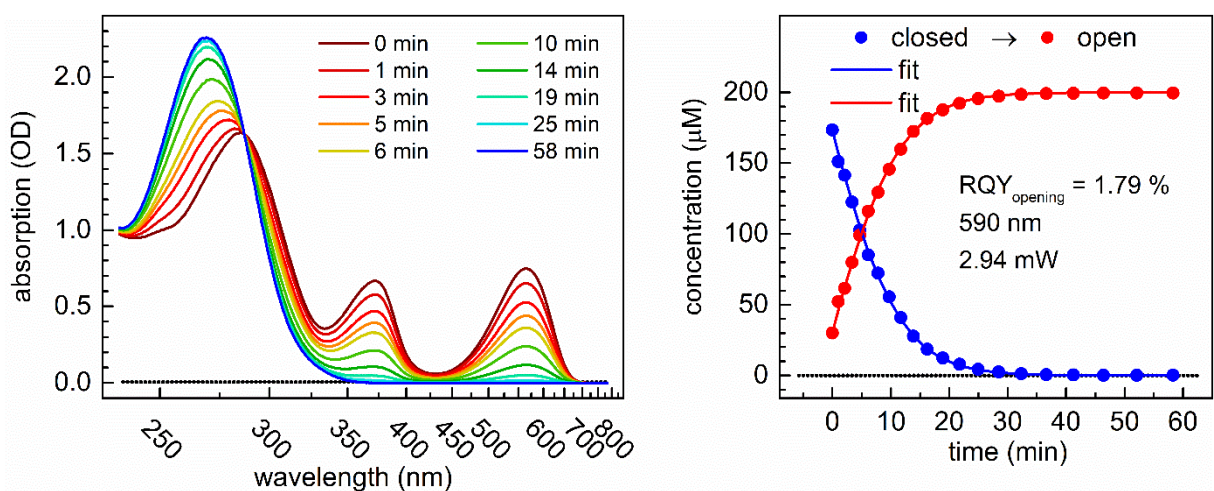


Figure 3-29 (left) Spectral changes of the closed form of DAE molecule upon illumination with 590 nm LED with the power in the sample of 2.94 mW. The solution was 200 μM in a 4 mm semi-micro-cuvette with volume of 760 μL . (right) Time evolution of concentrations during the illumination and numerical simulation (fit).

3.7.3 Reaction quantum yield of azobenzene

The azobenzene is widely accepted as a standard actinometer [Gau76, Gau84, Kuh04]. Due to its thermodynamically stable isomers [Rau82], its robustness under prolonged illumination, and its commercially available pure form [Kuh04], azobenzene became an excellent candidate for establishment as a standard in photochemistry.

In addition, azobenzene can be directly analyzed by UV/vis spectroscopy, and its spectra and RQYs are measured and published in a variety of solvents [Bor79, Fis60, Yam62, Sia87]. Last but not least, there are several publications discussing the mechanism of the isomerization process, but this topic seems to remain open for further discussion and investigations [Ban12, Mer21, Qui14].

Recently, however, several groups have addressed the problem of inconsistency in RQY measured when using azobenzene and ferrioxalate as actinometers [Lad17, Ans15, Cor16]. When searching the literature for the RQY of azobenzene dissolved in various solvents, one encounters a large scatter of values, in some cases even exceeding 30%, in extreme cases almost by a factor of two is found (see Table 3.2).

Table 3.2 Summary of literature values for azobenzene photoisomerization.

solvent	RQY $\pi \rightarrow \pi^*$ excitation ≈ 300 nm		RQY $n \rightarrow \pi^*$ excitation ≈ 440 nm	
	(E) \rightarrow (Z)	(Z) \rightarrow (E)	(E) \rightarrow (Z)	(Z) \rightarrow (E)
acetonitrile	0.15 ^[Bor79]	0.21 ^[Bor79] 0.35 ^[Sia87]	0.31 ^[Bor79]	0.46 ^[Bor79]
H₂O/ethanol 80:20	0.21 ^[Bor79]	0.15 ^[Bor79] 0.40 ^[Sia87]	0.35 ^[Bor79]	0.41 ^[Bor87]
methanol	0.13 ^[Gau85] , 0.14 ^[Ron74]	0.30 ^[Gau85] , 0.37 ^[Sia87]	0.22 ^[Gau85] , 0.28 ^[Ron74]	0.63 ^[Gau85]
	0.09 ^[Geg68] , 0.14 [*]	0.40 ^[Geg68] , 0.33 [*]	0.25 ^[Geg68] , 0.32 [*]	0.40 ^[Geg68] , 0.47 [*]
ethanol	0.15 ^[Bor79] , 0.12 ^[Rau84]	0.24 ^[Bor79] , 0.31 ^[Rau84]	0.28 ^[Bor79] , 0.24 ^[Rau84]	0.51 ^[Bor79] , 0.53 ^[Rau84]
	0.22 ^[Bir83] , 0.14 ^[own]	0.69 ^[Bir53] , 0.43 ^[own]	0.36 ^[Bir53] , 0.23 ^[own]	0.45 ^[Bir53] , 0.44 ^[own]

* re-determined RQY published in work of Wirz's group [Lad17]

The group of Wirz [Lad17] approached the problem that the molar absorptivities of the two pure isomers are crucial for a highly accurate calculation of RQY. They found that the well-

accepted molar absorptivities in methanol were not pure from the other isomer. Therefore, they re-measured the (E)- and (Z)-azobenzene in methanol as well as the RQYs. They also found that the 1 nm deviation in the wavelength calibration of the monochromator resulted in an 8% deviation in the RQY. In addition, the practical recommendations are summarized when working with azobenzene as an actinometer. Finally, they suggested that these new observations should be considered in further work with azobenzene. [Lad17]

Considering the above development and facts about azobenzene, it is reasonable to accept azobenzene as the standard in photochemistry. The following topic therefore covers a further study on azobenzene.

In this section, the impact of varying illumination power on the reaction quantum yield of azobenzene is investigated. The variation of the optical intensity on the sample may be regarded as disputable due to the fact, that up to date no explicit expertise was performed.

However, according to the results (see Tab. 3-3) the reaction quantum yield is independent on the illumination power of the incident light. It is reasonable to assume, that the molecular dynamics with one absorption band remains relatively constant and hence the RQY is not wavelength dependent. For this set of experiments, the excitation light of a 400 nm LED (Luxeon LHUV-0400-0450) was used.

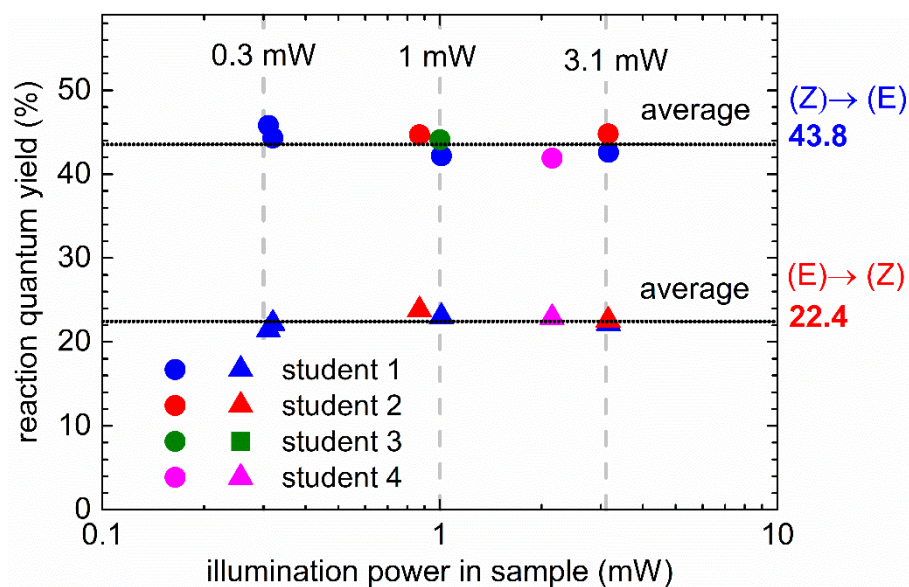


Figure 3-30 Photoinduced isomerization of azobenzene in ethanol upon illumination with a 400 nm LED. The measurements were performed by students in Munich and Heidelberg.

Table 3-3 Reaction quantum yield of azobenzene in ethanol in dependence on the illumination power of the incident light with central wavelength at 400 nm.

400 nm	illumination power				average (%)	standard deviation (%)
	0.3 mW	0.9 mW	1.0 mW	3.1 mW		
$\phi(\text{Z}) \rightarrow (\text{E})$ (%)	44.3	44.7	42.2	44.8	43.8	1.4
$\phi(\text{E}) \rightarrow (\text{Z})$ (%)	21.2	23.8	23.0	22.6	22.4	0.9

Unfortunately, these own measured values of RQY in ethanol (see Tab. 3-3) cannot be directly compared with the values recently reported by Wirtz's group, since their work used methanol instead of ethanol as a solvent (see Tab. 3-2 blue values).

Nevertheless, the azobenzene can be still regarded as one of the most suitable systems to verify a reproducibility of the QYDS measurement, since as shown here, there is no correlation between illumination power and RQY. Additionally, its good commercial availability of the pure (E)-isomer [Ku04] makes azobenzene a favorable candidate as a model system.

Thus, the reaction quantum yield of the azobenzene was measured by various students on different setups and in different cities. The results are summarized in the Fig. 3-30 and Tab. 3-3. The measured values fluctuate only within a relative error of 5%.

In summary, azobenzene was used as a model system to verify the reproducibility of RQY measured with QYDS. The results show that the measurements are well reproducible and the relative error is well below 5%.

3.8 Application of the Fisher method for extraction of the product spectrum to azobenzene as a model system.

In order to apply the Fischer method [Fis67], there are several **requirements** that have to be met:

- The system under study must be a reversible two stage photosystem $A \rightleftharpoons B$ (typically two isomers).
- Both isomers must be thermally stable.
- The exact molar absorptivity of one isomer must be known.
- Upon illumination well defined and stable PSS states must be reached.
- Neither degradation nor creation of a side product is present, the total concentration remains constant.

The chosen model system – azobenzene – fulfills all above-mentioned requirements. The thermodynamically stable (E)-azobenzene is commercially available in spectroscopically acceptable purity [Kuh04] and hence, the molar absorptivity of the (E)-isomer can be straightforward measured.

The Fisher method is based on generally valid and adapted assumption, that the RQY remains constant while excitation is guaranteed within one separated electronic band. Hereby, it is expected that the same electronic state is excited and the molecular dynamics is expected to be quite similar. Therefore, a series of two measurements is performed with two different light sources for excitation of the same absorption band.

The following **procedure** for the analysis is proposed:

i. Illumination up to the PSS with two different wavelengths.

The ethanolic (E)-azobenzene solution (119 μM) is illuminated with a 300 nm LED (Nikkiso, VPC1A1) and in the next run a 340 nm LED from Seoul Viosys (CUD4AF1B) until the PSS is reached each time. A moderate illumination power of 740 μW for the 300 nm LED and 610 μW for the 340 nm LED was used.

In this work two freshly prepared samples were used. In principle, one sample (after illumination with 300 nm) can be illuminated with a 400 nm LED to promote the reverse reaction. This PSS then consists of 85% (E) isomer and 15% (Z) isomer. This sample can then be illuminated again with 340 nm LED. Here, however, it is important that the cuvette

has proper ceiling to avoid evaporation and changes in concentration.

ii. Analysis of the product amount in the PSS state

Since the higher conversion is observed for the 340-nm LED, this measurement is preferred for further analysis. The amount of the (E)-azobenzene in the PSS is estimated to be between 0% and 6%. An even higher amount would lead to a formally negative absorption spectrum (see red dotted line in Fig. 3-31).

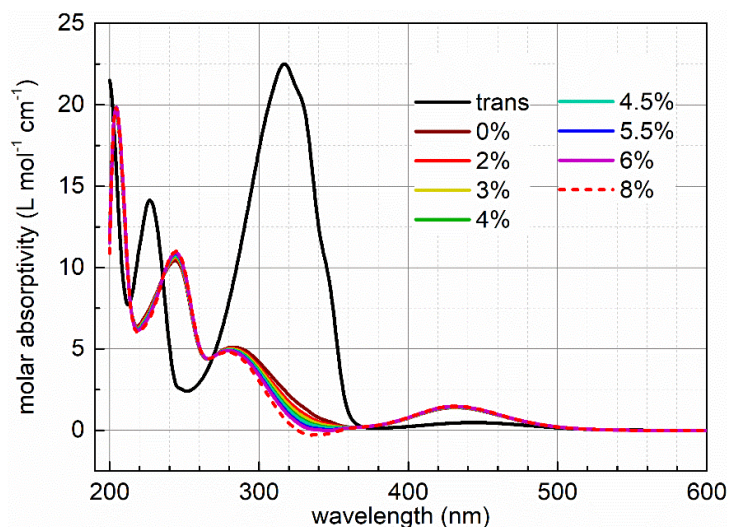


Figure 3-31 Calculated (Z)-azobenzene spectra in ethanol over different amounts of (E)-azobenzene in PSS upon illumination with 340 nm LED.

iii. Determination of the RQY using the product spectrum from the previous step

The various molar absorptivities from Fig. 3-31 are subsequently used for evaluation of both datasets. The RQY determination is performed as described in Chapter 3.6.4 using numerical integration (propagation) of equations 3.20 and 3.21. As a result, RQYs for both forward as well as backward reaction are obtained.

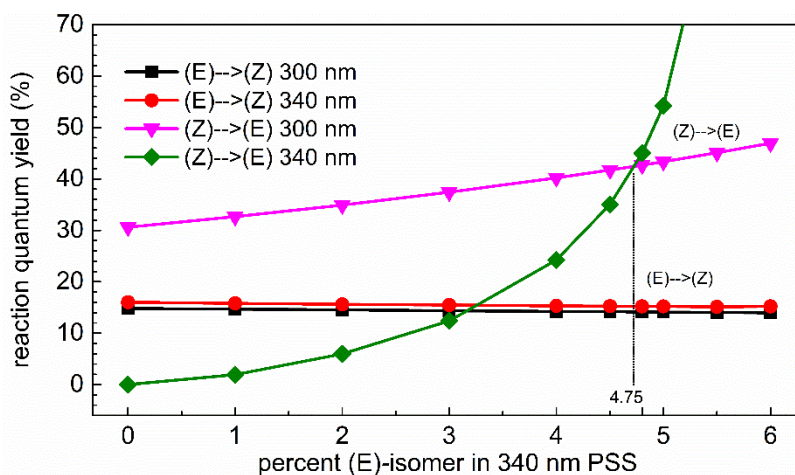


Figure 3-32 Dependence of the reaction quantum yield values on the product spectrum extracted from PSS reached by 340 nm LED.

iv. Results and final determination of product amount in the PSS

Finally, the RQY obtained in the previous step (depending on the product spectrum used) is plotted against the percentage of product in the PSS. According to the results shown in Fig. 3-32, the RQY of isomerization from E to Z is rather independent on the product spectrum. However, the back reaction reveals a strong dependency on the product spectrum. Due to the fact, that the RQY is expected to be wavelength independent, the final amount of the reactant in the PSS can be easily extracted from the plot in Fig. 3-32. The amount of the reactant in the PSS state reached by 340 nm LED is exactly at the point where the green and magenta curves in Fig. 3-32 intersect. This corresponds to 4.75% of product in the PSS.

In conclusion, the Fischer method is an elegant approach for determination of the molar absorptivity for reversible two stage system. In case of azobenzene it was observed, that for high accuracy of the back reaction an exact molar absorptivity of the product spectrum is required.

3.9 Reaction quantum yield - more than just one number

The reaction quantum yield measurement up to the PSS contains more information than the absolute number of the RQY as a cost of the photoinduced process. So far, only the value above one $RQY > 1$ indicated some more information about the mechanism of the reaction. Such reactions are typically connected with a radical chain reaction process [Lov19, Cis15, Rei21]. However, also a system with $RQY < 1$ may disclose many more details on the reaction mechanism. As an example, a photoreduction of the $[Ni^{II}(\text{Mabiq})]\text{Otf}$ with a sacrificial donor dimethylaniline (**DMA**) is introduced (see Fig. 3-33). For simplicity of the notation, the reactant is denoted as **Ni-Mabiq** and the reduced product **Ni-Mabiq^{red}**.

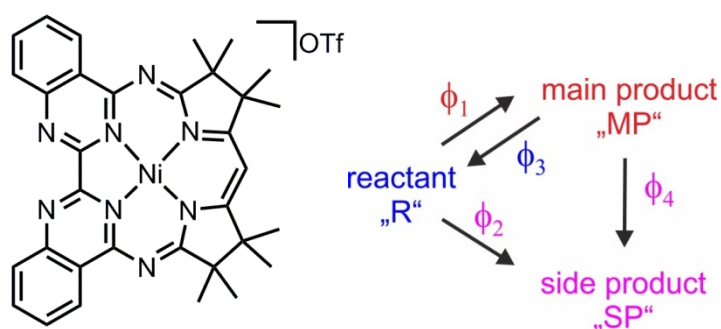


Figure 3-33 (left) Macrocyclic biquinazoline ligand based $[Ni^{II}(\text{Mabiq})]\text{Otf}$. (right) Reaction model, in which a side product may originate from the reactant as well as from the product. Reactant “R” represents **Ni-Mabiq**, main product “MP” corresponds to **Ni-Mabiq^{red}** and “SP” is the side product.

Upon illumination with a 455 nm LED, the **Ni-Mabiq** molecule is excited and reduced to **Ni-Mabiq^{red}**. This reaction is apparently accompanied by the creation of a side product. According to the analysis, the side product has absorption bands between the deep UV and the 500 nm region and it can repeatedly absorb illumination light. An educated guess of the possible reaction scheme (Fig. 3-33 right) is transferred into the following kinetic model:

$$\frac{dN_R(t)}{dt} = \int [-(\phi_1 + \phi_2) \text{Frac}_R(t, \lambda) + \phi_3 \cdot \text{Frac}_{MP}(t, \lambda)] N_{Ph}(\lambda) \cdot A(t, \lambda) d\lambda \quad (3.22)$$

$$\frac{dN_{MP}(t)}{dt} = \int [\phi_1 \cdot \text{Frac}_R(t, \lambda) - (\phi_3 + \phi_4) \text{Frac}_{MP}(t, \lambda)] N_{Ph}(\lambda) \cdot A(t, \lambda) d\lambda \quad (3.23)$$

$$\frac{dN_{SP}(t)}{dt} = \int [\phi_2 \cdot \text{Frac}_R(t, \lambda) + \phi_4 \cdot \text{Frac}_{MP}(t, \lambda)] N_{Ph}(\lambda) \cdot A(t, \lambda) d\lambda \quad (3.24)$$

These set of differential equations are solved numerically, whereby the RQY are the only

free parameters to fit. The results are shown in Fig. 3-34.

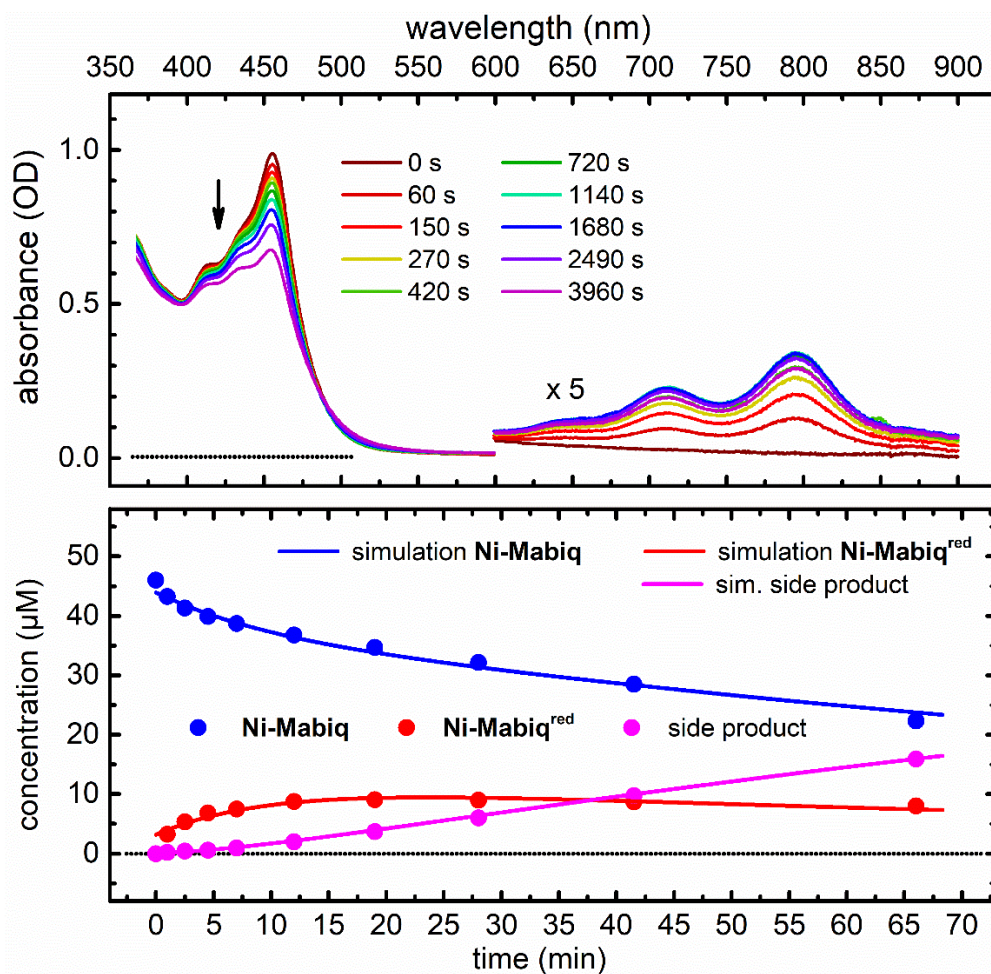


Figure 3-34 (top) Spectral changes during the photoreduction of **Ni-Mabiq** (51 μM), by **DMA** (255 mM) in THF/MeCN = 1:1 upon 455 nm excitation with power of 245 mW in 10 mm cuvette and volume 2 mL. (middle) Fit residuals resulting from projection of measured UV/vis data onto basis spectra. (bottom) Time evolution of concentrations with the reaction quantum yields of $\phi_1 = 0.5 \times 10^{-4}$, $\phi_2 = 0 \times 10^{-4}$, $\phi_3 = 2.7 \times 10^{-4}$ and $\phi_4 = 1.1 \times 10^{-4}$. The side product amounted to 34.5 % and **Ni-Mabiq^{red}** amounted to 17.4 % of the reaction mixture upon 66 min of illumination.

The result (see Fig. 3-34 bottom) revealed a predominant backreaction from **Ni-Mabiq^{red}** to **Ni-Mabiq** with a high quantum yield of 2.7×10^{-4} . This value is one order of magnitude higher than the classical light promoted reduction from **Ni-Mabiq** to **Ni-Mabiq^{red}**. The side product originates only from the further excitation of the product molecules. The creation of the side product directly from the reactant can be regarded as negligible.

In conclusion, the detailed analysis of the whole data set results not only in a number, but it can describe the data fully, i.e., it can suggest and differentiate rather complex reaction models. In recent investigations it was even found that after the actual photo-initiated process a rather slow thermal process on the time scale of many minutes follows. Such a situation can readily be analyzed with the presented techniques if not only photo-dependent but also purely temporal terms are used in the reaction scheme.

3.10 Conclusion and Outlook

In this work we have introduced the optical instrument and detailed measurement approach for facile and exact RQY determination under standard lab conditions. The modular setup consists of commercially available optics and it can be easily customized for the user's requirements. The introduction of new components and features, i.e., the electronic shutter, the I/U converter and the SCD contributes to the enhanced precision of the RQY determination. The GUI interface provides compact information of the experimental parameters and observables that are used for the extensive analysis of the whole data set up to the PSS. The QYDS approach is validated for all photoreaction types and in contrast to the chemical actinometry it can be used without limitations for any photosystem. It should be particularly noted that the spectral range of the classical actinometry is limited by practical considerations to the UV and blue part of the spectrum [Kuh06] while our new method can readily be extended up to 1100 nm (application relevant for NIR window in biological tissues, e.g., blood [Li20a]) by just the choice of LED and even beyond if an InGaAs detector were used.

The chemical actinometry has been developed primarily due to the missing equipment for the quantification of light in the 30-ties and 60-ties of last century. Since the power meters are nowadays commercially available in a moderate price category, the chemical actinometer can be regarded as redundant. Due to the reproducibility and straightforward determination of the RQY, the QYDS can readily replace chemical actinometry and offer precise RQY determination with an accuracy better than 5% relative error.

Appendix for Chapter 3

Appendix 3-A

List of QYDS users

AG Prof. Burkhard König (Universität Regensburg)

AG Prof. Henry Dube (Friedrich-Alexander-University Erlangen-Nürnberg)

AG Prof. Axel Griesbeck (Universität zu Köln)

AG Prof. Andres Jäschke (Universität Heidelberg)

AG Prof. Josef Michl (ÚOCHB AV ČR Prague)

AG Prof. Carsten Streb (Universität Ulm)

AG Prof. Axel Jacobi von Wangelin (Universität Hamburg)

AG Prof. Hans-Achim Wagenknecht (Karlsruhe Institute of Technology)

AG Prof. Eric Meggers (Philipps-Universität Marburg)

AG Prof. Chris Ritchie (The University of Melbourne)

AG Prof. Corinna Hess (Technische Universität München)

AG Prof. Oliver Trapp (Ludwig-Maximilians-Universität München)

AG Prof. Stefan Hecht (Humboldt-Universität zu Berlin)

AG Prof. Thomas Huhn (Universität Konstanz)

AG Prof. Dominik Wöll (RWTH Aachen Universität)

AG Prof. Lisa McElwee-White (University of Florida)

AG Prof. A. Jacobi von Wangelin (University of Hamburg)

Appendix 3-B

LEDs specifications and maximal illumination power in sample

Table 3-B LEDs specifications and maximal illumination power in sample.

manufacturer	type	nominal spectral			max.	max.	spot size	intensity
		λ (nm)	width (nm)	I_{\max} (mA)	power (mW)	power (mW)	(mm ²)	(mW/cm ²)
					best form lens	aspheric/plano-convex lens		
LG Innotek	UV-C 6060 PKG	255	11	350	1.6	4.5	4.8 x 4.8	20
LG Innotek	LEUVA66G00HV00	278	12	500	37.3	100	2.6 x 2.6	1479
Bolb	Hex-S6060-125	260-278	11	500	17.8	68	2.2 x 3.0	1030
LG Innotek	LEUVA66H100KU00	305	13	500	30	77.4	2.6 x 2.6	1145
Dowa	EOLS-310-667	310	15	600	23.6	68.7	3.6 x 3.6	530
Dowa	EOLS-325-697	325	13	600	9.5	32.2	2.5 x 2.5	515
Dowa	EOLS-325-667	325	12	600	17	47.5	3.4 x 3.4	597
Dowa	EOLS-325-637	325	12	600	22	56.2	5.0 x 5.0	225
Seoul Viosys	CUD4AF1B	340	10	500	9.2	42.5	2.8 x 2.8	542
Dowa	EOLS-340-667	340	7	600	26.2	69	3.4 x 3.4	597
Dowa	EOLS-340-637	340	7	600	22.3	63	6.0 x 6.0	175
Seoul Viosys	CUN6GB1A	365	9	1400	422	1600	6.6 x 6.4	3788
Seoul Viosys	CUN8GB1A	385	10	1400	435	1816	6.6 x 6.4	4299
Luxeon	LHUV-0400-0450	400	11	1000	117.3	448	3.0 x 3.0	4978
Luxeon	LHUV-0415-0600	415	13	1000	146.2	542	3.3 x 3.3	4977
Luxeon	LHUV-0420-0650	420	13	1000	154	597	3.4 x 3.4	5164
Luxeon	LHUV-0425-0600	425	14	1000	146.2	581	3.8 x 3.8	4024
Osram OSLOON SSL 80	LD-CQ7P-1U3U	455	21	1000	264	1000	6.4 x 6.0	2604
Osram OSLOON SSL 80	LBCP7P-GYHY	470	16	1000	162	733	6.6 x 6.6	1683
Osram OSLOON SSL 80	LVCK7P-JYKZ	505	33	1000	84.2	305	5.4 x 6.3	897
Osram OSLOON SSL 80	GT CS8PM1.13	521	30	1000	84.1	337	8.7 x 8.7	445
Luxeon	Rebel ES Lime	567	103	1000	88.2	511	6.5 x 6.6	1191
Osram OSLOON SSL 80	GY CS8PM1.23	593	16	1000	32	115	7.6 x 7.6	199
Osram OSLOON SSL 80	LACP7P-KPKR	617	18	1000	108	483	6.3 x 6.3	1217
Osram OSLOON SSL 80	LRC7P-JRJT	625	19	1000	144	500	6.3 x 6.3	1260
Osram OSLOON SSL 80	LHCP7P-2T3T	645	23	1000	141	594	5.4 x 5.4	2037
Osram OSLOON SSL 80	Hyper Red	660	17	1000	189	721.5	6.6 x 6.6	1656
Roithner	SMB1N-690D	690	22	600	43.8	237	3.3 x 3.3	2176
Roithner	SMB1N-690D-02	690	21	600	88.6	362	10.3 x 10.3	341
Osram OSLOON SSL 80	Far Red	730	31	1000	88.2	385	8.5 x 8.5	533
Roithner	SMB1N-780-02	780	28	800	106	390	3.5 x 3.5	3184
Roithner	SMB1N-810D-02	810	27	800	92.5	354	10.3 x 10.3	334

Table 3-B (contd) LEDs specifications and maximal illumination power in sample.

Manufacturer	Type	nominal spectral			max.	max.	spot size	intensity
		λ (nm)	width (nm)	I_{\max} (mA)	power (mW)	power (mW)	(mm ²)	(mW/cm ²)
					best form lens	aspheric/plano-convex lens		
Roithner	SMB1N-810D-02	810	27	800	92.5	354	10.3 x 10.3	334
Osram OSOLON Black	ILH-IW01-85SL-SC221-WIR200	850	30	1500	179	619	3.6 x 3.6	4776
Roithner	SMB1N-890DS-02	890	32	1000	182	708	9.0 x 9.0	1656
Osram OSOLON Black	ILH-IO01-94SL-SC201-WIR200	940	38	1000	149	501	5.5 x 5.5	1656
Roithner	SMB1N-980D	980	38	800	62.8	308	8.4 x 8.4	437
Roithner	SMB1N-1050-02	1050	72	600	3.55	16.5	5.5 x 5.5	55

Appendix 3-C

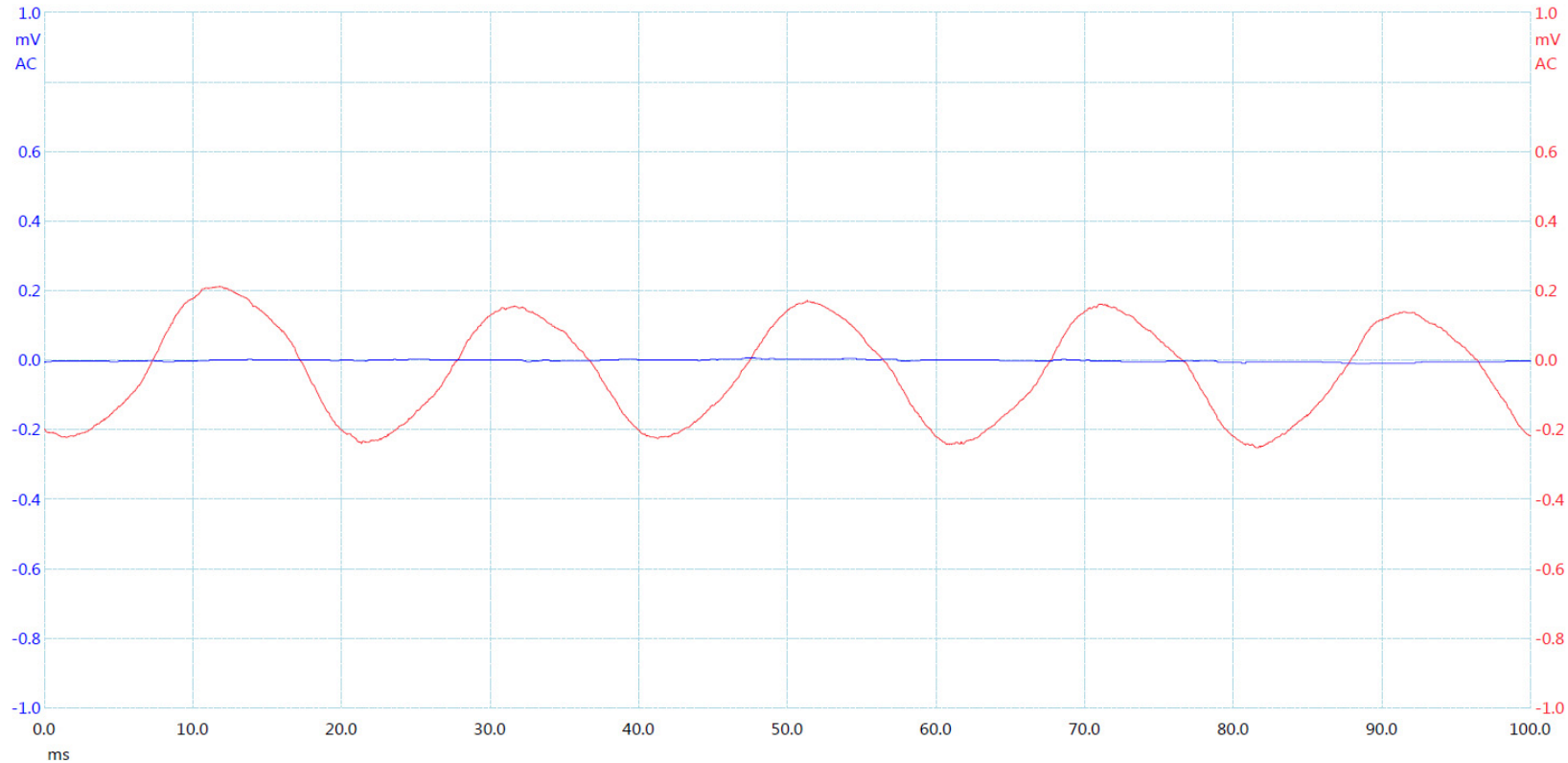
Specifications of spectral distribution of LEDs in dependence of driving current.

Table 3-C Specifications of spectral distribution of LEDs in dependence of driving current. The values for central wavelength are measured at 300 mA.

manufacturer	type	λ_{nominal}	$\Delta\lambda_{\text{C}} (I_{\text{min}})$	λ_{c}	$\Delta\lambda_{\text{C}} (I_{\text{max}})$	ΔFWHM
Nikkiso	VPC131	265	-0.1	269.2	0.1	0.5
LG Innotek	LEUVA66G00HV0	278	0.5	284.3	0.2	0.2
Nikkiso	VPC 171	285	-0.1	288.6	0.3	1.1
Nikkiso	VPC 1A1	300	-0.2	307.0	0.9	1.6
Seoul Viosys	CUD4AF1B	340	-0.9	348.1	0.8	0.5
Seoul Viosys	CUN6GB1A	365	-0.3	369.8	4.3	2.0
Seoul Viosys	CUN8GF1A	385	0.0	386.8	2.2	1.8
Luxeon	LHUV-0400-0450	400	-0.7	402.8	1.9	1.6
Luxeon	LHUV-0415-0600	415	-0.2	420.6	1.0	2.6
Luxeon	LHUV-0420-0650	420	-0.1	425.9	0.7	2.0
Osram OSLOM SSL 80	LDCQ7P-1U3U	455	0.6	454.8	0.5	4.5
Osram OSLOM SSL 80	LBCP7P-GYHY	470	1.7	467.7	1.4	11.3
Osram OSLOM SSL 80	LVCK7P-JYKZ	505	1.3	506.9	1.7	7.6
Osram OSLOM SSL 80	LTCP7P-KXKZ	528	3.6	529.4	-1.8	7.6
Luxeon	Rebel ES Lime	567	-0.8	566.6	2.5	3.0
Osram OSLOM SSL 80	LYCP7P-JRJT	590	-2.7	592.1	9.9	4.5
Osram OSLOM SSL 80	LACP7P-KPKR	617	-1.6	620.0	8.0	6.3
Osram OSLOM SSL 80	LRCP7P-JRJT	625	-1.3	630.4	6.0	5.5
Osram OSLOM SSL 80	LHCP7P-2T3T	645	-1.3	656.4	5.8	9.4
Osram OSLOM SSL 80	Hyper red	660	-1.2	654.2	2.3	7.7
Osram OSLOM SSL 80	Far red	730	0.5	725.9	0.2	18.9
Osram OSLOM Black	ILH-IW01-85SL-SC221_WIR200	850	-1.4	845.6	10.2	22.0
Osram OSLOM SSL 80	ILH-IO01-94SL-SC201-WIR200	940	-1.1	932.2	3.0	19.4

Appendix 3-D

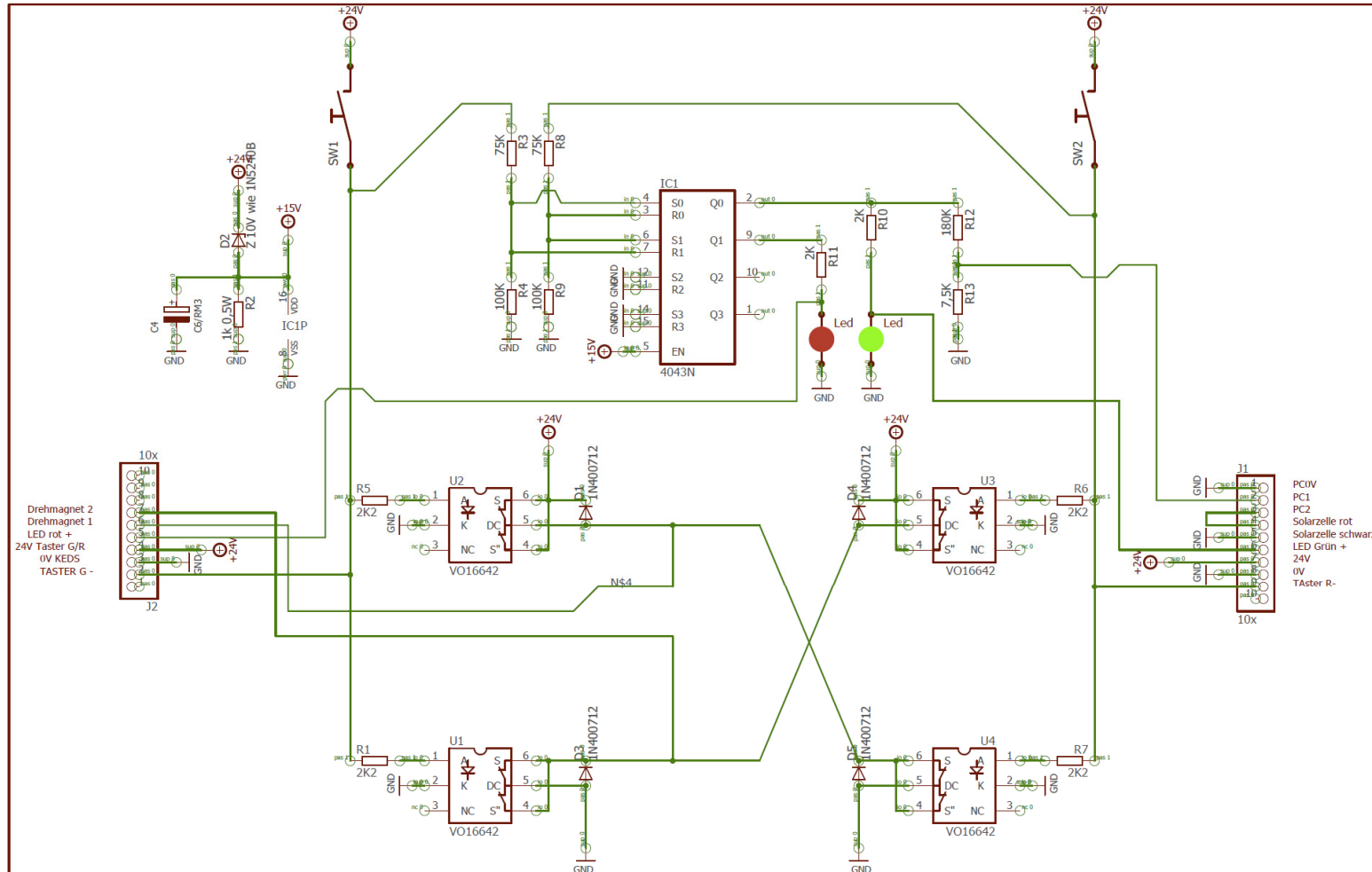
Residual noise on I/U converter



Kanal	Name	Spanne	Wert	Min.	Max.	Mittelwert	Standardabweichung
A	DC Average	Gesamte Spur	-1.617 μ V	-1.617 μ V	586.8 nV	-711.5 nV	623.6 nV
B	DC Average	Gesamte Spur	-33.26 μ V	-47.84 μ V	-29.64 μ V	-38.93 μ V	7.016 μ V
A	AC RMS	Gesamte Spur	3.217 μ V	2.881 μ V	5.737 μ V	3.961 μ V	824.6 nV
B	AC RMS	Gesamte Spur	142 μ V	132.5 μ V	143.1 μ V	138.7 μ V	3.339 μ V
B	Frequenz	Gesamte Spur	49.65 Hz	49.52 Hz	50.18 Hz	49.84 Hz	189.2 mHz

Appendix 3-E

Circuit diagram for shutter control



Appendix 3-F

Conditions for a measurement of an optimal baseline for UV/vis spectra

A possible source of systematic error in a detailed analysis of an UV/vis absorption spectrum is the diminished quality of the baseline of the photometric measurement. The form of the baseline is directly connected with the measurement of the reference. Since the correct baseline correction is critical for the accurate determination of molar absorptivity and thus for the determination of photospecies concentration, it is important to address the measurement of an optimal baseline for UV/vis spectra. The optimal baseline corresponds to $OD = 0$ over the entire spectral range when non-absorbing substrate is measured. The recommended procedure and the reasons for it are explained in detail below.

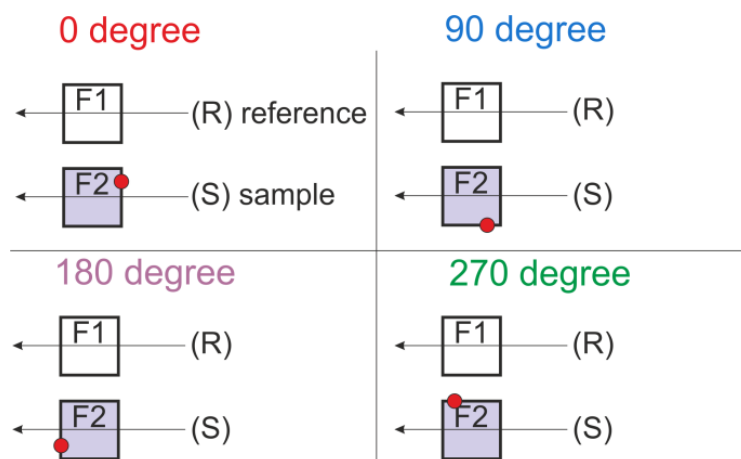


Figure 3-F1 Schematic representation of the various orientations in the double beam spectrophotometer. The reference cuvette remains unchanged. The sample cuvette F2 was rotated by 90 degrees. The red dot is demonstrated only as a guide to the eye. Finally, the cuvette F2 was replaced by another cuvette F3. The experiment was performed analogously with absorption cuvettes A1, A2 and A3, however using rotation of 180° .

A double beam UV/vis spectrophotometer utilizes two beams, one passing the reference cuvette (R) and one passing the sample cuvette (S) (see Fig. 3-F1). The baseline is measured before the first real measurement of the absorbing substance. It was observed that the individual differences of cuvettes as well as their orientations have a severe impact on the baseline. The observed deviations originate from the deviations in the parallelism of the cuvette windows and/or variations in the optical pathway.

In order to understand this effect, the following experiment was performed (see. Fig. 2-12). Three fluorescence (F1-F3, four polished sides) and three absorption cuvette (A1-A3, two polished sides) having an optical pathway of 10 mm, (Hellma) were filled with 2 mL of ethanol. A baseline scan was performed first. Then the baseline was measured using the cuvettes 1 (R) and 2 (S), thereafter the orientation of the cuvette 2 (S) was varied (see Fig, 3-F1). In addition, the effect of the new cuvette 3 (S) measured under the previous baseline conditions was examined. The results are demonstrated in Fig. 3-F2 and Fig. 3-F3.

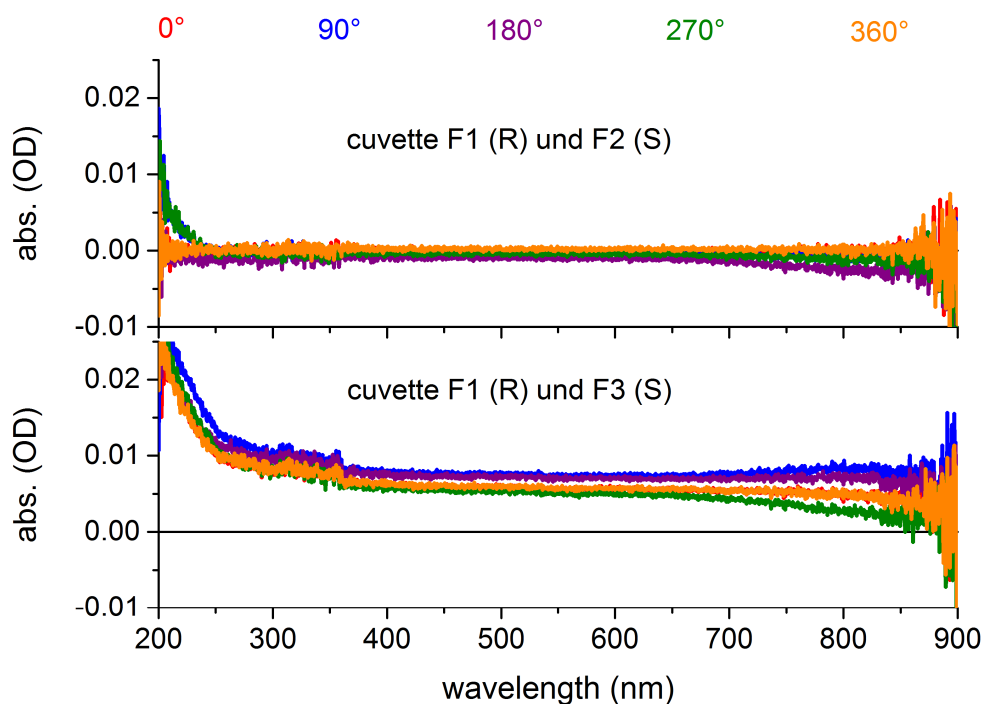


Figure 3-F2 Impact of the fluorescence cuvette orientation on the baseline in an UV/vis spectrophotometer (SHIMADZU UV-2600).

Two fluorescence cuvettes F1 and F2 were filled with 2 mL ethanol. First, a baseline scan was performed with cuvettes F1 and F2 in the 0° orientation. Then the UV/vis spectra were measured in the different orientations 0° - 360° of F2 (top) with 0° orientation of F1. In addition, the measurement was repeated using a different fluorescence cuvette F3 instead of F2 (bottom). Any change of orientation or introduction of a new cuvette leads to noticeable deviations in the baseline.

According to the resulting deviations in the absorption spectra, it is recommended to consider following points for a double beam spectrometer:

- a. measure the baseline with two cuvettes filled with a solvent
- b. subsequently, empty and dry the signal cuvette and fill it with the sample
- c. preserve the orientation of the cuvette during the measurement

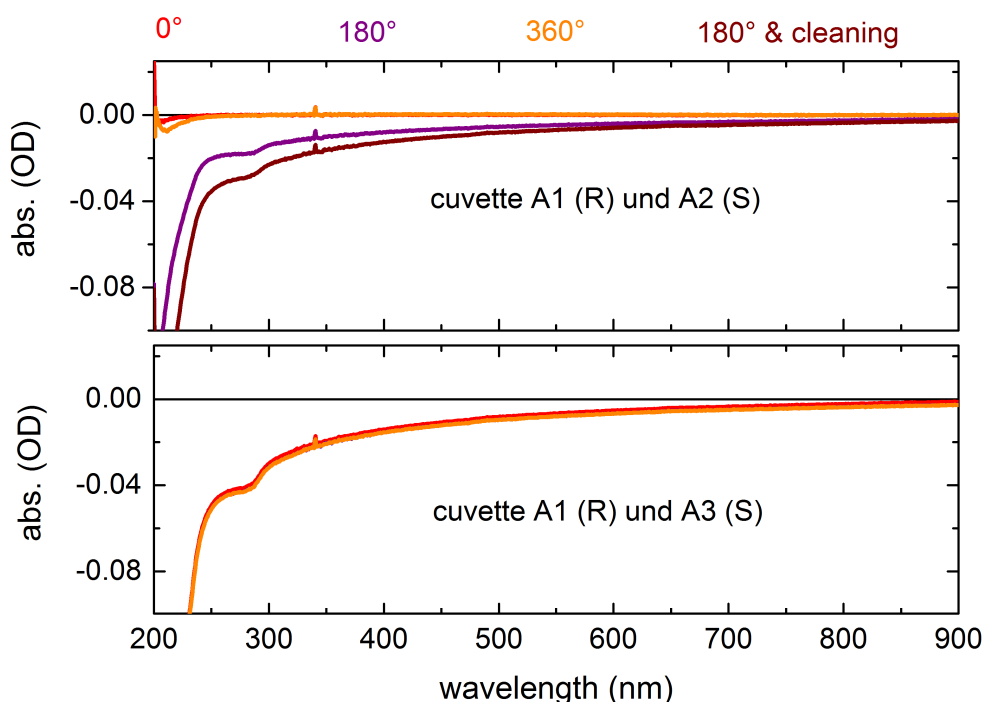


Figure 3-F3 Analog to Figure 3-F2, measured with absorption cuvettes.

Two absorption cuvettes A1 and A2 were filled with 2 mL ethanol. First, a baseline scan was performed with cuvettes A1 and A2 in the 0° orientation. Then the UV/vis spectra were measured in the different orientations 0° - 360° of F2 (top) with 0° orientation of A1. In addition, the measurement was repeated using a different absorption cuvette A3 instead of A2 (bottom). Any change of orientation or introduction of a new cuvette leads to noticeable deviations in the baseline.

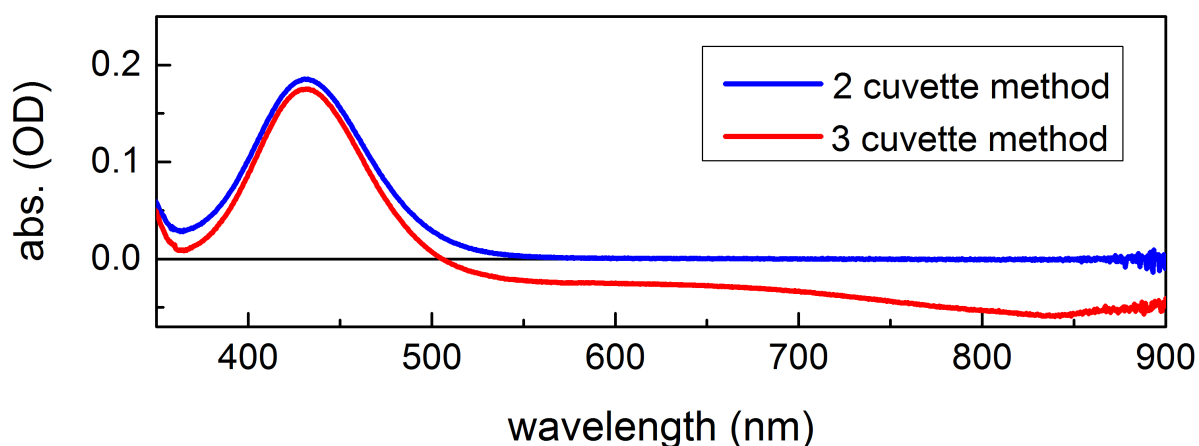


Figure 3-F4 Impact of the measurement method on the spectrum/baseline of azobenzene in ethanol measured with the procedures described above.

In some cases of nearly constant shift of the baseline it is reasonable to try to clean the cuvette. On the other hand, assuming correct handling of the cuvette, the windows are not expected to be contaminated and no additional cleaning is required.

According to recent experience, the use of the third cuvette may be advantageous under these circumstances. The third cuvette serves as a reference after the baseline has been measured using the two-cuvette method mentioned above. In this way, an additional cuvette is spectroscopically defined and can be used at regular time steps to check the quality of the baseline.

In summary, it is recommended to use only two cuvettes for the whole UV/vis measurement ("2 cuvette method"). The application of an additional cuvette that is not concerned in the baseline correction may in extreme cases as demonstrated in Fig. 3-F4 lead to extensive deviation in the baseline ("3 cuvette method").

In some special cases, a longer illumination period than 12 hours is required to follow the photochemical or photocatalytic reaction. In such cases, deviations in the baseline may occur (e.g., drift), which must be taken into account in the evaluation.

According to recent experience, the use of the third cuvette may be however advantageous under these circumstances. The third cuvette serves as a reference after the baseline has been measured using the two-cuvette method mentioned above. In this way, an additional cuvette is spectroscopically defined and can be used at regular time steps to check the quality of the baseline.

Appendix 3-G

Degradation of the *o*-nitrobenzaldehyde

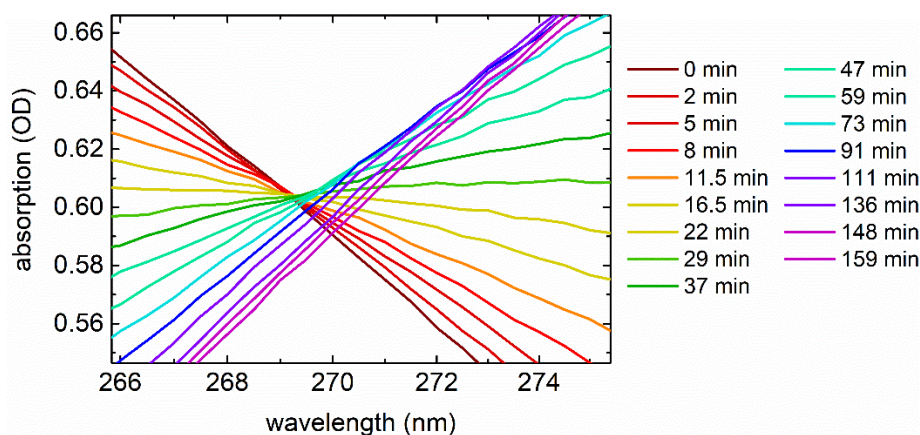


Figure 3-G Isosbestic point of photoinduced transformation of *o*-nitrobenzaldehyde. After 37 minutes of illumination a spectral shift of the isosbestic point can be observed.

Appendix 3-H

Summary of the validation for QYDS methodology

Table 3-H Summary of the validation for QYDS methodology.

	excitation wavelength	RQY in literature	this work
DAE Irie	300 nm	0.45 ± 0.02 [Sum14]	0.47 ± 0.02
	590 nm	0.0166 [Sum14]	0.0179
<i>o</i> -nitrobenzaldehyd	325 nm	0.43 ± 0.03 [Gal10, Sta18a]	0.41 ± 0.02

4. Ultrafast switching of diarylethene based molecular photoswitches

4.1 Introduction

Photochromic molecules undergo a reversible transformation between two or more isomeric forms. Typically, each of these forms has different optical and electronic properties. Such molecules, which upon illumination undergo reversible structural and electronic changes and can be interconverted between two states, are known as photoswitches.

Diarylethenes (DAE) are a widespread family of photoswitches. DAE attracts much attention due to their excellent properties such as high thermal irreversibility [Iri00], robust fatigue resistance [Her15], rapid photoresponse performance [Jia16] and good photocyclization quantum yields [Iri00]. Consequently, DAE are interesting for applications in the field of optoelectronics [Iri00, Tia04, Bae13] such as optical memory storage [Uno11, Sha13] or optical transistors [Org14, Gem15]. Additionally, DAE are also to find in photocontrolled biological applications as imaging of biomolecules [Rou17], super-resolution microscopy [Uno19] or photopharmacology [Cah13].

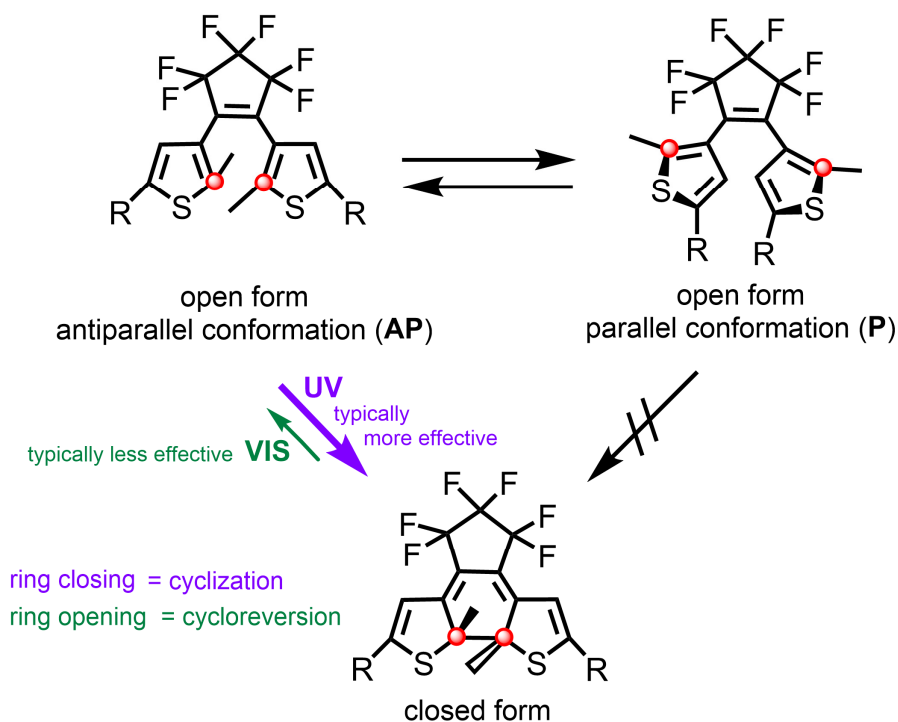


Figure 4-1 Antiparallel and parallel conformations of the open form of DAE with allowed and prohibited reactions to the closed form. The red dots demonstrate guide to the eyes for considering the proximity of the reactive carbon atoms relevant for formation of the bond.

Due to such a broad range of applications, there are still efforts to improve the design and properties of DAE. Hence, novel DAE molecules are frequently published [Kol21, Oru20, Uno19]. Correspondingly in the first part of this chapter a unique furan-based DAE system with an extended π -conjugation system is investigated.

In this work, the combination of transient absorption measurements with the determination of the reaction quantum yield (RQY) provides a deeper understanding for the bond formation and its cleavage upon light absorption. The findings for this particular DAE are subsequently discussed and compared to other representatives from the DAE family.

The second part of this chapter is based on the JACS paper [Xu18]. In this publication the RQY of the first diarylethene-polyoxometalate coordination complex (DAE-POM) is introduced that can be switched between two stable forms upon irradiation with light.

4.2 Photochemical properties and reaction quantum yield

The molecules from the DAE family in general undergo isomerization from an open form (**o**) into a closed form (**c**) upon illumination with UV light (**o**→**c**), while the reversed reaction (**c**→**o**) proceeds under visible light, see Fig. 4-1 [Iri88].

The reaction quantum yield (RQY) for the ring closing reaction (**o**→**c**) is limited by coexistence of two different open form conformers:

- a) the first conformer has two rings in mirror symmetry C_s (parallel conformer, **P**, see Fig. 4-1 top right)
- b) the other conformer in C_2 symmetry (antiparallel conformer, **AP**, see Fig. 4-1 top left).

According to the Woodward-Hoffmann rules, the photocyclization reaction is allowed only from the **AP** conformer in conrotatory mode [Woo70, Nak88]. The **P** form is thus photoinactive. The ratio between [**AP**] and [**P**] can be analyzed by steady state NMR spectroscopy [Iri92a, Uch99]. Since the ratio [**AP**]:[**P**] is typically close to 1:1 (true only if the R substituent in Fig. 4-1 is large), the maximum RQY cannot exceed 50%. A typical value of RQY for ring closing is between 20% and 50% [Iri00].

In this work, the DAE system under study is 1,2-bis(2-methyl-5-((E)-(1-methylthio-1-iminomethylhydrazono)methyl)furan-3-yl)perfluorocyclopentene shown in Fig. 4-2 top right. This molecular switch is also known as **MTSC** (notation originates from the

methylthiosemicarbazone side chain). **MTSC** is closely related to another structure assigned as **TSC**. **TSC** has an identical DAE core as **MTSC**, but the methyl group on the sulfur atom is missing (see Fig. 4-2 bottom right). Both molecules were originally designed by Huhn's group [Sys11, Sys12].

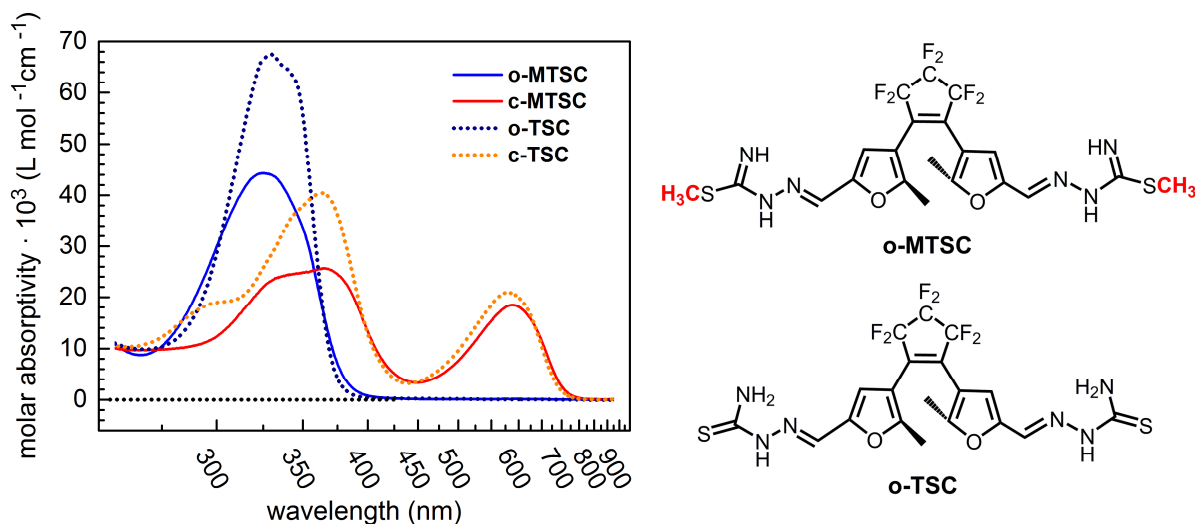


Figure 4-2 Molar absorptivities of the **MTSC** and **TSC** in acetonitrile. The molecular structures are shown on right.

In contrast to the commercially available DAE switch developed by Irie [Han92, Iri95] **TSC** and **MTSC** have no thiophene, but a furan switching core. The furan moiety has a stronger diene character in contrast to thiophene and hence enhanced switching properties are predicted [Kho17, Sys11]. Additionally, by introducing the vinylogous side chains in **TSC** and **MTSC** the π -conjugation system is extended [Sys11]. This side chain modification is relevant for their promising application as single molecule junctions [Bri12b]. In the following, the UV/vis spectra of both switches in acetonitrile are compared and discussed.

The UV/vis spectrum of the open and closed form for **MTSC** and **TSC** in acetonitrile is shown in Fig. 4-2 left. The presence of the methyl group has a remarkable impact on the optical properties of the molecules. The typical single UV absorption band of the open form for **o-TSC** is by a factor 1.5 higher than in **o-MTSC** and the absorption maximum is shifted by 4 nm ($\lambda_{\text{max,o-TSC}} = 325 \text{ nm}$ and $\lambda_{\text{max,o-MTSC}} = 329 \text{ nm}$). Upon illumination with UV light, the open form of both systems undergoes the cyclization process, which results in the closed form.

During the illumination with UV-light an additional red shifted absorption band around 600 nm appears (see Fig. 4-2 and Fig. 4-3). This band is related to the closed form and

originates from the spreading of the conjugated π -system through the molecule [Iri00]. Although the red absorption maximum of the **c-MTSC** ($\lambda_{\max, \text{c-MTSC}} = 588 \text{ nm}$) is red shifted by 8 nm relative to the **c-TSC** absorption band ($\lambda_{\max, \text{c-TSC}} = 580 \text{ nm}$), both switches have comparable molar absorptivity in the red spectral region.

For further discussion of photoinduced reactions, it is important to consider the difference between the RQY and the chemical yield when irradiated with light. The latter defines the final "turnover number" - the percentage of molecules that are converted into the product. A chemical yield of less than 100% is often associated with the formation of undesirable by-products or decomposition/degradation of reactants and/or products.

RQY, on the other hand, provides information on how effective the photoinduced reaction is - or in other words - how many absorbed photons per molecule are required for a successful photoreaction.

Following the above explanation of RQY and chemical yield, the discussion of properties of **TSC** and **MTSC** continues below.

a) Chemical yield

Unlike other DAE systems, the photoreaction under UV light leads to a complete conversion of all **TSC** and **MTSC** molecules into a closed form. Therefore, the chemical yield is 100% without any formation of by-products. The chemical yield of the cycloreversion is also 100%. This ability of complete conversion of both isomers to exclusively open or exclusively closed form makes the system unique. Another advantage of the **TSC** and **MTSC** system is the thermal stability of both isomers. Consequently, the photoinduced measurements are not limited in time.

b) RQY

The RQY of both **TSC** and **MTSC** are limited to below 50%. This can be explained by the presence of the **[P]** and **[AP]** forms predicted by the MM2 and DFT calculations of the single point energies in a 1:1 ratio under solvent-free conditions.

In the following, the RQY for **MTSC** and **TSC** in three different solvents is discussed. The RQY was determined using the QYDS approach as described in Chapter 3. This approach allows the RQY of two competing processes (i.e., cyclization and cycloreversion) to be determined at the same time in only one measurement. For further details on QYDS

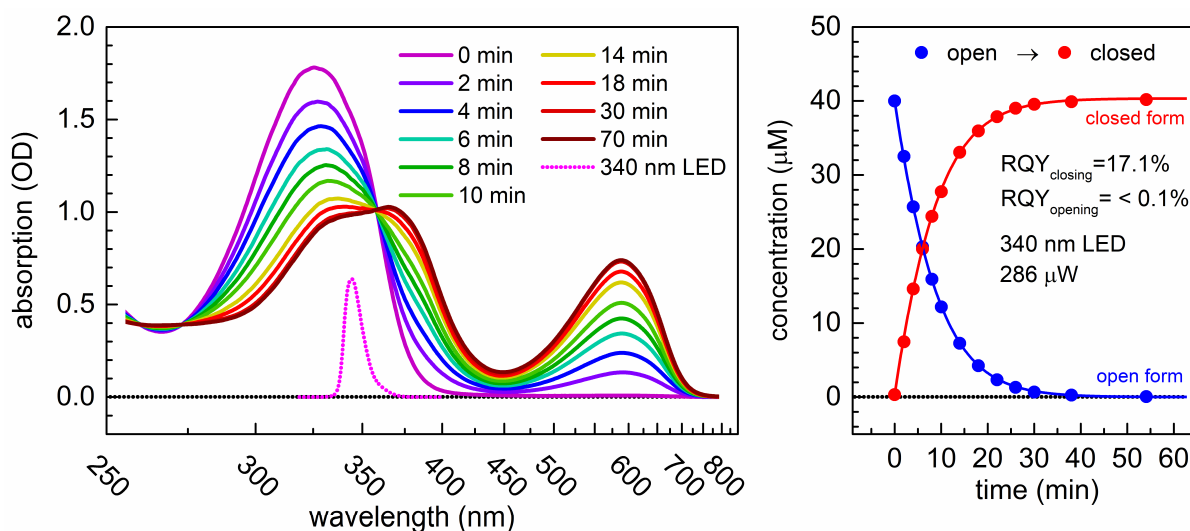


Figure 4-3 (left) Spectral changes of **o**-MTSC in acetonitrile upon illumination with a 340 nm LED (CUD4AF1B, Seoul Viosys Co.) with the illumination power of 286 μ W. A solution of 40 μ M in a 10 mm absorption cuvette with a volume of 2 mL was used. (right) Time evolution of concentrations during the illumination and numerical simulation (solid lines).

Table 4-1 Summary of RQY for ring closing of **o**-MTSC and **o**-TSC in various solvents.

	decreasing polarity of solvent →		
molecule	methanol	acetonitrile	ethanol
polarity (Snyder)	6.6	6.2	5.2
ϵ (25°C)	32.66	35.94	24.55
o -TSC (closing)	28.0% ^{*a}	47.1% ^d	39.0% ^{c, d}
o -MTSC (closing)	38.0% ^{*a}	17.1% ^c	14.5% ^b
c -TSC (opening)	-	< 0.1%	< 0.1%
c -MTSC (opening)	-	< 0.1%	< 0.1%

*from ref. [Sys11], ^a excitation at 313 nm

^b this work, excitation at 266 nm (VPC131, Nikkiso Co.)

^c this work, excitation at 340 nm (CUD4AF1B, Seoul Viosys Co.)

^d this work, excitation at 325 nm (EOLS-325-696, Dowa Electronics Materials Co.)

approach the reader is referred to Chapter 3.

In Fig. 4-3 an example of the stepwise illumination is shown (**o**-MTSC in acetonitrile by 340 nm LED). The rest of the measurement data can be found in Appendix 4-A3 – 4-A7. The RQY as well as transient absorption measurements were performed in ethanol and acetonitrile. The data for methanol originates from reference [Sys11].

Summarizing the results in Table 4-1, two lines of reasoning for trends related to RQY are conceivable:

a) Photoswitching in protic and aprotic solvents

The results can be categorized in photoswitching in aprotic solvent (acetonitrile) and in protic solvents (ethanol and methanol).

Ethanol and methanol as protic solvents contain labile H^+ as a proton donor in the solvent. The presence of protons enables the formation of hydrogen bonds with the molecular switches. The results show that these hydrogen bonds may have a negative effect on the photoswitching efficiency, since the RQY decreases in protic solvents. It is suggested that the formation of hydrogen bonds affects the molecular orientation and disfavors the formation of the C-C bond in the reactive center of the photoswitch.

This trend is observed for **o**-TSC and for **o**-MTSC in ethanol and acetonitrile. However, the reported unexpectedly high RQY of 38% [Sys11] for **o**-MTSC in methanol does not follow the above-mentioned trend. Since this unexpectedly high value originates from an actinometric measurement, it might be of interest to re-measure and validate this value with high accuracy using the QYDS approach.

b) Photoswitching in dependence of solvents polarity

Although the differences in the polarity of the solvents in the series of acetonitrile, methanol and ethanol are rather modest, it is nevertheless reasonable to consider this as a possible reasoning option as well. According to the results in Tab. 4-1 the RQY of **o**-TSC increases from methanol over ethanol to acetonitrile. This can be explained by a more favorable stabilization of the open form in the excited state, as already reported in the literature [Iri92b, Ish16]. According to this theory [Iri92b, Ish16], the excited open form in nonpolar solvents is in a planar conformation, which is geometrically very close to the closed form, so that the new bond can be formed more easily. On the other hand, a twisted conformation occurs in polar solvents, so that the two carbons relevant for bond formation are spatially farther apart

and cyclization is thus disadvantaged [Iri92b, Ish16]. This very same trend is evidently observed also for **o**-TSC. However, as mentioned above, this trend cannot be observed for **o**-MTSC. The unexpectedly high value of RQY does not fit the above argumentation.

Both lines of argument a) and b) are based on empirical observations only. For a deeper understanding and discussion, theoretical calculations of the molecular structures in the ground state as well as in the excited state are required.

In the following the results of the transient absorption (TA) spectroscopy for the open and closed form are discussed on the fs-ps and ns- μ s time scale.

4.3 Transient absorption for the cyclization (ring closing) process

Preparation of the TSC and MTSC species for transient absorption measurement included re-irradiation with a 625-nm LED (Osram LR CP7P, Osram Licht AG) to ensure that only open-form isomers were exposed to pulsed laser excitation. Since both systems (TSC and MTSC) and isomers (open and closed form) are thermally stable, there was no limit to the measurement time.

The excitation light was selected in advance considering the molar absorptivity of both the open and closed isomers. Although the UV/vis spectra of both forms overlap, it is possible to determine the ideal wavelength for photoexcitation such that even in the photostationary state (PSS) the open form is primarily excited.

Figure 4-4 shows the transient absorption of **o**-MTSC dissolved in acetonitrile upon illumination with 340 nm light. The negative signal around 335 nm is related to the GSB, while the positive signal around 385 nm and 525 nm at very long time delays corresponds to the formation of the desired closed form (see solid red and dotted green curve in Fig. 4-4 in top panel).

The transient absorption measurement is firstly evaluated by a maximum entropy analysis [Kut13]. This method results in a probability density that a certain decay constant τ is present. The obtained information is comparable to the information from DADS spectra of a global analysis. The negative signal represents the decrease of the GSB, stimulated emission or product formation. The positive signal corresponds to a decrease of ESA. The resulting color map distribution is shown in Fig. 4-5. Since the maximum entropy analysis is independent of any model as it originates from the transform of the data, it is analyzed first.

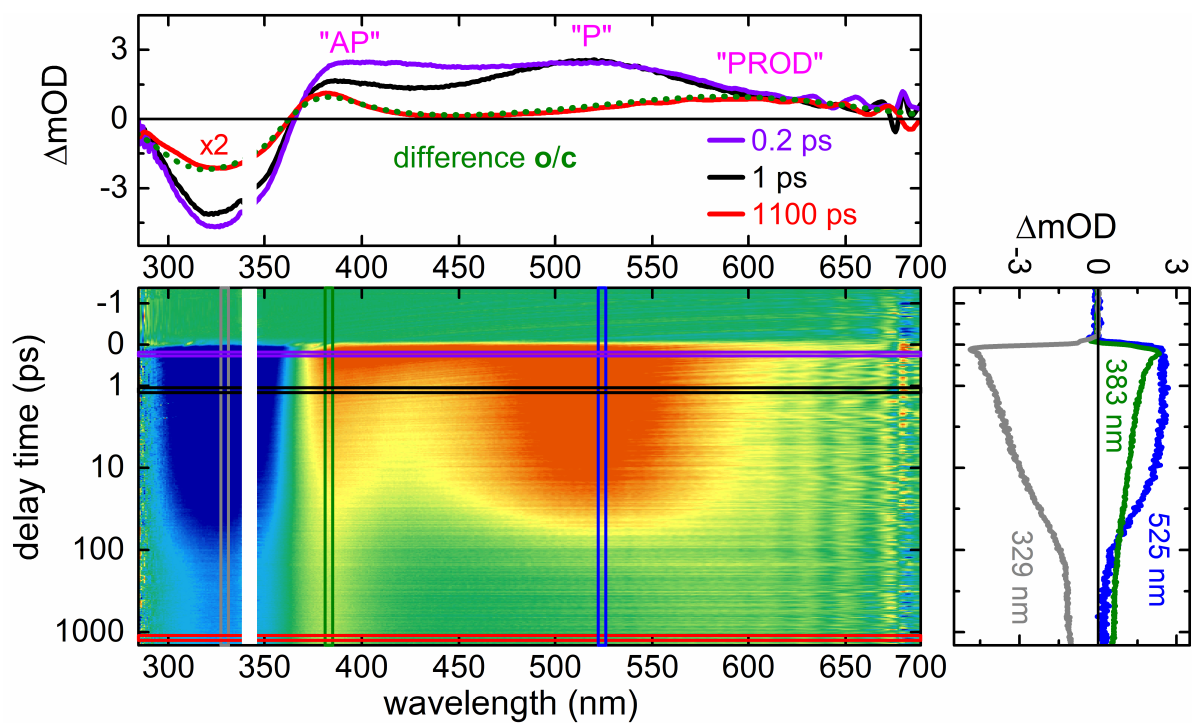


Figure 4-4 Transient absorption of **o**-MTSC in acetonitrile under standard conditions measured in a 250 μm thick flow cell after excitation with 80 fs pulses centered at 340 nm with a pulse energy of 25 nJ.

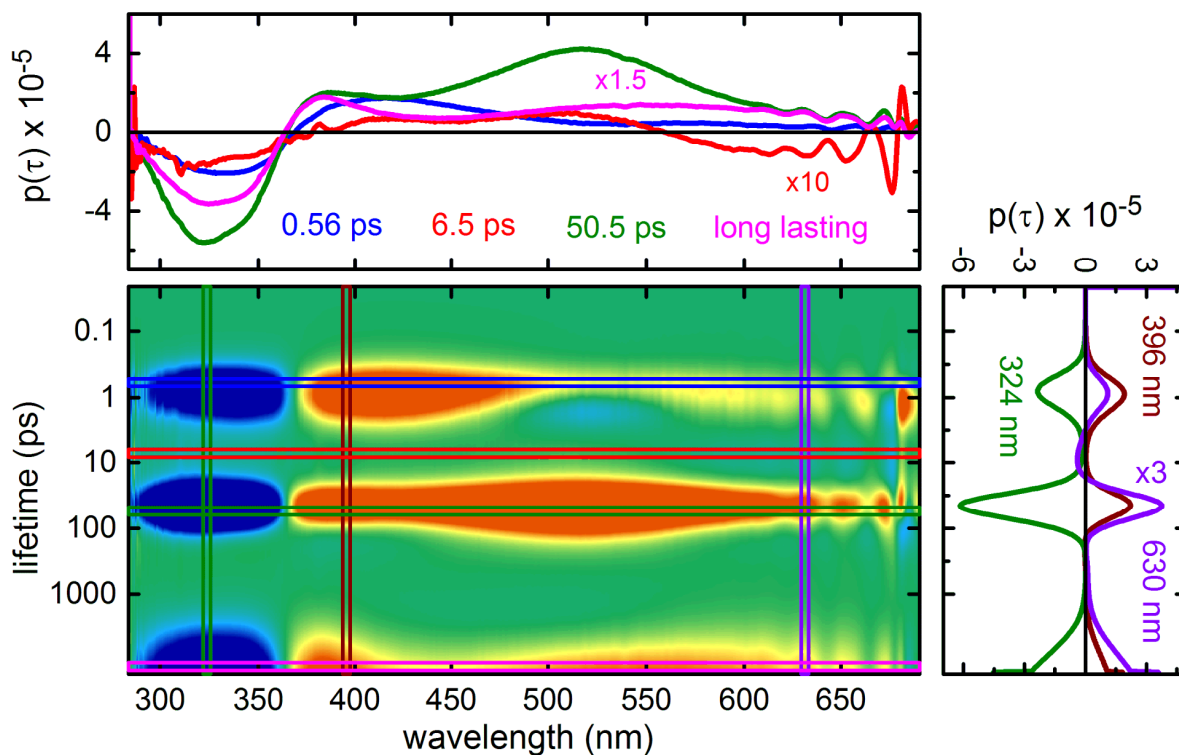


Figure 4-5 Maximum entropy analysis for the fs/ps data set in Fig. 4-4 for **o**-MTSC in acetonitrile.

The color map reveals four spectral regions, in which the spectral changes appear. The peak width correlates with uncertainty in lifetime. The first time constant is around 0.56 ps, the second with low contribution at 6.5 ps, the third around 50.5 ps and the last one is behind the time window covered by this experiment ($\gg 1.5$ ns). Consequently, the photodynamics is expected to include three different molecular states. The result of the maximum entropy gives a very good agreement with the values obtained from the single line fit and global analysis, which are discussed in the following.

As shown in the TA data in Fig. 4-4 (violet horizontal line), within 180 fs a very broad ESA absorption covering almost the whole spectral region appears. A part of this signal decreases within 500 fs through the specific spectral region between 375 nm - 500 nm as shown with positive signal in the DADS for 0.5 ps (blue line in Fig 4.6b). It is reasonable to assume, that this time decay is related to a pre-switching phase comprising processes such as vibrational cooling or pre-structural evolution rather than the switching process itself. Since the RQY is 17.1%, the significant part of the population is expected to decay back to the ground state and consequently GSB recovery is expected. As shown in Fig. 4-6a no significant changes up to 0.5 ps in the GSB region are observed [Bar18] and hence the time decay of 0.5 ps is assigned to the pre-switching dynamics. For the further analysis of the dynamics, three regions designated with "AP" (antiparallel), "P" (parallel) and "PROD" (product) are introduced.

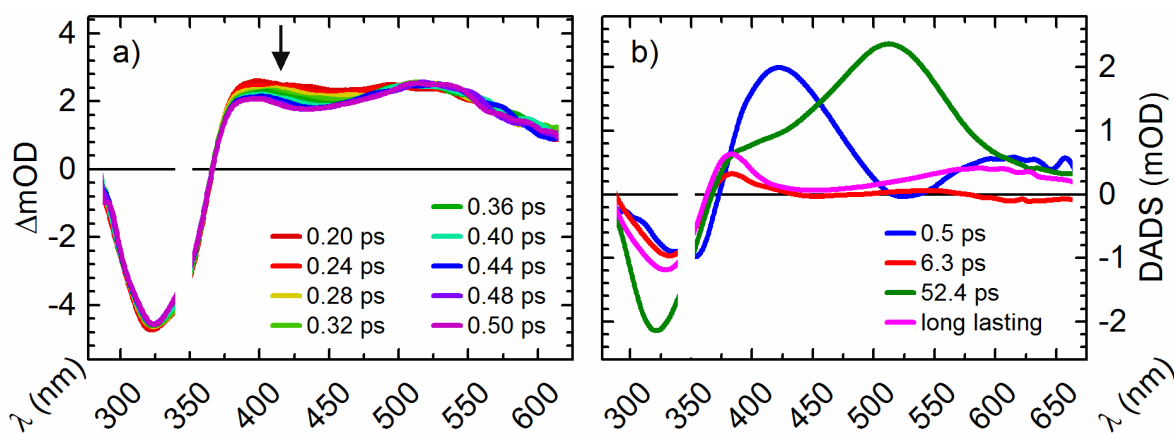


Figure 4-6 a) Transient absorption spectra of **o**-MTSC in acetonitrile at time delays between 0.2 ps and 0.5 ps. b) Decay associated difference spectra obtained from the global fit analysis for **o**-MTSC in acetonitrile.

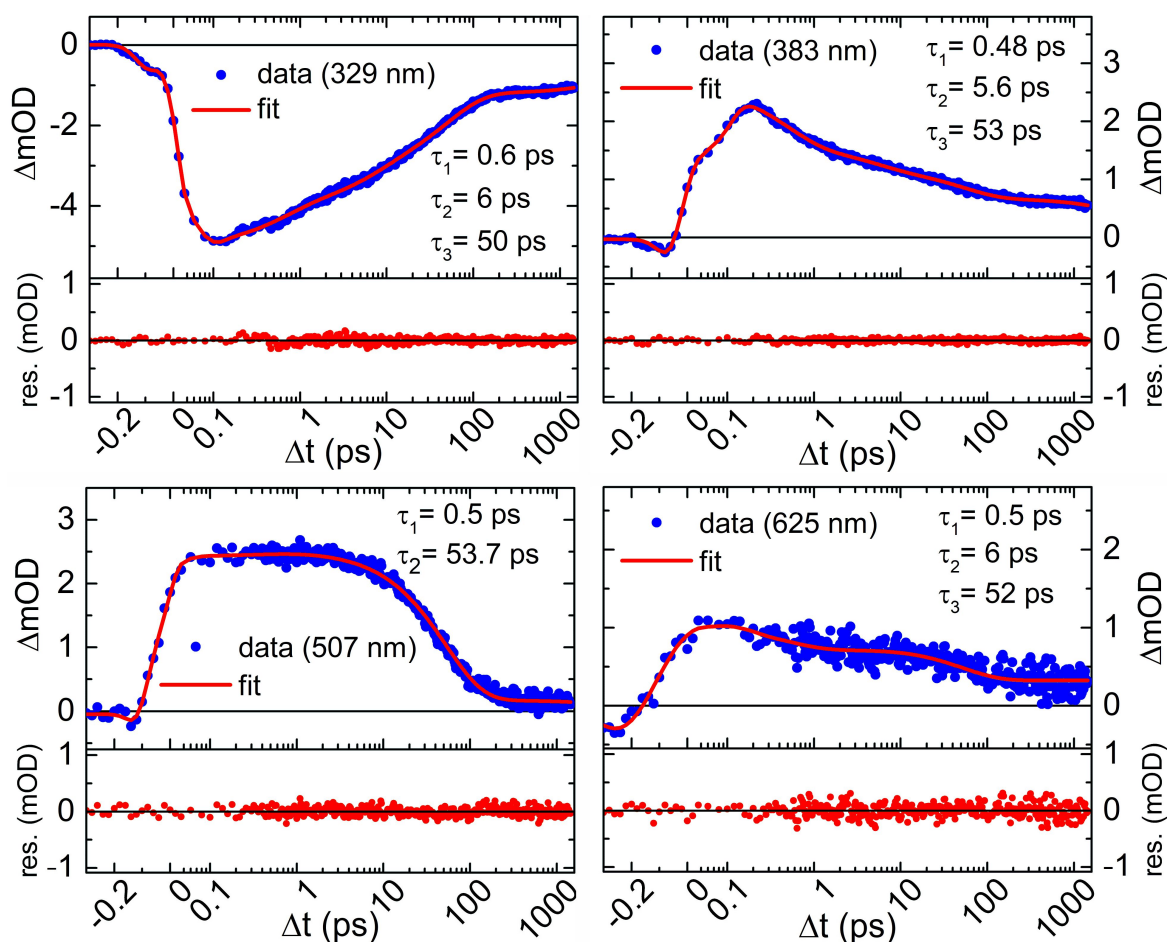


Figure 4-7 Kinetic traces at selected wavelengths fitted with a multiexponential decay model for **o**-MTSC in acetonitrile from Fig. 4-4.

In the region "P" around 525 nm the dynamics of the non-reactive parallel form is traced. The **P** conformation of the **o**-MTSC cannot react to the desired product because of the molecule's geometrical orientation. The broad ESA relaxes with two time constants of 0.5 ps and 52 ps (see trace of 507 nm in Fig. 4.7). Directly after excitation the molecule relaxes within 0.5 ps into a lower electronic state and subsequently within 52 ps decays unchanged back to the ground state. This process is also obviously observed in the DADS spectrum for 52 ps. The broad positive signal around 520 nm corresponds to decreasing of the ESA related to the **P** form, while a very strong negative signal around 325 nm corresponds to GSB recovery. Such an ESA band of the **P** form is typically found in the region between two steady state absorption bands of the open and closed form and was reported with similar spectral distribution by several groups [Han02, Han05, Ham16, Pon14]. Consequently, the time decay of 52 ps is assigned to the decay of the non-reactive **P** form back into the ground state.

In the "PROD" region between 500 nm and 700 nm, a broad positive signal of the product

around 625 nm is present. This spectral feature corresponds to the absorption band of the closed form **c-MTSC** (see red solid line and green dotted line in Fig. 4-4). The fit of the single kinetic trace at 625 nm reveals three different constants of 0.5 ps, 6 ps and 52 ps (see Fig. 4-7). Additionally, similar decay constants (0.48 ps, 5.6 ps and 53 ps) are found in the spectral region around 383 nm designated with **AP**. This spectral region can be related to the singlet state of the **AP** form from which the ring closing occurs. As shown in the DADS for 6.3 ps in Fig. 4-6b, the decrease of the **AP** band around 385 nm is accompanied by the product formation around 625 nm (see negative contribution of the red line in Fig. 4-6b at 625 nm). The observed GSB recovery originates from the population that does not cyclize and relaxes back to the ground state.

Table 4-2 Summary of molecular dynamics and lifetimes for ring closing of various switches from the DAE family.

ref.	pre-switching dynamics	ring closing	lifetime AP form	lifetime P form	post-switching dynamics	RQY
[Alo14]	90 fs	0.8 ps	-	120 ps	-	40%
[Els09]	500 fs	10 - 20 ps	-	1000 ps	-	22%
[Ham16]	200 fs	0.1 ps	2 ps*	55 ps*	-	46%
[Pon14]	-	0.3 ps	-	23 ps*	-	40%
o-MTSC (MeCN)	500 fs	6 ps	-	52 ps	-	17%

*decay to triplet state, for more detailed table see Tab. 4-A in the Appendix.

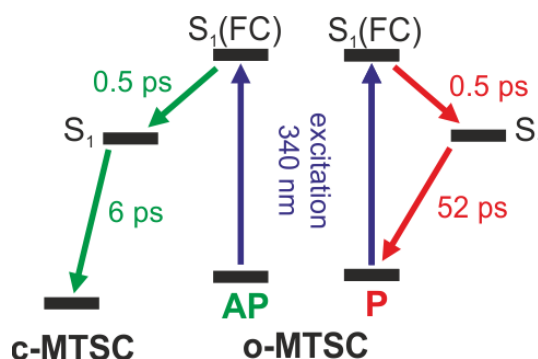


Figure 4-8 Possible photoinduced dynamics for cyclization of **o-MTSC** in acetonitrile.

In summary, the proposed mechanism is similar to those reported for other DAE derivatives and is sketched in Fig. 4-8. After the excitation, the molecules experience a pre-switching phase containing processes such as vibrational cooling or rapid excited state mixing [Han05] with decay constants spanning from 50 fs to 500 fs (see Tab. 4-A in Appendix). The observed 500 fs for **o**-MTSC give a good agreement with these values. According to the literature, the reactive **AP** form undergoes cyclization on the timescale from 100 fs to 20 ps. The measured 6 ps lies fairly within the aforementioned region. According to other works, the non-reactive **P** form has a singlet lifetime spreading from the sub-picosecond region up to the nanosecond time scale. The measured lifetime of 52 ps for the non-reactive **P** form lies fairly within the reported values. In references [Pon14, Ham16, Fre20] it is proposed that the non-reactive **P** form decays within a couple of tens of picoseconds to the triplet state having a triplet lifetime of several microseconds. Hamdi *et al.* [Ham16] proposed that even the reactive **AP** form may decay in 2 ps into the triplet state with a triplet lifetime of 25 μ s. However, such dynamics with a triplet lifetime of several tens of microseconds is not observed for the **o**-MTSC species.

In the following, the switching dynamics of the **o**-MTSC in the more polar ethanol in comparison to the above-described behavior of **o**-MTSC in acetonitrile is investigated (see Fig.4-9). The emphasis is placed on how the solvent polarity and the presence of H⁺ affects the rate of the switching process and lifetime of the non-reactive **P** form. As in the previous case, the excitation wavelength is 340 nm.

In contrast to acetonitrile with the longest time decay of 51 ps the molecular dynamics in ethanol spread up to one nanosecond. Additionally, the product absorption is in ethanol more pronounced. The ESA for **AP** and **P** are shifted toward each other and overlap more strongly. The global fit reveals three time constants: 1 ps, 21.5 ps and 550 ps. The longest time constant can be attributed to the lifetime of the non-reactive **P** form. The DADS spectrum of this state spreads through the whole spectral region and has a negative contribution around the GSB, meaning that this state decays back to the ground state.

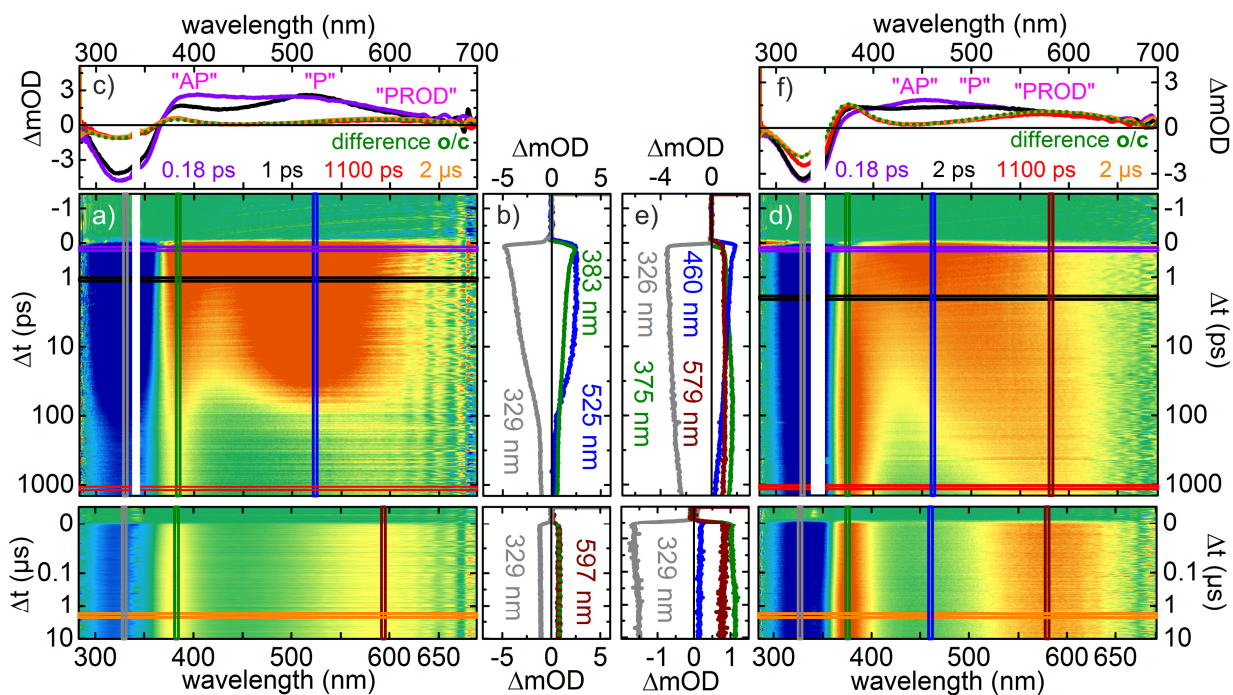


Figure 4-9 a) and d) fs-TA of **o**-MTSC in acetonitrile (left) and ethanol (right) under standard conditions measured in a 250 μm thick flow cell after excitation with 150 fs pulses centered at 340 nm with a pulse energy of 25 nJ, respectively. The lower part corresponds to ns-TA after excitation with 340 nm with a pulse energy of 25 nJ and 50 nJ, respectively. c) and f) Transient spectra at selected probe delays according to horizontal lines. b) and e) Kinetic traces at wavelengths extracted from the vertical marker lines.

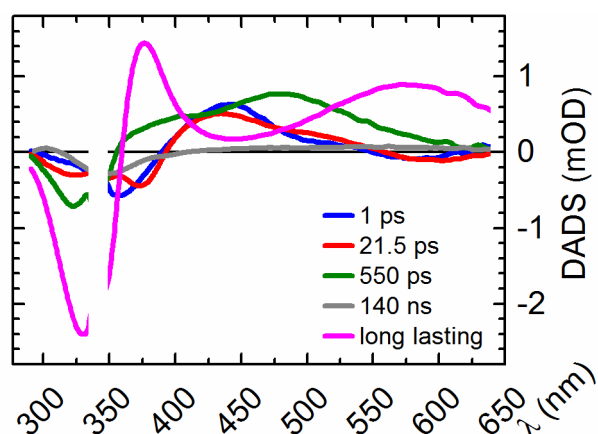


Figure 4-10 Decay associated difference spectra obtained from global fit analysis for **o**-MTSC in ethanol.

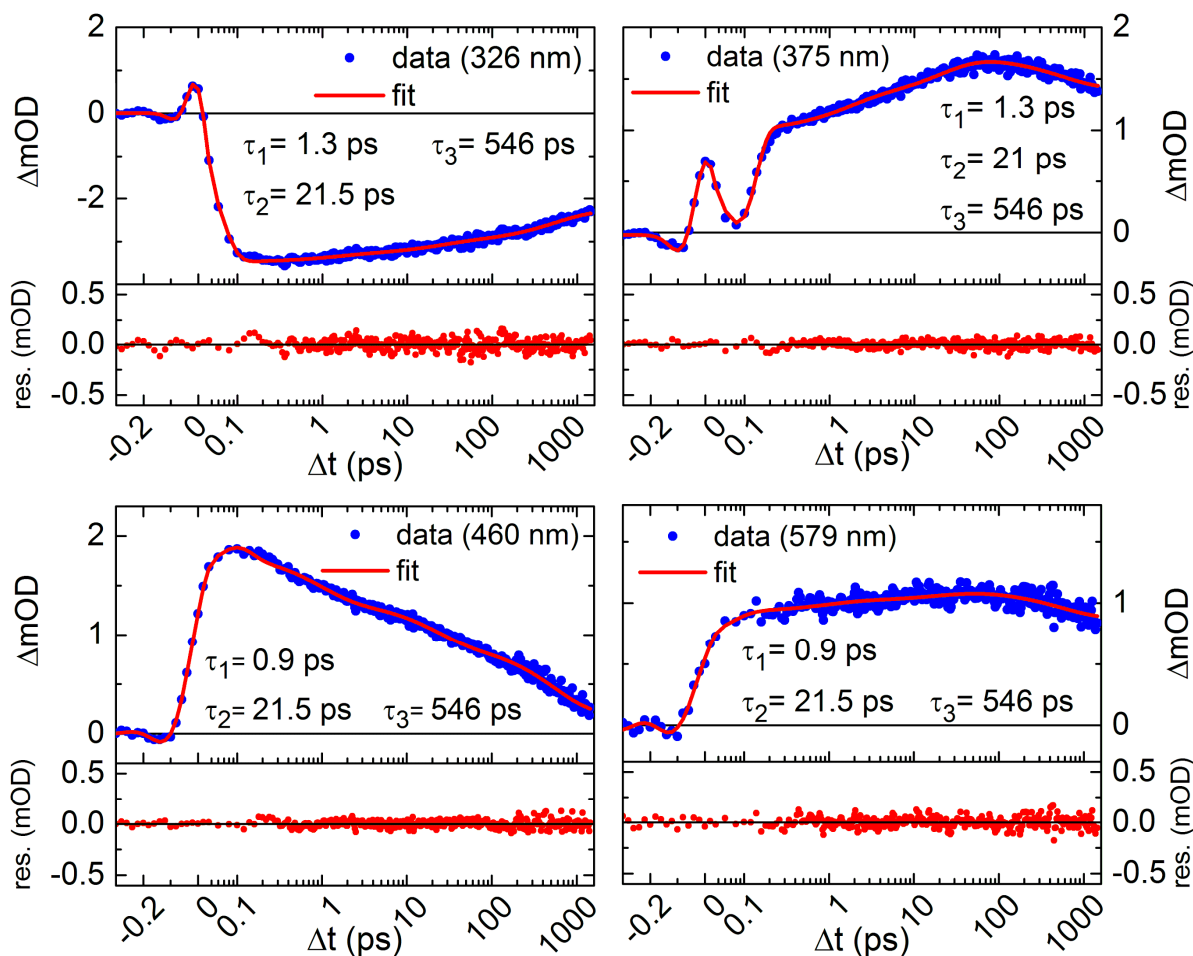


Figure 4-11 Kinetic traces at selected wavelengths fitted with a multiexponential decay model for **o**-MTSC in ethanol.

In contrast to acetonitrile the two shorter decay constants (1 ps and 21.5 ps) show a very similar DADS in shape (see Fig. 4-10). In both cases a negative contribution around 600 nm is present which implies, that the product is formed. The time decay of 0.9 ps lies within a range typical for vibrational cooling. It cannot be excluded, that part of the population may cyclize within this cooling process, since the negative contribution of DADS and single line fit suggest this process. Regarding the single line fit at 579 nm in Fig. 4-11, the amplitude of the 21.5 ps decay is almost one order of magnitude higher than for 0.9 ps. Hence it is reasonable to assume, that although both time constants may contribute to the ring closing reaction, the 21.5 ps time is predominantly related to the switching process. The identical molecular dynamics is also observed for **o**-TSC dissolved in ethanol, but not in acetonitrile. Hence it appears that this phenomenon of ring closing with two decay constants is solvent specific and occurs in the case of **o**-TSC and **o**-MTSC in the protic solvent ethanol.

Table 4-3 Summary of cyclization RQY and time constants for photoinduced cyclization of **o**-MTSC and **o**-TSC.

	MTSC		TSC	
	ethanol	acetonitrile	ethanol	acetonitrile
RQY _{0 → c}	14.5%	17.1%	39.0%	47.1%
ring closing	21.5 ps	6 ps	20 ps	13 ps
lifetime P form	546 ps	52 ps	752 ps	1348 ps
average solvation time [Hor95]	16 ps	0.26 ps	16 ps	0.26 ps

← increasing solvent polarity
← increasing solvent polarity

Comparing the cyclization process for acetonitrile and ethanol it can be concluded that the cyclization time decreases in the series ethanol to acetonitrile (see Tab. 4-3). The shorter cyclization times result in more effective ring closing with higher RQY. The same trend is observed for **o**-TSC (for data see Appendix 4-B).

Although the polarity differences between ethanol and acetonitrile can be regarded as rather modest, it is reasonable to consider this argumentation line, since this is well discussed in the literature [Iri92b, Ish16].

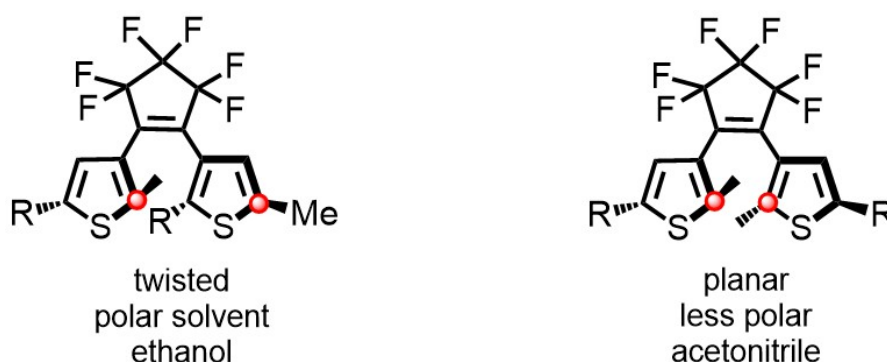


Figure 4-12 Planar and twisted orientation of the furan moieties in excited state of DAE.

The phenomenon based on solvent polarity was firstly predicted and described by Irie *et al.* [Iri92b]. According to his work, both conformers are present in the excited state, but the nature of the solvent has an effect on the stabilization of one of the two possible conformers.

Consequently, this one conformer becomes dominant in the solvent, which explains the dependence of RQY on solvent polarity.

In less polar solvents, the reactive **AP** form with planar geometry of the furan moieties (see Fig. 4-12 right) is more stabilized and hence it is predominantly present in the solvent. This conformation is analogous to the closed form and thus a concerted ring-closing reaction occurs.

The situation is different in more polar solvents, in which the **P** form is more stabilized than the **AP** form. The **P** form has a perpendicular arrangement of furan moieties (see Fig. 4-12 left) and is unfavorable for the ring closure reaction. The ratio between the **AP** and **P** form correspondingly changes with solvent polarity as also reported by Ishibashi *et al.* [Ish16].

Instead of using polarity, however, it is useful to base the argumentation on application of protic and aprotic solvents. As discussed in Section 4.2, the presence of hydrogen bonds appears to have a moderate effect on the time constant responsible for closure and thus on the efficiency of the cyclization process. It is likely that the hydrogen bonding network influences the molecular pre-orientation such that the spatial proximity of the two relevant carbon atoms is unfavorable for bond formation.

Typically, the molecular dynamics is also influenced by the solvation process of the solvent. Considering the solvation time for acetonitrile with a value of 0.26 ps [Hor95], the relevant lifetime for cyclization (6 ps) is far outside the solvation process. A similar trend is also observed for ethanol. Here, the solvation process can be considered rather slow at 16 ps [Hor95]. In fact, again, the cyclization time constant for ethanol is higher than its average solvation time. Consequently, it appears that the nature of the solvent and its solvation process may possibly influence the cyclization process.

Both argumentations (solvent polarity and (a)protic solvents) are only hypothesis that is derived from the measurement data. In order to confirm or reject the above-mentioned hypothesis theoretical calculations with appropriate analysis are required.

The presence of the additional methyl group in the **MTSC** system has a major impact on the reaction time scale in particular for acetonitrile (compare Fig. 4-4 and Fig. 4-B9 in Appendix). The cyclization occurs more rapidly in **o-MTSC** (6 ps for ring closing) than in **o-TSC** (13 ps for ring closing). The prolongation of the whole excited state dynamics in the **o-TSC** is even more pronounced for the lifetime of the non-reactive **AP** form. In this case the lifetime of 52 ps for **o-MTSC** is extended to about 1.3 ns for **o-TSC**. The longer time

scale for excitation dynamics appears to create more favorable conditions for a successful creation of the C-C bond, since the RQY of **o**-TSC is about 2.5 times higher than for **o**-MTSC.

4.4 Transient absorption for the cycloreversion (ring opening) process

In contrast to the cyclization reaction, there is an additional feature on the excited-state potential energy surface (red color in Fig. 4.13) in the cycloreversion reaction, which is referred to as the effective activation barrier in the literature [Gui02, Nak07, Pas03, Ish12]. This effective activation barrier is responsible for the very low RQY (few %) of the cycloreversion process [Iri00, Iri88] since the deactivation channel back to the ground state is more favored. After crossing the activation barrier, the system reaches a branching conical intersection (CI). After the CI, the molecule proceeds either in the regeneration of the reactant form or in the formation of the product [Asa04, Pas03]. The lifetime of this excited state relevant for switching is in the range between sub-ps and several tens of ps [Fre20, Ham16, Ish12, Ish16, Shi07, Sot20, Tan08].

In the following, the photophysics of the cycloreversion process for the **c**-MTSC in acetonitrile is discussed in detail.

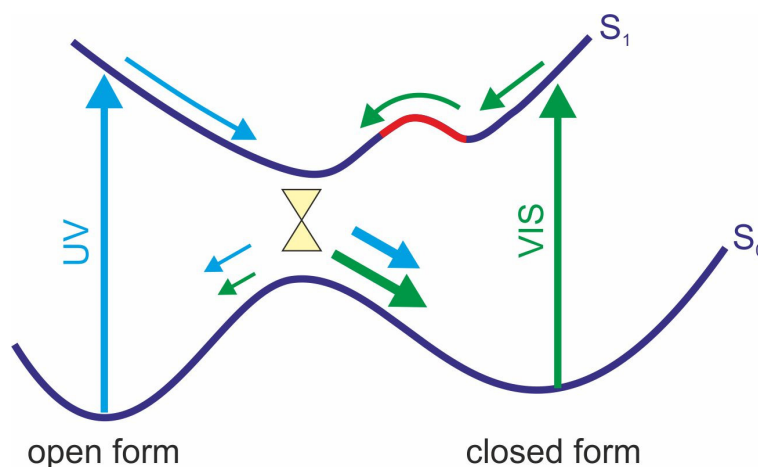


Figure 4-13 Schematic representation of the potential energy surfaces and reaction paths for the photoinduced processes in DAE, adapted from reference [Iri14]. The effective potential energy surface for the ring opening process is shown in red color. The thickness of the arrows correlates with the efficiency of the photoreaction.

The transient absorption upon 580 nm excitation for **c-MTSC** dissolved in acetonitrile is shown in Fig. 4-14. The negative GSB signal is observed around 350 nm and 560 nm, while an intense positive ESA signal is observed at 440 nm and less intense, but very broad ESA around 700 nm is detected. Practically all spectral features disappear completely within 10 ps, only a very small negative signal around 360 nm remains unchanged with prolonged delays. This minor signal corresponds to the formation of a very small amount of the product, since the RQY of this reaction is below 0.5% (see Fig. 4-A4 and Fig. 4-A6 in the Appendix for own measurements and results in reference [Sys11]).

For the characterization of the excited state dynamics only a two step kinetic model is required. The single kinetics traces at selected wavelength as well as the global fit reveal two decay constants of 0.5 ps and 5 ps, whereby the shorter time constant has the major contribution. As shown in the DADS for 0.5 ps Fig. 4-15d, the strong decay of the ESA and strong recovery of the GSB is related to the lifetime of the excited state relevant for the ring opening reaction. This timescale of 0.5 ps for the ring opening reaction is in good agreement with typical values reported for other DAE molecules (see Tab. 4-4).

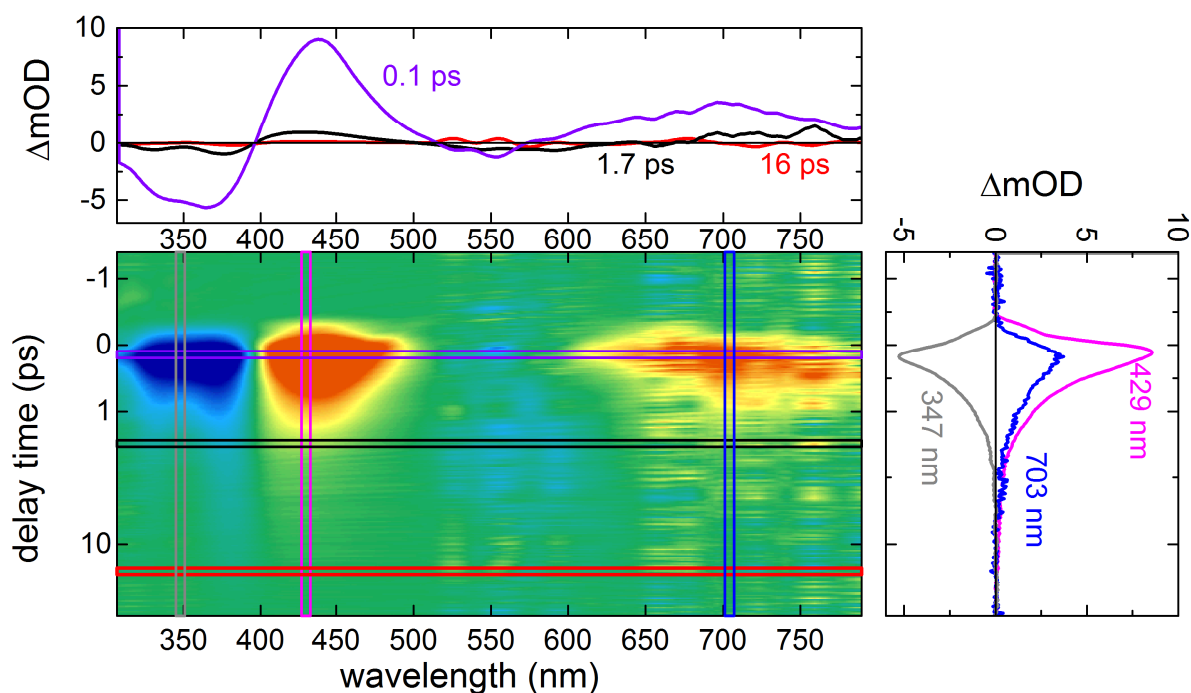


Figure 4-14 Transient absorption of **c-MTSC** in acetonitrile under standard conditions measured in 250 μm thick flow cell after excitation with 80 fs pulses centered at 580 nm with a pulse energy of 300 nJ.

The longer decay constant of 5 ps can be attributed to the post-switching dynamics that may include relaxation from the hot ground state by vibrational cooling. The shape of the DADS spectrum extracted for 5 ps exhibits an absorption band with positive contribution just to the red of the GSB, but in comparison to the measured ESA it is blue shifted. As reported in reference [Hon20] such a spectral position is typical for a signature related to the decay of the vibrationally hot ground state. This phenomenon is particularly expected for molecular switches in which the major fraction of the excited population relaxes back to the ground state without successful ring opening [Hon20]. As the RQY lies below 0.5% and the spectral distribution of the 5 ps DADS is in close agreement with those reported in reference [Hon20], the 5 ps is attributed to the vibrational cooling of the hot ground state.

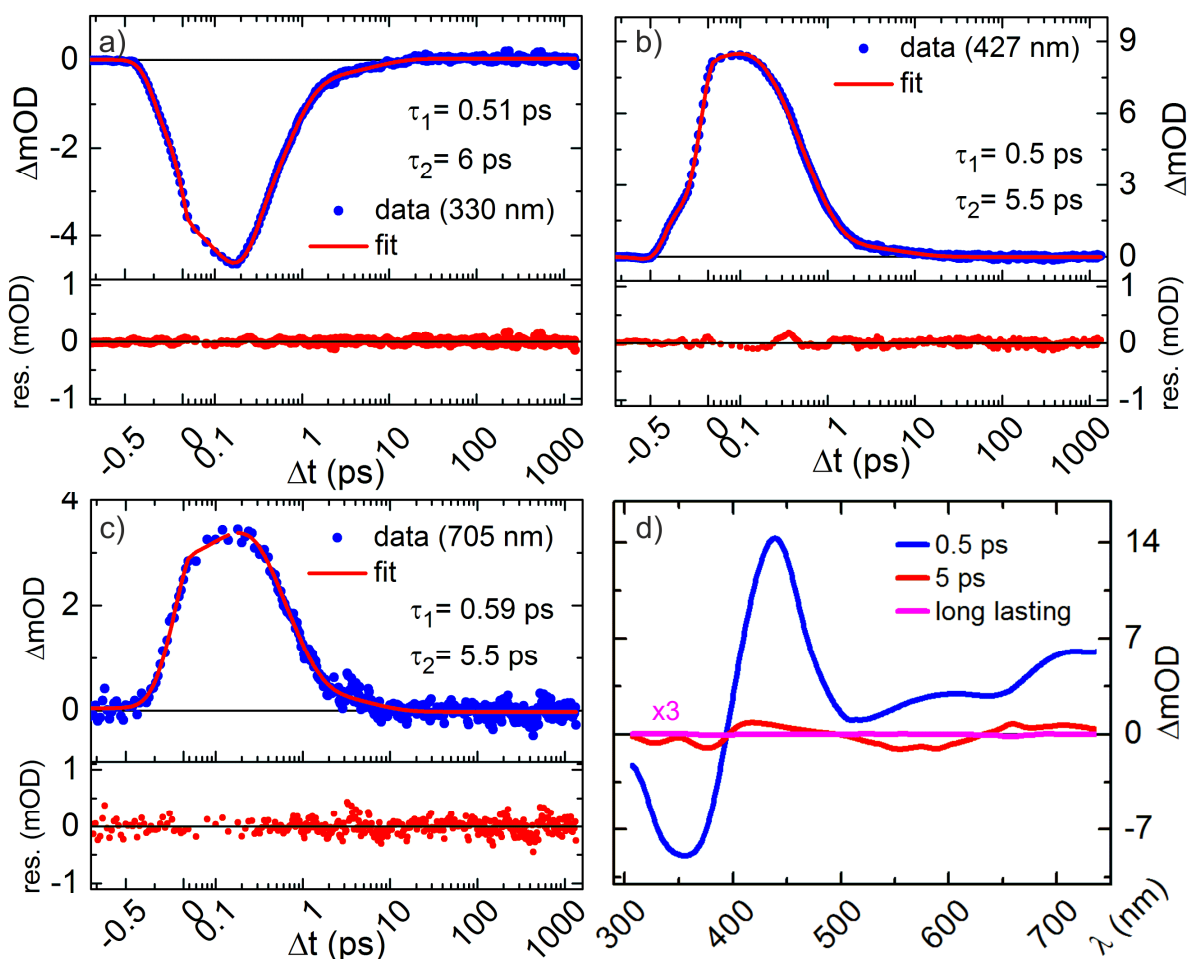


Figure 4-15 a-c) Kinetic traces at selected wavelengths fitted with a multiexponential decay model. d) Decay associated difference spectra obtained from global fit analysis for c-MTSC in acetonitrile.

The dynamics of the **c-MTSC** and **c-TSC** are compared with literature values and summarized in Table 4-4 (for full TA data see Appendix 4-B). In most DAE systems, a fast structural evolution combined with vibrational cooling between 0.1 ps and 3 ps is reported. The group of Elles [War12] assigns this time constant to the time required to overcome the activation barrier on the potential energy surface (see red barrier in Fig. 4-13). For the **c-MTSC** as well as for **c-TSC** no distinct pre-switching dynamics is observed. Such an

Table 4-4 Summary of the reported lifetimes of excited states for ring opening of DAE-based molecules.

ref.	pre-switching dynamics		ring opening	post-switching dynamics
[Sot17, 20]	200 fs ^a	3 ps ^d	6.5-12 ps	-
[War12]	100 fs ^a	3 ps ^e	9 ps	90 ps ^f
[Hon20]	300-570 fs ^b	-	3-9 ps	8-18 ps ^f
[Ham16]	190 fs ^c	-	6 ps	-
[Fre20]	170-350 fs ^a	-	0.7-1.5 ps	-
[Ern01]	-	-	8 ps	-
[Ish16]	-	-	10-25 ps	-
c-MTSC (MeCN)	-	-	0.5 ps	5 ps
c-TSC (MeCN)	-	-	0.5 ps	5.8 ps
c-MTSC (EtOH)	-	-	0.7 ps	3.7 ps
c-TSC (EtOH)	-	-	0.7 ps	3 ps

^a internal conversion from 1B to 1A state, ^b fast structural evolution in excited state, ^c lifetime of hot FC state, ^d vibrational cooling, ^e crossing of activation barrier, ^f vibrational cooling of hot ground state.

observation is not exceptional, since there are examples in the literature, in which no pre-switching processes are detected [Ern01, Ish16]. The reported lifetimes of the excited state from which the ring opening may occur is in the range between 0.7 ps and 9 ps. The measured 0.5 ps and 0.7 ps can be regarded as rather short lifetimes. Interestingly, the post-switching dynamics are reported only occasionally. The decay constant for such a deactivation process spans from 8 ps to 18 ps [War12], or even 90 ps as reported by Honick *et al.* [Hon20]. The measured values between 3 ps and 5.8 ps lie within the range typical for

vibration cooling from the hot ground state.

In conclusion, the **TSC** as well as the **MTSC** system has comparable molecular dynamics to other representatives from the **DAE** family. Directly after the UV excitation of the open form the molecule is in the pre-switching phase that is accompanied by vibrational cooling. Thereafter, the ring closing process occurs and the whole process is completed by a cooling process from the hot ground state. Hereby, the selection of the solvent has a major impact on the molecular dynamics which is related to the efficiency of the process by **RQY**. The higher **RQY** is measured in acetonitrile. According to the results, it is assumed that the cyclization process is more effective in aprotic solvents, since the H^+ in solvent may have a negative influence on the formation of the C-C bond, as the spatial pre-orientation may be distorted by the presence of hydrogen bonding interactions to **DAE**.

The results also showed that there could be a relationship between the solvation time of the solvent and the time constant relevant to the photoswitching process. This seems plausible since the solvation process influences the distribution of the dipole moment.

The change in distribution between **AP** and **P** forms as a function of solvent polarity due to stabilization of the only one conformer is the main argument in the literature. According to this theory, the reactive **AP** form is more stabilized in less polar solvents and is therefore predominantly present in the reaction mixture. The **AP** form is advantageously pre-oriented for effective cyclization. [Iri92b, Ish16].

The observation of two different time constants for the ring closing in ethanol is an interesting result. Both are related to the switching process. A presumption, that one of the switching times could originate from the interconversion from the non-reactive **P** form to the reactive **AP** form is unfeasible, since this thermal process occurs on the NMR time scale, i.e., milliseconds, and thus it is too slow for the switching time scale. To the best of our knowledge, there is only one study [Han02] that reports a switching mechanism with two decay constants related to the switching process. In this work of Duppen and Feringa [Han02], the first decay constant of 4.2 ps is related to the creation of the C-C bond. This ring formation subsequently induces a rotational movement of the side groups that results in a more co-planar arrangement with a time constant of 8 ps.

The very ineffective cycloreversion process with a low **RQY** of ca. 0.1% or below is in good agreement with the observations by other groups. The whole ring opening process including the vibrational cooling of the hot ground state is completed within a few picoseconds.

In the case of the cycloreversion, even the change of solvent from ethanol to acetonitrile has a rather small effect on the time constant with which the ring opening process proceeds (0.5 ps for acetonitrile versus 0.7 ps for ethanol). Therefore, conclusions based on the polarity of the solvent or the presence of hydrogen bonds are rather secondary.

The following assumption seems more plausible: the cleavage of the C-C bond may be very rapid, but since a rotational motion suggested for the spatial separation of the two associated carbons is rather slow, they remain close to each other and the bond is restored.

Interestingly, the ultrafast reactions are not automatically related to high efficiency processes. Although the bond cleavage does occur on the sub-ps time scale in cycloreversion, the rather slow motion of the molecule, twisting away from the original orientation, hinders the efficiency of the process significantly.

These empirical observations and the initial assumptions about molecular dynamics mentioned above provide an ideal starting field for theoretical calculations and its corresponding further analysis.

4.5 The first polyoxometalate diarylethene coordination complex

Since the majority of the DAE systems requires UV light for the cyclization process, there is a significant interest to improve the design of DAE systems so that the switches photoisomerize upon preferably visible light illumination. A well-known option is to elongate the conjugated π -system which results in a shift of the UV absorption band towards longer wavelengths [Fuk14]. This can be achieved by incorporation of aromatic dyes in the side groups. However, such functionalization of DAE results in a considerably decreased photoreactivity [Ben98, Kaw01].

In 2018 the group of Ritchie reported as first a unique system in which a pyridyl-containing DAE switch is in coordination with a polyoxometalate (POM) complex. The system can switch between two states using visible light exclusively and is described in the following.

This chapter is based on the publication: J. Xu, H. Volfova, R. J. Mulder, L. Goerigk, G. Bryant, E. Riedle, C. Ritchie, *Visible-Light-Driven “On”/“Off” Photochromism of a Polyoxometalate Diarylethene Coordination Complex*, *J. Am. Chem. Soc.* **2018**, *140*, 10482-10487 [Xu18].

The POMs are environmental friendly [Omw15] metal oxide clusters that are widely studied due to their interesting photocatalytic [Lv12, Wan15, Yao19] and photochromic properties [Ma16, Li19a, Li19b]. In our system electron-deficient cobalt(III)-substituted Keggin anions $[B^{III}W^{VI}_{11}O_{39}Co^{III}]^{6-}$ are used as the **POM** system (see inset of Fig. 4-16b). As a ligand

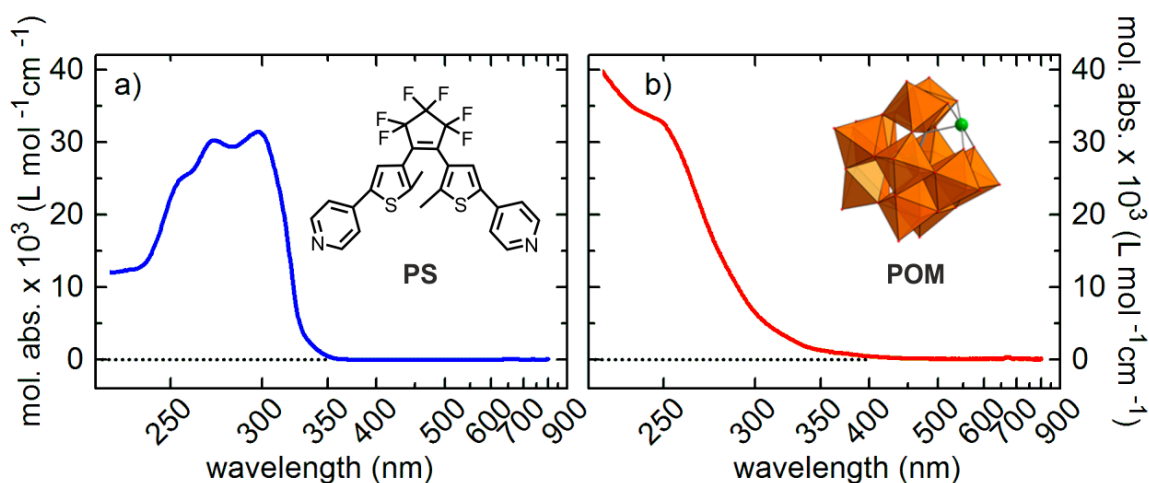


Figure 4-16 Molar absorptivity and molecular structure of a) **o-PS** (DAE switch) and b) **POM** dissolved in cyclohexane.

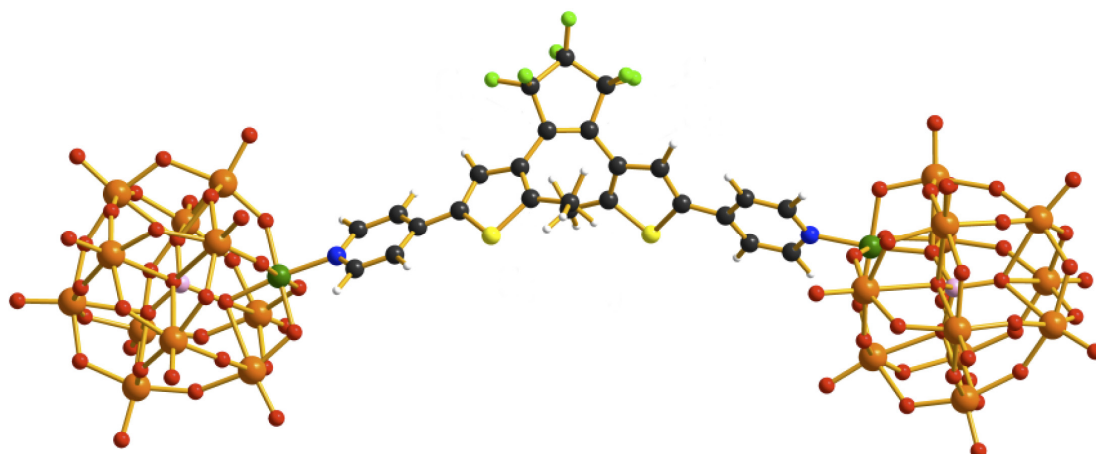


Figure 4-17 Optimized structure of the **PS-POM** structure in ball and sticks representation black = C, light green = F, yellow = S, blue = N, dark green = Co, red = O, orange = W, pink = B from reference [Xu18].

a pyridyl-containing DAE photoswitch in open form **o-PS** is used (see inset of Fig. 4-16a). Both species show a strong absorption band in the UV region originating from the π - π^* transition in the case of **o-PS** [Iri00] and for the **POM** system it is ligand-to-metal charge transfer originating from the $O_{2p} \rightarrow W_{5d}/Co_{3d}$ transition [Wea73].

After mixing the **o-PS** and **POM** system in the ratio of 1:3, it coordinates to the **o-PS-POM** complex with a molecular dumbbell structure $[(C_{25}H_{16}N_2F_6S_2)(B^{III}W^{VI}_{11}O_{39}Co^{III})_2]^{12-}$, whereby the photoswitch remains in the open form (see Fig. 4-17). Regarding the UV/vis spectrum of **o-PS-POM**, an additional absorption band around 400 nm appears (see Fig. 4-18a) that is absent in both of the pure starting agents **o-PS** and **POM**.

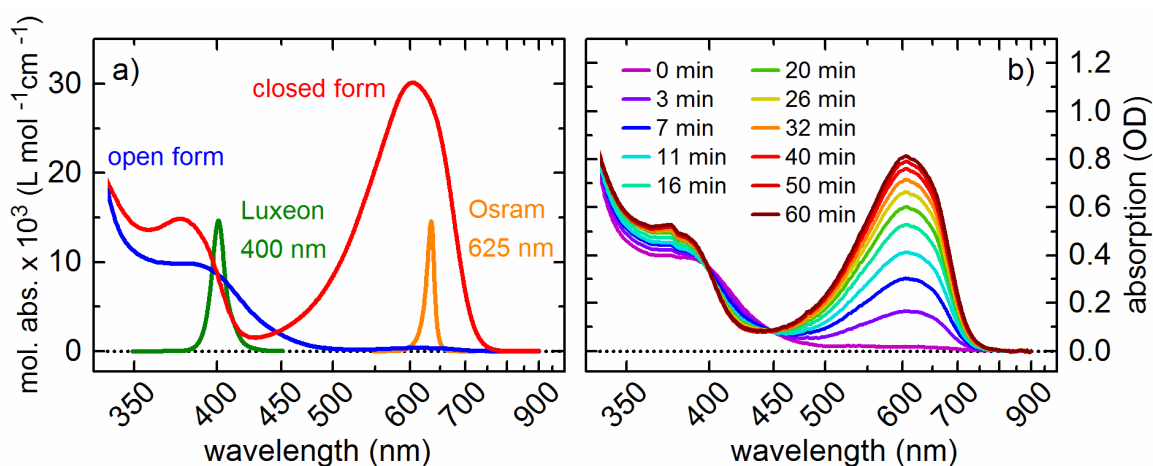


Figure 4-18 a) Molar absorptivity for the open and closed form of the **PS-POM** complex with spectral distribution of the LED used for the RQY determination. b) spectral changes upon illumination with the 400 nm LED.

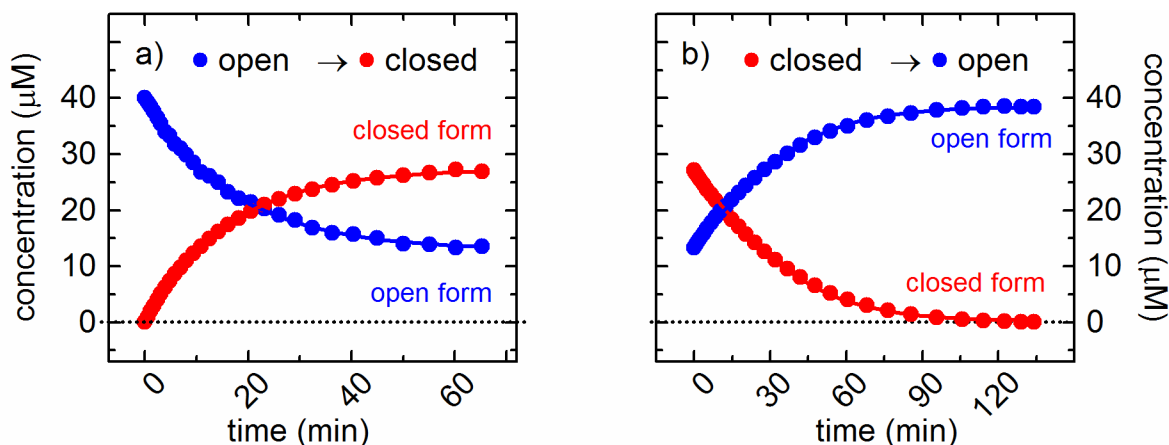


Figure 4-19 Time evolution of the concentrations during the illumination of a) open form with a 400 nm LED b) closed form with a 625 nm LED. The solid lines represent the numerical simulation.

The origin of the 400 nm absorption band is tentatively assigned to a *d-d* transition as reported for similar Co^{III} -containing POM pyridyl complexes [Wea67, Gla14].

As shown in Fig. 4-18b the open form of **PS-POM** complex isomerizes to the closed form upon illumination with the 400 nm LED (Luxeon Z UV LHUV-0400, Lumileds Holding B.V.). Hereby, two clean isosbestic points at 400 nm and 448 nm are observed. In the photostationary state 66% of the closed form and 34% of the open form are found (see Fig. 4-19a).

The relatively low RQY of 0.97% is assumed to be related to the significant electron-withdrawing capacity of the coordinated polyanion. The reversed reaction triggered by the 625 nm LED (Osram LR CP7P, Osram Licht AG) results in the complete isomerization to the pure open form. The RQY is with value of 0.02% even one order of magnitude lower than for the opposite reaction, which corresponds to the trend reported for the molecules from the DAE family [Iri95, Mat03, Tak12].

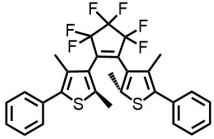
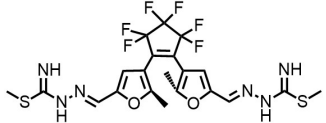
In summary, the first photochromic coordination complex of DAE and POM was characterized. The coordination complex isomerizes to the open and closed form upon illumination with light. In contrast to the non-coordinated parent DAE, the photoswitching can be promoted by solely visible light. The very modest RQY of the **PS-POM** leads to an assumption that a significant population relaxed back to the ground state without any isomerization. The further optimization of the dimension and charge of the POM as well as modifications in the DAE structure may lead to an improved DAE-POM designs with enhanced RQY and electronic properties.

Appendix for Chapter 4

Appendix 4-A

Table 4-A Summary of reported molecular dynamics and lifetimes for the ring closing (o→c) of various switches from the DAE family.

ref.	solvent	pre-switching dynamics	ring closing	lifetime AP form	lifetime P form	post-switching dynamics	RQY
[Alo14]	n-hexane	90 fs	0.8 ps	-	120 ps	-	40%
[Els09]	MeCN	500 fs	16 ps	-	1300 ps	-	22%
[Fre20]	MeCN	-	650 fs	650 fs	48 ps* 3.8 μs [†]	-	51%
[Ham16]	CH ₃ Cl	200 fs	0.1 ps	2 ps* 25 μs [†]	55 ps* 2.5 μs [†]	-	46%
[Han02, 05]	Cyclohexane	50-150 fs	4 ps	-	7 - 100 ps	50 ps	5 %

[Ish11, 16]		n-hexane or MeCN	-	0.45 ^a – 1.5 ps ^b	-	150 ^a – 200 ^b ps	-	47-64%
[Pon14]		Cyclohexane	-	0.3 ps	-	23 ps*	-	
o-MTSC		MeCN	500 fs	6 ps	-	52 ps	-	

*decay to triplet state, † lifetime of triplet state, ^a n-hexane, ^b acetonitrile

UV/vis spectroscopy

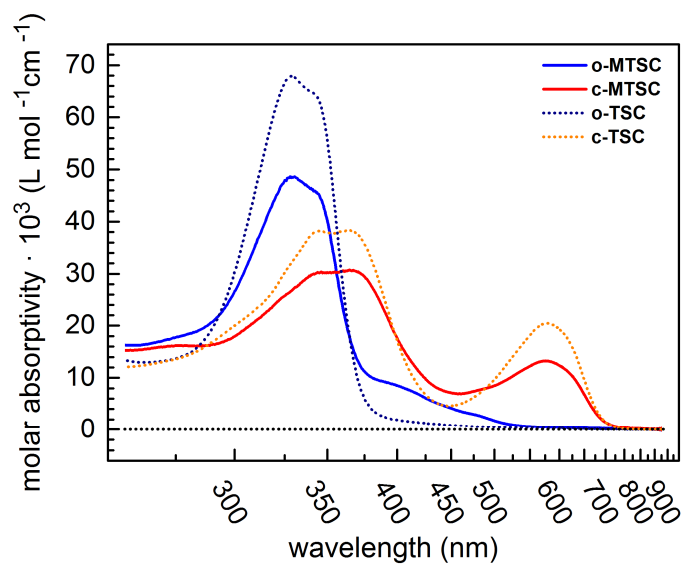


Figure 4-A1 Molar absorptivities of the **MTSC** and **TSC** in ethanol.

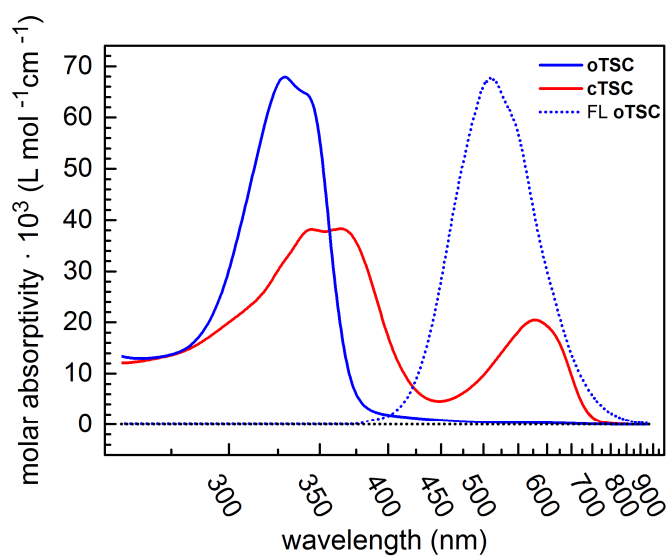


Figure 4-A2 Molar absorptivities of the **TSC** molecule in ethanol. The dotted blue line represents the fluorescence of the open form.

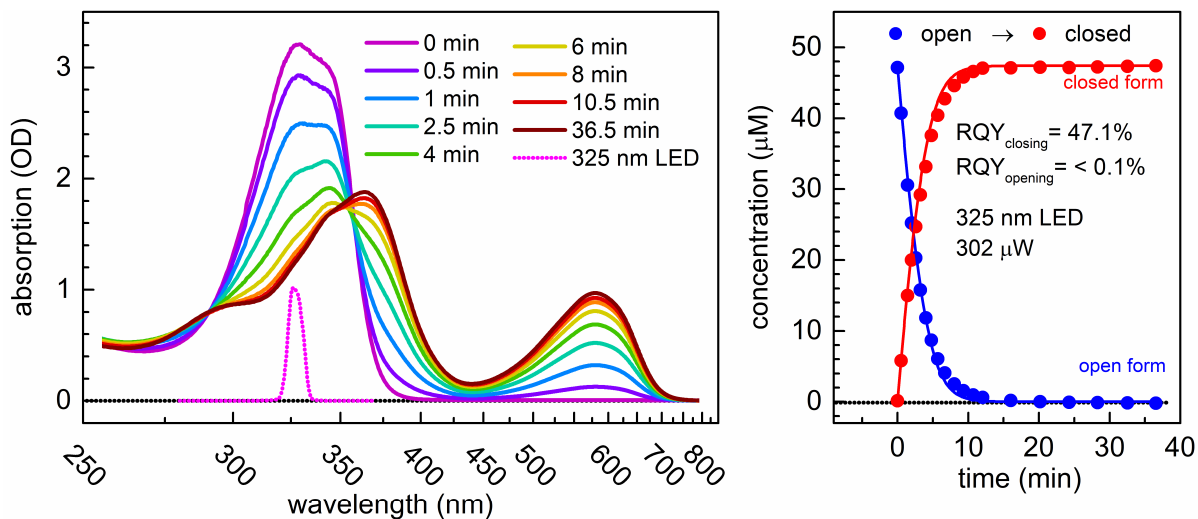


Figure 4-A3 (left) Spectral changes of the open form of the **o**-TSC molecule in acetonitrile upon illumination with a 325 nm LED (EOLS-325-696, Dowa Electronics Materials Co.) with the power in the sample of 302 μW. Solution of a 47.4 μM in a 10 mm absorption cuvette with a volume of 2 mL. (right) Time evolution of concentrations during the illumination and numerical simulation (solid lines).

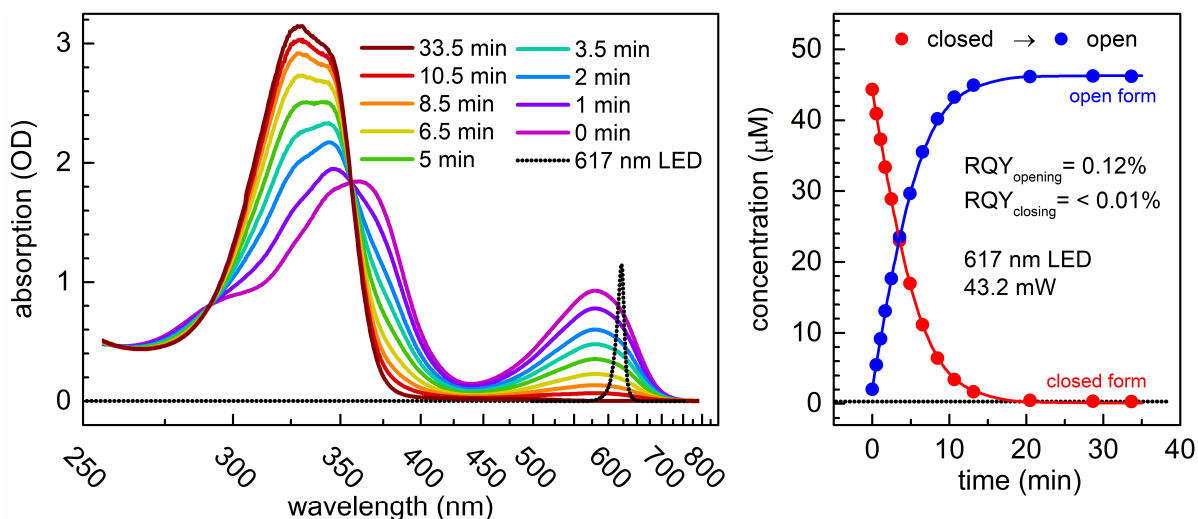


Figure 4-A4 (left) Spectral changes of the open form of the **c**-TSC molecule in acetonitrile upon illumination with a 617 nm LED (LACP7P-KPKR, Osram Licht AG) with the power in the sample of 43.2 mW. Solution of a 46.2 μM in a 10 mm absorption cuvette with a volume of 2 mL. (right) Time evolution of concentrations during the illumination and numerical simulation (solid lines).

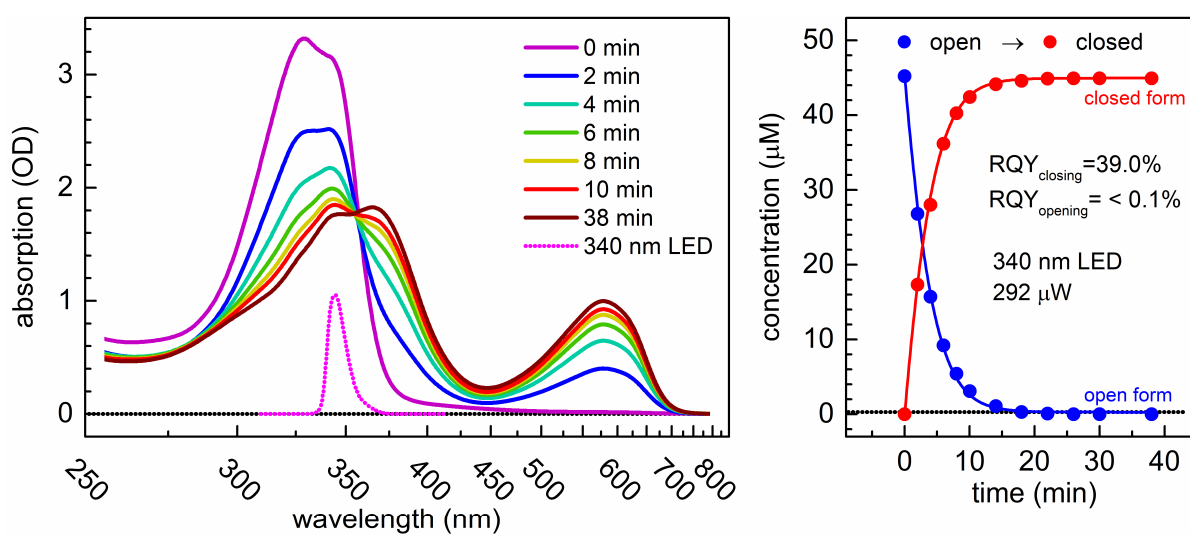


Figure 4-A5 (left) Spectral changes of the open form of the **o**-TSC molecule in ethanol upon illumination with a 340 nm LED (CUD4AF1B, Seoul Viosys Co.) with the power in the sample of 292 μW . Solution of a 45 μM in a 10 mm absorption cuvette with a volume of 2 mL. (right) Time evolution of concentrations during the illumination and numerical simulation (solid lines).

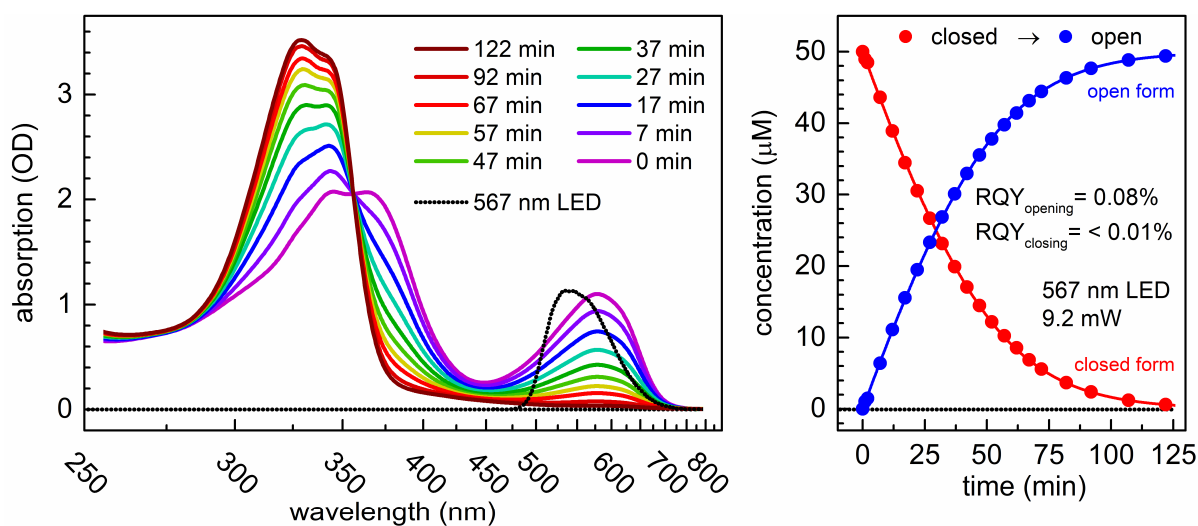


Figure 4-A6 (left) Spectral changes of the closed form of the **c**-TSC molecule in ethanol upon illumination with a 567 nm LED (Luxeon SP-01-L1, Lumileds Holding B.V.) with the power in the sample of 9.2 mW. Solution of a 50 μM in a 10 mm absorption cuvette with a volume of 2 mL. (right) Time evolution of concentrations during the illumination and numerical simulation (fit).

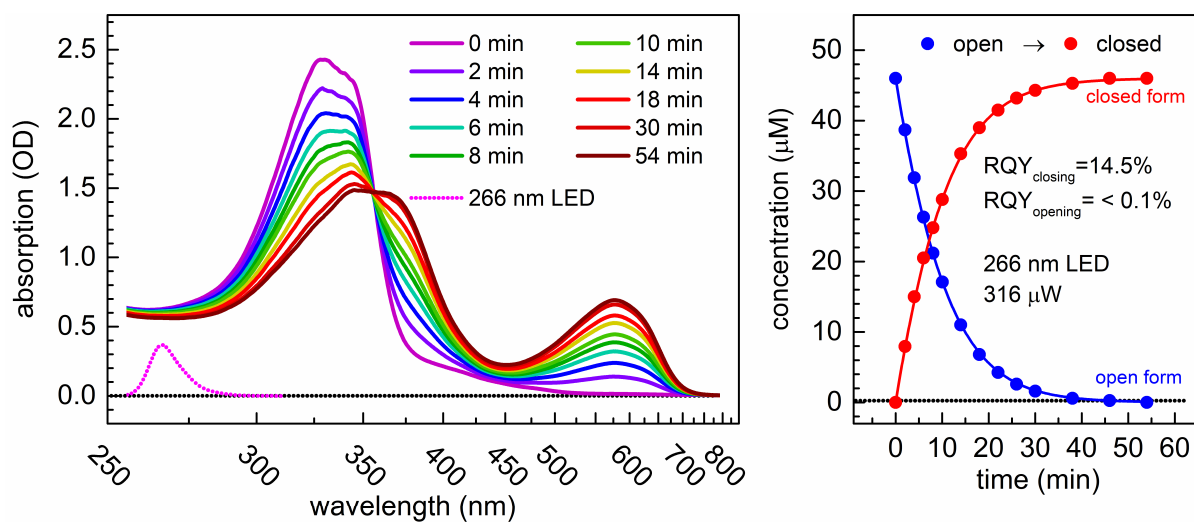


Figure 4-A7 (left) Spectral changes of the open form of the **o**-MTSC molecule in ethanol upon illumination with a 266 nm LED (VPC131, Nikkiso Co.) with the power in the sample of 316 μW . Solution of a 46 μM in a 10 mm absorption cuvette with a volume of 2 mL. (right) Time evolution of concentrations during the illumination and numerical simulation (solid lines).

Appendix 4-B

Transient absorption

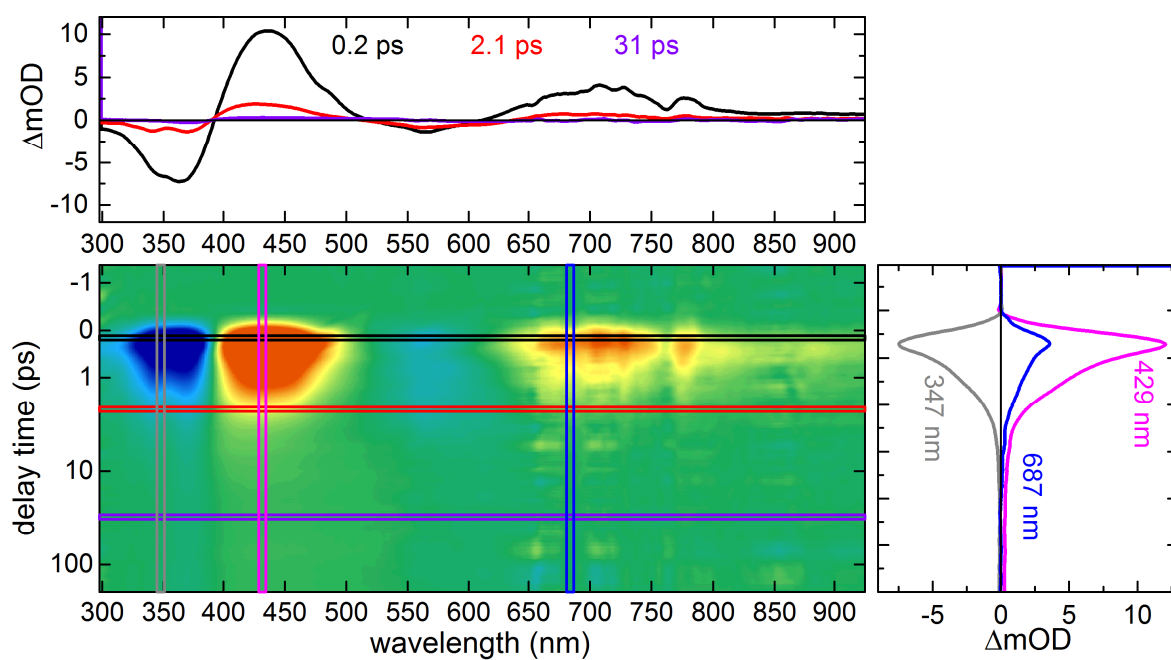


Figure 4-B1 Transient absorption of c-TSC in ethanol under standard conditions measured in 250 μm thick flow cell after excitation with 150 fs pulses centered at 580 nm with a pulse energy of 200 nJ.

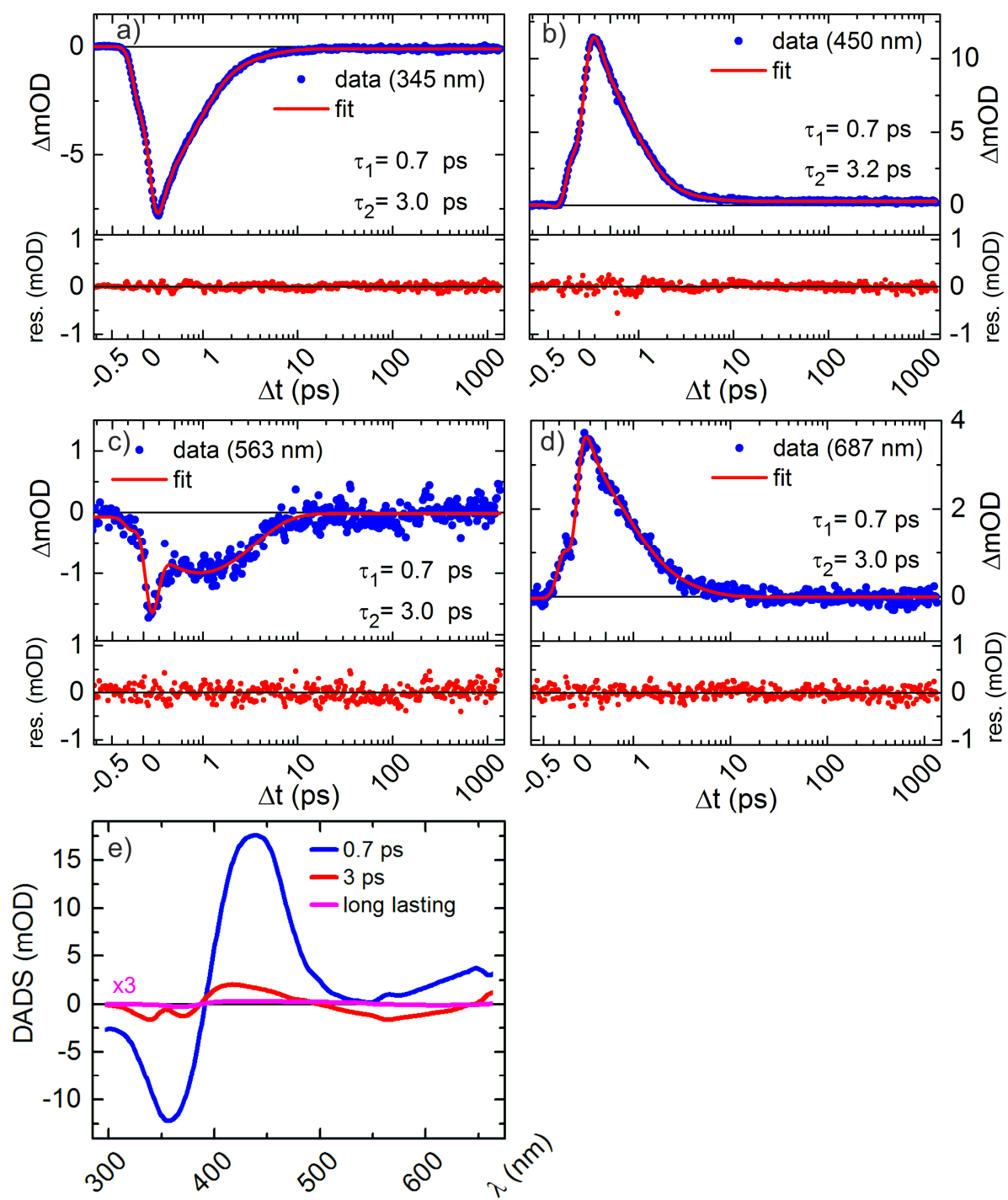


Figure 4-B2 a-d) Kinetic traces at selected wavelengths fitted with a multiexponential decay model. e) Decay associated difference spectra obtained from a global fit analysis for **c-TSC** in ethanol.

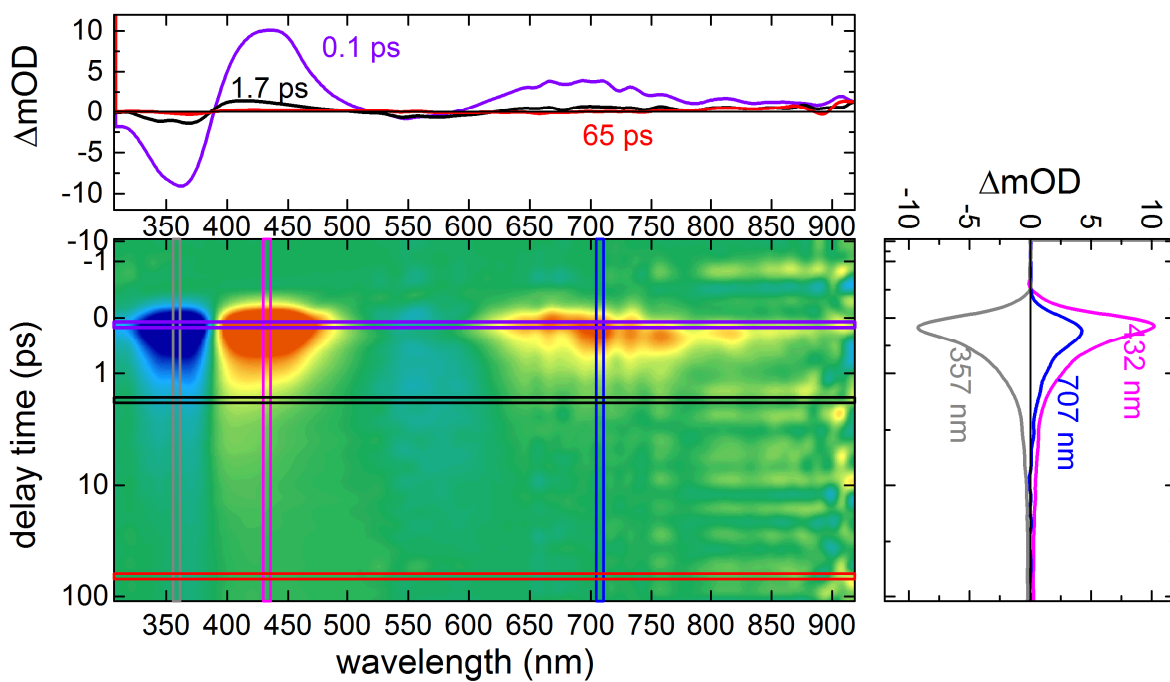


Figure 4-B3 Transient absorption of **c-TSC** in acetonitrile under standard conditions measured in 250 μm thick flow cell after excitation with 150 fs pulses centered at 580 nm with a pulse energy of 200 nJ.

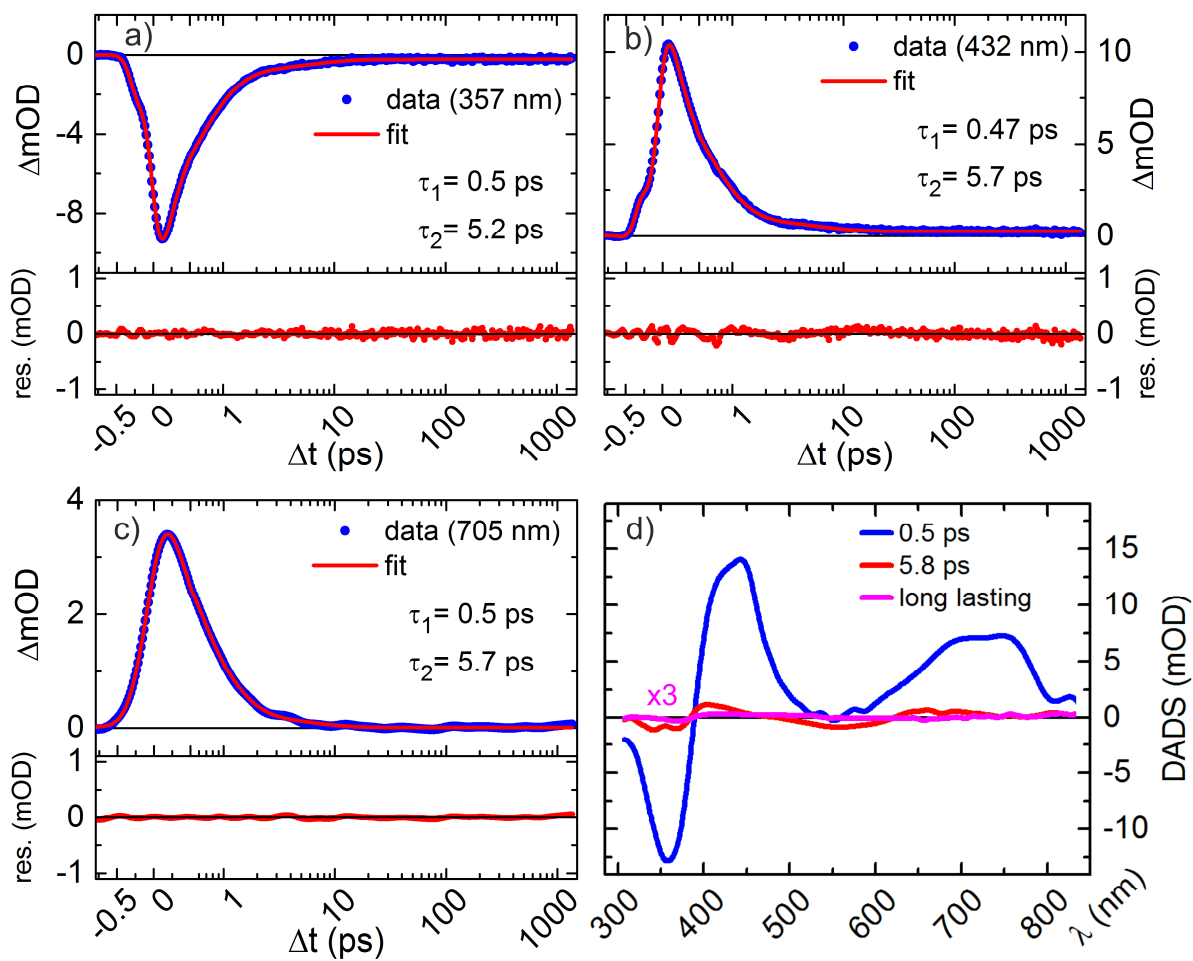


Figure 4-B4 a-c) Kinetic traces at selected wavelengths fitted with a multiexponential decay model. d) Decay associated difference spectra obtained from a global fit analysis for **c-TSC** in acetonitrile.

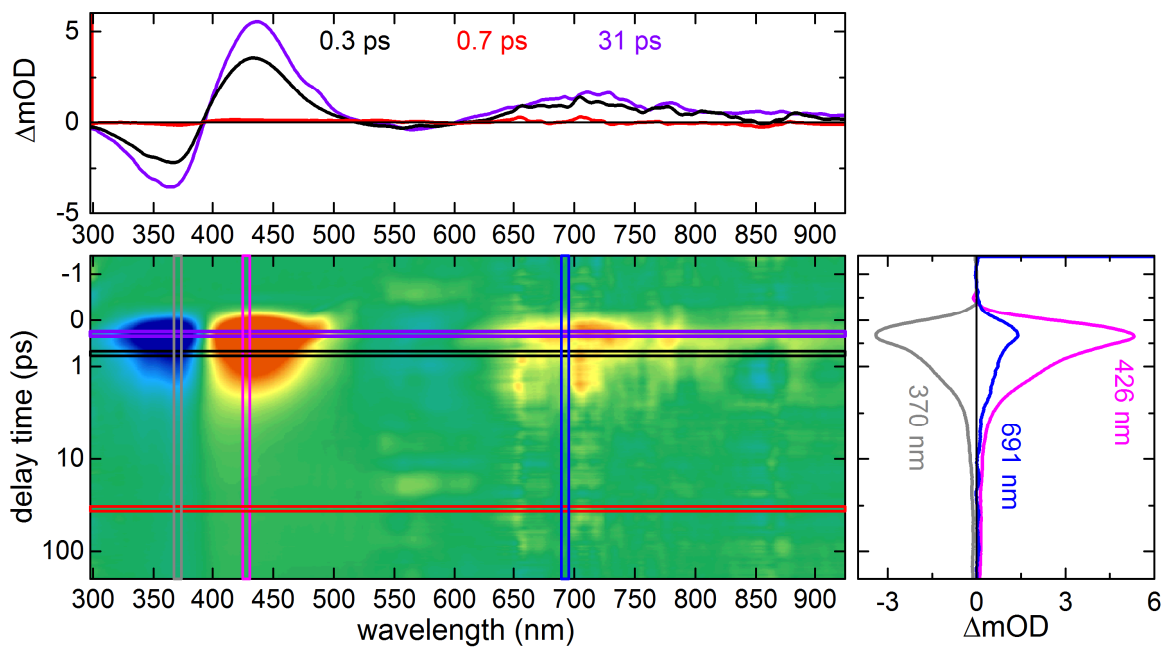


Figure 4-B5 Transient absorption of **c-MTSC** in ethanol under standard conditions measured in 250 μm thick flow cell after excitation with 150 fs pulses centered at 580 nm with a pulse energy of 200 nJ.

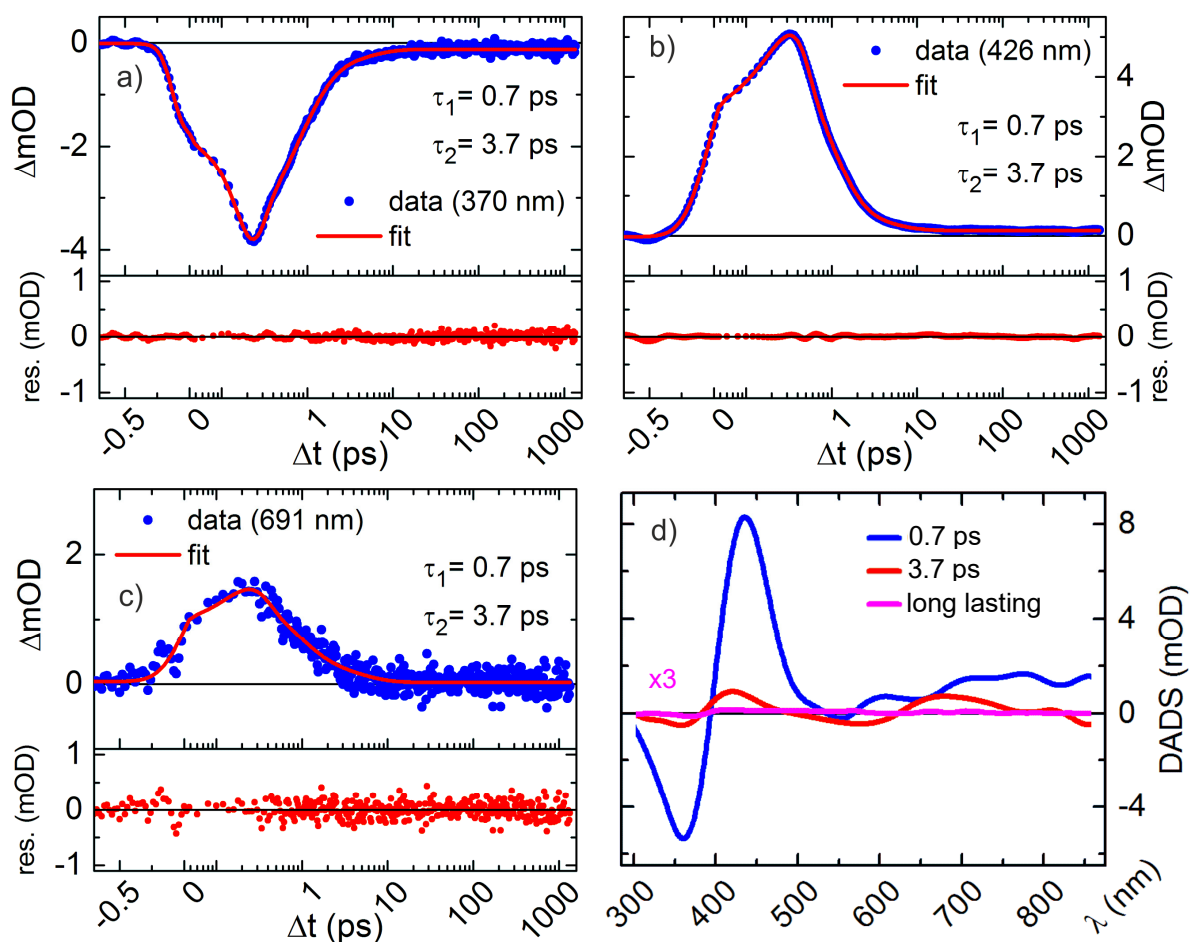


Figure 4-B6 a-c) Kinetic traces at selected wavelengths fitted with a multiexponential decay model. d) Decay associated difference spectra obtained from a global fit analysis for **c-MTSC** in ethanol.

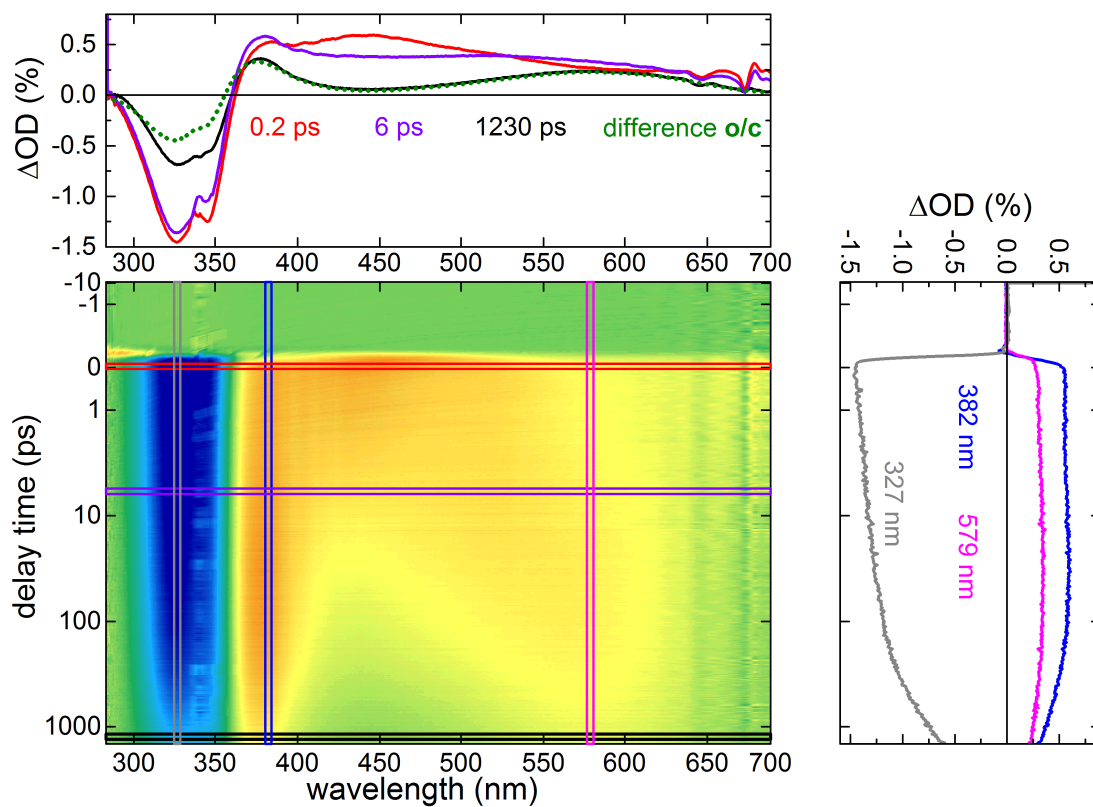


Figure 4-B7 Transient absorption of **o**-TSC in ethanol under standard conditions measured in 250 μm thick flow cell after excitation with 150 fs pulses centered at 340 nm with a pulse energy of 25 nJ.

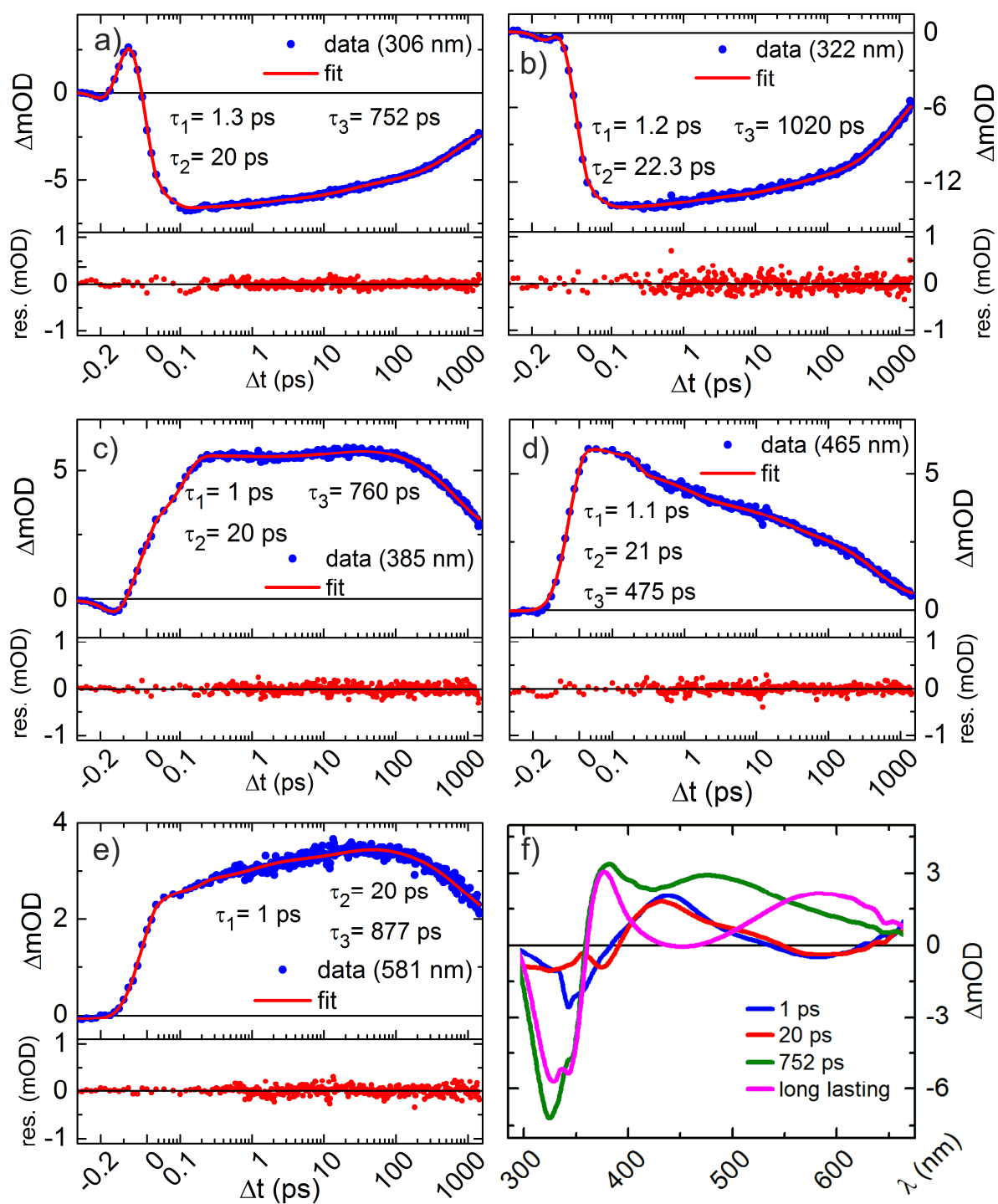


Figure 4-B8 a-e) Kinetic traces at selected wavelengths fitted with a multiexponential decay model. f) Decay associated difference spectra obtained from a global fit analysis for *o*-TSC in ethanol.

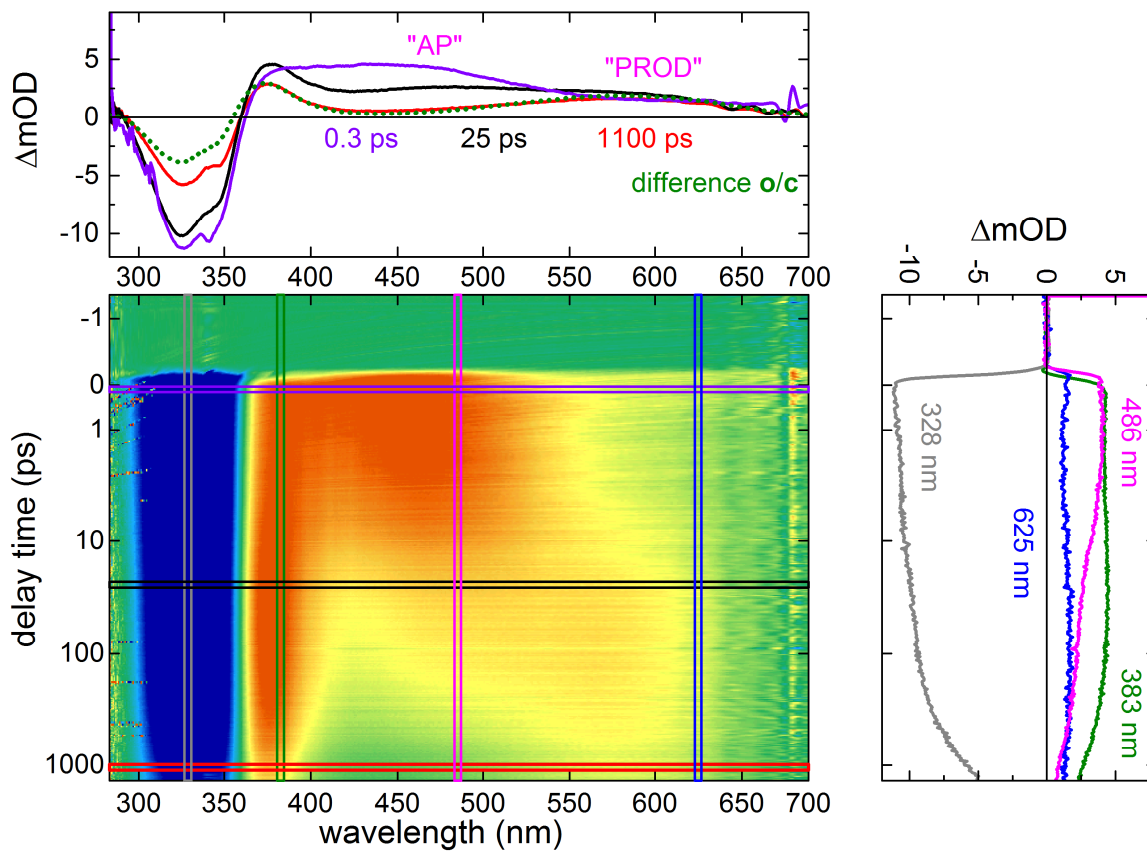


Figure 4-B9 Transient absorption of **o-TSC** in acetonitrile under standard conditions measured in 250 μm thick flow cell after excitation with 150 fs pulses centered at 340 nm with a pulse energy of 50 nJ.

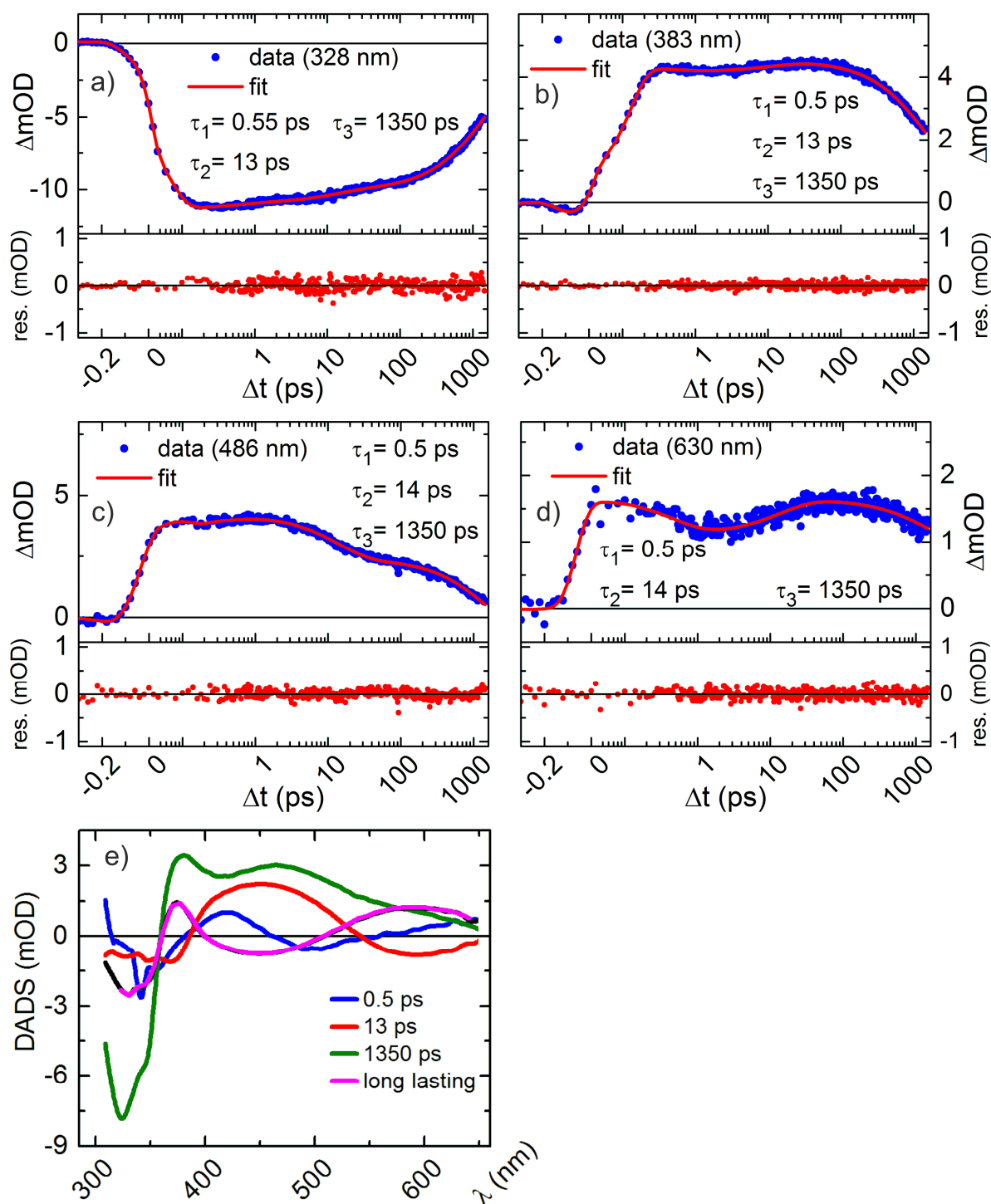


Figure 4-B10 a-d) Kinetic traces at selected wavelengths fitted with a multiexponential decay model. e) Decay associated difference spectra obtained from a global fit analysis for *o*-TSC in acetonitrile.

5. Decarboxylative photomacrocyclization of N-phthaloylated GABA derivatives

5.1 Introduction

Photoinduced electron transfer (PET) is one of the most relevant processes in the field of photochemistry. PET can proceed under excitation with light either inter- or intramolecularly in which a donor transfers its electron to an accepting moiety. In this work we describe a PET in N-phthaloylated GABA derivatives as a key step in the decarboxylative photomacrocyclization which results in the formation of benzopyrrolizidines.

N-phthaloylated GABA derivatives consist of two basic moieties as shown in the upper part of Fig. 5-1. The green N-phthaloyl structure has its origin in the phthalimide (black structure top left), while the red GABA structure corresponds to **G**amma-**A**mino**B**utyric **A**cid. The photoinduced reaction in an acetonitrile/water mixture with 0.5 equivalents (eq) of potassium carbonate results in the benzopyrrolizidine motif having a high reaction quantum yield (RQY).

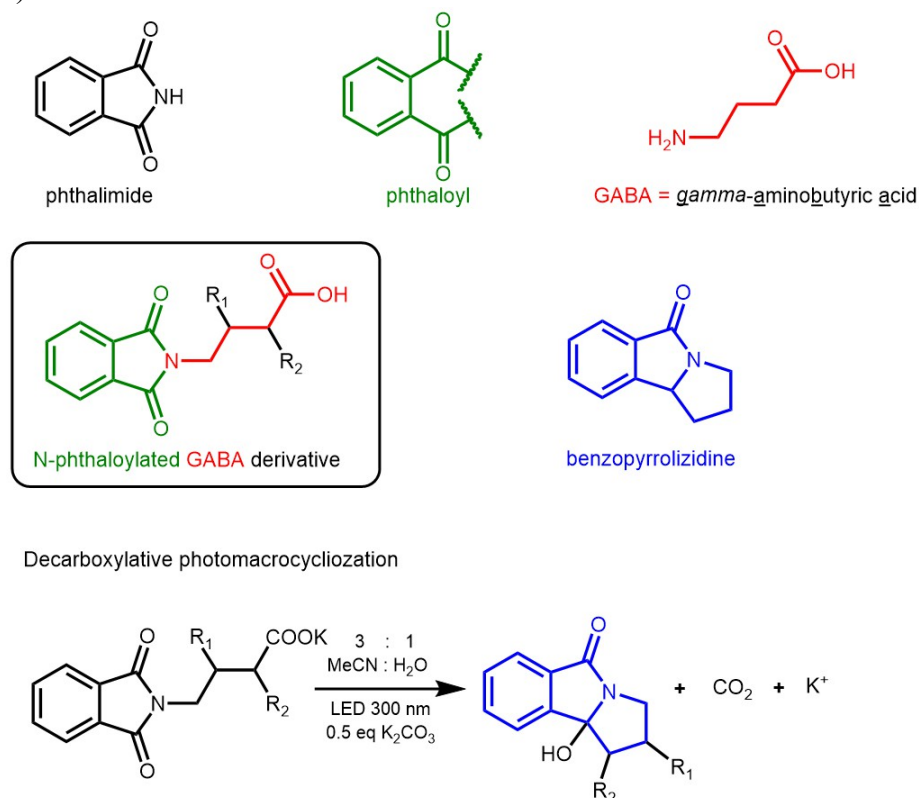


Figure 5-1 (top) System under study: heterocyclic N-phthaloylated GABA derivative with the corresponding sub-units and parent phthalimide skeleton. (bottom) Photomacrocyclization reaction accompanied by decarboxylation and ring annulation.

5.2 UV/vis spectroscopy and RQY

The UV/vis absorption spectra of the GABA based reactant and product are shown in Fig. 5-2. During the photoreaction the absorption band of the reactant around 300 nm (n, π^*) [Oel02, Coy78] decreases due to the conversion of the imide into amide [Gri07, Oel02] and an additional absorption band around 250 nm appears. The molar absorptivities with a magnitude of $10^3 \text{ L} \cdot \text{mol}^{-1} \cdot \text{cm}^{-1}$ or below can be considered as rather modest.

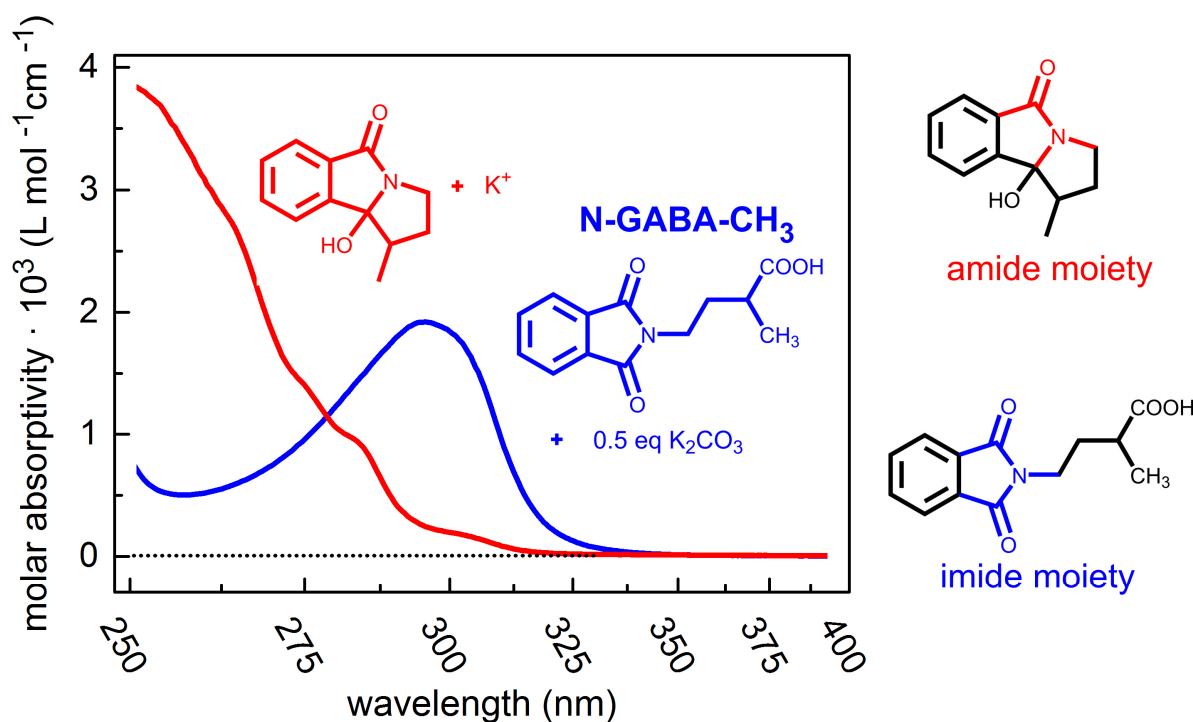


Figure 5-2 Molar absorptivity for N-GABA-CH₃ in acetonitrile/water solution 3:1. The reactant (blue) reacts upon illumination with UV light (305 nm) to the product (red). The corresponding imide and amide moieties are shown on the right.

The reaction mechanism of the ring annulation was proposed by Griesbeck in 1997 [Gri97, Goe01] consisting of: a) triplet formation, b) intramolecular PET, c) decarboxylation and d) intramolecular radical recombination producing the new ring (see Fig. 5-3 upper pathway). However, the last step may be in competition with an additional electron transfer from an imide radical anion to the terminal carbon radical. Such ET results in a carbanion that is readily protonated by a water molecule (see Fig. 5-3 lower pathway). This simple decarboxylation reaction is also known as CO_2/H^+ exchange [Gri99a]. The ratio of both possible products can be controlled by the reaction conditions. For example, the presence of water equivalents suppresses the formation of the CO_2/H^+ exchange product. This can be explained with the rapid protonation of the intermediate oxygen atom of the ketyl radical.

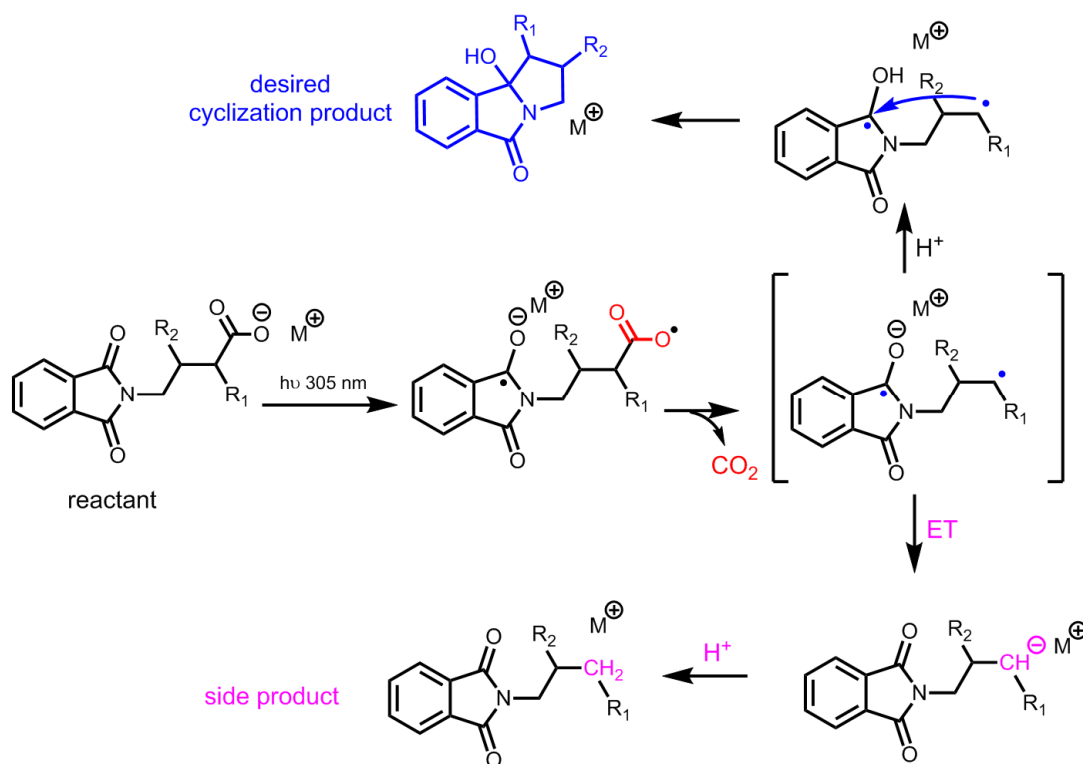


Figure 5-3 Two possible reaction pathways of N-phthaloylated GABA derivatives upon illumination with 305 nm light. M⁺ corresponds to the group I and II metal cations.

Besides water, potassium carbonate has also a major impact on the formation of the two possible products and its ratio. It is highly relevant to study additives and their role in the photoreaction, since such analysis typically yields a deeper understanding of the reaction mechanism.

For this purpose, the equivalents of the potassium carbonates are varied from 0.1 eq up to 1 eq under a constant illumination power of 4.49 mW (LED 305 nm, LUEVA66H100KU00, LG Innotek). A solvent mixture of acetonitrile/water with a ratio of 3:1 was used for each experiment. In the following, the impact of the additive on the photoreaction is discussed in detail.

As shown in Fig. 5-4 the amount of potassium carbonate is a crucial factor which influences the reaction progress. This can be clearly observed by the remarkably different spectral shapes of the photostationary state (PSS). For a photoreaction with 0.5 eq of K₂CO₃ each spectrum can be projected onto the basis spectra of reactant and product without any significant residuum (Fig. 5-4 left). This is not the case for the light induced reaction below 0.1 eq of K₂CO₃ (Fig. 5-4 right and Fig. 5-B3 in Appendix). Beside the reactant and the main product, a third species is obviously present. Since this side product is reasonable according to

the reaction pathway (see Fig. 5-3), it is important to quantify its amount in the PSS and determine its molar absorptivity.

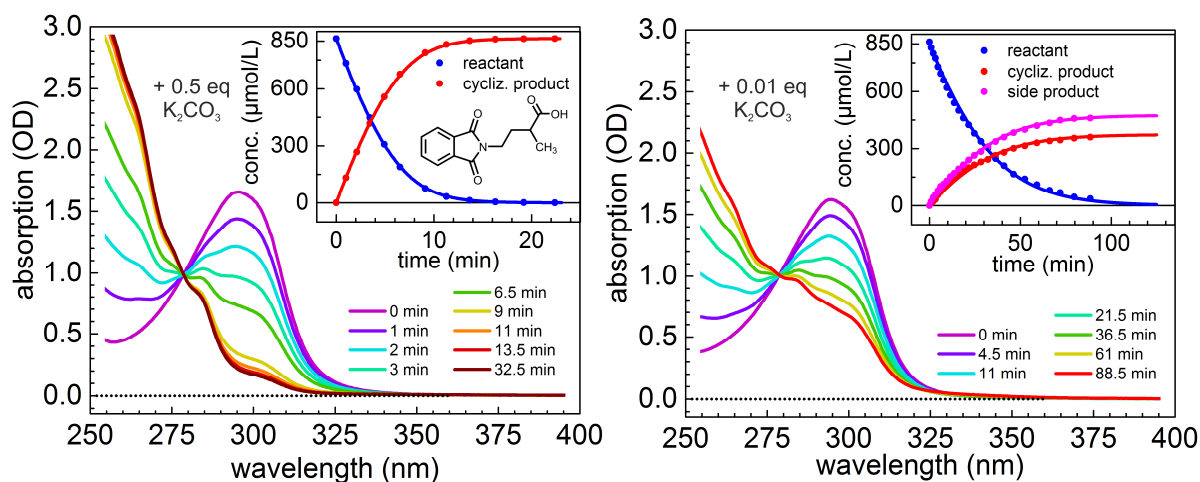


Figure 5-4 Selected UV/vis spectra of **N-GABA-CH₃** with 0.5 eq (left) and 0.01 eq (right) of K_2CO_3 under illumination with 305 nm light with an illumination power of 4.49 mW. The inset shows the time dependent concentration of reactant and products with the solid lines representing the numerical fit.

The first option to extract the molar absorptivity of the side product is the so-called TEM method developed by Thulstrup, Eggers, and Michl [Mic70a, Mic70b, Mic87] (for more details see Chapter 2). Analyzing the second derivative of the vibronic features leads to a prediction of around 15.5% of the side product in the PSS, when illuminating the reaction mixture with 0.1 eq of the additive.

The second option is a NMR analysis which provides not only quantitative information about the side product in PSS, but also about its molecular structure. Since the acetonitrile/water solvent mixture has a significant impact on the species ratio in the PSS, the NMR analysis was measured in the correspondent deuterated solvent mixture. Despite this uncommon measurement environment the NMR spectrum could be measured with the support of Prof. K. Karaghiosoff. The evaluated NMR data are shown in Fig. 5-A in the Appendix, whereby the letters correspond to signals of the main product and the numbers are related to the signals originating from the side product. The NMR analysis confirms that the side product is created by a simple decarboxylation as demonstrated in the lower part of Fig. 5-3. The amount was calculated to be 16.5% which is in good agreement with the TEM method. The extracted spectrum of the side product based on the NMR analysis is shown with a magenta line in Fig. 5-5.

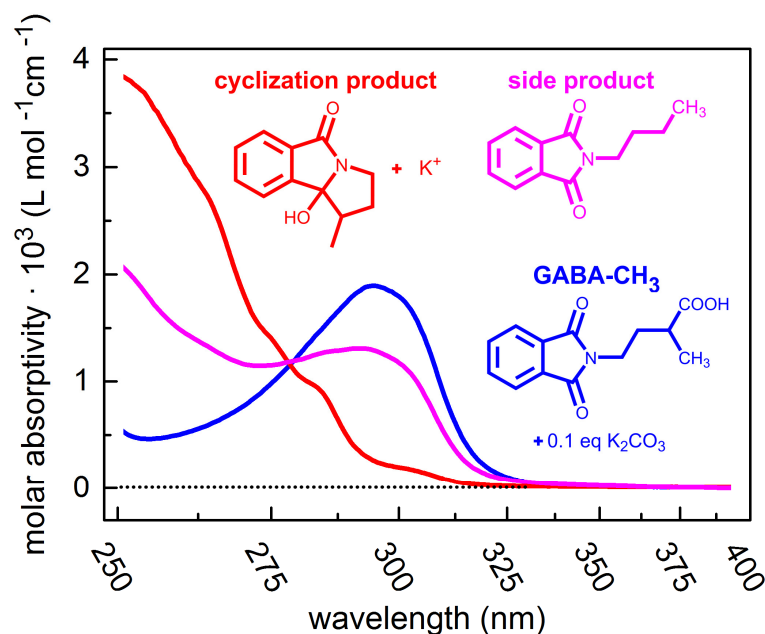


Figure 5-5 Molar absorptivity for **GABA-CH₃** in acetonitrile/water solution 3:1. The reactant (blue) reacts upon illumination with UV light (305 nm) to either the cyclization product (red) or the side product (magenta).

By comparing the spectral bands of reactant (blue line) and side product (magenta line) in Fig. 5-5, it is notable that both species have a comparable distribution around 290 nm. This is expected, since the chromophore core remains preserved. In contrast to the reactant with no remarkable band around 260 nm, the side product shows an additional band in the deep UV region that can be presumably related to the missing carboxylic group.

Since the molar absorptivities of all species are now known, the deconvolution onto basis spectra is straightforward. The residua of this linear combination are clearly within the experimental error as shown in the Appendix in Fig. 5-B1 and Fig. 5-B2.

Table 5-1 Percentage of main product and side product in the PSS in dependence on the K_2CO_3 for **N-GABA-CH₃** in acetonitrile/water = 3:1 under irradiation with 305 nm LED with 4.49 mW of illumination power into a 10 mm cuvette.

K_2CO_3	1 eq	0.5 eq	0.1 eq	0.01 eq
% main product	100%	100%	83.5%	6 %*
% side product	0%	0%	16.5%	44%*

* estimated value by extrapolation of the experimental data since a photo-decomposition during conversion of the last 3% of reactant was observed.

According to the results summarized in Tab. 5-1 the ring cyclization can be selectively favored by an addition of 0.5 eq of potassium carbonate. On the other hand, the missing amount of K_2CO_3 favors the formation of undesired side product. It is worth to mention that a prolonged illumination with 0.01 eq of K_2CO_3 leads to a decomposition of the photoproduct. Hence, the experimental data are evaluated up to 88 min, where a clear isosbestic point is still present.

The most important quantitative issue of any photochemical reaction is the effectivity in form of the reaction quantum yield (RQY). The RQY with better than 5% relative error can be determined straightforwardly for any two state system when using the Quantum Yield Determination Setup (QYDS) [Meg10, Vol19]. The QYDS approach can be regarded as a powerful method, since the reaction model can be rapidly adapted into any feasible reaction scheme. In this case, the simple reaction from reactant to product is extended to consider the creation of a side product that originates from the reactant, but not from product (see Fig. 5-6).

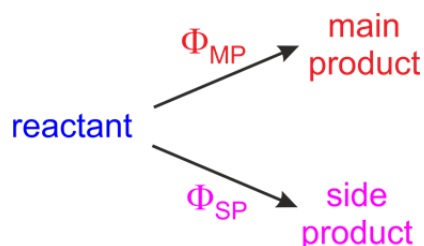


Figure 5-6 Reaction model considering the creation of the side product used for the determination of the RQY.

The simple two state model considering the conversion of the reactant **R** into the main product **MP** can be calculated by numerical integration (propagation) of the differential equation. The quantum yield Φ_{MP} is the only free parameter that can be optimized.

$$\frac{dN_{MP}(t)}{dt} = +\Phi \int \frac{c_R(t)\epsilon_R(\lambda)}{c_R(t)\epsilon_R(\lambda) + c_{MP}(t)\epsilon_{MP}(\lambda)} \frac{P_{ref} \cdot f(\lambda) \cdot \lambda}{h \cdot c} A(t, \lambda) d\lambda \quad (5.1)$$

with the total absorption defined as:

$$A(t, \lambda) = 1 - 10^{-d \cdot [c_R(t)\epsilon_R(\lambda) + c_{MP}(t)\epsilon_{MP}(\lambda)]} \quad (5.2)$$

where:

$N_x(t)$	=	number of molecules of species x at time t
$c_x(t)$	=	concentration of species x at time t
$\epsilon_x(\lambda)$	=	extinction coefficient of species x for wavelength λ
$f(\lambda)$	=	spectral distribution of the LED light
$A(t, \lambda)$	=	absorption of the sample at time t and wavelength λ
d	=	thickness of the cuvette (10 mm)

For the sake of simplicity, the following terms are combined and introduced:

$$\text{Frac}_R(t, \lambda) = \frac{c_R(t) \cdot \epsilon_R(\lambda)}{\sum_{i=1}^n c_i(t) \cdot \epsilon_i(\lambda)} \quad (5.3)$$

$\text{Frac}_R(t, \lambda)$ corresponds to the fraction of photons absorbed by the reactant **R** when **n** different species are present. The fraction for other species is calculated likewise. The total absorption of the sample $A(t, \lambda)$ and number of the photons per second $N_{\text{Ph}}(\lambda)$ are calculated as:

$$A(t, \lambda) = 1 - 10^{-d \cdot \left(\sum_{i=1}^n c_i(t) \cdot \epsilon_i(\lambda) \right)} \quad (5.4)$$

$$N_{\text{Ph}}(\lambda) \left[\frac{1}{\text{s}} \right] = \frac{P_{\text{ref}} \cdot f(\lambda) \cdot \lambda}{h \cdot c} \quad (5.5)$$

The three-state model with the side product **SP** shown in Fig. 5-6 results in the following set of differential equations:

$$\frac{dN_R(t)}{dt} = \int \left[-(\phi_{\text{MP}} + \phi_{\text{SP}}) \text{Frac}_R(t, \lambda) \right] N_{\text{Ph}}(\lambda) \cdot A(t, \lambda) d\lambda \quad (5.6)$$

$$\frac{dN_{\text{MP}}(t)}{dt} = \int \left[\phi_{\text{MP}} \cdot \text{Frac}_R(t, \lambda) \right] N_{\text{Ph}}(\lambda) \cdot A(t, \lambda) d\lambda \quad (5.7)$$

$$\frac{dN_{\text{SP}}(t)}{dt} = \int \left[\phi_{\text{SP}} \cdot \text{Frac}_R(t, \lambda) \right] N_{\text{Ph}}(\lambda) \cdot A(t, \lambda) d\lambda \quad (5.8)$$

These differential equations are solved numerically by propagation in Mathcad Prime 5.0. Both the RQY of the main product as well as the one for the side product can be correspondingly extracted at the same time from one complete measurement. Such detailed RQY analy-

ently extracted at the same time from one complete measurement. Such detailed RQY analysis provides not only information about how effective the reaction proceeds, but it also gives a deeper understanding of the reaction mechanism.

The resulting RQYs are summarized in Tab. 5-2. The RQY of the ring annulation under addition of 0.5 eq or 1 eq of K_2CO_3 is 47%. By reducing the K_2CO_3 amount from 0.5 eq over 0.1 eq to 0.01 eq the RQY of the cyclization decreases massively down to 4% (see Tab. 5-2). This trend can be directly seen in the reaction time required to reach the PSS, since the same illumination power of 4.49 mW was applied (compare Fig. 5-4 and Fig. 5-B3 in Appendix). On the other hand, the RQY of the side reaction appears to remain relatively constant with ca. 4.5% for both cases using low additive amount.

The various equivalents of K_2CO_3 leads to different pH values. The pH was measured with a calibrated pH meter (pH 1000 L, VWR International bvba). The cyclization RQY shows a strong dependence on the pH (see Fig. 5-C). The same sigmoidal trend was also published in ref. [Gri07]. This leads to an assumption, that the reaction medium plays an important role in the reaction progress.

Table 5-2 RQY in dependence of pH for **N-GABA-CH₃** in acetonitrile/water = 3:1 under irradiation with 305 nm LED with 4.49 mW of illumination power into a 10 mm cuvette.

K₂CO₃	1 eq	0.5 eq	0.1 eq	0.01 eq
pH	10.8	10.32	9.82	8.94
QY (cyclization)	47.3%	46.8%	21.7%	3.9%
QY (side product)	0%	0%	4.3%	4.9%

Since potassium carbonate acts as a weak base and it can be expected to deprotonate the carboxylic group, it might be assumed that any organic base leads to the desired photoactivation. However, as described in references [Gri95, Oel01] this is not the case. Thus, it is expected that potassium cations play a major role in the preorientation of the molecule favoring the ring annulation. According to the results published for the phthalimido acetic acid, potassium cations serve as an intramolecular bridge between the carbonyl group and the terminal carboxylate of the phthalimide [Oel01, Gri95, Gri97]. Applying this picture to the GABA derivatives, it is reasonable to assume, that the coordination to the potassium cations brings

the two relevant carbon radicals in sufficient proximity for an effective bond formation (see two green carbon atoms in Fig. 5-7). This assumption is supported by the fact, that the addition of K_2CO_3 shifts the absorption spectra moderately into the red (see Fig. 5-8). This shift may originate from the stronger delocalization of the electron system. Consequently, at a sufficient concentration of potassium carbonate the ring annulation product can be formed exclusively.

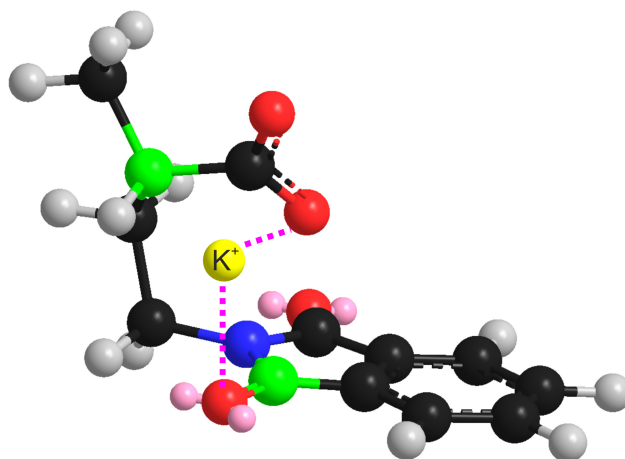


Figure 5-7 Coordination of the carbonyl group and the terminal carboxylate to the potassium cation in **N-GABA-CH₃**. The green color designates the two carbon atoms participating in the C-C bond formation (black = carbon, red = oxygen, grey = hydrogen, pink = lone pairs, yellow = potassium cation).

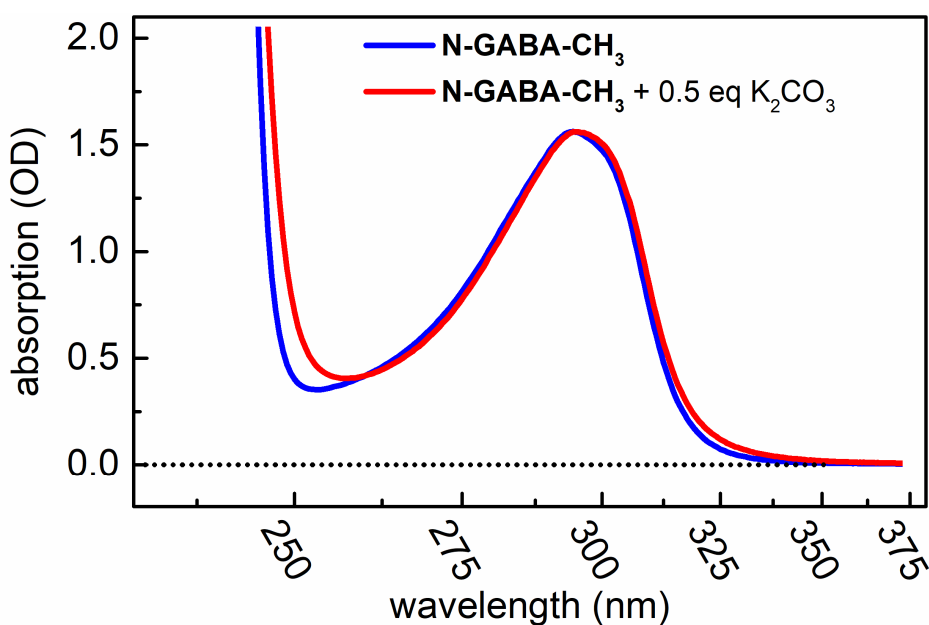
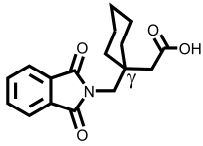
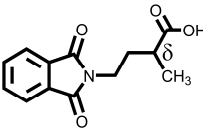
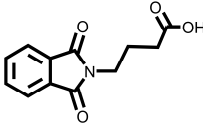


Figure 5-8 Spectral changes of 850 μM **N-GABA-CH₃** upon addition of K_2CO_3 in acetonitrile/water solvent mixture in ratio 3:1.

Interestingly, the 0.5 eq of the additive appears to be in a sufficient amount for a successful reaction. This leads to the tentative conclusion that the potassium cation coordinates at least one more molecule. This theory would agree with the observations from the crystal analysis in ref. [Oel01] in which one potassium cation coordinates in pentagonal bipyramidal fashion two water molecules, three carboxylic O atoms, and two carbonyl O-atoms. Hence, the coordination to two **GABA** derivatives could be plausible.

The RQYs of three different GABA derivatives are summarized in Tab. 5-3. The highest RQY of 48.7% shows the GABA derivative with a methyl group in the δ -position. It is reasonable to assume, that the methyl group contributes to a stabilization of the geometrical arrangement required for a successful ring annulation, since the RQY of the parent **N-GABA** without any side substituents shows a lower RQY of 34%. A reduced RQY of 14.7% is observed for a GABA derivative with a cyclohexyl group in the γ position. In contrast to the other two species, the cyclohexyl moiety is rather bulky and may complicate the pre-orientation phase of the photoinduced process. Noteworthy, the degassing of the reaction mixture seems to have no influence on the RQY despite of the triplet intermediate as observed for the parent **N-GABA** molecule.

Table 5-3 RQY of GABA derivatives with 0.5 eq of potassium carbonate in acetonitrile/water = 3:1 under irradiation with 305 nm LED.

	conc. ($\mu\text{mol/L}$)	P_{ill} (mW)	RQY (%)
	85	7.90	10.4
N-GABA-CHX	859	10.65	14.6
	45	5.90	41.3
N-GABA-CH₃	905	4.25	48.7
	45	3.88	34.0
N-GABA	900	1.39	34.0
	950	4.24	34.4*

* degassed with Argon

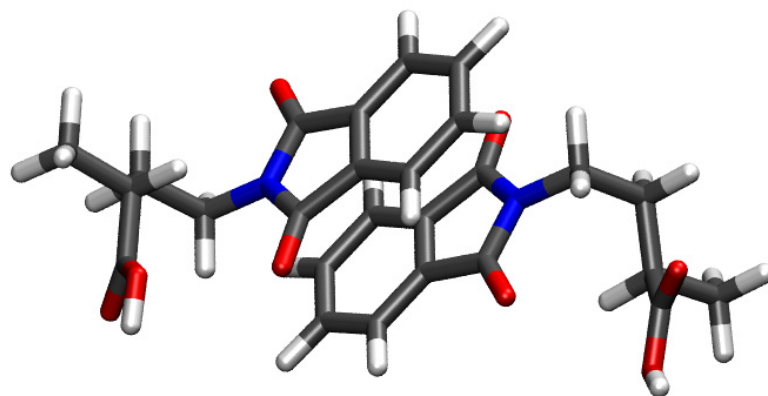


Figure 5-9 Predicted non-covalent dimer for **N-GABA-CH₃** based on M06-2X/aug-cc-pvdz + D3 + PCM (Acetonitril) level of theory (with kind permission of the de Vivie-Riedle research group).

Interestingly, the RQY appears to be concentration dependent. The RQY at concentrations in the region of 1 mM is by several percent higher than the RQY determined from experiments with a concentration of around 50 μ M. The increased RQY at higher concentration could be related to the formation of dimers. According to DFT calculations (M06-2X/ aug-cc-pvdz with the D3 version of Grimme's dispersion and polarizable continuum model), a non-covalent dimer in antiparallel arrangement of the phthalimide moieties is predicted (see Fig. 5-9). The combination of dimer formation and coordination with potassium cations appears to create more favorable conditions for the ring annulation. Additionally, the concentration dependent lifetime of the triplet state was already observed in ref. [Rei19b] and hence it can be deduced, that the concentration has an impact on the photoreaction efficiency.

5.3 Transient absorption measurements

In order to give a deeper insight into the reaction mechanism of the GABA derivatives, a time resolved spectroscopy for the parent molecule **N-GABA** in the ns/ μ s regime was performed. The transient absorption data collected after 280 nm excitation with 2.5 ns pulses are shown in Fig. 5-10. Hereby, a strong excited state absorption (ESA) signal around 330 nm overlaps with the ground state bleach (GSB) at 295 nm. The reactant and product spectrally overlap in this aforementioned region. Since the molar absorptivity of the reactant is factor of 4 stronger, the GSB eventually becomes dominant.

According to the analysis only two different excited states are required to describe the population dynamics. The first state demonstrated with a horizontal green line in Figure 5-10 is

populated immediately after excitation. This singlet state decays with a time constant below the IRF and populates a second state demonstrated with a red horizontal line. The process is here accompanied by a spectral shift and a change of the absorption maximum. This “reactive state” could be a triplet state, since its spectral distribution and shape is similar to those reported for the parent core N-methylphthalimide [Rei19b]. Considering the comparably high RQY of the ring annulation, it is expected that a substantial portion of the excited population decays into the triplet state. For example, the quantum yield for ISC of the parent N-methylphthalimide was determined to be 70% in acetonitrile/water = 1:1 [War06] and thus only a minor part relaxes back into the ground state through fluorescence or internal conversion.

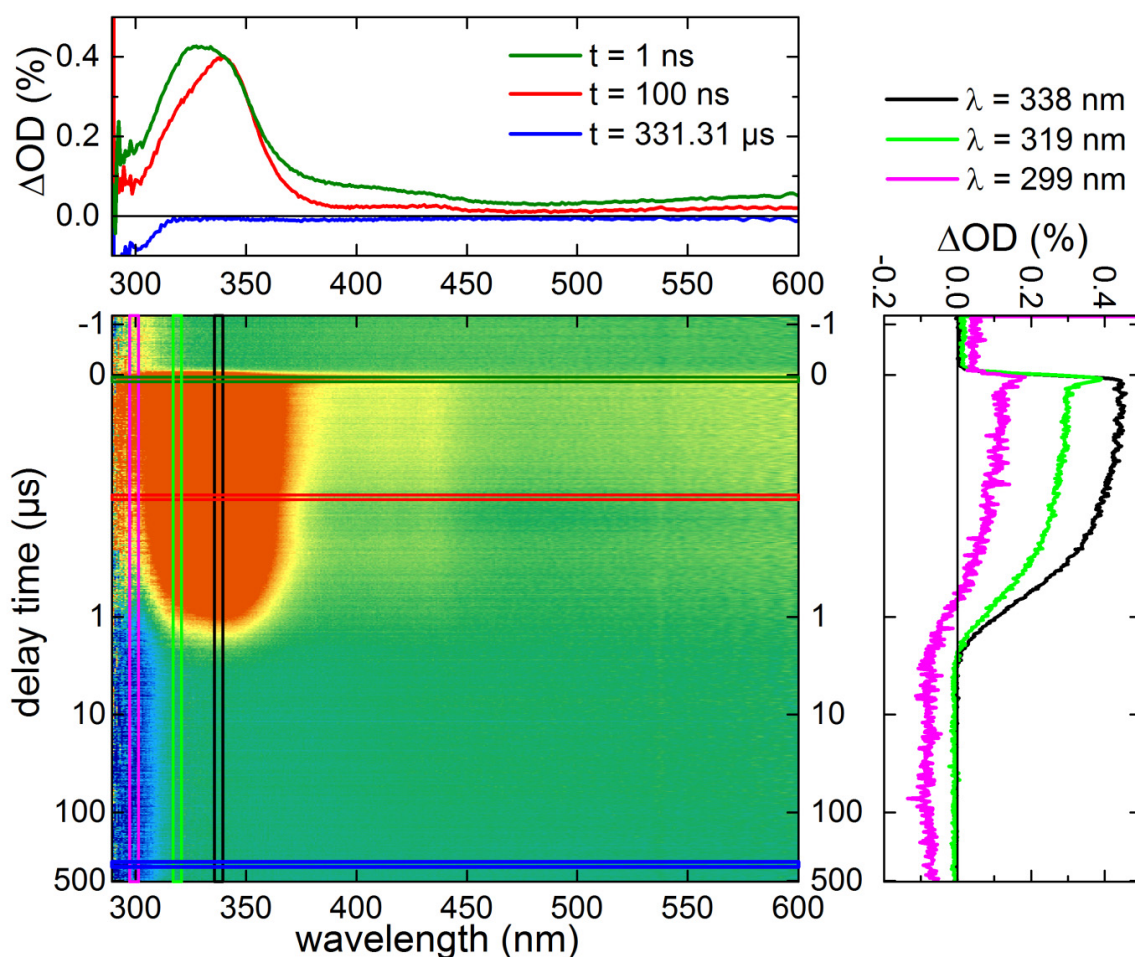


Figure 5-10 Transient absorption for **N-GABA** (2.3 mM) in acetonitrile/water = 3:1 with 0.5 eq K_2CO_3 measured under standard conditions after excitation with a 280 nm pulse in a 1 mm flow cell. Cold colors (blue) correspond to decreased absorption due to the ground state bleach. Warm colors (red) signalize increased absorption originating from excited state absorption.

However, the aforementioned “reactive state” does not have to be a clean covalent triplet state. Another reasonable option is a biradical intermediate originating from the PET process. This assumption is supported by the relatively long lifetime of the intermediate with 710 ns that results from the global fit analysis. At longer delay times only the negative GSB signal remains, which signalizes that the product formation is completed. In contrast to other reported reactions showing a cyclization time constant of 100 ns [Mat13] the present value of 710 ns is unexpectedly high. The long lifetime could also arise from the required pre-coordination to the potassium cation as well as a geometrical post-arrangement required to expell the K^+ cation and to stabilize the new ring. The open question remains, if the decarboxylation take place in the sub-ns regime through a conical intersection or the photoprocess is rather a concerted reaction in which the decarboxylation and ring annulation occurs in a single step.

In summary, the N-phthaloylated GABA derivatives react upon illumination with 300 nm light into the cyclization product as long as a solvent acetonitrile/water mixture 3:1 and 0.5 eq or more of potassium carbonate are used. The RQY of this reaction spans from 15% to about 48% which corelates with the type of substituents on the GABA chain. A varied amount of the K_2CO_3 has an impact on the RQY and presence of the side reaction. The careful evaluation of the QYDS data enables to calculate the RQY of both possible reactions and hence it provides a valuable information about the reaction mechanism.

From the mechanistic point of view the photoinduced reaction starts with a very short lived singlet state that decays either back to the ground state or to the “reactive state” with either triplet or diradical character. The longest decay constant for the **N-GABA** substrate was determined to be 710 ns, that is attributed to the ring annulation. In contrast to the previous work [Oel02, Gri07], the ring annulation is photoinduced without need of triplet sensitizers.

Appendix for Chapter 5

Appendix 5-A

NMR Analysis

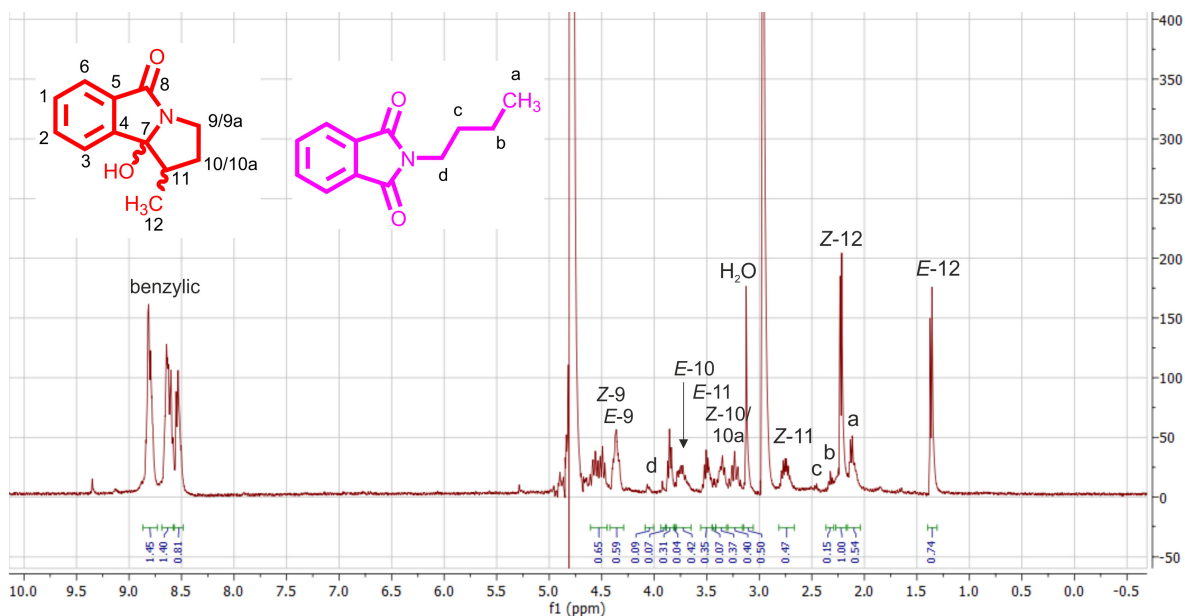


Figure 5-A NMR spectrum of cyclic product and side product resulting from illumination of **GABA-CH₃** with 0.1 eq of potassium carbonate until PSS in deuterated acetonitrile/water solution 1:3. The mainly formed product with 83.5% is the cyclization product (red), the amount of the minor side product (magenta) is 16.5%. No reactant signals are identified.

Appendix 5-B

Spectral decomposition

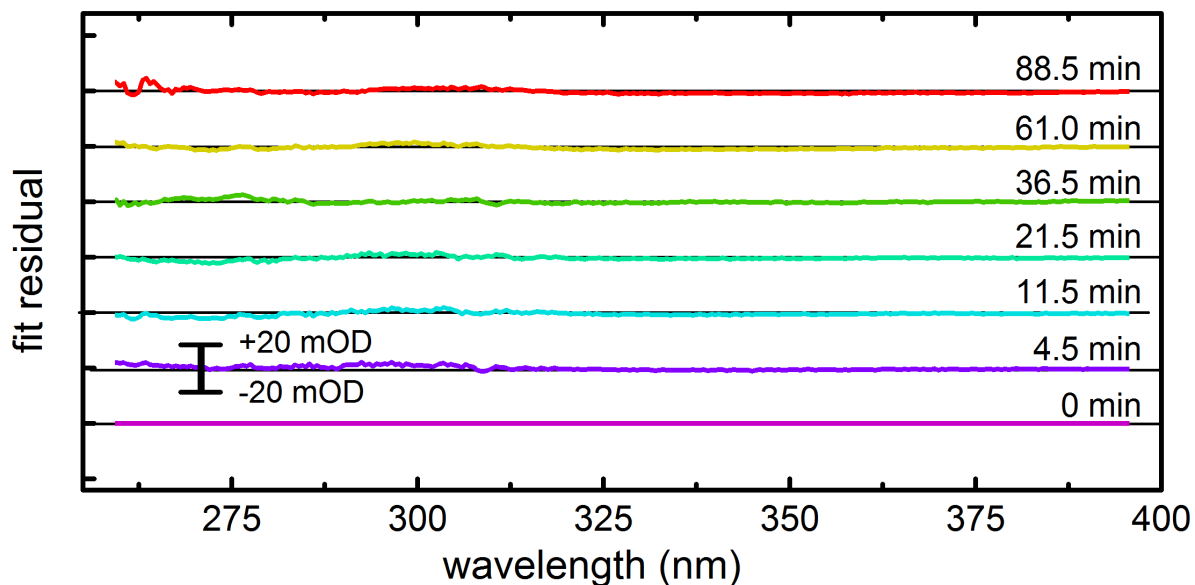


Figure 5-B1 Fit residuals resulting from projection of the measured UV/vis data onto basis spectra for **GABA-CH₃** with 0.01 eq of potassium carbonate from Fig. 5.4 right.

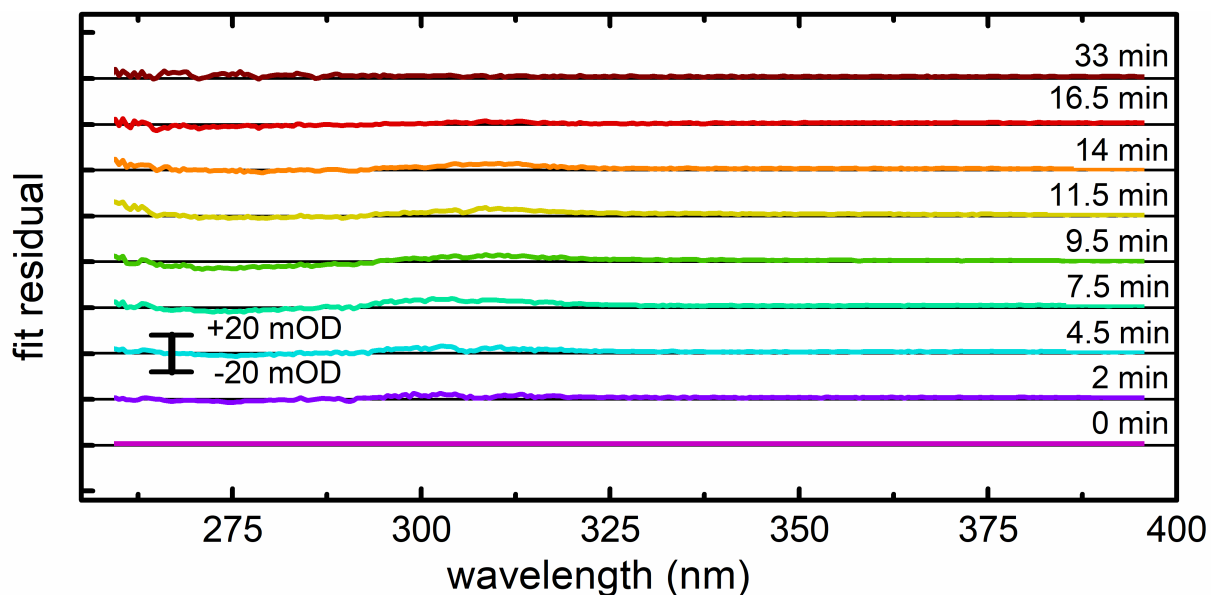


Figure 5-B2 Fit residuals resulting from projection of the measured UV/vis data onto basis spectra for **GABA-CH₃** with 0.1 eq of potassium carbonate.

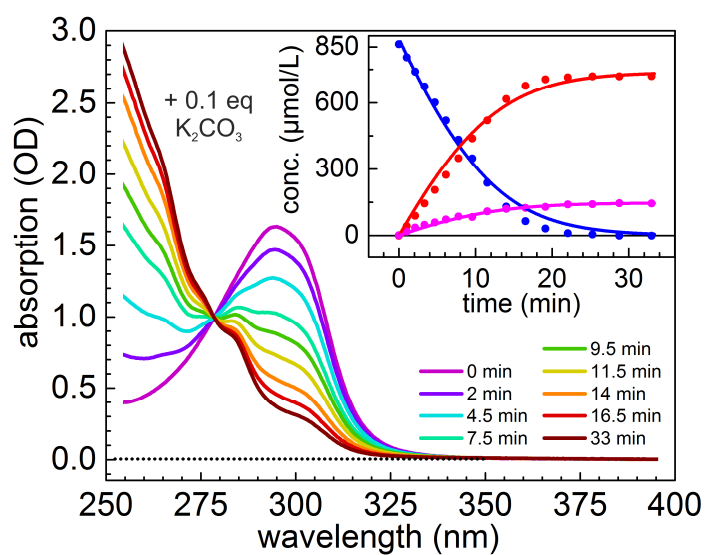


Figure 5-B3 Selected UV/vis spectra of **GABA-CH₃** with 0.1 eq of **K₂CO₃** under illumination with 305 nm light with illumination power of 4.49 mW. The inset shows the time dependent concentration of reactant and products with the solid lines representing the numerical fit.

Appendix 5-C

pH dependence

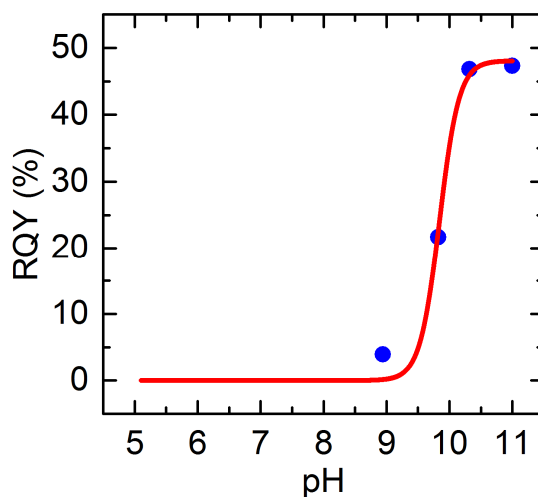
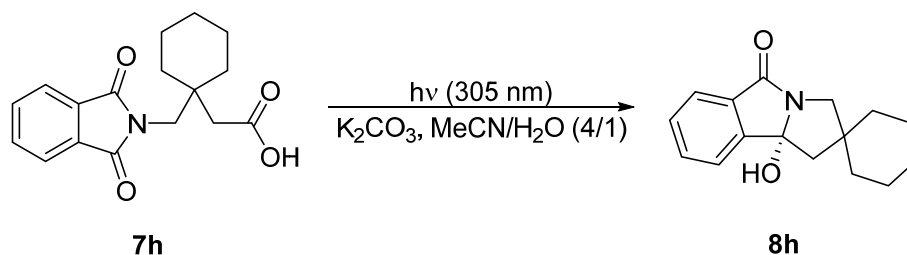


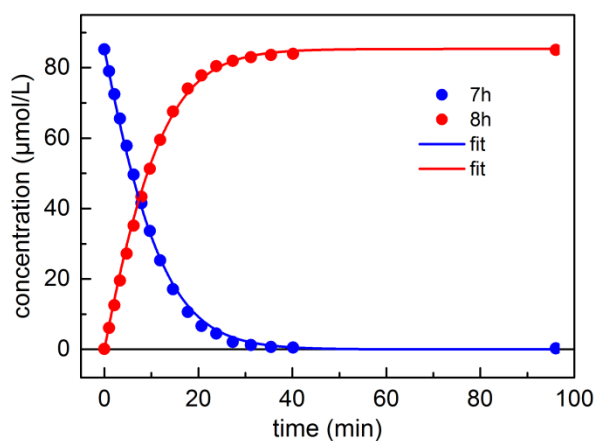
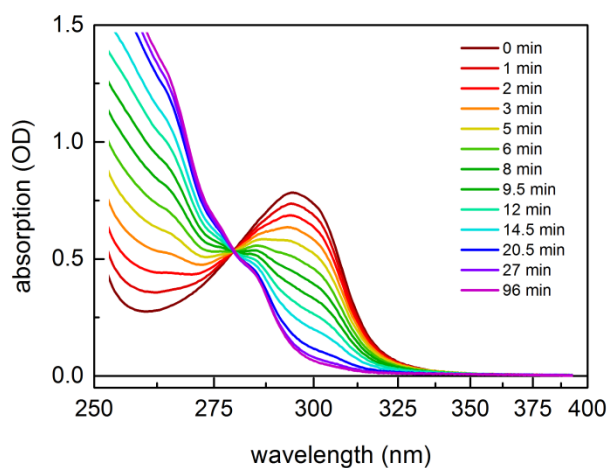
Figure 5-C pH dependence of **GABA-CH₃** under illumination with 305 nm light

Appendix 5-D

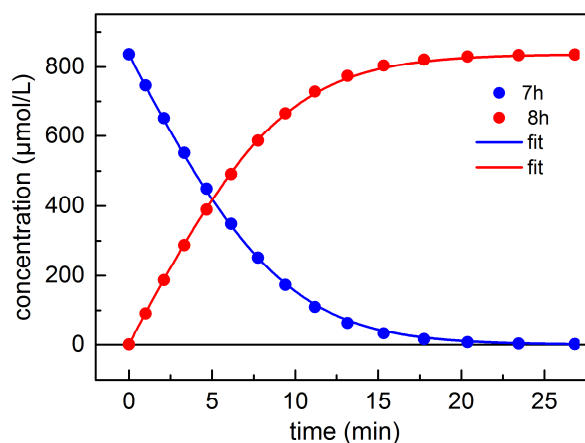
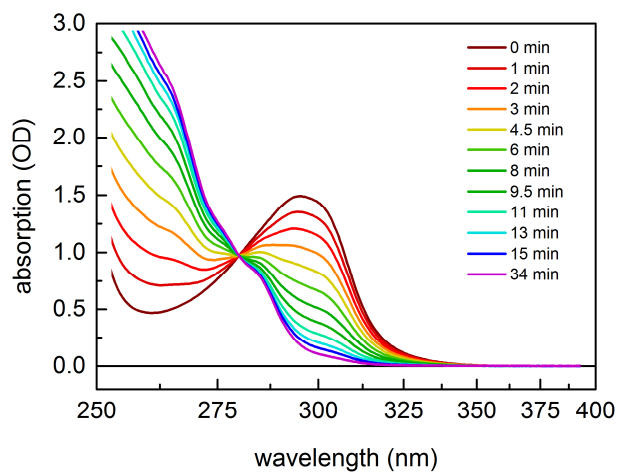
QYDS measurements

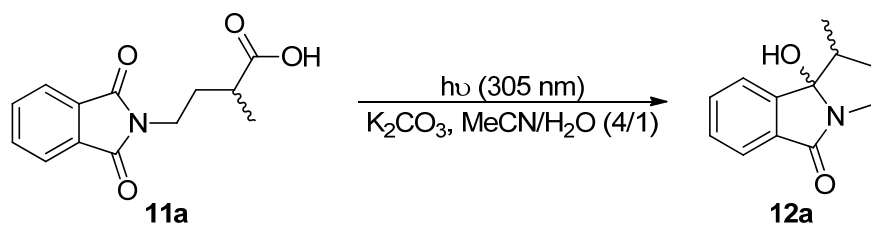


LG Innotek 305 nm
concentration = 85 μM
 $P_{\text{ill}} = 7.90 \text{ mW}$
QY = 10.4%

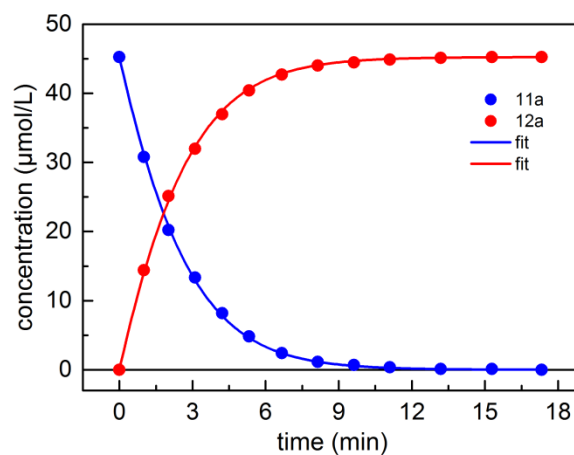
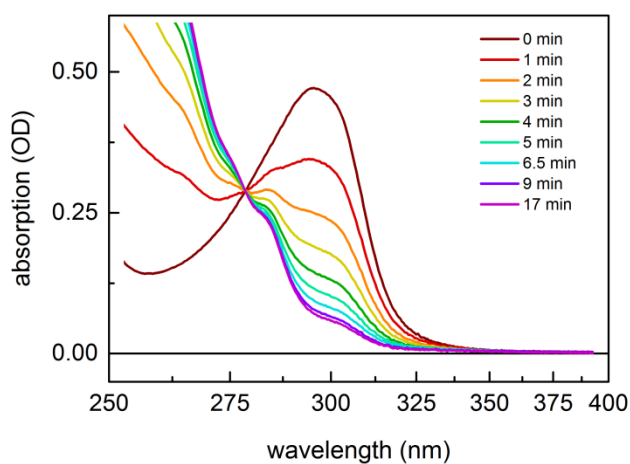


LG Innotek 305 nm
concentration = 859 μM
 $P_{\text{ill}} = 10.65 \text{ mW}$
QY = 14.7%

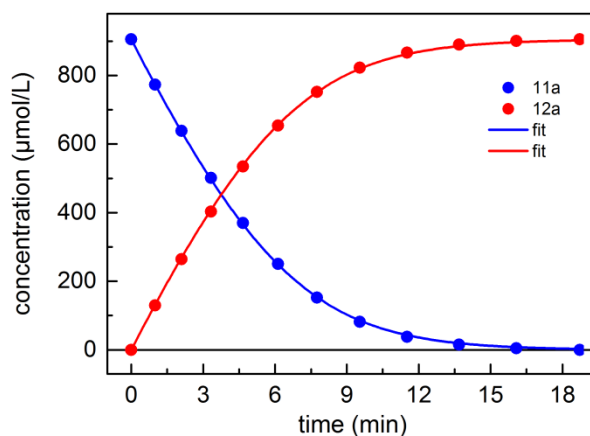
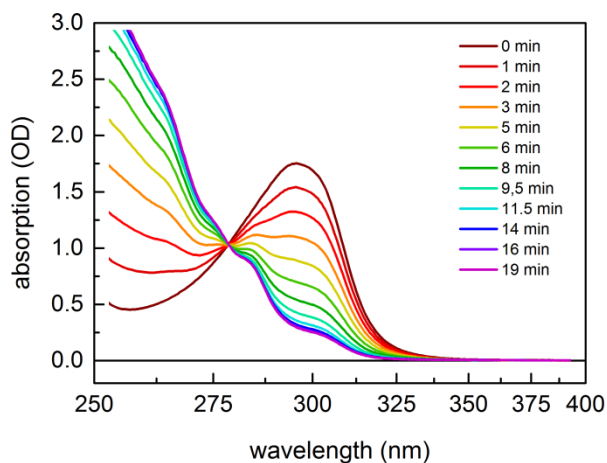


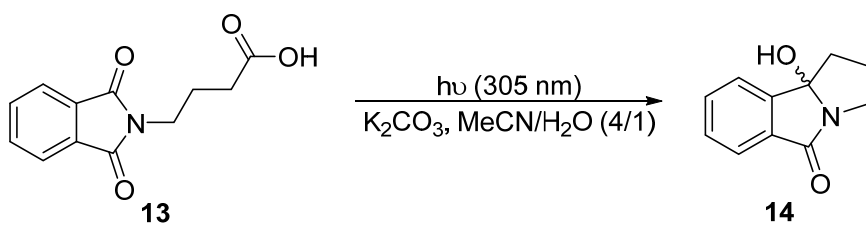


LG Innotek 305 nm
 concentration = 45 μM
 $P_{\text{ill}} = 5.90 \text{ mW}$
QY = 41.3%

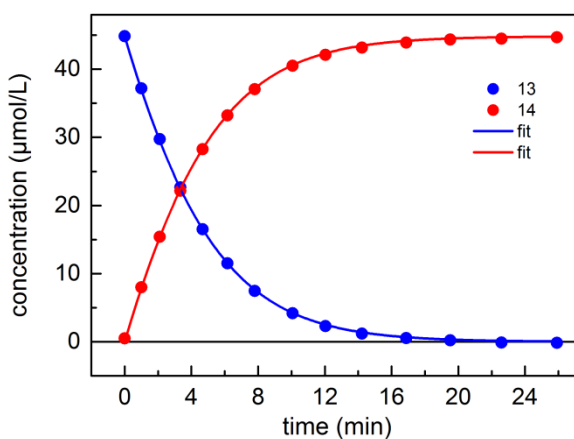
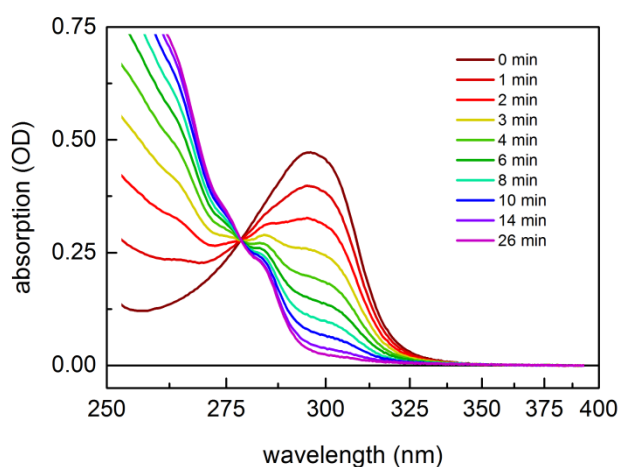


LG Innotek 305 nm
 concentration = 905 μM
 $P_{\text{ill}} = 4.25 \text{ mW}$
QY = 48.7%

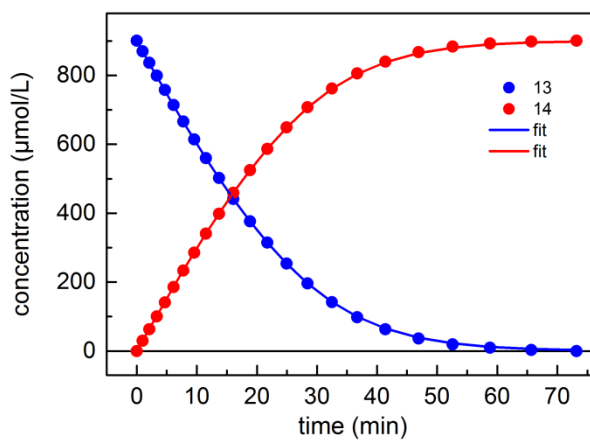
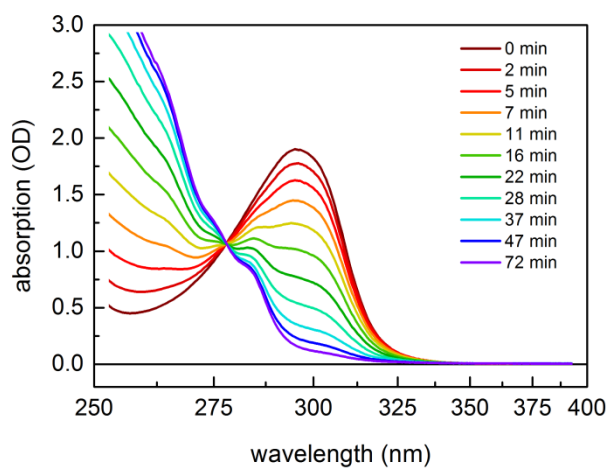




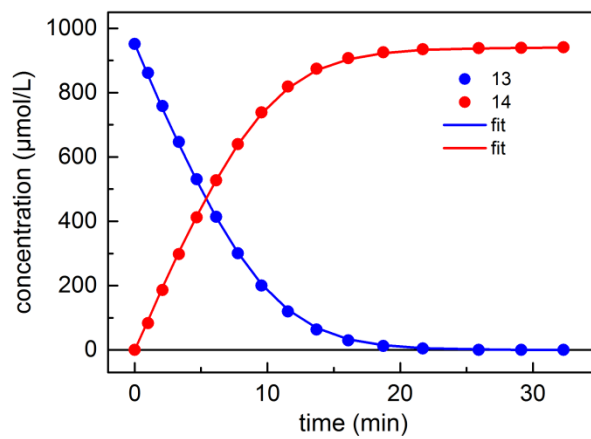
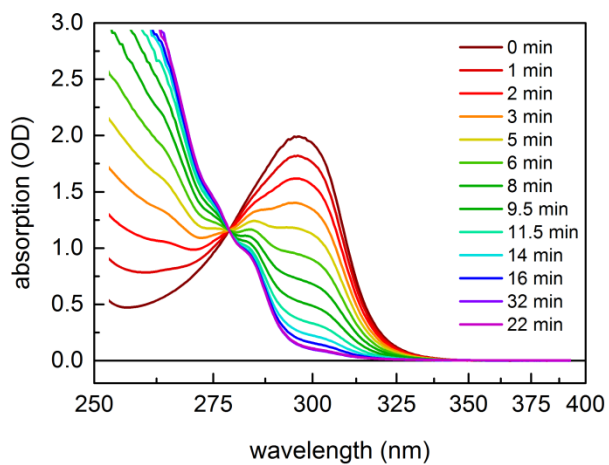
LG Innotek 305 nm
 concentration = 45 μM
 $P_{\text{ill}} = 3.88 \text{ mW}$
QY = 34.0% (standard conditions)



LG Innotek 305 nm
 concentration = 900 μM
 $P_{\text{ill}} = 1.39 \text{ mW}$
QY = 34.0% (standard conditions)



LG Innotek 305 nm
concentration = 950 μM
 $P_{\text{ill}} = 4.24 \text{ mW}$
QY = 34.4% (degassed with argon)



6. Comprehensive study of photo-induced properties of Ni- and Zn-Mabiq

The following chapter is reproduced from reference [Lau21] with permission from the Royal Society of Chemistry: “*The central role of the metal ion for photoactivity: Zn- vs. Ni-Mabiq*” by R. Lauenstein, S. L. Mader, H. Derondeau, O. Z. Esezobor, M. Block, A. J. Römer, C. Jandl, E. Riedle, V. R. I. Kaila, J. Hauer, E. Thyrhaug, C. R. Hess. *Chem. Sci.* **2021**, *12*, 7521-7532.

6.1 Introduction

In recent years, photoredox catalysis has become an important segment of organic chemistry [Cri20, Rom16, Sha16]. Most photocatalysts are based on a noble metal core (Rb, Ir) or other heavy metal atoms (Os, W and Re) [Rot16, Tuc12b, Koi14, Bue17]. The use of the late first row transition metals as new photocatalysts would provide a much more cost-effective and earth-abundant alternative [Gru18].

Motivated by the above requirements, the focus of this study is on the characterization of **Ni-Mabiq** and **Zn-Mabiq** photosensitizers. Both species are characterized using spectroscopic methods.

The molecular dynamics of **Ni-Mabiq** and **Zn-Mabiq** are studied by transient absorption spectroscopy. In addition, the measurement of the reaction quantum yield using the Quantum Yield Determination Setup (QYDS) is discussed in detail. The QYDS approach allows not only quantification of the efficiency of **Ni-Mabiq** and **Zn-Mabiq** photosensitizers in various photoinduced reactions, but it is also an elegant method that provides qualitative analysis of the chemical reactions (identification of side products) in only one measurement.

The aim of this work is to give a deeper understanding of the photochemical and photophysical properties and to compare and to explain their different chemical behavior and photoactivity.

6.2 Molecular and electronic structure

The parent molecule is known as uncoordinated **H-Mabiq** and was originally synthesized by von Zelewsky [Mue88]. His goal was to develop a bimetallic system with photocatalytic properties [Mue88, Put15]. The metal-free **H-Mabiq** can be modified by coordination with a metal cation, e.g., Co [Mue88], Fe [Ban09] or Ni [Gru18].

In this work, the **Ni-Mabiq** - $[\text{Ni}^{\text{II}}(\text{Mabiq})\text{Otf}]$ and **Zn-Mabiq** - $[\text{Zn}^{\text{II}}(\text{Mabiq})\text{OTf}]^1$ systems are studied. These are based on the macrocyclic biquinazoline ligand, with the triflate (OTf) in the apical position. The chemical and molecular structures are shown in Fig. 6-1.

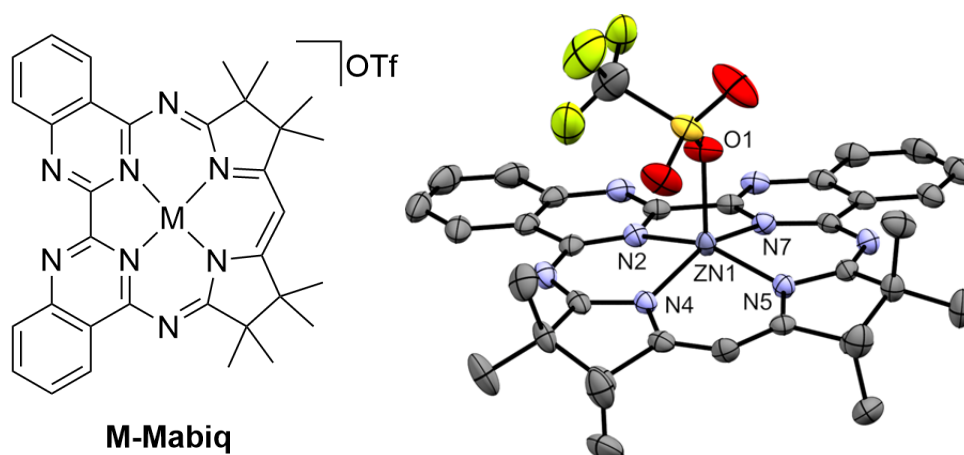


Figure 6-1 Chemical (left) and molecular structure (right) of the **M-Mabiq** complex. The abbreviation “M” corresponds to metal, in this case it is Ni, Zn, Co and Fe. The colored structure at the top right is the triflate (OTf).

6.3 Electronic properties (UV/vis spectra)

The UV/vis spectra of the **Ni-Mabiq** and **Zn-Mabiq** compounds in a solvent mixture of THF and MeCN (1:1) are shown in Fig. 6-2. The shape and position of the absorption bands are comparable to other metal (M) **M-Mabiq** systems [Ban09, Put15, Sta18b]. The first absorption band in the green/blue region is related to **Mabiq- π - π^*** transitions [Mue88]. The second absorption band is in the UV region.

Since no spectral shift is observed when using different solvents, it can be concluded that the electronic transitions are ligand localized and have no charge transfer character (see Appendix 6-A).

¹ **Mabiq** = 2-4:6-8-bis(3,3,4,4-tetramethyldihydropyrrolo)-10-15-(2,2-biquinazolino)-[15]-1,3,5,8,10,14-hexaene1,3,7,9,11,14-N₆)

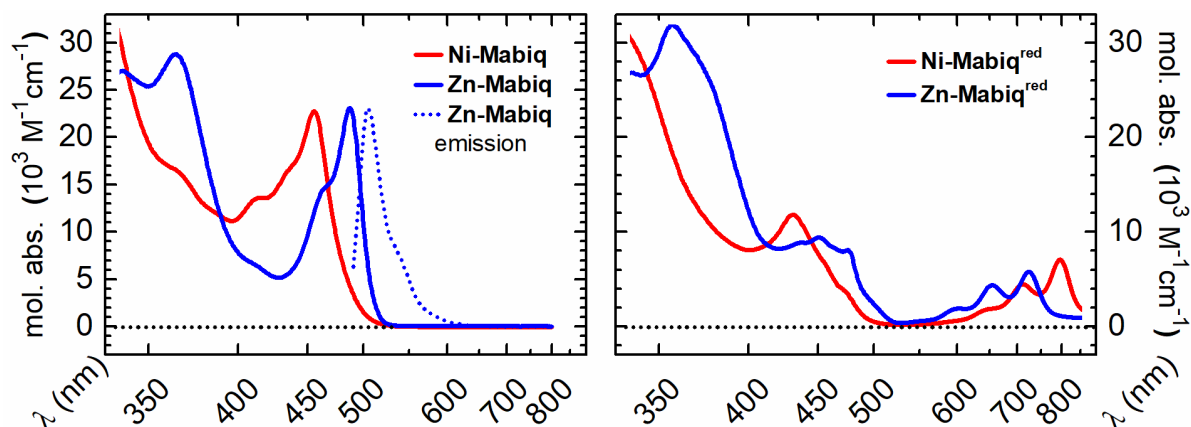


Figure 6-2 UV/vis spectra of **Ni-** and **Zn-Mabiq** (left) in the solvent mixture THF/MeCN = 1:1 with the correspondent photoreduced form (right). The emission spectrum of **Zn-Mabiq** is denoted by a dotted line.

The detectable photoluminescence of **Zn-Mabiq** is shown in Fig. 6-2 on the left. The fluorescence signal (FL) approaches a mirror image of the absorption spectrum. The emission is similar to the uncoordinated **H-Mabiq** system reported in references [Sta18b, Lau21]. It is expected that the lack of photoluminescence of **Ni-Mabiq** is related to a very low FLQY of less than 10^{-4} .

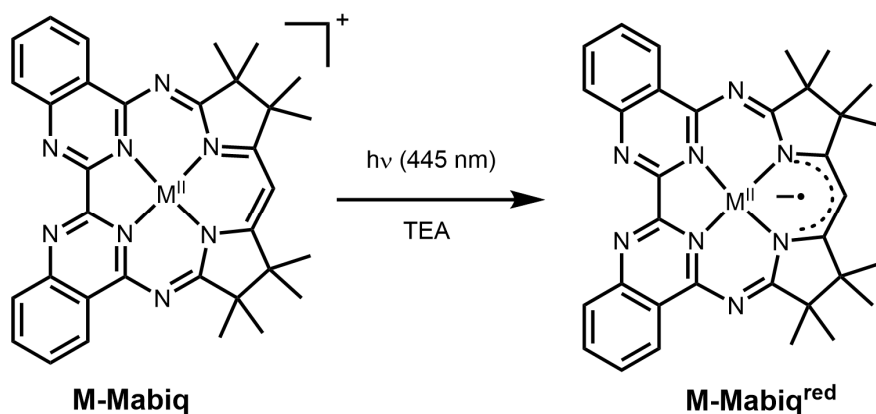


Figure 6-3 **M-Mabiq** (M = Fe, Co, Ni, Zn) can be photoreduced upon illumination with light and in presence of a sacrificial electron donor.

M-Mabiq can be photoreduced to the one-electron reduced form **M-Mabiq^{red}** if a suitable quencher, e.g., triethylamine (**TEA**), is present and royal blue light is used ($\lambda_{\text{central}} = 445$ nm, OSRAM 455 nm, LD-CQ7P-1U3U, hereafter referred to as LED 455 nm). The reduced form **M-Mabiq^{red}** has an additional spectral feature around 750 nm, see Fig. 6-2 right. The

chemical structure of the photoreduced form is shown in Fig. 6-3 right. The photoreduced forms are chemically stable under exclusion of oxygen.

6.4 Reaction quantum yield of the photoreduction

Since photoreduction appears to be an important step in a photocatalytic reaction [Gru18], it is reasonable to approach the issue of how effective photoreduction is - in means of the reaction quantum yield (RQY). The Quantum Yield Determination Setup (QYDS) used [Meg10, Vol19] not only provides absolute numbers for the RQY, but also helps to qualitatively characterize the reaction. Hence, it provides a deeper understanding of the reaction mechanism. According to the results summarized in Tab. 6-1, the **Fe-**, **Co-** and **Ni-Mabiq** have a very modest RQY, which is in the range of 10^{-4} (see Appendix 6-B for measurement data). Since the RQY for **Zn-Mabiq** (see Fig. 6-4) is three orders of magnitude higher (RQY = 0.79), it can be assumed that the character of the metal center has a large impact on the photochemical and photophysical properties.

Table 6-1 Summary of reactions conditions with resulting RQY for photoreduction of **M-Mabiq** in the solvent mixture THF/MeCN =1:1.

	Fe-Mabiq	Ni-Mabiq	Co-Mabiq	Zn-Mabiq
conc. (M-Mabiq)	66 μ M	67 μ M	77 μ M	69 μ M
conc. (TEA)	33 mM	33.5 mM	38.5 mM	0.345 mM
P_{illum}	245 mW	245 mW	245 mW	1.4 mW
RQY	1.8×10^{-4}	2.9×10^{-4}	3.6×10^{-4}	0.79



increasing RQY

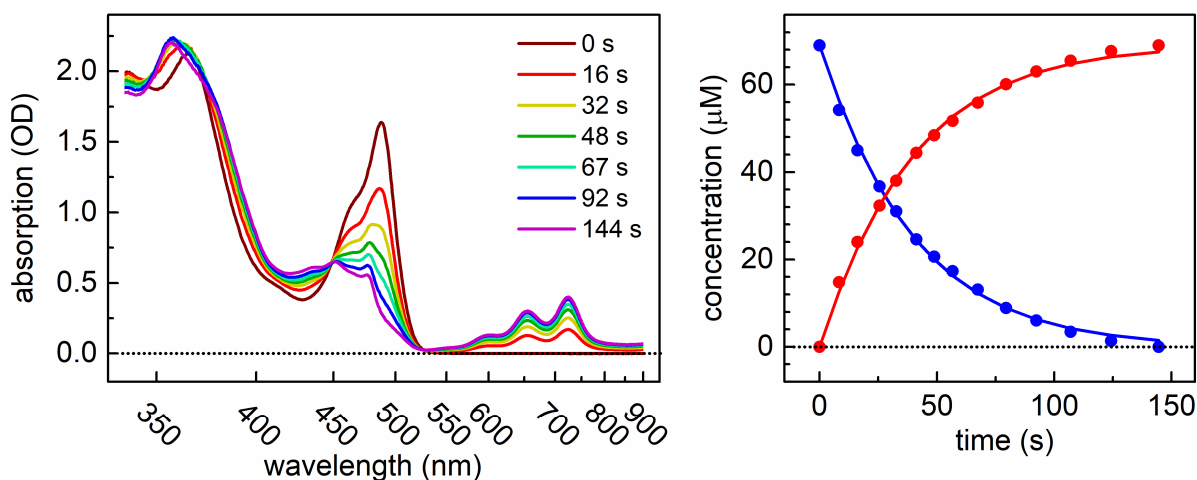


Figure 6-4 (left) Spectral changes of **Zn-Mabiq** (69 μM) mixed with **TEA** (345 μM) upon illumination with a 455 nm LED with the power in the sample of 1.4 mW. The volume of the solution in a 10 mm cuvette was 2 mL. (right) Time evolution of the concentrations during the illumination and numerical simulation (fit). The RQY is 0.79.

The very high RQY for **Zn-Mabiq** may be related to the ability of **TEA** to coordinate to the Zn-complex, as observed in [Lau21]. However, **TEA** pre-coordination may also contribute to the photoinstability of the generated product **Zn-Mabiq^{red}**, since the prolonged illumination leads to degradation of the sample. In this process, the absorption band around 600 nm disappears and a new absorption feature below 500 nm appears (see Appendix 6-C). The decomposition is proven to be light-driven, as the chemically synthesized **Zn-Mabiq^{red}** is stable as long as no photoexcitation is applied. The **Fe-**, **Co-** and **Ni-Mabiq** are photostable under these reaction conditions.

In order to investigate the role of the sacrificial donor two other quenchers with comparable oxidation potentials to **TEA** were examined. The first is dimethylaniline (**DMA**) and the second one the bulky N-(2,4,6-trimesitylbenzyl)dicyclohexylamine (**bulky**)². Both new quenchers were studied in the reaction with **Ni-Mabiq** only. However, as well as in the previous case of **TEA**, no evidence for the pre-coordination to **Ni-Mabiq** is observed in the ¹H-NMR analysis [Lau21].

² E^{ox} (vs. SCE, MeCN): **DMA** = ca. 0.7 V [Tin20], **bulky** = 0.78 V [Gru18].

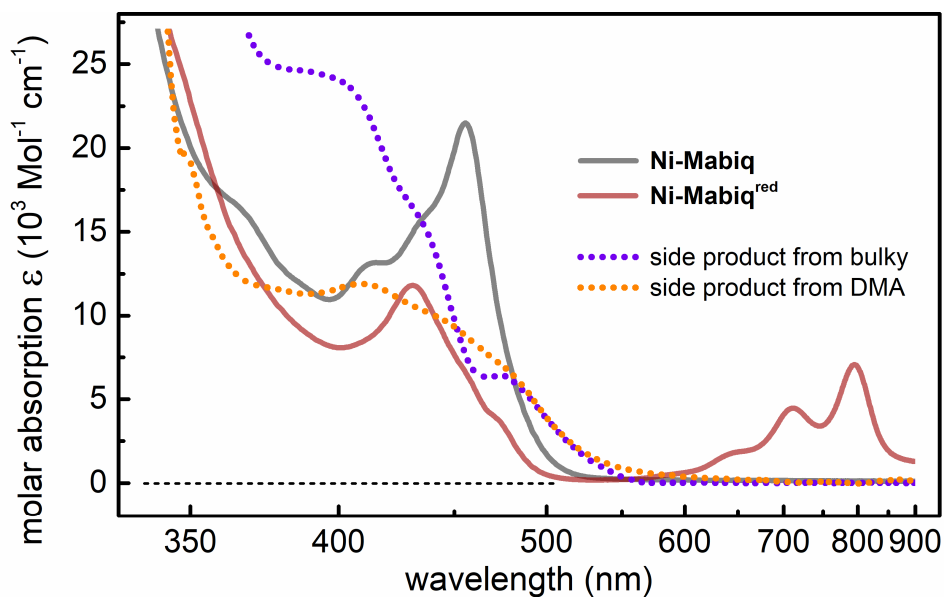


Figure 6-5 Molar absorption of **Ni-Mabiq**, **Ni-Mabiq^{red}** and side products in THF/MeCN = 1:1. The spectrum of the side product was extracted according to the TEM method [Mic70a, Mic70b, Mic87]. The violet dotted trace corresponds to the side product resulting from the photoreduction of **Ni-Mabiq** and the **bulky** quencher. The orange dotted line shows the side product originating from the photoreduction of **Ni-Mabiq** with **DMA**.

The photoreduction of the two new quenchers is shown in Fig. 6-7 and Fig. 6-8. Unlike previous photoreactions, a simple reaction model of **Ni-Mabiq** to **Ni-Mabiq^{red}** cannot explain the observed trend in the data. Apparently, a third species is observed, referred to as a side product, which increases in concentration with time.

For further analysis, the molar absorptivity of the side product must be precisely known. The molar absorptivity can be extracted from the photostationary state spectra using the TEM method developed by Thulstrup, Eggers, and Michl [Mic70a, Mic70b, Mic87] (for more details, see Chapter 2). The extracted molar absorptivities of the side products are shown in Fig. 6-5. The side products have absorption bands between the deep UV and the 500 nm region, and the spectrum extracted from the experiment with DMA (orange line in Fig. 6-5) is very similar to the spectrum of the uncoordinated **H-Mabiq** [Mue88].

The molar absorptivities of all three species are subsequently used for deconvolution onto basis spectra. The residuals of this linear combination lie within experimental error as shown in Fig. 6-7 and Fig. 6-8 in the middle panel.

The ability of the side product to absorb part of the excitation light is implemented into the kinetic model and considered in the determination of the RQY. The scheme shown in Fig. 6-6 allows the direct formation of the main product “MP” and side product “SP” with yields ϕ_1 and ϕ_2 upon excitation of reactant “R”. Since the transformation from “R” to “MP” is by electron transfer, the back transfer with quantum yield ϕ_3 is allowed. Finally, the “MP” can also be photoexcited, according to the overlapping absorption spectra, and produces “SP” with quantum yield ϕ_4 .

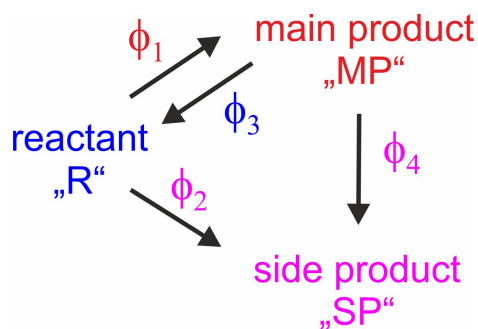


Figure 6-6 Reaction model used for the determination of the RQY. This model considers the creation of the side product from the reactant as well as from the main product. The back reaction to the reactant is allowed only from the main product.

The reaction model in Fig. 6-6 then results in the following system of differential equations:

$$\frac{dN_R(t)}{dt} = \int [-(\phi_1 + \phi_2) \text{Frac}_R(t, \lambda) + \phi_3 \cdot \text{Frac}_{MP}(t, \lambda)] N_{Ph}(\lambda) \cdot A(t, \lambda) d\lambda \quad (6.1)$$

$$\frac{dN_{MP}(t)}{dt} = \int [\phi_1 \cdot \text{Frac}_R(t, \lambda) - (\phi_3 + \phi_4) \text{Frac}_{MP}(t, \lambda)] N_{Ph}(\lambda) \cdot A(t, \lambda) d\lambda \quad (6.2)$$

$$\frac{dN_{SP}(t)}{dt} = \int [\phi_2 \cdot \text{Frac}_R(t, \lambda) + \phi_4 \cdot \text{Frac}_{MP}(t, \lambda)] N_{Ph}(\lambda) \cdot A(t, \lambda) d\lambda \quad (6.3)$$

The more detailed explanation of each term and variable can be found in Chapter 3 and Chapter 5. After the numerical integration (propagation) in Mathcad Prime 5.0 and using the standard least square fitting to find the best values, the resulting RQY are obtained. The results are shown in Figures 6-7 and 6-8 in the bottom panel and summarized in Table 6-2.

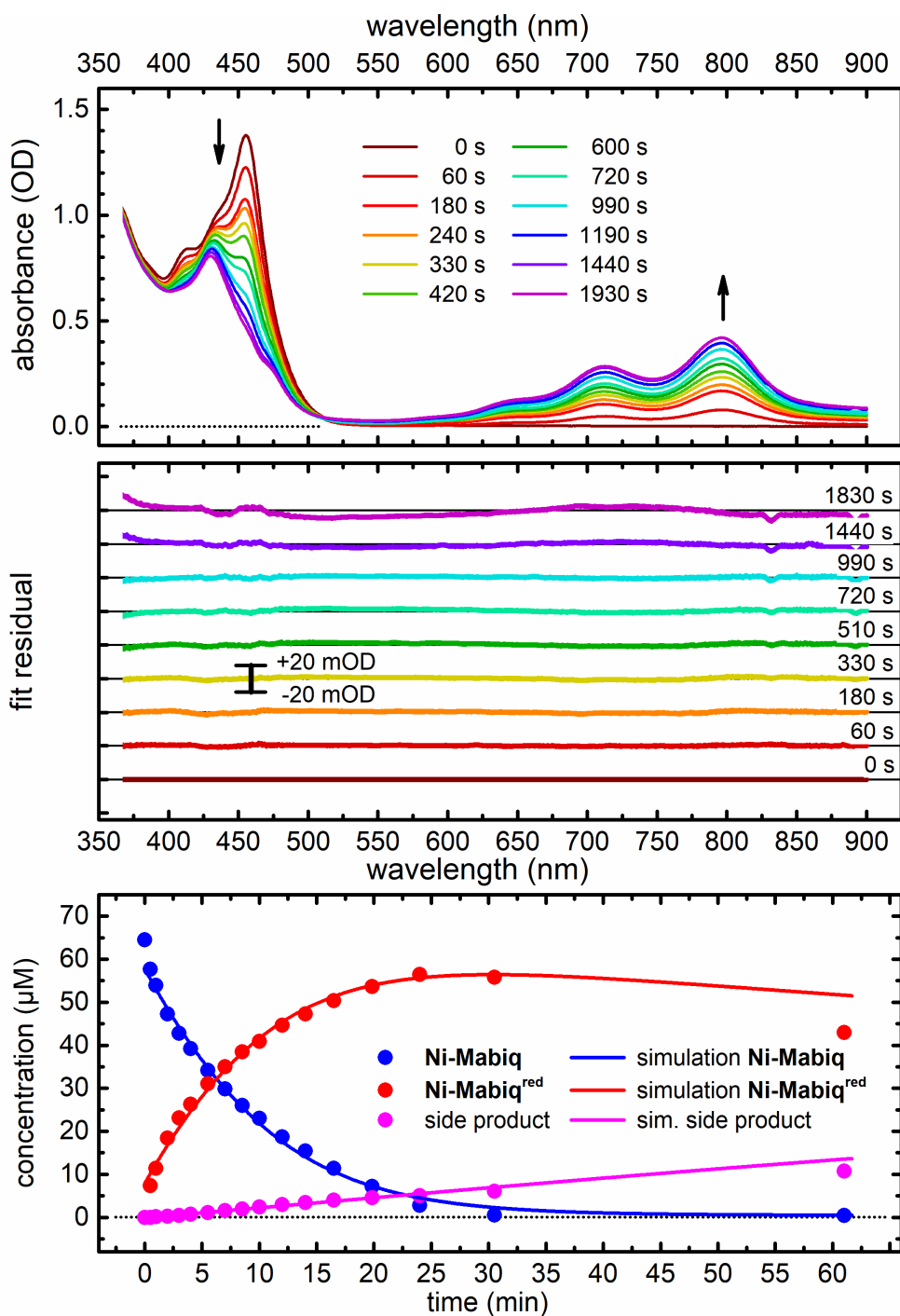


Figure 6-7 (top) Spectral changes during the photoreduction of **Ni-Mabiq** (67 μM) by the **bulky** quencher (33.5 mM) in THF/MeCN = 1:1 upon 455 nm excitation with a power of 245 mW in 10 mm cuvette and volume 2 mL. (middle) Fit residuals resulting from projection of the measured UV/vis data onto basis spectra. (bottom) Time evolution of the concentrations with the reaction quantum yields of $\phi_1 = 2.1 \times 10^{-4}$, $\phi_2 = 0.09 \times 10^{-4}$, $\phi_3 = 0.04 \times 10^{-4}$ and $\phi_4 = 0.1 \times 10^{-4}$. The side product amounted to 20% of the reaction mixture upon 61 min of illumination.

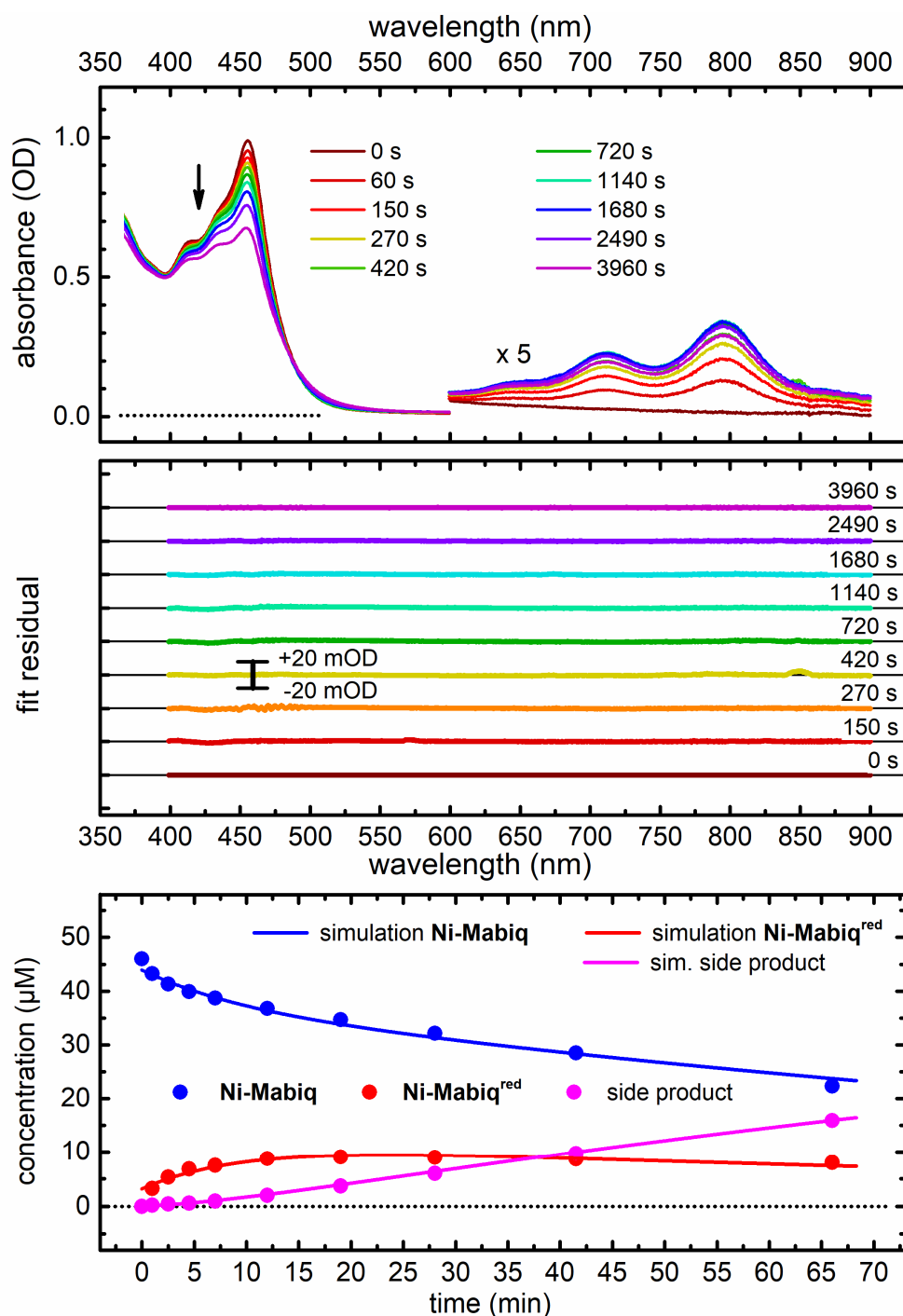


Figure 6-8 (top) Spectral changes during the photoreduction of **Ni-Mabiq** (51 μM), by **DMA** (255 mM) in THF/MeCN = 1:1 upon 455 nm excitation with power of 245 mW in 10 mm cuvette and volume 2 mL. (middle) Fit residuals resulting from projection of measured UV/vis data onto basis spectra. (bottom) Time evolution of concentrations with the reaction quantum yields of $\phi_1 = 0.5 \times 10^{-4}$, $\phi_2 = 0 \times 10^{-4}$, $\phi_3 = 2.7 \times 10^{-4}$ and $\phi_4 = 1.1 \times 10^{-4}$. The side product amounted to 34.5% and **Ni-Mabiq^{red}** amounted to 17.4% of the reaction mixture upon 66 min of illumination.

Table 6-2 Summary of the photoreduction quantum yield for **Ni-Mabiq** using various quenchers.

quencher	TEA	DMA	bulky
conc (Ni-Mabiq)	67 μ M	51 μ M	67 μ M
conc (quencher)	33.5 mM	255 mM	33.5 mM
P _{illum}	245 mW	245 mW	245 mW
RQY photoreduction	2.9×10^{-4}	0.5×10^{-4}	2.1×10^{-4}
RQY backreaction	-	2.7×10^{-4}	0.04×10^{-4}
RQY side product from reactant	-	-	0.09×10^{-4}
RQY side product from product	-	1.1×10^{-4}	0.1×10^{-4}
degassed	yes	yes	yes
chemical yield main product	100%	17.4%	ca. 75%
chemical yield side product	0%	34.5%	25%
concentration substrate after reaction	0%	48.1%	0%

The results show that the quenching reaction from **Ni-Mabiq** to **Ni-Mabiq^{red}** is dominant with the quantum yield of 2.1×10^{-4} when the **bulky** quencher is used (see Fig. 6-7). The main channel for the formation of the side product results from the repeated excitation of the product **Ni-Mabiq^{red}**. The order of magnitude for the photoinduced backreaction is comparable with the formation of the side product directly from the reactant. The further illumination would result in the increasing concentration of the side product and decreasing concentration of the desired **Ni-Mabiq^{red}**.

The photoinduced reduction using **DMA** as a quencher (see Fig. 6-8) reveals a predominant backreaction from **Ni-Mabiq^{red}** to **Ni-Mabiq** with a quantum yield of 2.7×10^{-4} . This value is one order of magnitude higher than the classical light promoted reduction from **Ni-Mabiq** to **Ni-Mabiq^{red}**. The side product is formed only by further excitation of the product molecules. The formation of the side product directly from the reactant can be regarded as negligible.

Since the repeated excitation of the photoreduced form appears to be an important issue in

the investigated photocatalytic reaction, it is reasonable to optimize the choice of the excitation light. An appropriate choice of LED can selectively reduce the amount of excited product molecules. For this purpose a Mathcad program was developed that considers the fraction of the excited reactant molecules to excited product molecules. The program can even consider filters that narrow the original LED spectrum. The comparison of four different LEDs are shown in Fig. 6-9.

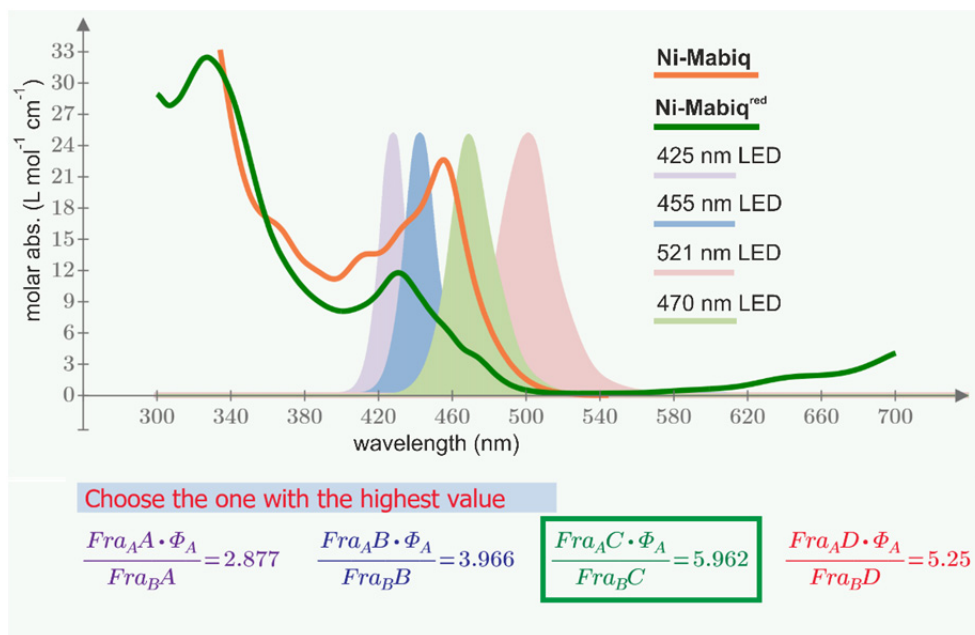


Figure 6-9 Screenshot of Mathcad program developed for choosing an optimal wavelength to excite minority of the created product. The most suitable LED is “470 nm” and it is highlighted by the green window.

As shown in Fig. 6-9, the optimal excitation light is the LED with the central wavelength of 468 nm (470 nm, Osram, LBCP7P-GYHY). Even more favorable would be implementation of a bandpass filter 470 nm with a FWHM of 10 nm (hard coated, OD 4.0, SN#65-144, Edmund Optics, Inc.).

In summary, the determination of RQY using the QYDS approach not only leads to the absolute number of the RQY, but also qualitatively characterizes the data, as shown here. Such additional information allows a deeper insight into the photochemical process and thus the tuning and optimization of the reaction conditions to exploit the full potential of the catalyst.

6.5 Ni- and Zn-Mabiq as photocatalyst

In the previous section, the photoreduction of the Ni- and Zn-Mabiq was investigated in a separated reaction since this was discussed as a relevant step in the photocatalytic indole cyclization that will be investigated as followed [Gru18]. The RQY for this photoreaction was reported to be 0.006 in the case of Ni-Mabiq as catalyst [Gru18], while in the case of Zn-Mabiq no product formation is observed, only degradation of the Zn-Mabiq complex occurs [Gru18].

The photocatalytic activity of both Mabiq complexes were examined in two reaction types:

- A) Reactions, in which the M-Mabiq is reduced by a sacrificial donor to give the reduced form M-Mabiq^{red}. The reduced form subsequently reacts with the substrate and results in the desired product. During this step, the reduced form M-Mabiq^{red} is regenerated to M-Mabiq.
- B) Reaction, in which the M-Mabiq reacts immediately in the first step with the substrate and activates the substrate for further reaction. During this step M-Mabiq is reduced to M-Mabiq^{red}. In order to regenerate M-Mabiq an additional oxidant is added to the reaction mixture.

Reaction type A

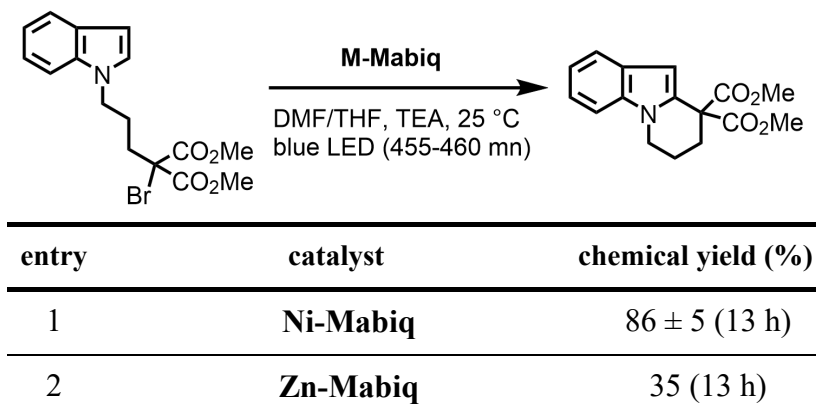
As a model reaction for the reaction type A the following reaction is discussed: photoredox-catalysed cyclization of an N-(ω -bromoalkyl)-substituted indole.

In this reaction, the M-Mabiq is reduced by TEA to the reduced form M-Mabiq^{red}. The next step is based on diffusion. Here the formed M-Mabiq^{red} initiates the ring closing reaction of the indole (see Fig. 6-D1 in Appendix).

The photocatalytic activity is examined as chemical yield – or in other words, how much product in % is formed. The chemical yield for M-Mabiq is 86% (see Table 6-3). In contrast, the chemical yield of Zn-Mabiq under the same illumination conditions is only 35%, although the RQY of the reduction step is higher than that of Ni-Mabiq as mentioned earlier. The reason for the low chemical yield is the very low photostability of Zn-Mabiq.

Observation of this reaction provides the same results as reported in previous studies [Gru18]: the metal center has a large effect on the reaction yield. This effect was also observed for Fe-, Co- and Cu-Mabiq, where additionally different selectivities were reported [Gru18].

Table 6-3 Summary of photoredox-catalysed cyclization of an N-(ω -bromoalkyl)-substituted indole.



[**M-Mabiq**] = 2 mM, [**indole**] = 30 mM, [**TEA**] = 60 mM, mixture of DMF and THF 1:1 as a solvent, light source: Avonec, 455-460 nm placed in a photoreactor.

The indole reaction has a specific initialization phase. In the indole reaction **M-Mabiq** is reduced by **TEA** in order to form reduced **M-Mabiq^{red}**. This reduced form is relevant for the further reaction with the substrate (see Fig. 6-D1 in Appendix). As observed, the repeated excitation of **Zn-Mabiq** leads to its degradation. The suggested improvement of the reaction conditions is intermittent illumination. This can control the amount of generated **Zn-Mabiq^{red}** and it can avoid the undesirable excitation of species during the further dark reaction.

Reaction type B

The reaction type B represents reactions that do not depend on the initial reduction with a sacrificial donor. In this work the following two reactions are investigated:

- B.1) oxidative C–H functionalization of N-phenyl-tetrahydroisoquinoline (Aza-Henry reaction)
- B.2) oxidative coupling of 4-methoxybenzylamine

The reaction B.1 is also known as Aza-Henry reaction. After excitation (step 1 in Fig. 6-10), the **M-Mabiq** is quenched by N-phenyl-tetrahydroisoquinoline (**THIQ**). During this process, **M-Mabiq** is reduced to **M-Mabiq^{red}** and **THIQ** is oxidized to the cation radical **THIQ⁺** (step 2 in Fig. 6-10). This step is expected to proceed on the low μ s timescale (see estimations in Fig. 6-F1 in Appendix).

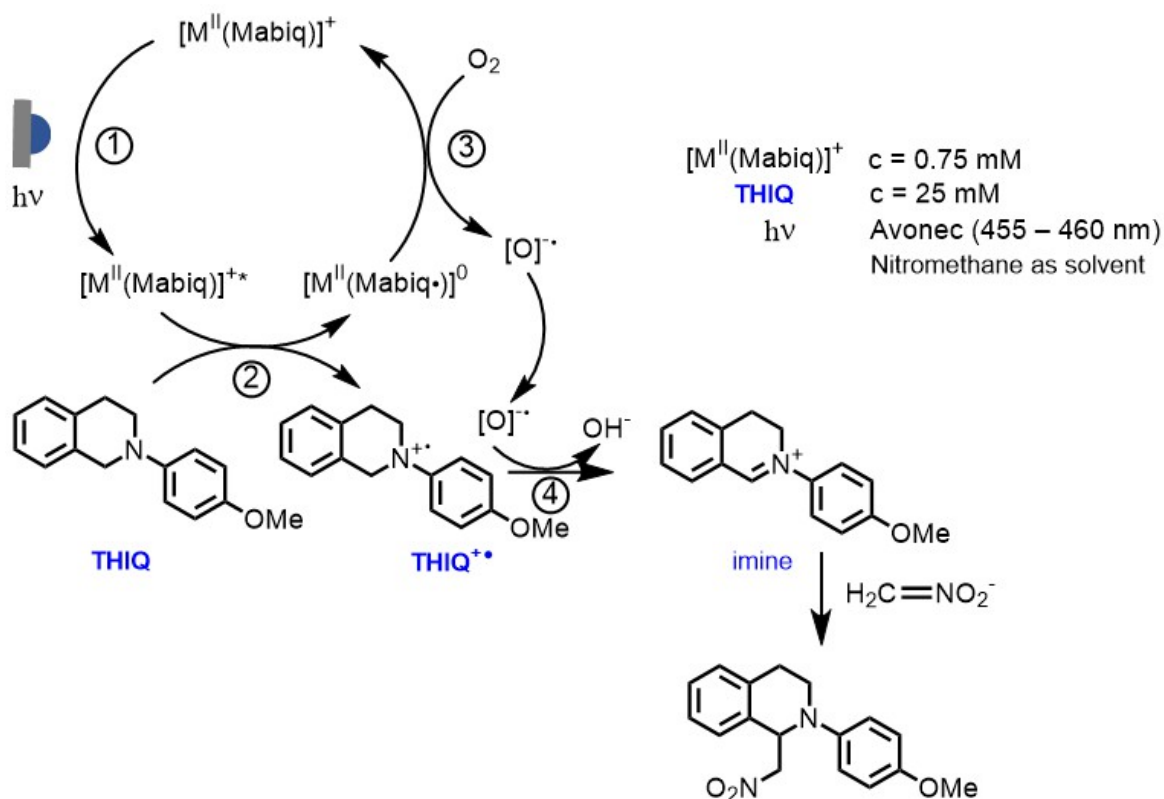
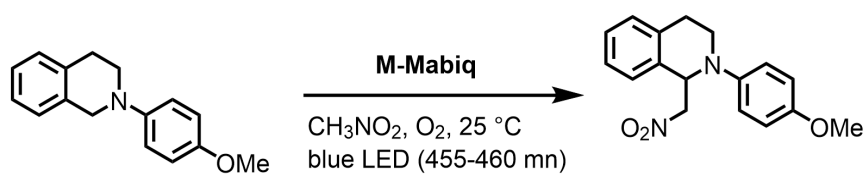


Figure 6-10 Proposed reaction mechanism of the Aza-Henry reaction [Rue11].

Table 6-4 Summary of photoredox catalysis – Aza-Henry reaction.



entry	catalyst	chemical yield (%)
1	Ni-Mabiq	82 ± 7 (5 h)
2	Ni-Mabiq /no irradiation	-
3	none	14 ± 6 (5 h)
4	Zn-Mabiq	36 ± 13 (30 min)

[M-Mabiq] = 0.75 mM, [THIQ] = 25 mM, nitromethane as a solvent, light source: Avonec, 455-460 nm placed in a photoreactor.

Subsequently, the **M-Mabiq^{red}** reacts with nitromethane (CH_3NO_2) and it is oxidized back to the original **M-Mabiq** form (step 3 in Fig. 6-10, here O_2 represents the part of the nitro-group of nitromethane). During this reaction, the co-substrate CH_2NO_2^- as an iminium ion is formed. The reactive oxygen from the regeneration process of **M-Mabiq** is subsequently used for the next step. Here, the reactive oxygen and **THIQ⁺** forms an imine and the hydroxyl anion OH^- is released (step 4 in Fig. 6-10). The reactive **THIQ⁺** is expected to remain in the close proximity of the co-substrate CH_2NO_2^- . This quasi-geminate step is expected to be fast and efficient, and it results in the formation of the product (step 5 in Fig. 6-10).

The results of the chemical yields are summarized in Tab. 6-4. In case of **Ni-Mabiq** the final chemical yield after 5 h of illumination is 82%. However, under the same photocatalytic conditions, the chemical yield of **Zn-Mabiq** is only 35%. The comparatively very low chemical yield of **Zn-Mabiq** is due to the massive degradation of the catalyst. Already within 30 minutes, a considerable part of the **Zn-Mabiq** was degraded.

The limit of the overall reaction quantum yield was estimated to be approximately 1.5×10^{-3} . This result is comparable with reported values when using $[\text{Ru}(\text{bpy})_2]^{2+}$ and $[\text{Ir}(\text{ppy})_2(\text{dtbbpy})]^+$ [Con10].

The massive degradation was also observed for **Ni-Mabiq**, but only in the case when no suitable oxidant was present. It can be assumed that in this case **Ni-Mabiq^{red}** is attacked by the isoquinoline radical. For the UV/vis spectra, the reader is referred to Fig. S58 and S59 in the supplementary information in reference [Lau21].

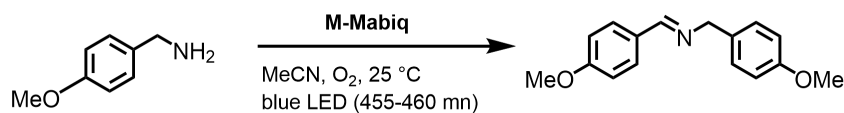
The pulsed illumination is irrelevant for this type of reaction. Here the **M-Mabiq** is reduced by the substrate in the initialization phase and the major role of **M-Mabiq^{red}** is only to be recovered to **M-Mabiq** by the nitromethane solvent.

The last reaction under study (B.2) is the oxidative coupling of 4-methoxybenzylamine (**4-MBA**). Here, two different reaction mechanisms are proposed [Joh15]:

- i) Energy transfer (see reaction pathway in Fig. 6-E1 in Appendix)
- ii) Electron transfer (see reaction pathway in Fig. 6-E2 in Appendix)

In the latter case the excited **M-Mabiq** oxidizes the substrate to the radical cation. The reduced form **M-Mabiq^{red}** is regenerated by oxygen. The reactive form of oxygen and radical cation reacts under formation of phenylmethanimine and reacts with another molecule of the substrate. During this reaction, the final product is formed.

Table 6-5 Summary of oxidative coupling of 4-methoxybenzylamine.



entry	catalyst	chemical yield (%)
1	Ni-Mabiq	27 ± 0 (17 h)
2	Ni-Mabiq /no irradiation	- (12 h)
3	none	- (12 h)
4	Zn-Mabiq	73 ± 12 (30 min)

[M-Mabiq] = 1 mM, [4-MBA] = 25 mM. acetonitrile as a solvent, light source: Avonec, 455-460 nm placed in a photoreactor.

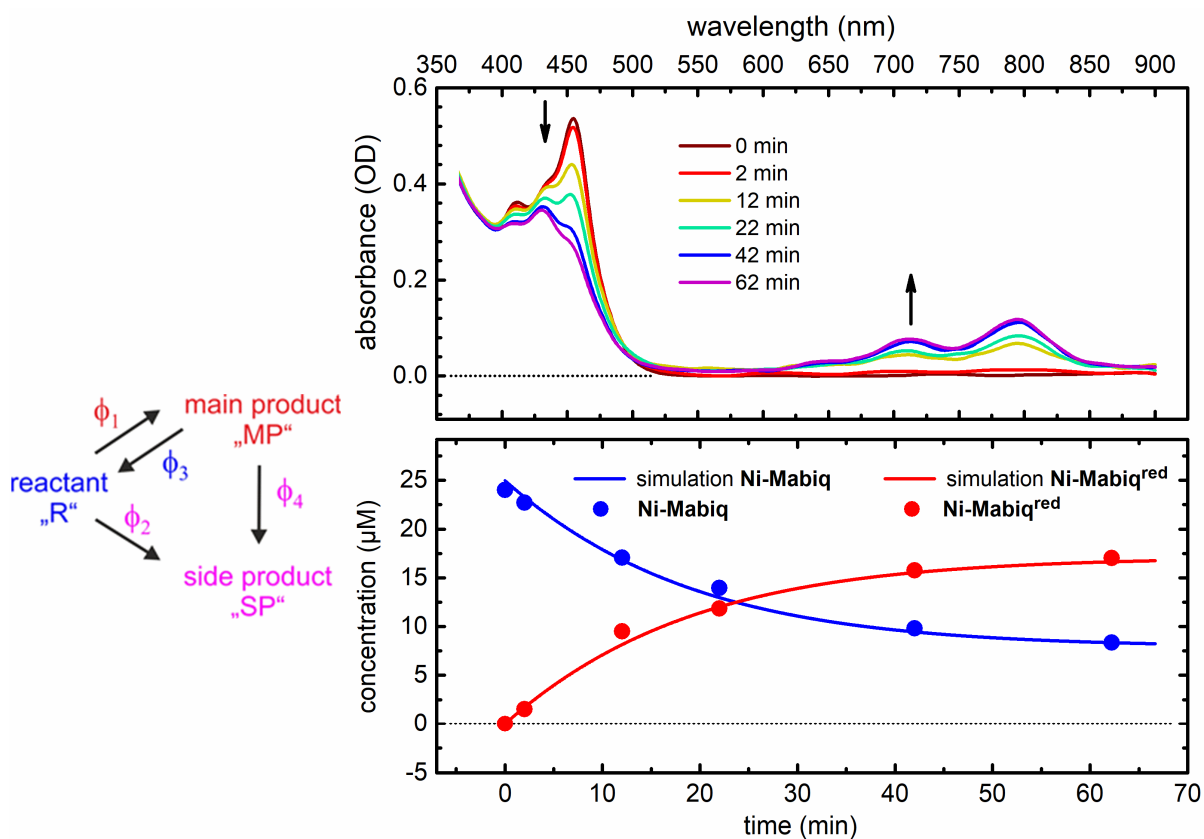


Figure 6-11 (top) UV/vis spectral evolution of Ni-Mabiq (20 μM) and 4-MBA (500 μM, 25 equiv.) in MeCN under inert atmosphere and illumination power of 568.5 mW using 455 nm LED light. (bottom) time evolution of concentrations of Ni-Mabiq and Ni-Mabiq^{red} with reaction quantum yields of $\phi_1 = 1.7 \times 10^{-5}$, $\phi_2 = 0 \times 10^{-5}$, $\phi_3 = 1.7 \times 10^{-5}$ and $\phi_4 = 0 \times 10^{-5}$.

As shown in Table 6-5, the chemical yield for **Ni-Mabiq** is 27% after 17 hours of illumination. Hereby, no significant formation of the side product is observed, and **Ni-Mabiq** remains stable. For **Zn-Mabiq**, on the other hand, the chemical yield is 73% after only 30 minutes. However, this reaction is accompanied by complete decomposition of the **Zn-Mabiq** catalyst.

For further fundamental reactivity studies, the first step of the aforementioned reaction is investigated below. For this purpose, both **Ni-Mabiq** and **Zn-Mabiq** are mixed with **4-MBA** and illuminated with a 455-460 nm LED (Avonec) under inert conditions.

The results show that **Ni-Mabiq** is photoreversible and exhibits a comparably efficient forward and reverse reaction between the **Ni-Mabiq** and **Ni-Mabiq^{red}** forms with an RQY of 1.7×10^{-5} (see Fig. 6-11). The low RQY is consistent with the low coupling product yields of 27% after 17 hours.

From the illumination conditions of this reaction for **Ni-Mabiq** with **4-MBA** a lower limit of the overall reaction quantum yield is estimated to be 4.3×10^{-4} . If one considers the reaction conditions from previous experiment - concentration of **4-MBA** (25 mM, see Tab. 6-5), and the linear dependence of the process on the quencher concentration – the RQY results in the value of 8.5×10^{-4} . Within the uncertainty of this estimate the two yields are equal, showing that indeed all steps after the first electron transfer occur with near unity.

In case of **Zn-Mabiq** a different behavior is observed. After initial formation of **Zn-Mabiq^{red}** a clear degradation of **Zn-Mabiq** is detected. The RQY of the quenching process to the reduced form **Zn-Mabiq^{red}** is 0.12. Additionally, the RQY of 0.20 to an unidentified side product is observed. The final spectrum of the side product is distinct from the **Zn-Mabiq** as well as from **Zn-Mabiq^{red}**.

The very high RQY for **Zn-Mabiq** may be related to the ability of amine to coordinate to Zn-complex [Lau21]. However, the amine pre-coordination may also contribute to photoinstability of the created product **Zn-Mabiq^{red}**, since the prolonged illumination leads to degradation of the sample. A similar trend is also observed for reaction accompanied with the pre-coordination with **TEA**. Hereby, the absorption band around 600 nm disappears and a new absorption feature below 500 nm increases (see Appendix 6-C). The decomposition is proven to be light driven because the chemically synthesized **Zn-Mabiq^{red}** is stable as long as no photoexcitation is applied. The **Fe-**, **Co-** and **Ni-Mabiq** are under these reaction conditions photostable.

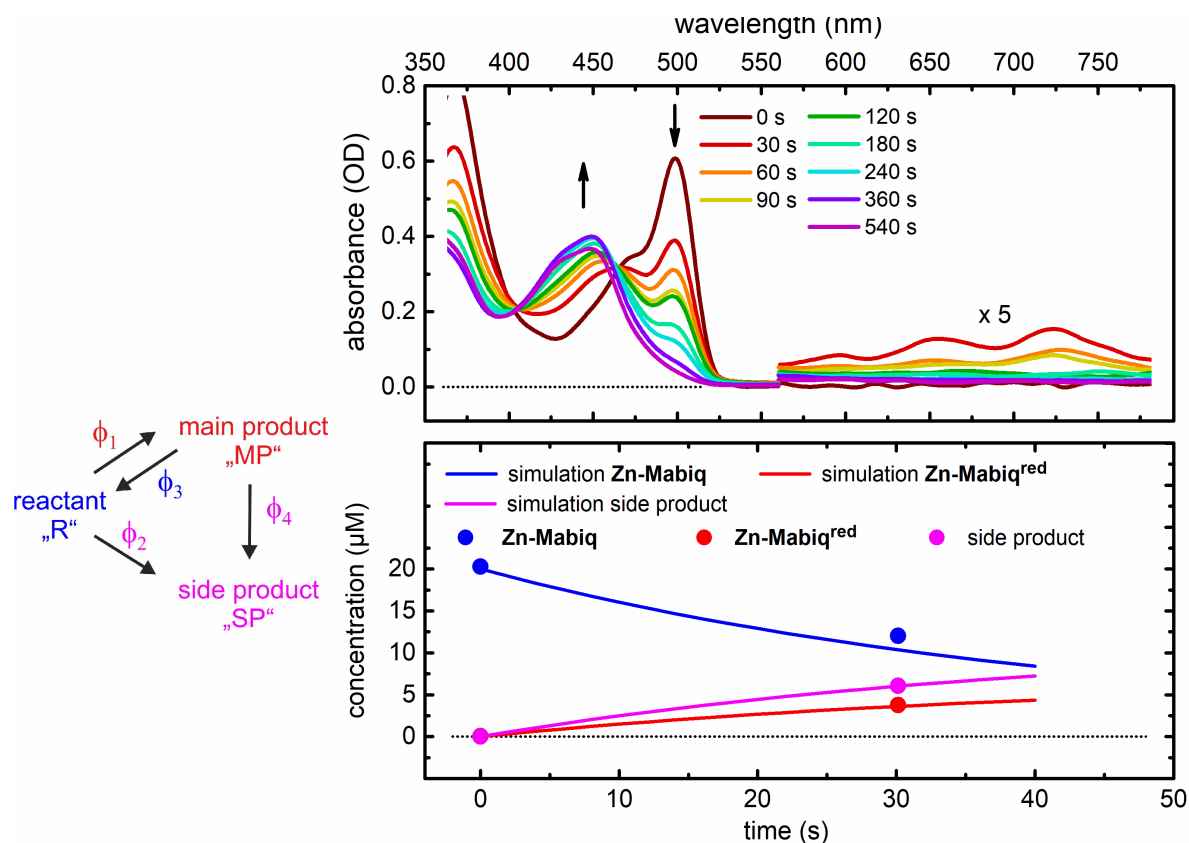


Figure 6-12 (top) UV/vis spectral evolution of **Zn-Mabiq** (20 μM) and **4-MBA** (500 μM , 25 equiv.) in MeCN under inert atmosphere and illumination power of 2.4 mW using 455 nm LED light. (bottom) time evolution of concentrations of **Zn-Mabiq** and **Zn-Mabiq^{red}** with reaction quantum yields of $\phi_1 = 0.12$, $\phi_2 = 0.2$, $\phi_3 = 0$ and $\phi_4 = 0$.

In summary, although both examined reaction revealed that the **Ni-** and **Zn-Mabiq** may figure as a photocatalyst but as discussed above there are still numerous factors that should be considered in order to optimize the reaction conditions.

6.6 Transient absorption

Regarding the diverse photoreduction properties of the **Ni-** and **Zn-Mabiq**, it is expected that the relaxation dynamics will differ extensively. In order to gain a deeper understanding of the relaxation processes, transient absorption in the fs/ps and ns/ μs regime is performed.

The data are evaluated using two methods. The first one is based on the singular values decomposition (SVD) and global fit, in which the whole dataset is fitted simultaneously with a selected set of time constants. Hereby, the dynamics is analyzed in the sense of the compartmental model, in which the transfer dynamics is strictly sequential between the

compartments in the model. The spectra associated with each “compartment” are designated as the evolution associated decay spectra (EAS) [Sto04]. The second method is a model neutral Maximum Entropy Analysis (MEA) [Kut13]. The MEA are shown in Appendix 6-G. Both approaches supply comparable time constants. The electronic character of the observed states were obtained from the theoretical calculations based on the time-dependent density functional theory performed in the group of Kaila [Lau21].

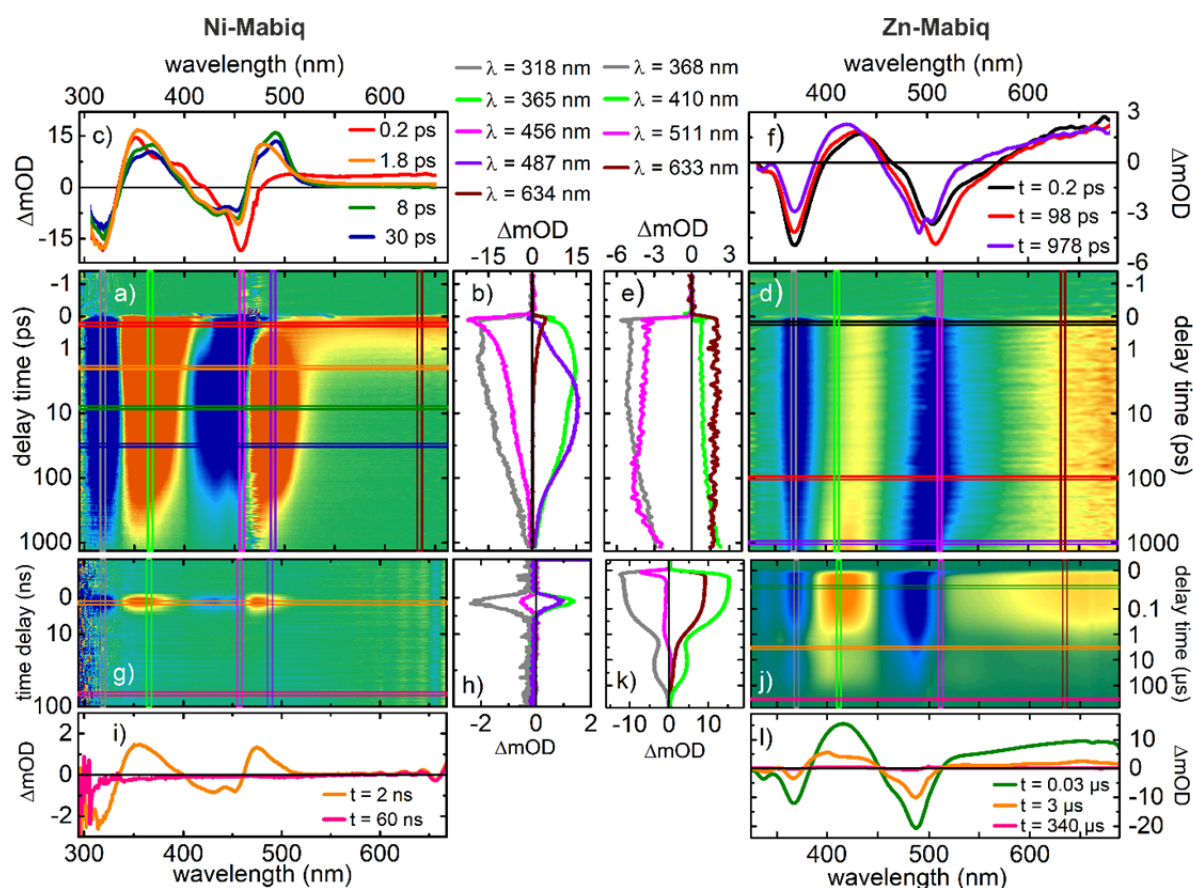


Figure 6-13 a), g), d) and j) Transient absorption of degassed **Ni-Mabiq** and **Zn-Mabiq** in THF/MeCN=1:1 upon excitation with 460 nm (70 fs pulse), 493 nm (49 fs pulse), 493 nm (2.5 ns pulse) and 450 nm (2.5 ns pulse) respectively. b), h), e) and k) Kinetic traces at wavelength extracted from vertical lines. c), i), f) and j) Transient spectra at selected probe delays according to horizontal lines.

Fig. 6-13 shows the significant differences in the excitation dynamics, where much faster and more complicated processes are found for **Ni-Mabiq** (left). In both cases for **Ni-Mabiq** and for **Zn-Mabiq**, excitation is immediately followed by stimulated emission (SE), which is shifted to the red compared to the excitation wavelength. Broad excited state absorption (ESA) extending into the near IR is observed. Such spectral evolution (SE and ESA) at the

early ps scale is typically due to ligand-localized singlet states. These singlet states are attributed to $^1\text{Ni}^{\text{II}*}$ and $^1\text{Zn}^{\text{II}*}$ (the designations singlet and triplet refer to the total spin state of the complex).

In the case of **Zn-Mabiq**, the SE signal decays with 1.1 ns, which gives good agreement with the 1 ns value observed in time-resolved fluorescence measurements [Lau21]. As can be seen in panel e) of Fig. 6-13, only small changes in the kinetic traces are observed in addition to the dominant SE contribution. These fast spectral changes correspond to solvation dynamics (2 ps) and geometric relaxation (62 ps), see the global fit results in Fig. 6-14 on the left.

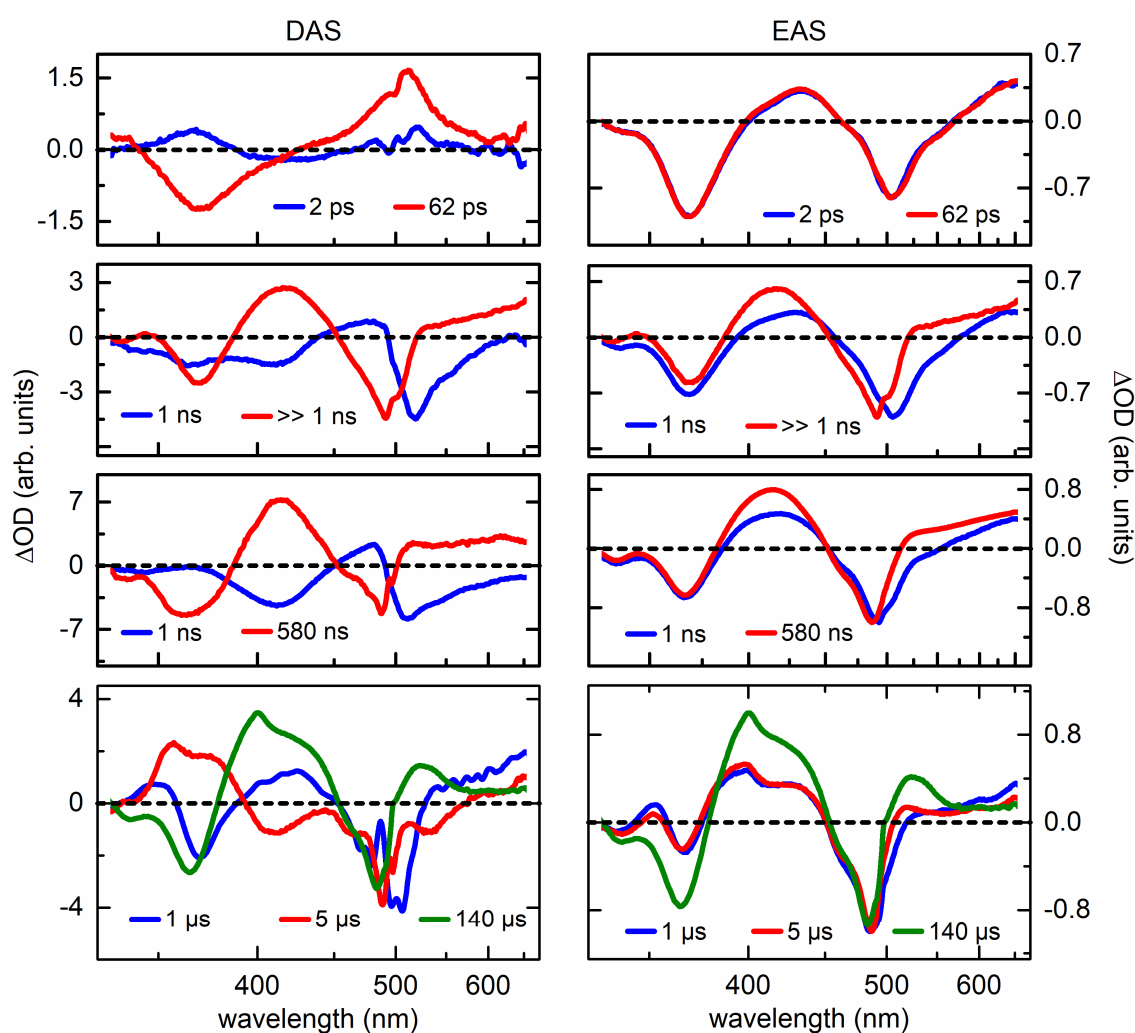


Figure 6-14 Global analysis of the transient absorption of **Zn-Mabiq**. Decay associated (DAS, left column) and evolution associated decay spectra (EAS, right column) extracted from the data in Fig. 6-11 right.

The relaxation dynamics of **Zn-Mabiq** continues in the ns/ μ s range (see Fig. 6-13, bottom right). This slower time scale is related to the ligand-centered $^3\text{Zn}^{\text{II}}$ state decaying with 580 ns and 1 μ s. The longer decay constants (5 μ s and 140 μ s) with lower contribution are likely related to ligand dissociation and non-geminate re-association. This seems plausible since **Zn-Mabiq** can coordinate a fifth ligand in the axial position.

The overall picture of the relaxation dynamics with the corresponding time constants is shown and summarized in Table 6-6.

The more complex dynamics is found for **Ni-Mabiq**. In order to analyze the dynamics in the range of the first tens of picoseconds, a zoom on selected probe delays of the TA measurement for **Ni-Mabiq** is used for further discussion (see Fig. 6-15).

The red line shown in Fig. 6-15 with a characterless ESA propagating into the NIR region is typical for locally excited organic molecules. However, within the next ten picoseconds, a defined structure is formed (see dashed black lines in Fig. 6-15). The first to form is a band around 465 nm, which can be attributed to the decay of the ligand-localized $^1\text{Ni}^{\text{II}*}$ state. The second distinct band forms later (after 30 ps) at 490 nm. The contribution of these two features can also be observed in the green and violet lines in panel b) of Fig. 6-13.

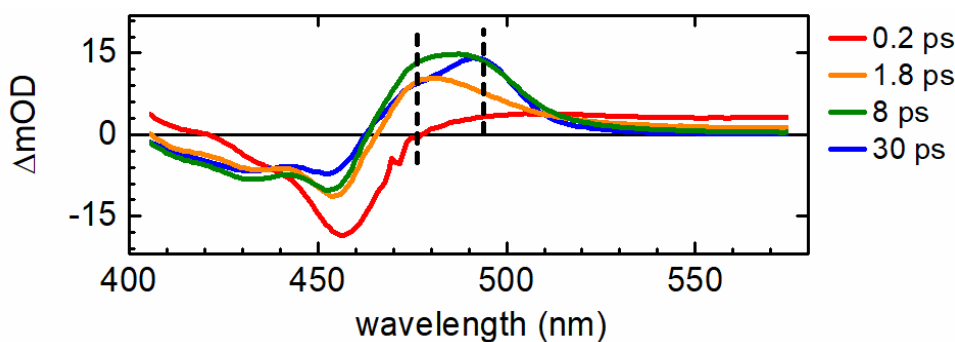


Figure 6-15 Transient spectra at selected probe delays for **Ni-Mabiq** - zoom in the panel from Fig. 6-11c. The broad structures ESA (red line) transforms into specific band around 475 nm that is followed by an additional feature at 490 nm.

Similar dynamics with a rapid decay of the SE and broad ESA features, followed by well-defined ESA bands are reported to be related to energy-transfer from optically bright ligand-localized states to dark metal-centered states in open d-shell transition metal complexes [Zam07, Ret03]. Regarding the relatively complex kinetic traces in Fig. 6-13 in panel b) as well as the time evolution in Fig. 6-15 we expect at least one short lived intermediate state.

Consequently, the decay of the SE as well as the ESA signal for **Ni-Mabiq** within 1.1 ps is attributed to an energy-transfer of the initially excited optically bright $^1\text{Ni}^{\text{II}*}$ state to optically dark metal-centered states. Such fast population transfer away from the emissive $^1\text{Ni}^{\text{II}*}$ state explains the missing photoluminescence of **Ni-Mabiq**. The very short time constant of 370 fs can be attributed to solvation, since comparable solvation times for the pure solvents are reported [Hor95] (see the summary of the time constants in Tab. 6-6).

For further discussion, the results of the global fit analysis are used. According to the results, six components are required for **Ni-Mabiq** and seven components for **Zn-Mabiq** to reproduce the data using the exponential decay model.

In Fig. 6-16, Decay Associated Spectra (DAS), are shown on the left, corresponding to the representation of the amplitude of each decay component as a function of wavelength. On the right side of Fig. 6-16, Evolutionary Associated difference Spectra (EAS) are plotted, representing compartments that do not necessarily correspond to the electronic eigenstates.

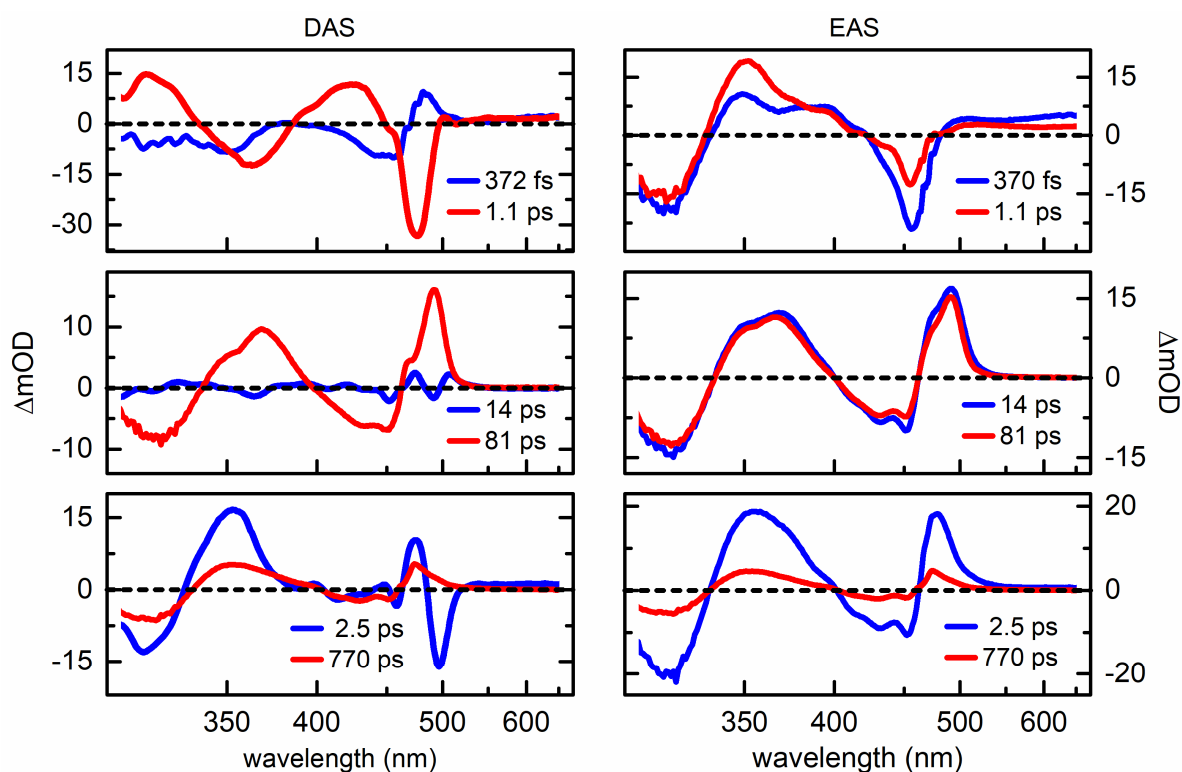


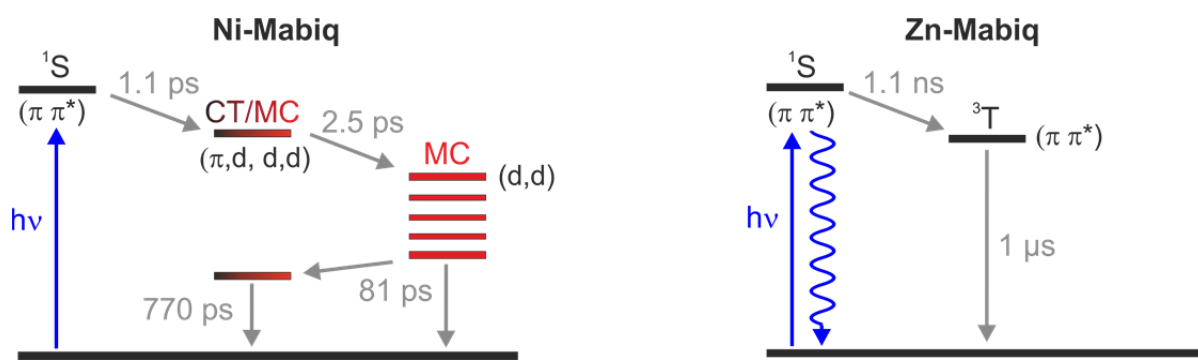
Figure 6-16 Decay associated- (DAS, left column) and evolutionary associated- (EAS, right column) decay spectra extracted from a global fit of the relaxation dynamics of **Ni-Mabiq**.

In a previous analysis, the decay constant of 1,1 ps was attributed to an energy-transfer of the initially excited optically bright $^1\text{Ni}^{\text{II}*}$ state to optically dark metal-centered states. This

time constant can also be observed in the Fig. 6-16 in the decay of the SE contribution and formation of the specific ESA feature close to 460 nm.

The initial relaxation of **Ni-Mabiq*** within 1 ps proceeds through several distinct intermediate states until the ground state is fully restored. The transition from ligand localization to metal-centered states involves a short-lived intermediate state with metal-centered (MC)/charge transfer (CT) character and a lifetime of 2.5 ps. After reaching the MC state, the population is almost completely positioned on the metal center, while the ligand is in a ground state distorted by the excited metal center.

Table 6-6 Summary of molecular dynamics of **Ni-** and **Zn-Mabiq**.



Ni-Mabiq	
0.37 ps	solvation dynamics
1.1 ps	$^1\text{Ni}^{\text{II}*} \rightarrow \text{MC/CT}$
2.5 ps	$\text{MC/CT} \rightarrow \text{MC}$
14 ps	spectral narrowing, e.g., vibrational relaxation
81 ps	combined $\text{MC} \rightarrow \text{GS}$ and $\text{MC} \rightarrow \text{MC/CT}$
772 ps	$\text{MC/CT} \rightarrow \text{ground state (GS)}$

Zn-Mabiq	
2 ps	solvation dynamics
62 ps	geometric relaxation
1.1 ns	SE loss / $^1\text{Zn}^{\text{II}*} \rightarrow ^3\text{Zn}^{\text{II}}$
580 ns	relaxation within $^3\text{Zn}^{\text{II}}$ manifold
1 μs	decay of ligand-centered $^3\text{Zn}^{\text{II}}$ state
5 μs	ligand dissociation (tentative)
140 μs	ligand re-association (tentative)

The time constants of 14 ps and 81 ps are related to these transitions with ligand-localized π - π^* character. The spectral narrowing of the 14 ps component observed in the DAS and EAS indicates vibrational cooling [Bal19] or heat dissipation [Miz99], see Fig. 6-16. The longer time constant of 81 ps corresponds to the lifetime of the MC state. After that, part of the population decays back to the ground state. The other part reaches the long-lived partial CT state with a lifetime of 770 ps. This branching character can be observed in the DAS spectra of the 80 ps and 772 ps components, see Fig. 6-16, both showing a GSB signature in the 400-460 nm region.

The decay constant of 772 ps corresponds well with the prediction of the lifetime of the reactive state. This lifetime can be extracted from a set of measurements in reference [Gru18], in which the dependence of the RQY on the **TEA** concentration is investigated. The analysis of the standard diffusion model [Kan95] and diffusion limited quenching rate typical of molecules comparable to our system ($\sim 10^{10} \text{ M}^{-1} \text{ s}^{-1}$) [Mon06] results in a predicted lifetime between 580 ns and 900 ns. The measured 772 ps lies fairly within this region and hence it is reasonable to assume, that the photoreduction occurs from this state with CT character.

Regarding that the concentration of **TEA** is 33.5 mM (see experiment in Fig. 6-B1 in Appendix) and the reactive lifetime is 772 ps for **Ni-Mabiq**, it is possible to estimate the photoreduction quantum yield. Assuming that the reaction is only diffusion limited with a diffusional constant of $10^{10} \text{ M}^{-1} \text{ s}^{-1}$, the estimated RQY is 0.2. The discrepancy to the experimentally determined RQY of 2.9×10^{-4} could originate, e.g., from the back electron transfer due to the cage effect or from the branching in the GSB recovery.

Considering the results of TA spectroscopy and photocatalytic measurements in Section 6.5, the following conclusions can be summarized. The catalytic activity of **M-Mabiq** is based on the ability of the excited state to participate in a single electron transfer with a sacrificial donor or substrate. The electron transfer process involving only singlet states is not possible because the lifetime of the relevant singlet states is in the range of a few picoseconds. Moreover, the close proximity of the generated ion pair would very likely lead to a back ET. In other words, there is no time for a spatial separation of catalyst and sacrificial donor/substrate. This fact makes the ET very unproductive.

When **M-Mabiq** reacts with the amine-based substrate, the reaction is expected to proceed via the triplet state. In this case, the backward ET is prohibited due to the Pauli principle [Meg11b]. In contrast to **Ni-Mabiq**, all key states for the photocatalytic reaction, including

the triplet states, are ligand-localized in case of **Zn-Mabiq**. Therefore, a beneficial catalytic effect is expected for **Zn-Mabiq**. However, the instability of **Zn-Mabiq** limits its wide application as a photocatalyst. This problem can be partially solved by adding an oxidizing agent, which is primarily used to regenerate **Zn-Mabiq**, but significant decomposition of **Zn-Mabiq** is still observed.

On the other hand, **Ni-Mabiq** is more robust in comparison to **Zn-Mabiq**. This can be explained with the rapid decay of the initially excited ligand-centered state into states of metal-centered and partial CT character. According to this observation, the participation of metal-centered states in **Ni-Mabiq** is crucial for the stability of the catalyst.

In summary, the dynamics of **Ni-Mabiq** start from ligand-centered singlet state, then relaxes into metal-centered triplet state. The final reactive state has CT character. The presence of MC and mixed MC/CT states are relevant for the photoredox activity. The partial metal character of the **Ni-Mabiq^{red}** make the system robust against degradation. On the other hand the less complex dynamics of **Zn-Mabiq** involves only ligand-centered π - π^* states. Although the lifetime of the excited states is expected to favor the photoredox activity of **Zn-Mabiq**, the instability of the reduced form hinders the reaction. The ability to coordinate the substrate directly on the metal center may be advantageous, but it is of great interest to improve first the stability of the reduced form. For this, further modifications on the **Mabiq** system are under consideration. For example, the optimization of the backbone structure of ligands or implementation of the second metal center as originally intended by von Zelewsky [Mue88]. After further improvements **M-Mabiq** systems may become an interesting earth-abundant catalyst in various photoredox reactions.

Appendix for Chapter 6

Appendix 6-A

Absorption spectra of Ni- and Zn-Mabiq in various solvents

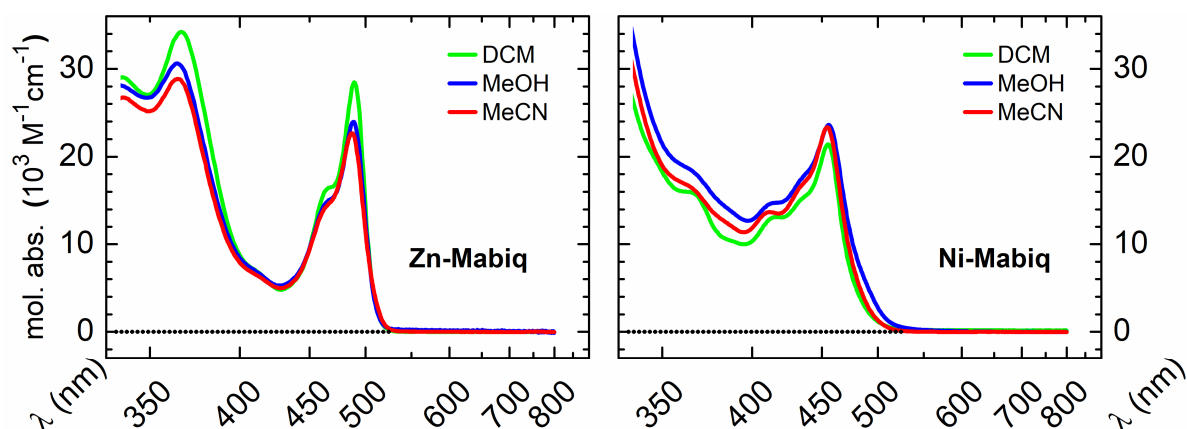


Figure 6-A1 Impact of solvent on the UV/vis absorption spectra of Ni- and Zn Mabiq.

Appendix 6-B

Photoreduction RQY for Ni-, Fe- and Co-Mabiq using TEA as a quencher

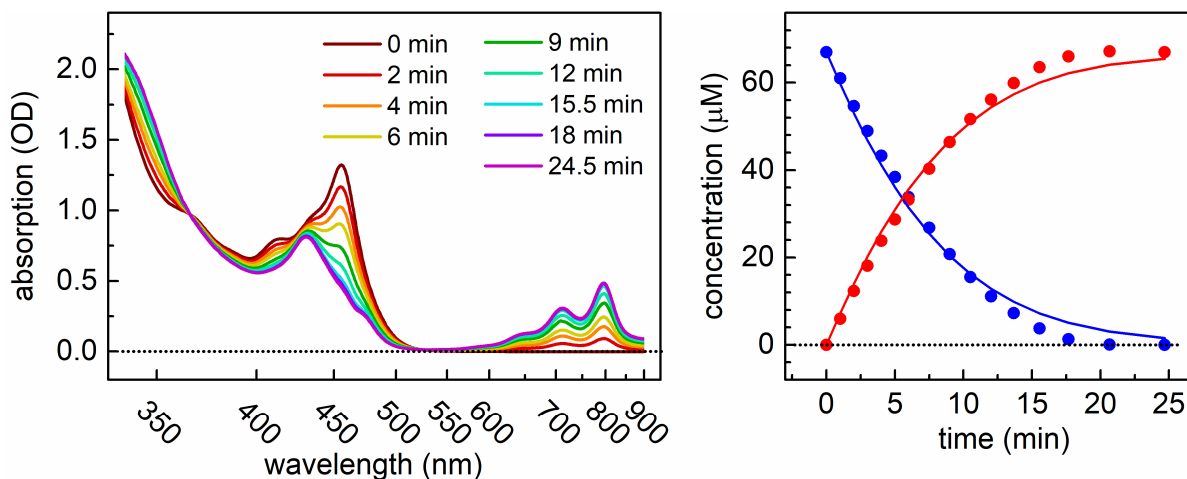


Figure 6-B1 (left) Spectral changes of Ni-Mabiq ($67 \mu\text{M}$) mixed with TEA (33.5 mM) upon illumination with 455 nm LED with the power in the sample of 245 mW. The volume of the solution in a 10 mm cuvette was 2 mL. (right) Time evolution of concentrations during the illumination and numerical simulation (fit). The RQY is 2.9×10^{-4} .

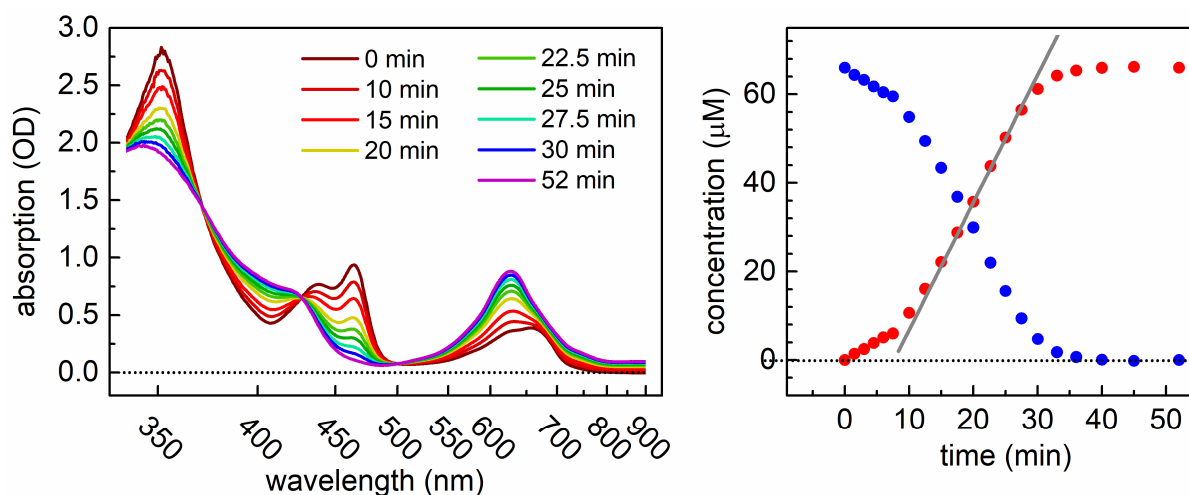


Figure 6-B2 (left) Spectral changes of **Fe-Mabiq** ($66 \mu\text{M}$) mixed with **TEA** (33 mM) upon illumination with 455 nm LED with the power in the sample of 245 mW . The volume of the solution in a 10 mm cuvette was 2 mL . (right) Time evolution of concentrations during the illumination and numerical simulation (fit). The RQY is 1.8×10^{-4} .

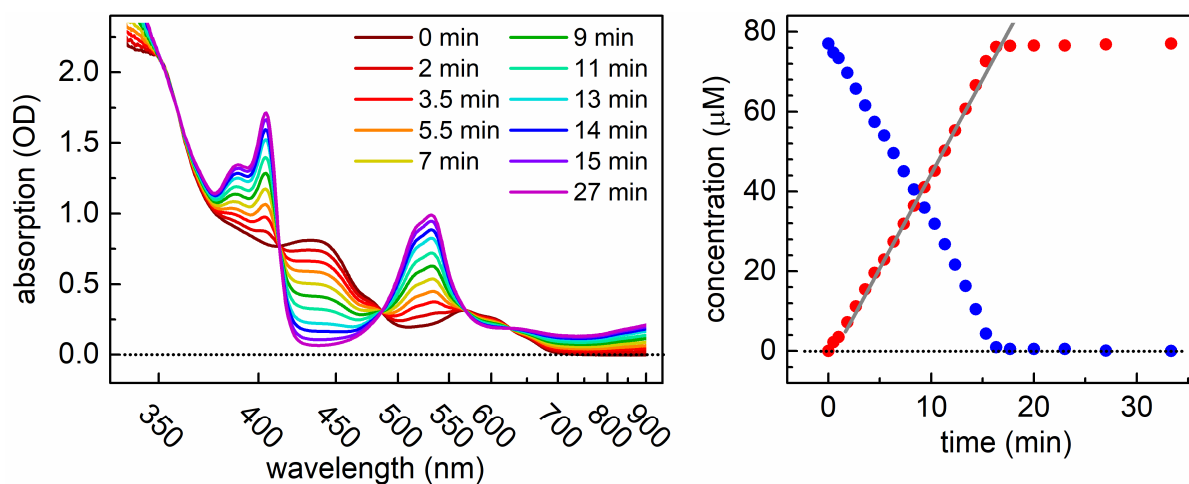


Figure 6-B3 (left) Spectral changes of **Co-Mabiq** ($77 \mu\text{M}$) mixed with **TEA** (38.5 mM) upon illumination with 455 nm LED with the power in the sample of 245 mW . The volume of the solution in a 10 mm cuvette was 2 mL . (right) Time evolution of concentrations during the illumination and numerical simulation (fit). The RQY is 3.6×10^{-4} .

Appendix 6-C

Light driven decomposition of the $\text{Zn-Mabiq}^{\text{red}}$

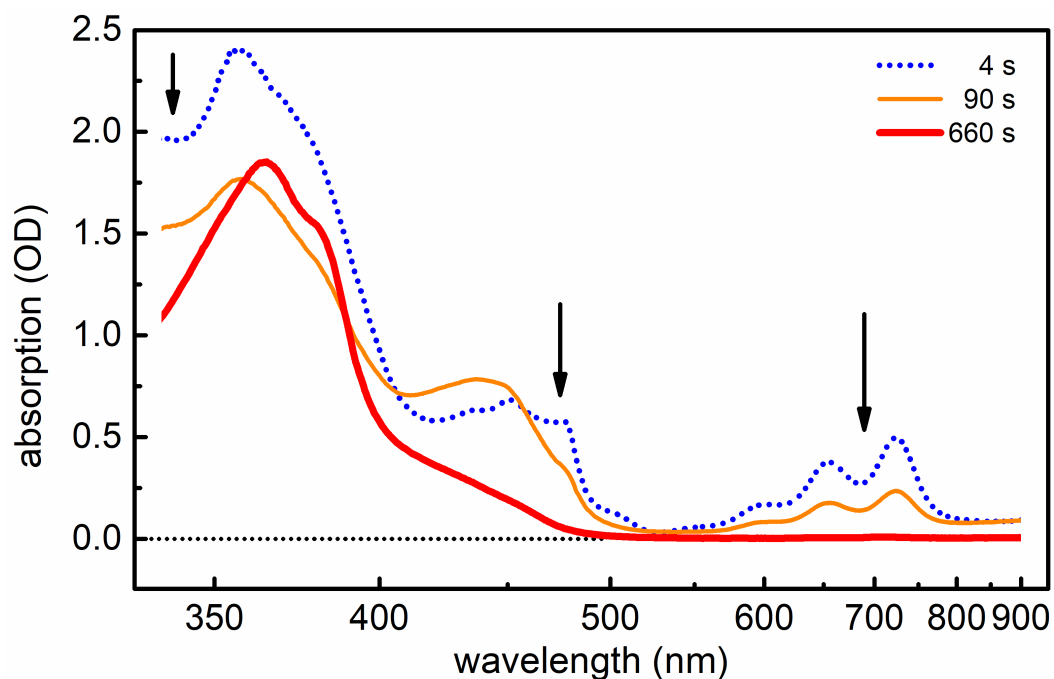


Figure 6-C1 Spectral changes after the photoreduction of Zn-Mabiq with concentration of $77 \mu\text{M}$, $\text{TEA} = 38.5 \text{ mM}$ in solvent mixture $\text{THF/MeCN} = 1:1$ upon illumination with 455 nm and power of 248 mW . The formation of $\text{Zn-Mabiq}^{\text{red}}$ is complete after just four seconds (blue dotted line), after which product degradation is observed. The final spectrum of the decay product (660 s irradiation time) is shown by the bold red line.

Appendix 6-D

Proposed reaction mechanism for photoredox-catalysed cyclization of an N-(ω -bromoalkyl)-substituted indole

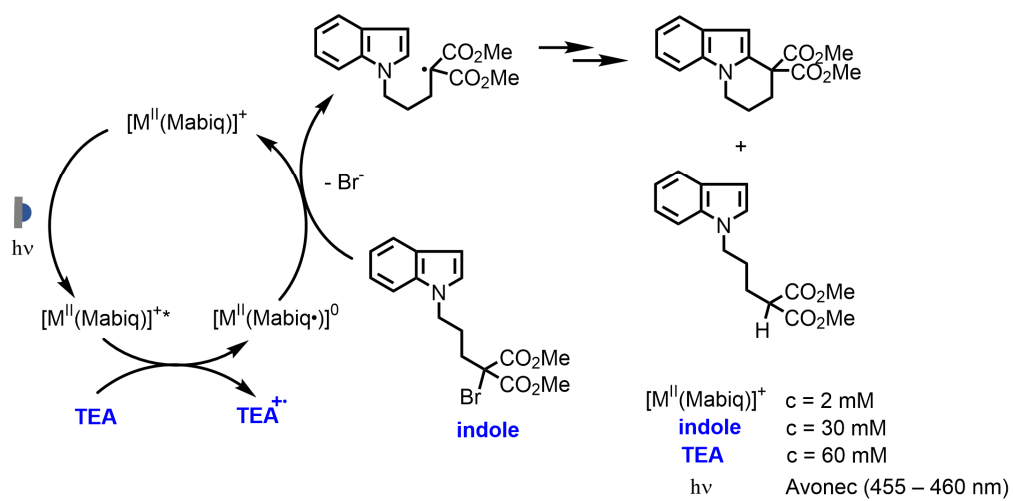


Figure 6-D1 Proposed reaction mechanism of TEA as previously reported [Gru18].

Appendix 6-E

Proposed reaction mechanism for coupling of 4-methoxybenzylamine

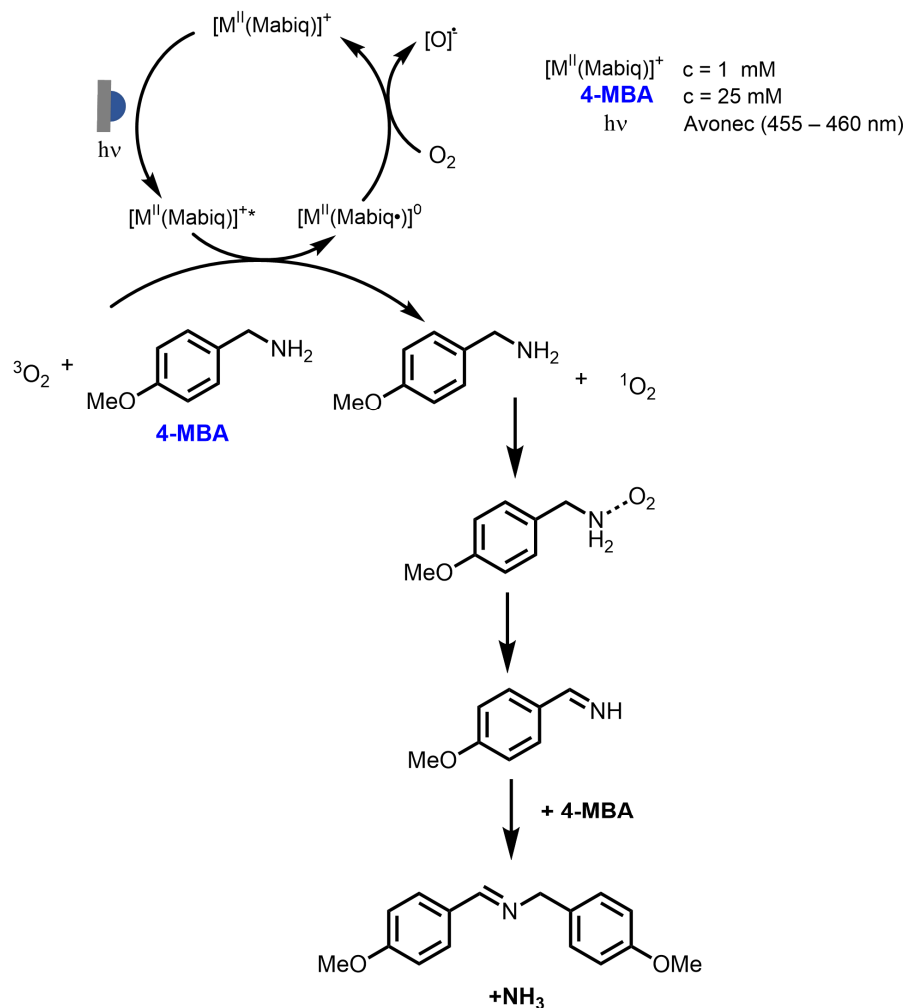


Figure 6-E1 Proposed reaction mechanism for coupling of 4-methoxybenzylamine based on the energy transfer.

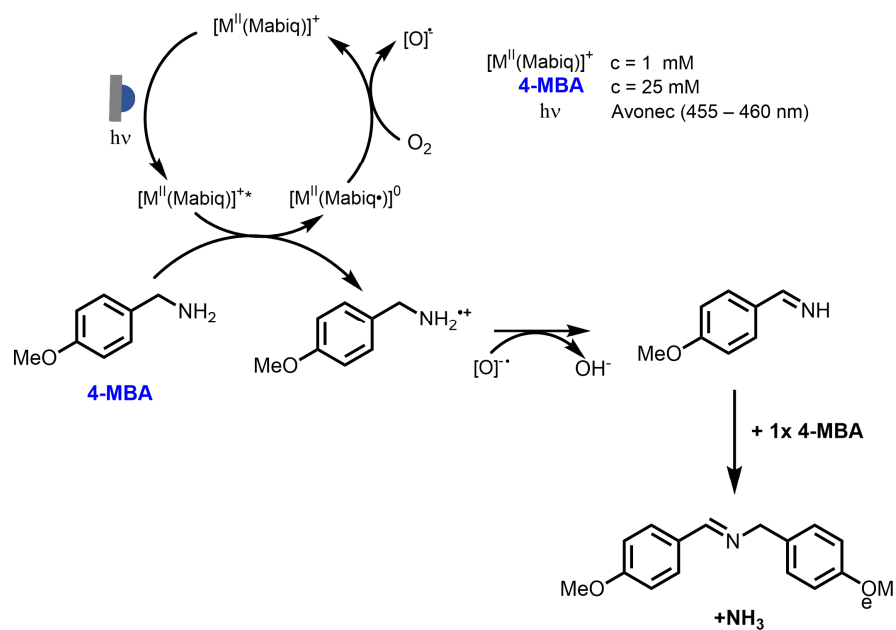


Figure 6-E2 Proposed reaction mechanism for coupling of 4-methoxybenzylamine based on the electron transfer.

Appendix 6-F

Calculations according to standard diffusion model [Kan95]

Diffusion coefficient			
Diameter of NiMabiq (from Sophie Mader)	$d_{Ni} := 18 \text{ Angstrom}$	$Temp := 298 \text{ K}$	
Diameter of THIQ (From 3D ChemDraw)	$d_{THIQ} := 13 \text{ Angstrom}$		
Viscosity ACN/THF=1:1	$\eta_{A_THF} := 0.3932 \cdot 10^{-3} \text{ Pa}\cdot\text{s}$	from ref [Mou06]	
	$D_{A_THF_THIQ} := \frac{k \cdot Temp}{6 \cdot \pi \cdot \eta_{A_THF} \cdot \frac{d_{THIQ}}{2}} = (8.54 \cdot 10^{-6}) \frac{\text{cm}^2}{\text{s}}$		$D_{A_THF_Ni} := \frac{k \cdot Temp}{6 \cdot \pi \cdot \eta_{A_THF} \cdot \frac{d_{Ni}}{2}} = (6.168 \cdot 10^{-6}) \frac{\text{cm}^2}{\text{s}}$
Volume of the solution	$V := 2 \text{ mL}$	Concentration of NiMabiq	$c_{Ni} := 3 \text{ mM}$
Cuvette Thickness	$d := 10 \text{ mm}$	Concentration of THIQ	$c_{THIQ} := 100 \text{ mM}$
Number of THIQ Molecules	$N_{THIQ} := V \cdot c_{THIQ} \cdot N_A = 1.2 \cdot 10^{20}$		
Number of THIQ Molecules pro Liter	$\rho_{THIQ} := \frac{N_{THIQ}}{V} = (6.022 \cdot 10^{22}) \frac{1}{L}$		
Distance between molecules THIQ	$d_{THIQ} := \frac{1}{\sqrt[3]{\rho_{THIQ}}} = 2.551 \text{ nm}$		
time required to diffuse to next neighbor molecule	$\tau_{THIQ} := \frac{(d_{THIQ} \cdot 0.5)^2 \cdot \pi}{D_{A_THF_THIQ}} = 5.99 \text{ ns}$		

Figure 6-F1 Estimation of the average distance and collision time between substrate and **M-Mabiq**.

Appendix 6-G

Transient absorption data

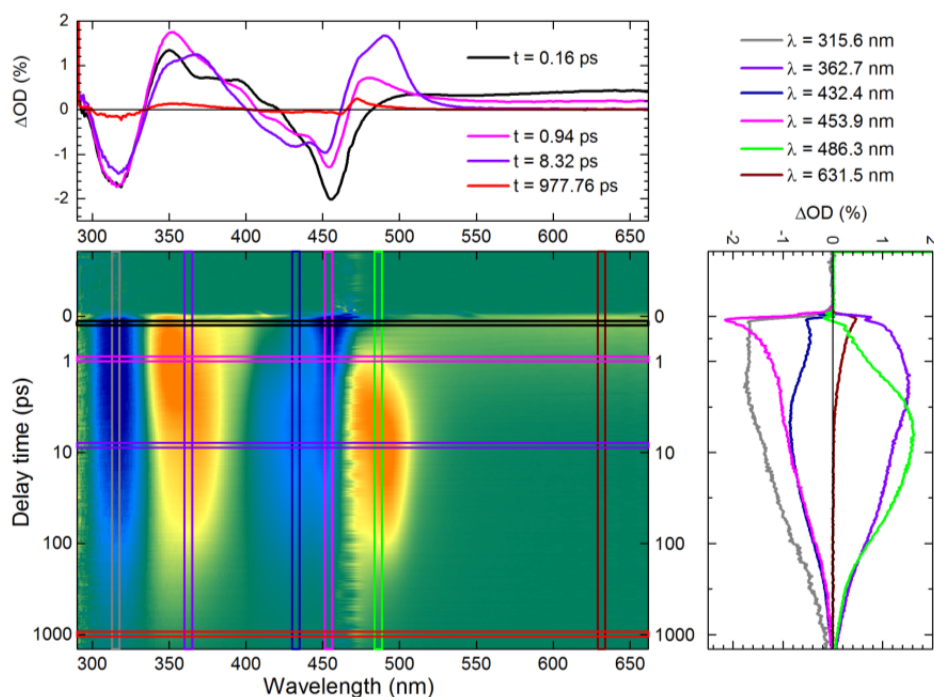


Figure 6-G1 Transient absorption data of a non-degassed 1mM solution of **Ni-Mabiq** in 1:1 THF/MeCN measured in a 250 μm thick flow cell after excitation with ~ 70 fs pulses centered at 460 nm having a pulse energy of 200 nJ.

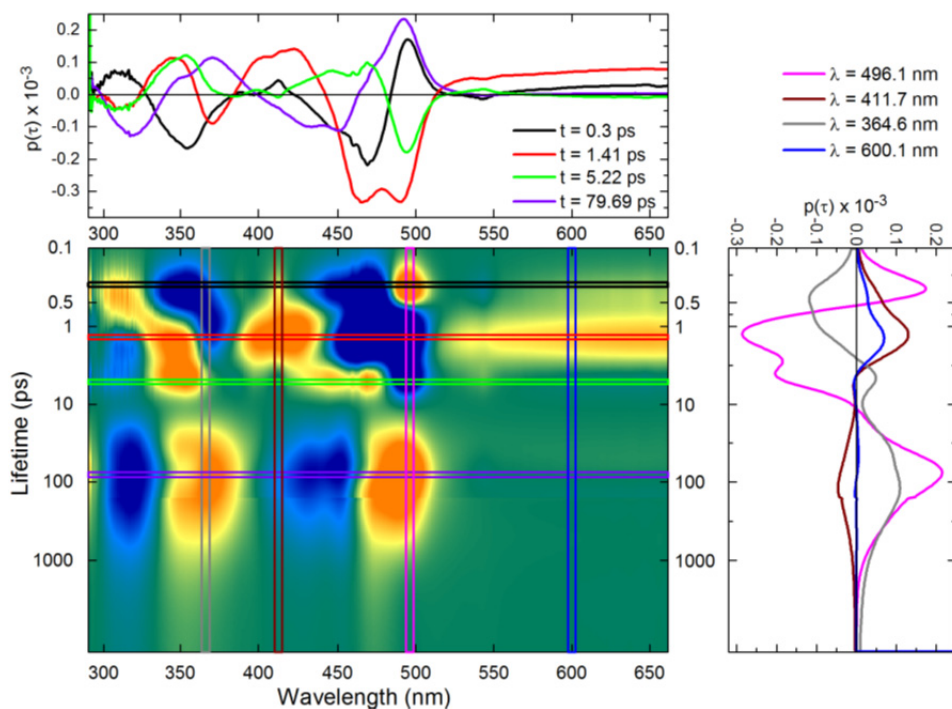


Figure 6-G2 Maximum entropy analysis of the data set for **Ni-Mabiq** in Fig. 6-G1.

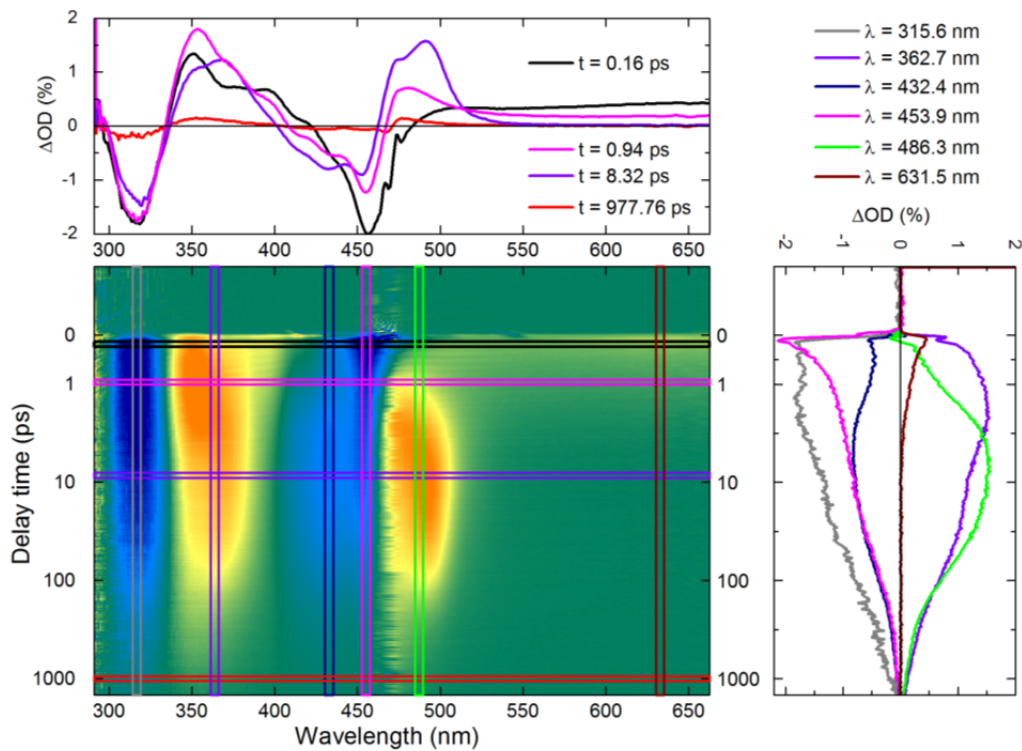


Figure 6-G3 Transient absorption data of a degassed 1 mM solution of **Ni-Mabiq** in 1:1 THF/MeCN measured in a 250 μm thick flow cell after excitation with ~ 70 fs pulses centered at 460 nm having a pulse energy of 200 nJ.

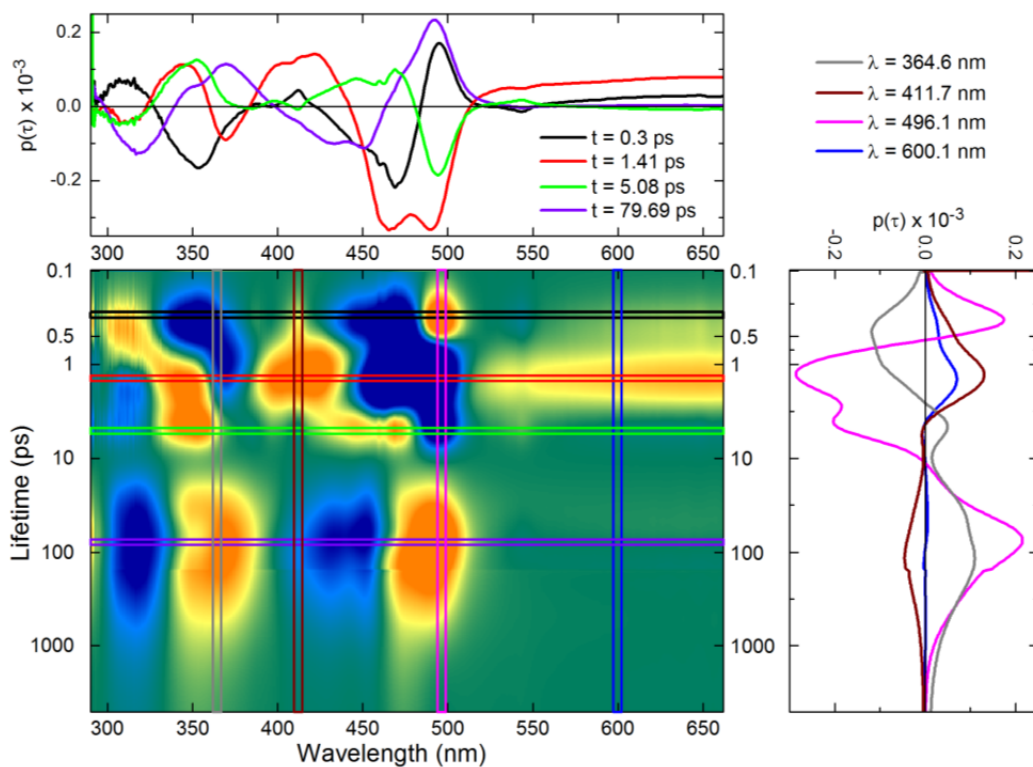


Figure 6-G4 Maximum entropy analysis of the fs/ps data set for **Ni-Mabiq** in Fig. 6-G3.

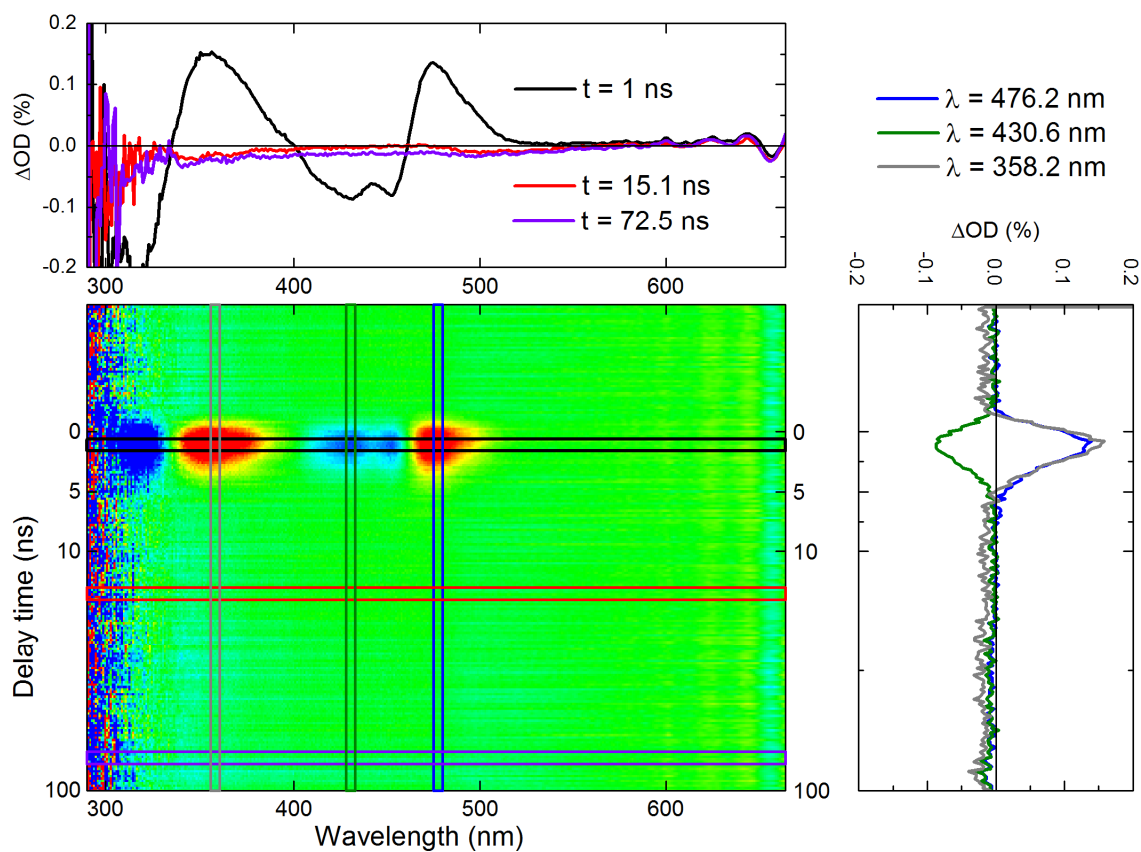


Figure 6-G5 Transient absorption spectra of **Ni-Mabiq** in degassed 1:1 MeCN/THF; 2.5 ns excitation pulse, 300 nJ pulse energy, 450 nm excitation wavelength.

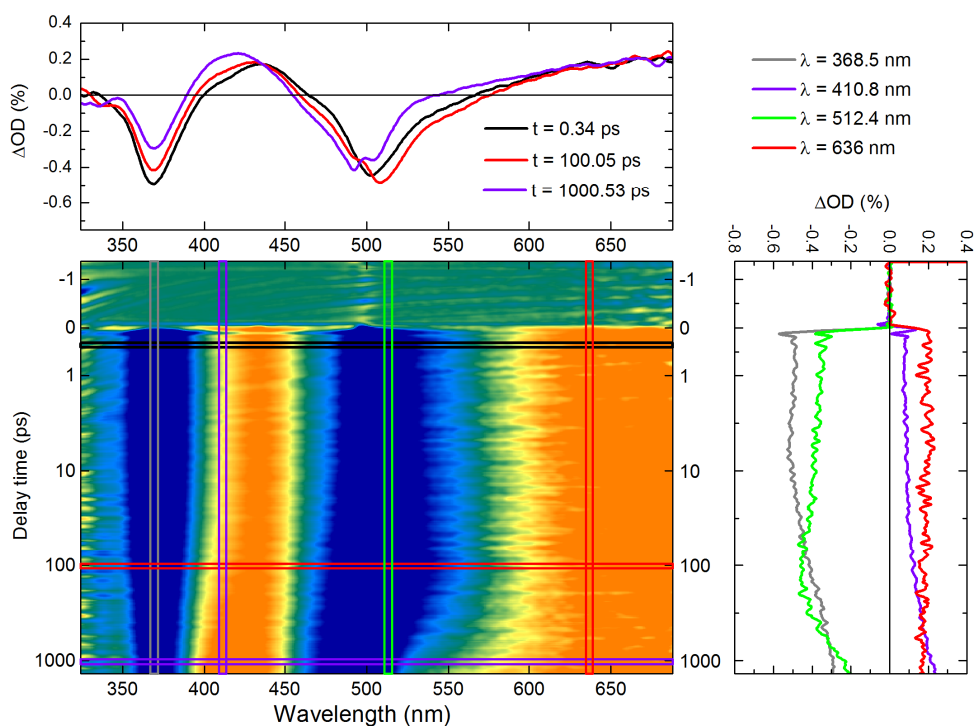


Figure 6-G6 Transient absorption data of a degassed 0.34 mM solution of **Zn-Mabiq** in 1:1 THF/MeCN measured in a 100 μm thick flow cell after excitation with 49 fs pulses centered at 493 nm having a pulse energy of 175 nJ.

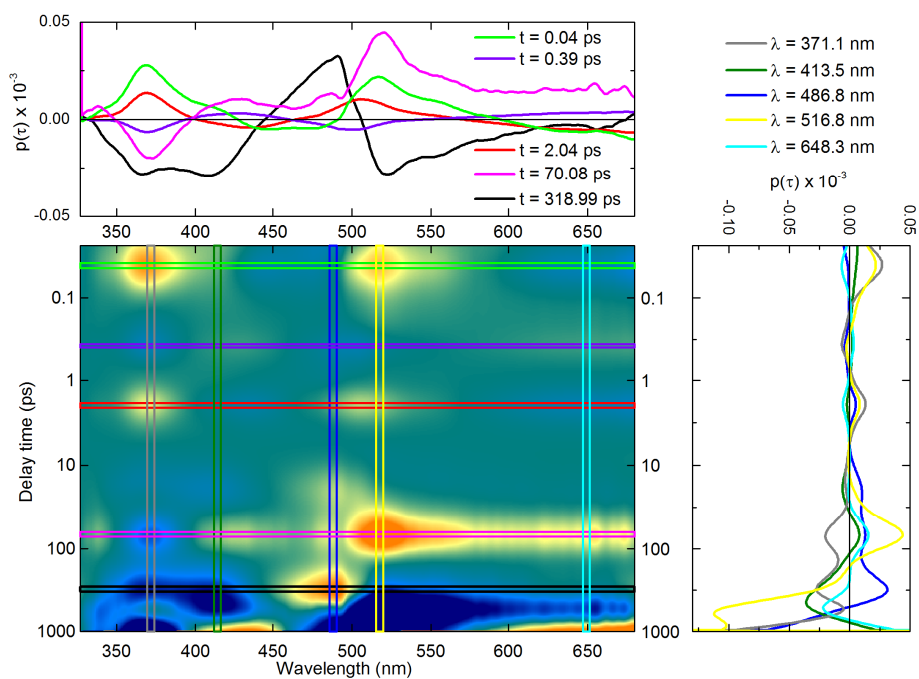


Figure 6-G7 Maximum entropy analysis of the fs/ps data set for **Zn-Mabiq** in Fig. 6-G6.

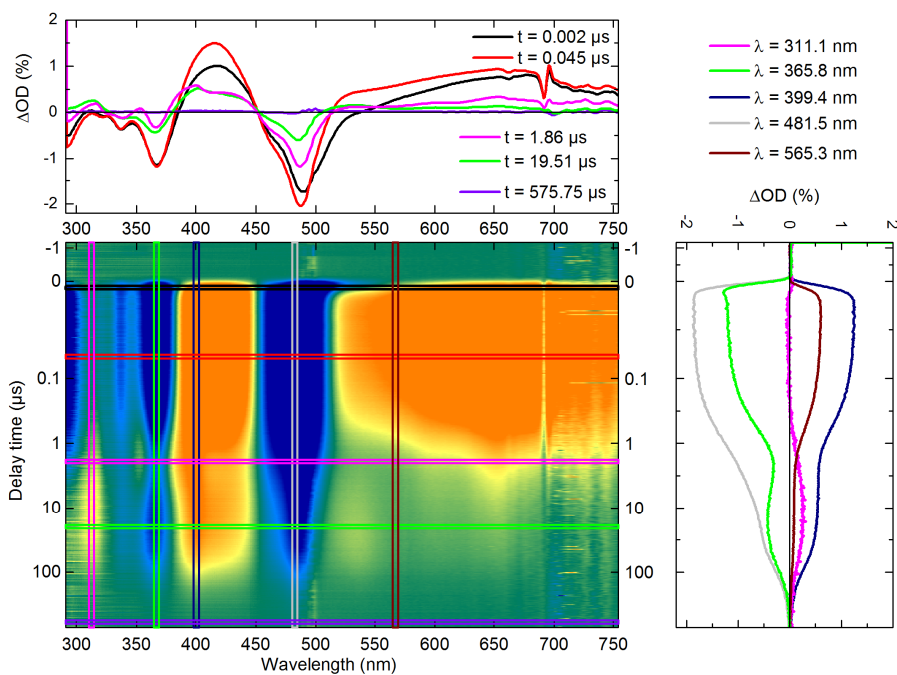


Figure 6-G8 Transient absorption data of a degassed 0.4 mM solution of **Zn-Mabiq** in 1:1 THF/MeCN measured in a 100 μm thick flow cell after excitation with 2.5 ns pulses centered at 493 nm having a pulse energy of 232 nJ.

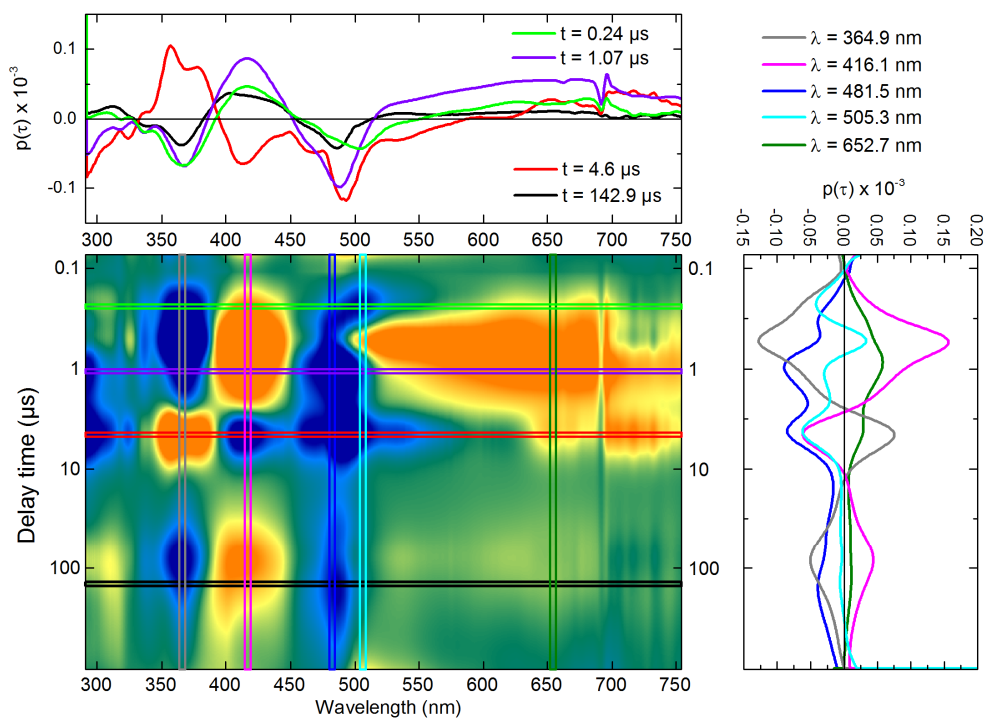


Figure 6-G9 Maximum entropy analysis of the ns/ μs data set for **Zn-Mabiq** in Fig. 6-G8.

7. LED based pump-repump-probe instrument for μs dynamics

7.1 Introduction

The standard transient absorption (TA) experiment uses expensive short pulse laser (fs or ns pulse duration) as a light source [Koe13, Meg09, Rie13, Zew00a]. Such laser based setups are outstanding for the investigation of the ultrafast processes in the fs-regime up to few hundreds of μs [Kov99, Lai08, Meg09]. However, in some reaction systems, the molecular dynamics may spread beyond this limit. This rather slow time scale in the ms-regime or even beyond is typical for intermolecular processes [Zew00a], processes in biological systems [Hau14, Kut17] or long lived intermediates [Li20b, Kut15]. Although an extension up to 20 ms has been shown for the laser based setups [Wil18], the experimental procedure can be regarded as rather cumbersome. In this work a compact LED based pump-repump probe setup is introduced, which is suitable for the investigation of the molecular dynamics in the $\mu\text{s}/\text{ms}$ regime or even beyond. The cost is only a small fraction of the conventional systems.

In the first part of this chapter, the basic concept and components of the setup are described. In the subsequent section, the dynamics of a photocatalytic system is investigated in order to demonstrate the principle of the novel setup. As a model system the photocatalytic reaction originally characterized by the group of Goetz [Nau18a] was chosen and analyzed in detail. The resulting observations are compared with the literature.

7.2 Setup

The compact setup with a footprint of $55 \times 40 \text{ cm}^2$ consists of commercially available parts and some mechanical adapters and electronic interfaces of our own design. All technical details of each component are summarized in Tab. 7-A in Appendix.

The high power LEDs in a pulsed mode [Vol19] are used as a pump source. The light is imaged into the sample using two-inch aspheric lenses. For the re-excitation, the second LED is positioned in perpendicular geometry and the light is reflected with the aid of a dichroic mirror. The sample is illuminated in a flow cell, whereby the flow speed is sufficiently to exchange the volume before the next pump pulse excites the molecules. The transmitted light is detected by a solar cell detector. Since the flow cell has four polished sides, the probe pulse is oriented in perpendicular geometry (see Fig. 7-1).

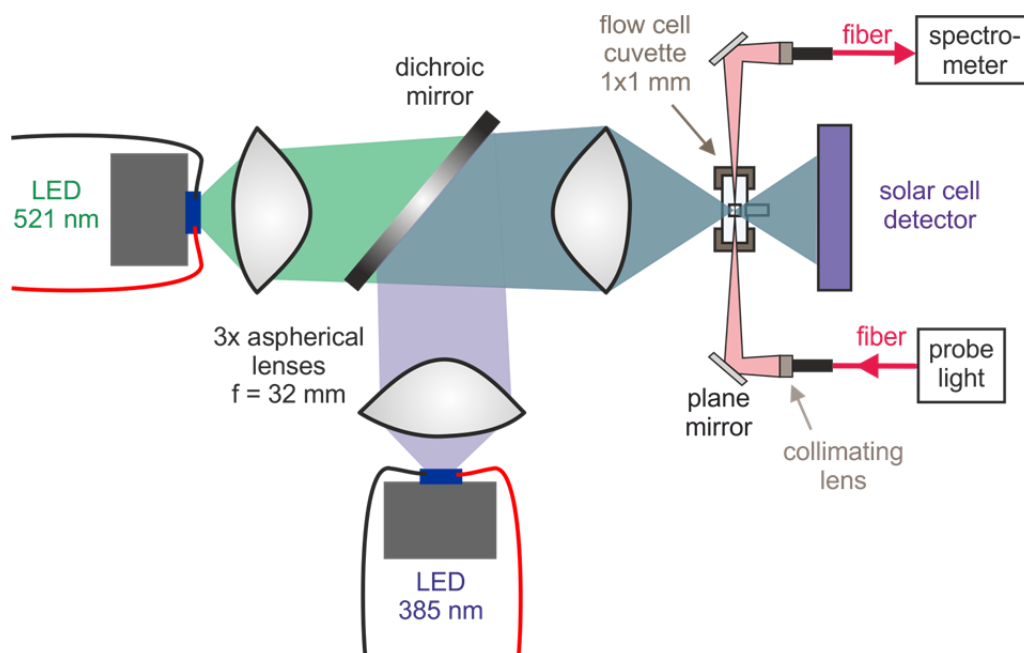


Figure 7-1 Schematic of the LED pump-repump-probe setup.

Conventionally, a short-pulsed laser is used as a typical light source in a transient absorption experiment [Mat13, Meg09, Meg11b, Tia20]. However, the pump laser may lead to a low transient signal in cases, in which the quantum yield of the photospecies is very low. In such conditions the high power LEDs are much more favorable for investigations of the $\mu\text{s}/\text{ms}$ dynamics. In contrary to lasers, μs - or ms -pulsed LEDs can simply accumulate the excited species, which results in the higher concentration of the excited species and hence, the measurement signal is significantly increased.

In addition, LEDs are inexpensive light sources that cover full range between 255 nm and 1050 nm, whereby the emission spectrum can be easily controlled by an additional optical filter. This spectral region covers completely the excitation required for aromatic molecules (UV and visible region) as well as electronic transitions extending into the NIR. The excitation wavelength can be adjusted by a fast and easy exchange of the LED. The position is controlled by two translational stages. The LED can operate in a continuous wave mode or in a pulsed mode. The shortest LED pulses that can be provided are in the region of $2.3 \mu\text{s}$ [Hu20, Vol19].

In order to collect the light emitted from the LED, two identical aspheric lenses with a focal length of $f = 32 \text{ mm}$ are used. The imaged object has consequently identical dimension as the original object. The typical active area of the LED (SMD chip) is about $1 \times 1 \text{ mm}^2$ which

corresponds with the dimension of the cuvette channel (see Fig, 7-2). Additionally, the collection efficiency of the used aspheric lenses is extremely high (more than 50% of the nominal irradiation power) and hence, the LEDs can provide very high illumination power inside the sample.

If a re-excitation is desired, the light is reflected with a long pass filter (color glass alternative (CGA) filter, 50.8 x 50.8 mm², Newport), which is chosen with respect to both excitation wavelengths. The CGA filter appears to be a suitable component for this purpose due to its very high reflectivity for shorter wavelengths as well as very sharp cut-off edge and high transmittance for longer wavelengths.

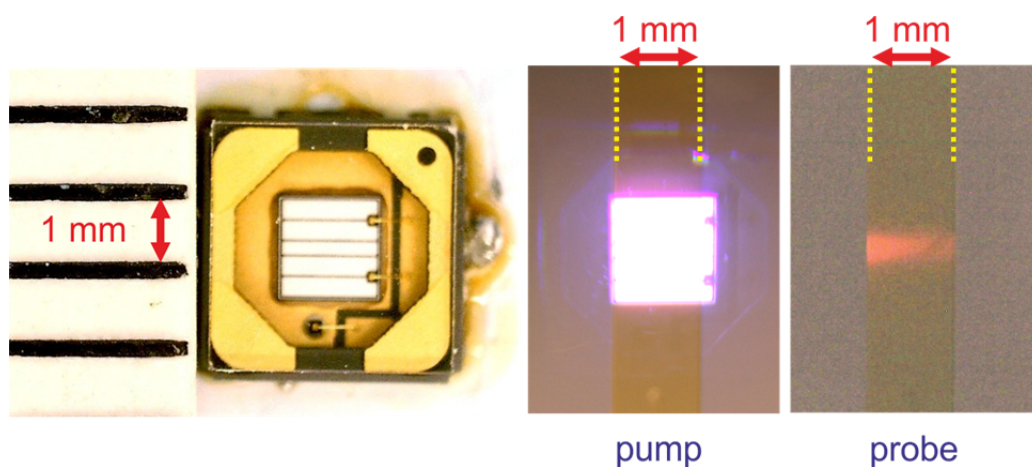


Figure 7-2 (left) SMD chip of LED Seoul Viosys 385 nm (CUN8GF1A) on a 1 mm scale. (middle) Cuvette with 1 mm thickness and channel width with the imaged LED light. (right) Position of the probe light, that overlaps well with the pump pulse. The yellow dotted line is a guide to the eyes that indicates the 1 mm channel of the flow cell.

The probe pulse can originate either from pulsed white LEDs (see below section 7.3) or from a xenon flash lamp (L9455-13, Hamamatsu Photonics K. K.). The flash lamp has a sub- μ s pulse length. As this is shorter than the LED pulse length, the temporal resolution of the new setup is purely given by the LED pulse. The probe light is coupled into the fiber (for the Xe flash lamp: $\varnothing=200\ \mu\text{m}$, high OH, Fiber Patch Cable, Thorlabs Inc.). The probe pulse is subsequently imaged into the sample by collimating lenses (COL-UV/vis, $f = 8.7\ \text{mm}$, Avantes BV). The ideal size of the probe pulse is about $600\ \mu\text{m}$. Since the diameter of the fibers is $200\ \mu\text{s}$, the desired magnification is three. By using the basic lens equation it is straightforward to estimate the imaging distance:

$$\frac{1}{f} = \frac{1}{g} + \frac{1}{b} \quad (7.1)$$

From the magnification $M=3$ can be extracted the following relation: $b = 3 \cdot g$. By inserting this term into the equation (7.1) the following relation is obtained:

$$g = \frac{4f}{3} \quad (7.2)$$

Since the focal length of the collimating lens is $f = 8.7$ mm the required distance between the lens and middle of the cuvette is 34.8 mm. Due to this relatively long optical path, a plain aluminum mirror (10 x 15 mm RAL – UV, QIOPTIQ) is used to reflect the light into the cuvette, see Fig. 7-3. This allows the precise alignment. The imaged probe light and the positioning with respect to pump pulse is shown in Fig. 7-2.

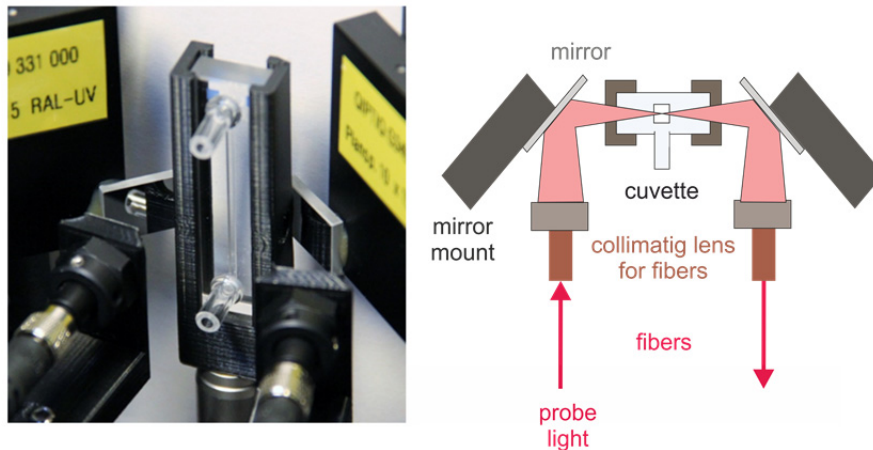


Figure 7-3 (left) Two plain mirrors glued onto the mirror mount are used to reflect the probe light coming from the fiber. (right) Schematics of the light pathway.

The probe light is recollimated by another collimating lens into the fiber and connected to a spectrophotometer (QE Pro, QEP01261, Ocean Insight BV). The delay generator (DG645, Stanford Research Systems) controls the time delay between pump and probe as well as the pulse duration of the LEDs. The data are collected by a LabVIEW program of our own design.

7.2.1 Measurement principle

The spectra are measured with an USB controlled spectrometer with an CCD array (S7301-1006S, Hamamatsu), which is thermoelectric cooled (set to -15 °C). Due to the nature of the

CCD array, the first and last 750 μs of the signal are required for reaching the maximum light sensitivity. This is shown in Fig. 7-4 as a signal ramp. The minimum acquisition time required for measurement of one spectrum is 8 ms. The principle of the data acquisition is demonstrated on a simple example – measurement of the steady state UV/vis spectra.

In order to improve the signal to noise ratio and to consider possible instabilities of the Xe-flash lamp it is reasonable to measure sufficient number of spectra. In this work, 100 spectra are chosen.

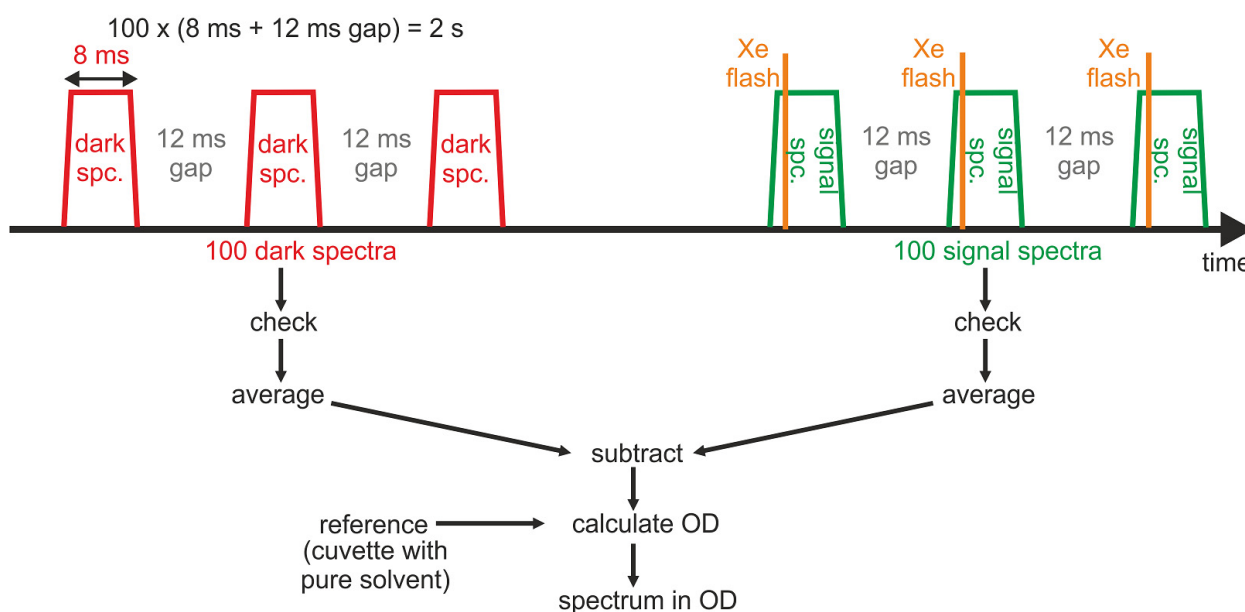


Figure 7-4 Basic principle of the UV/vis measurement using the CCD spectrometer and the Xe flash lamp.

In the first step, 100 dark spectra are measured. Hereby, the stray light, broken pixels, white noise and other derivations are detected. These spectra are measured without the Xe-lamp pulse. Thereafter, 100 spectra of the signal spectra are measured. The light from the Xe-lamp coupled into the fiber passes through the sample dissolved in a cuvette. The recollected transmitted light is directed into the spectrometer. In both cases, 100 taken spectra are controlled (empty or half spectra are not used) and averaged. The averaged dark spectrum is subsequently subtracted from the average signal spectrum and the spectrum in OD is calculated as shown in Fig. 7-4.

For the measurement of the transient absorption, the measurement procedure is shown in Fig. 7-5. Basically, the spectra with and without pump light are measured in transmission

mode for all time delays. The spectra without pump are measured analogous to the previous example for a standard UV/vis measurement. The 100 averaged spectra of the white noise as well as the 100 averaged spectra of the probe light transmitted after the sample are subtracted. This results in the transmission without pump pulse $T_0(\lambda)$. Similarly, the spectra with pump pulse are measured. Here the dark spectra II are monitored under the presence of the pump pulse, whereby the probe pulse is not used. This step enables to consider the white noise, stray light of the LED and fluorescence of the sample. Thereafter, the spectra with defined time delay between pump and probe are taken. The dark II and signal II spectra are averaged, checked for integrity and subtracted. The resulting transmission with pump $T^*(\lambda, \Delta t)$ is used for the calculation of the change in the optical density:

$$\Delta OD = -\log\left(\frac{T^*(\lambda, t)}{T_0(\lambda)}\right) \quad (7.3)$$

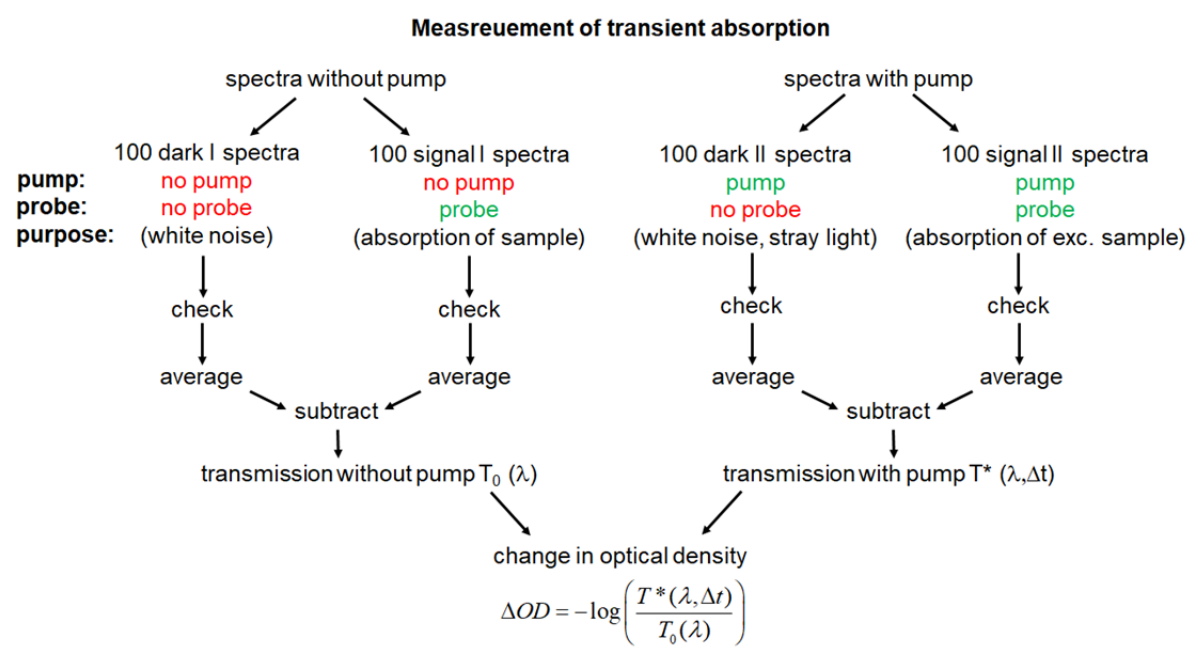


Figure 7-5 Schematics of the transient absorption measurement.

The synchronization between spectrometer, pump LEDs and the Xe flash lamp is ensured by the correct configuration of the delay generator. The summary of the signal amplitudes as well as the pulse durations and delays are summarized in Tab. 7-B in the Appendix.

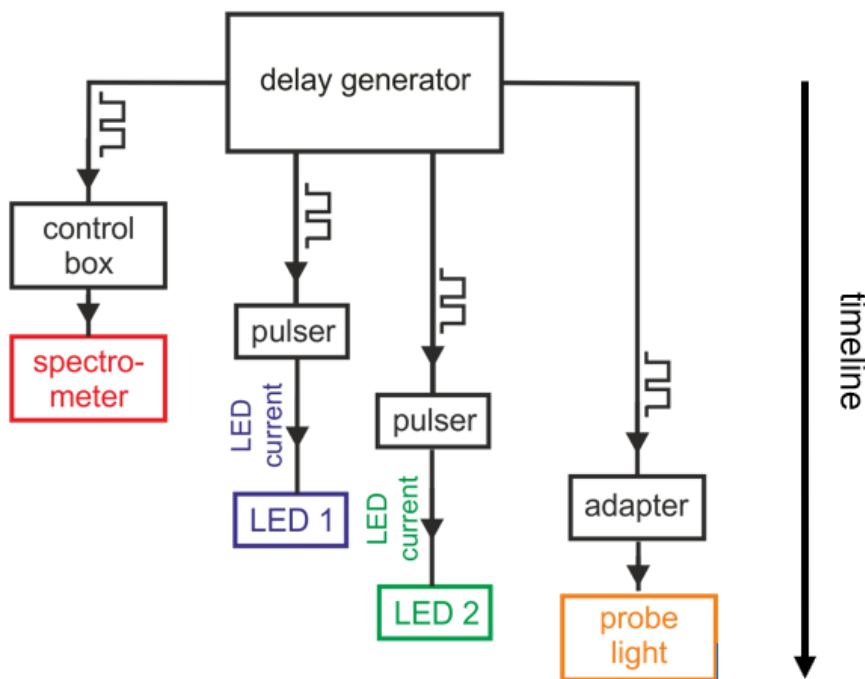


Figure 7-6 Schematics of the signals to control pump-repump-probe measurement.

The first signal triggers the spectrometer. The additional control box between the delay generator and spectrometer introduces an adapter between BNC cable and the 32 pole cable that is compatible with the spectrometer. A pulser of own design [Hu20] is used for intermittent illumination of the LEDs. The LED pulser provides the driving current for the high power LEDs. Hereby, the maximum current is limited according to the LEDs specifications. The last signal triggers the Xe-lamp through an adapter.

7.2.2 Detection of the one electron reduced intermediate

To demonstrate the operation of the introduced setup, the following photocatalytic cycle is investigated. The photocycle was originally described by the group of Goetz [Goe14, Nau17, Nau18a, Nau18b, Nau18c, Nau18d]. It is based on the widespread catalyst ruthenium-trisbipyridyl $[\text{Ru}(\text{bipy})_3]^{2+}$. The catalyst is excited from the ground state (**GS**) using a high power LED (520 nm, S2UHP-T-LED-520, Prizmatix, $P_{\text{illum}} = 1.8 \text{ W}$). The excitation is followed by intersystem crossing and it results in the metal-to-ligand charge-transfer excited state $^3\text{MLCT}$. The natural lifetime of the $^3\text{MLCT}$ state is in competition with the quenching process provided by the ascorbate dianion Asc^{2-} , see Fig. 7-7 left. The ascorbate dianion originates from the ascorbic acid that is deprotonated due to the strong basic conditions ($\text{pH} = 12.7$). The quenching process results in the one electron reduced catalyst (**OER**). The **OER** corresponds to a localized bipyridine radical anion, that has a strong $\pi-\pi^*$ absorption

band in the green region [Goe14], see Fig. 7-7 right. The lifetime of the **OER** intermediate is reported to be several milliseconds [Goe14, Nau18a].

The additional excitation of the **OER** with the second green pulse can eject a solvated electron, whereby the **GS** of the catalyst is recovered. Interestingly, in order to create the solvated electron upon illumination with a green LED the catalyst should be preferably incorporated into the anionic micelle (of sodium dodecyl sulfate; **SDS**) [Nau18b]. The surface of the micelle has a negative charge. The **GS** and ³**MLCT** as dications are embedded into the micelles, near their surface [Nau18a, Sny89]. The quenched form of the ascorbate **Asc^{•-}** is a negative radical anion and hence due to the negative surface of the micelles it is separated spatially from the **OER**. In this way the backreaction, i.e., recombination of the **OER** with the quenched **Asc^{•-}** is suppressed.

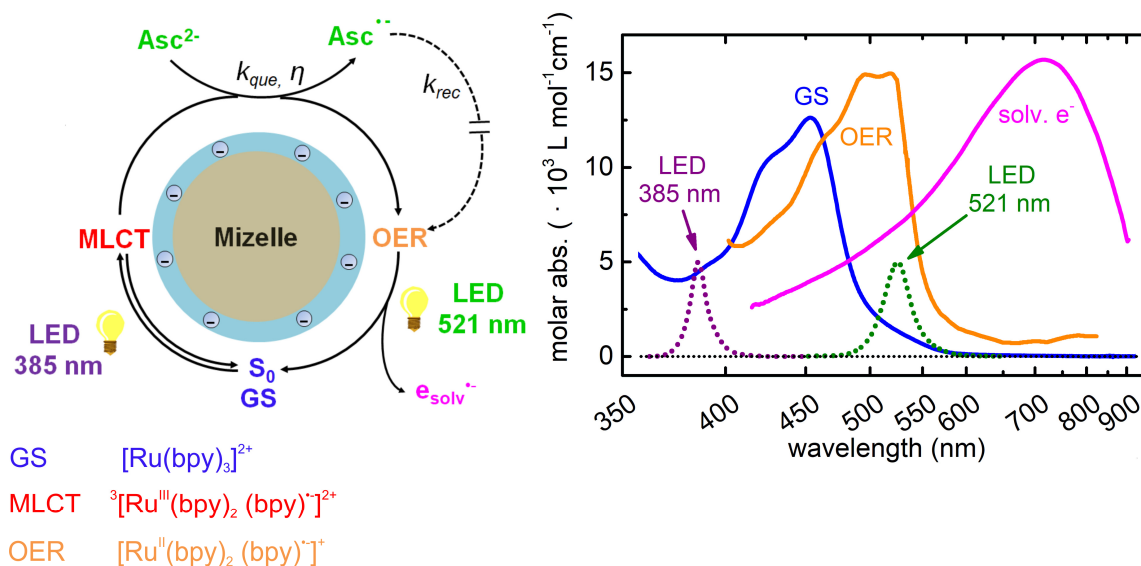


Figure 7-7 (left) Schematics of the reaction mechanism. (right) Molar absorptivities of the species in the photocatalytic cycle [Nau18a]. The purple and green dotted lines represent the excitation light used in this work.

However, in reference [Nau18a] the solvated electron could not be directly observed by spectroscopic methods despite the application of the micelles. The evidence of the solvated electron is here given only indirectly - by monitoring of the subsequent reaction with an additional substrate in form of chloroacetate. In this reaction the solvated electron reacts with the toxic chloroacetate under creation of the harmless acetate. The dechlorination [Bra16, Li12a, Li12b] and defluorination [Par09, Gu16] induced by solvated electrons is a reaction of the utmost interest since this process converts the hazardous waste into non-toxic com-

pounds. On the other hand, the micelles are not required for photoexcitation with a laser and the solvated electron can be in this case spectroscopically observed [Nau17].

In the work of Goetz [Goe14, Nau17, Nau18a, Nau18b, Nau18c, Nau18d], a single color excitation (520 nm) was used. As shown in Fig. 7-7 right, the green light is ideal for the re-excitation of the **OER**, but it is rather unfavorable for the excitation of the **GS** catalyst. Upon illumination with 385 nm LED (CUN8GF1A, Seoul Viosys), the transient signal is larger by more than the factor of 3, which correlates with the molar absorptivity.

In the left panel of Fig. 7-8 the transient absorption data under excitation with the 385 nm LED are shown. The negative signal corresponding to ground state bleach (GSB) is observed around 425 nm, which overlaps with the positive excited state absorption (ESA) around 520 nm. The ESA spreads out into the NIR with a broad positive band with rather modest absorption. This ESA with the dominant electronic transition around 520 nm and weak absorption in the NIR corresponds to the **OER** as reported in the literature [Mal78, Mie82].

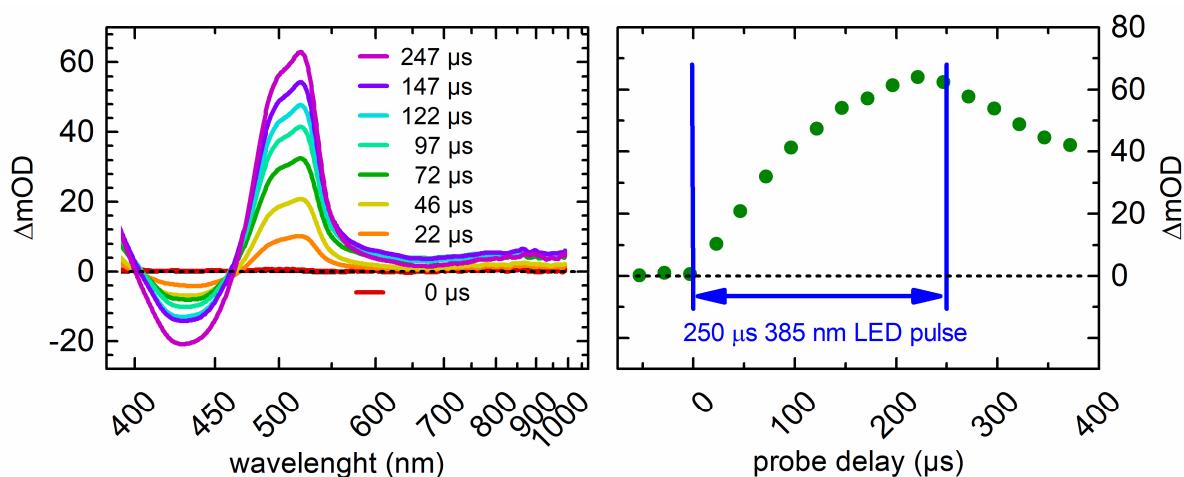


Figure 7-8 (left) Transient absorption spectra using 385 nm LED with 250 μs pulse duration. In this special case the delay time $\Delta t=0$ is defined there, where the pump pulse temporally begins, not ends. The experimental details can be found in Tab. 7-C in Appendix.

The right panel of Fig. 7-8 shows the accumulation of the **OER** due to the 250 μs pulse duration. Here, the detected signal reaches the maximal value of above 60 mOD. An even higher concentration of the **OER** is reached with prolonged pulse duration. As demonstrated in Fig. 7-9 the accumulation of the **OER** reaches the saturation with the LED pulse duration of about 6 ms. For a reasonable excitation it is suggested to use the value at which 80% of **OER** is reached. In this special case the pulse duration corresponds to 1.1 ms.

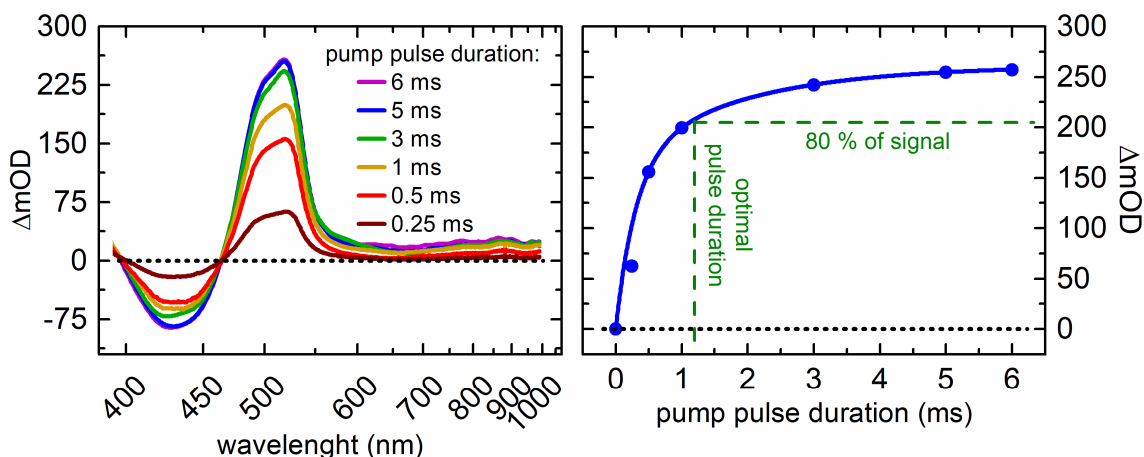


Figure 7-9 (left) Maximum transient absorption signal upon 385 nm LED excitation with various pulse durations. (right) Effect of the pulse duration on the transient absorption signal. The experimental details are summarized in Tab. C in Appendix.

The detected TA signal is a sum of GSB, stimulated emission (SE) and intermediate species spectra, i.e., the **OER** spectrum and that of the ascorbate radical anion $\text{Asc}^{\bullet-}$. In this special case, the stimulated emission does not contribute to the signal, since it decays on the sub-ps scale [Bha02, Wal05]. By subtracting the correct amount of the GSB from the TA signal it is possible to obtain the sum of the **OER** and $\text{Asc}^{\bullet-}$ spectra. Hereby, the method developed by Thulstrup, Eggers and Michl [Mic70a, Mic70b, Mic87] is applied, in which the second derivative of the specific vibronic feature is considered in order to obtain the correct scaling factor for the subtraction of the GSB. Since the concentration of **OER** and $\text{Asc}^{\bullet-}$ is expected to be approximately the same, the pure **OER** spectrum can be straightforward extracted, see orange line in Fig. 7-10 left. The spectral bands as well as the molar absorptivity of **OER** gives an exceedingly good agreement with the literature (see Fig. 7-10) [Nau18a].

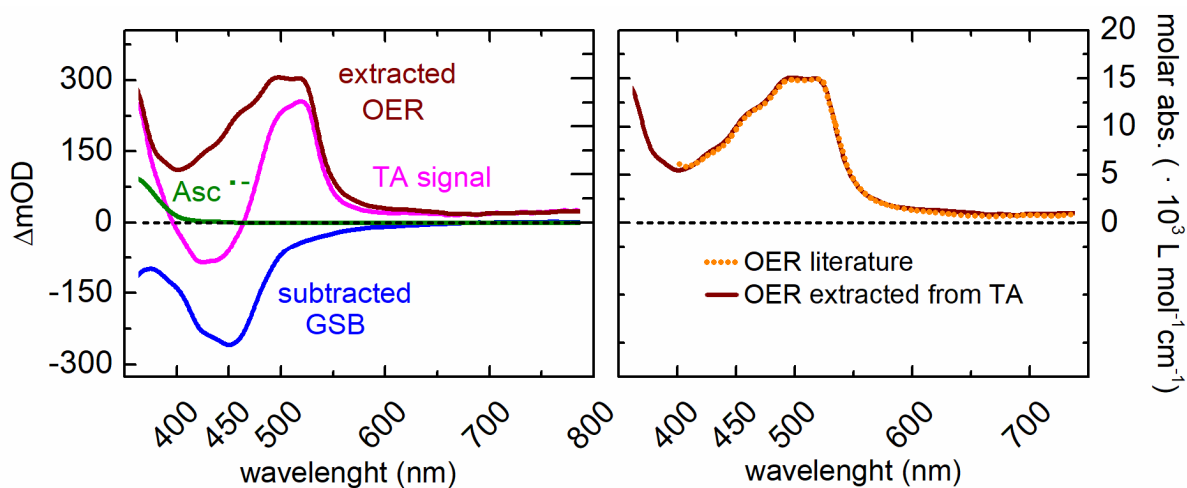


Figure 7-10 (left) Spectral decomposition of the TA signal with 3 ms pulse duration used to extract the **OER** spectrum and its calculated molar absorptivity shown on right. (right) Comparison of molar absorptivity for **OER** extracted from TA measurement with the literature [Nau18a].

The lifetime of the **OER** (see Fig. 7-11) is determined from the kinetic trace at 519 nm, which corresponds to the wavelength with the signal maximum. The calculated lifetime is 5.8 ms lies fairly within the range of several milliseconds published in the literature [Goe14, Nau18a, Nau18b, Nau18c].

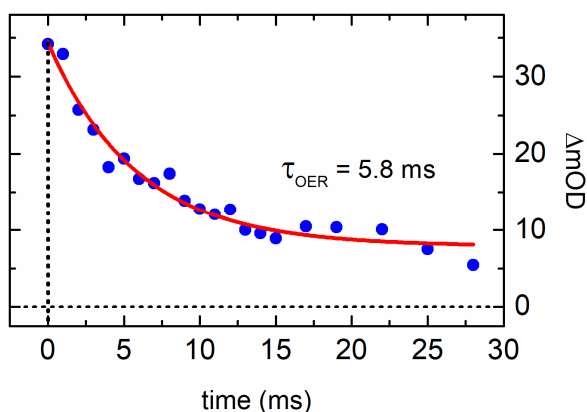


Figure 7-11 Exponential decay of TA signal at 519 nm used for the determination of the **OER** lifetime (5.8 ms).

For the pump-repump probe experiment, the additional green LED for the repump was used (521 nm, OSOLON GT CS8PM1.13, Osram Licht AG). However, the signal corresponding to the solvated electron was not yet observed. The identical observation was reported by Goez, when using LED as an excitation source. For the future experimental work it is recommend-

ed to degas the sample, since the solvated electron may react with the oxygen [Bux88]. Hereby, it is worth to mention, that simple inlet of the protective gas directly into the solution is not favorable due to the strong foaming properties of the SDS micelles. The created foam remains stable for hours, which causes difficulties for the flow cell. The sample can be alternatively prepared directly in the glove box or it can be degassed by the freeze-pump-thaw method, which is rather cumbersome.

However, according to the recent work of Goez, the solvated electrons can be created under micelle-free conditions [Nau18d]. In this reaction, the ascorbate as quencher is replaced with the dianionic form of the uric acid Ur^{2-} . This replacement is beneficial for the photostability of the reaction, since the ascorbate degrades and turns brown under prolonged illumination independent on presence of micelles [Nau18b]. The degraded ascorbate absorbs the photons that are originally intended for the excitation of the catalyst.

The primary role of the micelles was to suppress the recombination of **OER** with the quencher $\text{Q}^{\bullet-}$ by its anionic surface. In the latest micelle-free reaction [Nau18d], the catalyst has attached carboxylate groups which leads to pentaanionic **OER** (in contrast to single anionic **OER**). Additionally, the urate as a quencher is advantageous for the photoreaction. After the urate dianion Ur^{2-} donated the electron to the catalyst, the radical anion form $\text{Ur}^{\bullet-}$ is immediately deprotonated to $\text{Ur}^{\bullet 2-}$ due to the lower acidity in comparison to $\text{Asc}^{\bullet-}$, which remains in this form. The double negative charge of the radical $\text{Ur}^{\bullet 2-}$ leads to enhanced repulsing forces to the pentaanionic **OER** (or anionic micelles) and thus, the undesired recombination back to starting materials is considerably suppressed. The lifetime of the **OER** is hence significantly increased, whereby an interesting observation was reported. The decay of **OER** is increasingly slowed with prolonged times and above 10 ms it appears to reach some specific level of concentration, at which the **OER** remains stable [Nau18b].

Since the lifetime of the **OER** correlates with the probability to be re-excited with the second photon, this may be beneficial for the detection of the solvated electron. As mentioned in reference [Nau18a], the solvated electron upon illumination with LED could not be spectroscopically observed due to its low concentration. This modified reaction may contribute to enhanced concentrations of solvated electron and hence its direct detection.

7.3 Outlook

As shown on the example above the current configuration of the setup enables to trace successfully molecular dynamics in the $\mu\text{s}/\text{ms}$ regime. In the next generation of the setup, it is intended to improve the probe light as well as apply a software triggered USB pulse through the special digital input/output interface - PIO adapter (USB-PIO, BMC Messsysteme GmbH). Hereby, the one pulse from the PC can be amplified to three pulses with $20 \mu\text{s}$ pulse duration, which can control the triggering of the pump LED, probe light and the spectrometer. Consequently, the measurement procedure could be easier automatized and controlled.

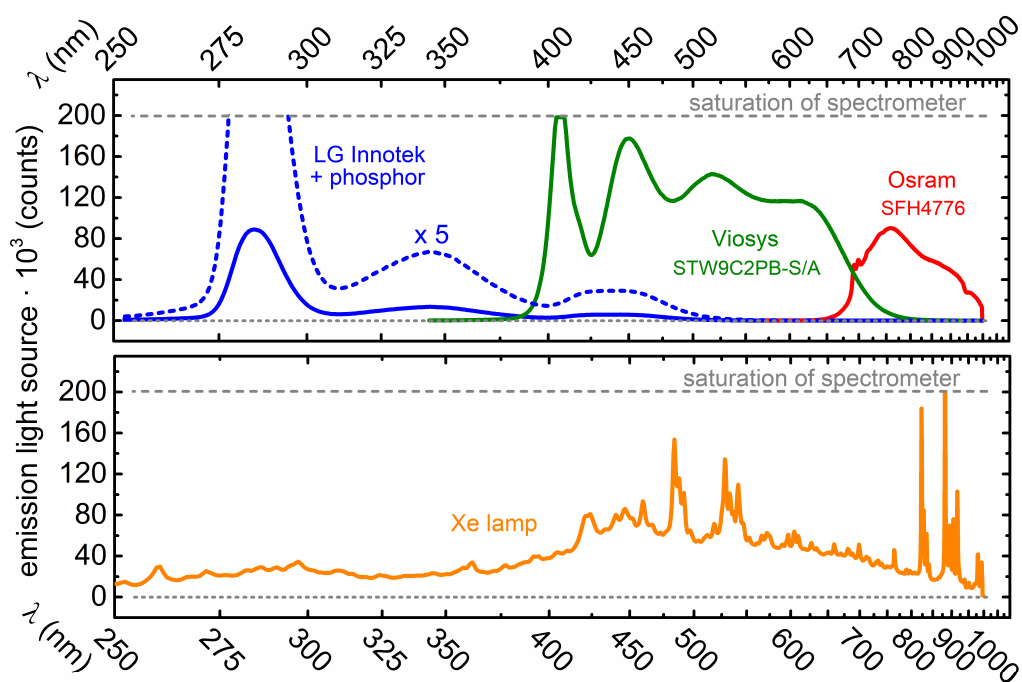


Figure 7-11 Spectral distribution of the white LEDs (top panel) and Xe flash lamp (bottom panel). The LEDs were coupled into the fibers using two Fresnel lenses with focal length of 10 mm and 15 mm. The LEDs were pulsed using driving current 1400 mA (blue line), 300 mA (green line) and 1000 mA (red line) and pulse duration of $20 \mu\text{s}$. Due to the short pulses, the driving current can be overdriven to about double of the max. value reported in the data sheet for cw-conditions.

An ideal broadband probe light spreads over the whole spectrum uniformly without any sharp intensity peaks. The Xe flash lamp has optimum distribution between 400 nm and 750 nm, but rather modest emission in the UV region. Additionally, the sharp signals in the NIR leads to a saturation of the detector. An elegant alternative to the Xe lamp represents a

white LED, which can be easily pulsed and coupled into the fiber. The LEDs are precisely glued in the middle of an Al block with dimensions 38 x 38 mm². Using two Fresnel lenses with short focal lenses ($f = 10$ mm, dia. = 12.7 mm and $f = 15$ mm, dia. = 25 mm) the light is coupled into the 600 μm high OH fiber (M114L01, Thorlabs Inc.).

Most of the white LEDs are based on the wavelength conversion. A typically used UV or blue LED excites a phosphor, which emits in the blue/yellow region. The resulting mixture gives a characteristic white spectrum. This phenomenon was also used for the customization of the UV-V LED (LEUVA66H70HF00, 100 mW, LG Innotek), which has an additional phosphor layer on the top of the SMD chip provided by Dr. Licht GmbH. The resulting spectrum is shown in Fig. 7-11. The other two LEDs are commercially available (Sunlike STW9C2PB-S/A, Seoul Semiconductor Co Ltd. and SFH4776, Osram Licht AG).

As shown in the top panel of Fig. 7-11, white LEDs have relatively uniformly distributed spectra without any intensity spikes. The emission intensity is higher by more than a factor of two for 20 μs long LED pulses which leads to an improved measurement accuracy.

In conclusion, since the majority of processes relevant for the photocatalysis occurs on the rather longer $\mu\text{s}/\text{ms}$ time scale [Zew00a], it is of utmost interest to establish a setup that is simple to use and that enables to give a deeper understanding of such photoinduced processes. In this work was introduced a compact LED based pump-repump probe setup for the measurements of the molecular dynamics in this time regime, which consists of inexpensive commercially available components and hence it can be easily reproduced and used in any laboratory conditions.

Appendix for Chapter 7

Appendix 7-A

Table 7-A Components used in the LED-based pump-repump probe setup.

component	manufacturer	type	serial number
translation stage for LED	Thorlabs	dovetail Translation Stage	DTS25/M
LED 385 nm	Seoul Viosys	near UV LED- 385nm	CUN8GF1A
LED 521 nm	Osram	Oslon SSL 80	GT CS8PM1.13
aspheric lens	Thorlabs	2" aspheric lens, f = 32 mm	ACL 50832U-A
CGA Filter	Newport	20CGA-435	HE654
plane mirror	QIOPTIQ	10×15 mm RAL – UV	G340 331 000
fiber optics	Avantes	collimating lenses	COL-UV/vis
fiber (in for Xe lamp)	Thorlabs	Ø200 µm high OH fiber patch cable	M92L02
fiber (out for Xe lamp)	Thorlabs	Ø200 µm solarization- resistance patch cable	M112L02
cuvette	Hellma	1×1 mm flow cell	custom made
pump drive	Masterflex	peristaltic pump	77390-00
spectrometer	Ocean Insight	QE Pro	QEP01261
digital delay/pulse generator	Stanford Research Systems		DG645
Xenon flash lamp	Hamamatsu Photonics		L9455-13

Appendix 7-B

Table 7-B Characterization of the signals required for synchronization of each component in transient absorption measurement.

	spectrometer	LED 1	LED 2	Xe lamp
amplitude	3 V	2 V	2 V	2 V
pulse duration	100 μ s	250 μ s	100 μ s	100 μ s
time delay between pulses	$T_{\text{spectrometer}} = 0$ s	$T_{\text{LED1}} = T_{\text{spectrometer}} + 1.5$ ms	$T_{\text{LED2}} = T_{\text{LED1}} + 200$ μ s	$T_{\text{Xe}} = T_{\text{LED2}} + \Delta T$ ($\Delta T = 0$ up to 100 ms)
repetition rate			10 Hz	

Appendix 7-C

Table 7-C Specification of the solution used for the pump-(repump) probe measurements.

substance	concentration
Tris-(2,2'-bipyridyl)-ruthenium(II)-chlorid Hexahydrat	1 mM
Na-L-Ascorbate	100 mM
Natriumdodecylsulfat	50 mM
solvent	water
pH	12.7
cuvette	1 mm
illumination power 385 nm LED (CUN8GF1A, Seoul Viosys), driving current 4.3 A for 250 μ s pulse duration, 10 Hz repetition rate	1.2 mW*
illumination power 521 nm LED (GT CS8PM1.13, Osram), driving current 4.3 A for 100 μ s pulse duration, 10 Hz repetition rate	1.7 mW**

*peak power = 1.2 W, **peak power = 1.7 W

8. Summary and Outlook

Light-driven reactions continue to attract the attention of photophysicists and photochemists. To gain a deeper understanding of photosystems, it is essential to have and use intuitive analytical devices in the laboratory that allow the rapid determination of important quantities or spectral features.

One of the particularly important quantities is the reaction quantum yield (RQY) that reports the fraction of absorbed photons that actually lead to the desired product. The RQY is an indicator of the efficiency of the photoinduced reactions. Although actinometry is currently the accepted standard for RQY determination, it has known limitations and shortcomings.

The overall concept of a RQY measurement, its accuracy and cost were investigated in this work. As a result, the Quantum Yield Determination Setup (QYDS) [Meg10] was completely rebuilt. The modernized QYDS version ensures rapid determination of RQY with a relative error of less than 5% for all types of photospecies: molecular switches, photochemical and photocatalytic systems. The QYDS setup and approach has been individually validated for all above photoreaction types, including the validation by different users in different cities.

The basic principle of the QYDS setup is the controlled illumination of the sample with LED light and two fused silica best-form lenses that image the LED light onto the sample. The commercially available LEDs fully cover the range between 250 nm and 1050 nm.

The modular setup can be customized to the requirements of user. The collection efficiency of the best form lens system is about 10% and it can be increased to above 50% if a 2" aspheric and a 2" plano convex lens are combined. This results in more than 1 watt of illumination power in the sample in the range between 360 nm and 470 nm.

The number of absorbed photons is measured directly with a NIST-traceable powermeter. Unlike actinometry, no additional time-consuming calibration experiments with additional chemicals are required. The introduction of the solar cell detector (SCD) as an alternative detector to the powermeter extends the power range of the detection.

The SCD as a low-cost, large-area detector is suitable for measuring low illuminance levels below 1 mW for all wavelength ranges from deep UV-C (290 nm) to NIR (900 nm). The combination of the SCD and the powermeter allows tracking of transmitted light from tens of μW to the range of one watt. The SCD can be considered as one of the most important

components of the QYDS.

The precise measurement of the low power ranges with SCD is only possible by converting the electric current into a voltage. This conversion is ensured by a specially developed I/U converter. The resulting voltage is permanently monitored by a digital oscilloscope.

The illumination light is blocked by an electronically controlled mechanical shutter. The electronics of the shutter are housed in the "QYDS box" together with the I/U converter.

The QYDS is not only an opto-mechanical device. It can also be considered as an approach that considers every single step and action during and after the measurement. It is the combination of setup and measurement procedure that makes the QYDS method so powerful and suitable to replace the actinometry.

For this purpose, a set of MathCad files were developed to guide the user through the entire measurement and evaluation procedure. All devices as well as the measurement log file required for the evaluation are controlled/generated via a graphical user interface (GUI) of our own design programmed in LabView 2016.

The QYDS approach recommends illuminating the sample under quasi-equilibrium conditions, which is ensured by constant stirring and illuminating the sample for at least one minute. Here, different stirring bars and stirring speeds were tested, and the optimal conditions for each cuvette type were defined and summarized.

The results also showed that the spectrophotometer can be used optimally. The so-called two-cuvette method reduces the drifts in the baseline of the UV/vis spectrum. Since the RQY is highly dependent on the accurate determination of the number of product molecules formed, it is of utmost interest to ensure accurate measurement of the UV/vis spectra.

According to our experience, the most challenging step in the RQY appears to be determination of the UV/vis spectrum of the product. Thus, four different approaches for extraction of the meta-stable species from the photostationary state (PSS) are summarized and discussed in detail.

The QYDS approach recommends the full illumination of the sample until the PSS is reached. For the subsequent analysis, the entire data set is used, covering the entire spectral range. After spectral decomposition of the UV/vis spectra to determine all species concentrations, the data are fitted to a kinetic model by numerically solving the differential equations for the time evolution of the concentrations.

The QYDS method is not limited to two-species systems. As shown for **Ni-** and **Zn-Mabiq**, evaluation of the complete data can suggest and differentiate rather complex reaction models with complete identification of the side product.

In summary, the QYDS setup and approach is a powerful method that not only allows fast and easy determination of the RQY, but also provides valuable information about the photo-reaction and its mechanism. As an outlook, we believe that deep understanding of the QYDS concept can even lead to a relative error of less than 3%.

The development of new devices of our own design usually begins where commercially available (often expensive) standard devices reach their limits. This was also the case with classic fluorescence spectrometers, which cannot meet measurement requirements such as the detection of extremely weak signals or easy detection in the NIR or IR range.

Our own-designed high end fluorescence setup with improved sensitivity is able to detect even very short-lived and weak fluorescence signals due to sub-ps relaxation after optical excitation. This is only possible by combining optimal excitation with LED light, sophisticated collection of the fluorescent light, and accumulation of the molecules in the excited state by using the constant-wave mode of the LED light instead of the laser excitation. In contrast to laser excitation, LED excitation results in species accumulation, which leads to a higher concentration of the excited species and a significant increase in the measurement signal.

The latter principle of accumulation of excited states has also been used in a second instrument. The LED-based Pump-Repump-Probe instrument was developed with the goal of tracking the μs time scale and beyond. This time scale is relevant to intermolecular reactions and long-lived intermediates. Currently, there is no commercially available instrument for this purpose. Our device was able to accumulate and detect 250 mOD of the intermediate state in the photocatalytic process with ruthenium trisbipyridyl.

As shown in this work, it is possible to design and build high-end devices at reasonable effort and cost that can push the known limits of commercially standard devices even further. Using such devices, it is possible to gain a deeper understanding of photosystems and to simplify everyday laboratory routine measurements.

Ultrafast transient absorption (TA) spectroscopy has been applied to comprehensively study a number of photosystems. The TA setup of own design is suitable for fs/ps dynamics and covers all excitation wavelengths between 220 nm and 740 nm [Wil97, Ric00, Cer03]. Typi-

cal detection with the probe light is between 285 nm - 720 nm, but if desired, the wavelength range can be extended to 225 nm - 1700 nm [Rie13]. The combination of 20 μ OD sensitivity of the TA spectra [Bra14] with the accuracy of about sub-30 fs [Meg09] (depending on the length of the pump pulse) makes the transient absorption setup very versatile. The fs/ps TA measurements can be extended to the ns/ μ s time regime by using a tunable optical parametric oscillator (OPO) from EKSPLA [Mat13].

The typical analysis of transient absorption spectra assumes a bilinear model in which the "transient spectra" are time-independent DADS or species spectra and the time constants are independent of the spectral position. Or in other words, every TA spectrum is a linear combination of the particular excited state of reactant, product and intermediates (if present). This is common in the so-called "global analysis" [Sto04, Van04, Fit06, Ruc12, Sla15]. However, this method reaches its limits when a band shift phenomenon occurs. For such cases an alternative method - spectral parameterization - is introduced.

The spectral parameterization uses a suitable set of functions in order to fit the spectral features [Wil18]. The careful evaluation of the fitting parameters, e.g., amplitude or central wavelength, provides more information about the dynamic process [Wil23]. As shown in the example of pyridinium-based betaines, the solvation time extracted from the band shifts gives good agreement with the solvation time in reference [Hor95]. In addition, the spectral parameterization also provides information about the real state population, since it is proportional to the integral of the associated fitting function.

Another model-free method for evaluation of the TA data is maximum entropy analysis [Kut13]. It provides information about the number of expected decay constants that can be extracted from probability density map. Although maximum entropy analysis and spectral parameterization have proven to be extremely beneficial for TA data analysis in this work, these methods are rarely found in standard applications. This is very unfortunate, since the effort involved is relatively manageable.

In this work all three types of photoreactions were studied: molecular switches, photochemical and photocatalytic reaction.

From the family of molecular switches, the diarylethene (DAE)-based molecules **TSC** and **MTSC** were studied using the ultrafast TA spectroscopy and QYDS approach. The results show similar dynamics to other DAE species. Here, the choice of solvent has an influence on the molecular dynamics and RQY. A higher RQY was observed for acetonitrile than for eth-

anol. It is assumed that the presence of H^+ in protic solvents negatively affects the pre-orientation of the molecule and sterically disadvantages the cyclization process. The time constants for cyclization spread from ca. 6 ps to 20 ps.

On the other hand, in the case of the cyclo-reversion reaction, the solvent has a rather modest influence (0.5 ps for acetonitrile versus 0.7 ps for ethanol). Interestingly, the ultrafast reactions are not automatically associated with highly efficient processes. Although the bond cleavage here occurs on a sub-ps time scale, the RQY is still below 1%. This can be explained as follows: C-C bond cleavage can be very fast, but since a rotational motion proposed for the spatial separation of the two associated carbons is rather slow, they remain close to each other and the bond is restored.

In this work, the first photochromic coordination complex of DAE and POM was characterized. The system undergoes photoisomerization upon illumination with solely visible light, unlike the non-coordinated DAE parent system. Since the RQY is rather modest at about 1%, it is assumed that a significant population returns to the ground state without isomerization. To increase the effectiveness of photoisomerization, further optimization of the dimension and charge of the POM as well as modifications in the DAE structure are necessary.

As a representative of the photochemical reaction, the decarboxylative photomacrocyclization of N-phthaloylated GABA derivatives was studied. They undergo photocyclization upon illumination with 300 nm light. The RQY ranges from 15% to about 48% and depends on the nature of the substituents on the GABA chain. Interestingly, the analysis revealed a strong influence of the amount of potassium carbonate on the RQY and the presence of the side reaction. The presence of the side reaction was first observed during the QYDS measurement and evaluation. The combination of QYDS approach, TEM method and NMR enabled to identify and quantify the side product.

As a photocatalytic reaction, the photoinduced properties of **Ni-** and **Zn-Mabiq** were investigated and compared. The TA measurements as well as QYDS results showed that the metal center has a profound influence on the molecular dynamics and photocatalytic activity.

The effects of diverse types of quenchers were studied in the case of **Ni-Mabiq**, since this is the first step of the possible photocatalytic reaction. The analysis revealed an overly complex mechanism with different possibilities of back reactions and a side product. This mechanism could be determined using the QYDS approach.

Both **Mabiq** systems were used in two types of reactions to photocatalytically synthesize the

desired products. Both **Ni-** and **Zn-Mabiq** act as photocatalysts with a chemical yield of over 80% for **Ni-Mabiq** and about 30% for **Zn-Mabiq**. The **Zn-Mabiq** with less complex dynamics was expected to favor the photoredox activity, but the instability of the reduced form hinders the reaction. The partial metal character of the **Ni-Mabiq^{red}** makes the system robust against the degradation. Here, the initial ligand-centered singlet state relaxes into a metal-centered triplet state. The reactive final state has CT character. Hence, it is of great interest to improve the stability of the backbone structure of ligands or to implement the second metal center [Mue88]. This would lead to further improvements of **M-Mabiq** systems that may become an interesting earth-abundant catalyst in various photoredox reactions.

In conclusion, in this work all photoreaction types were investigated using ultrafast TA spectroscopy and QYDS approach. Additionally, various devices for understanding of the molecular dynamics were developed. However, it is important to note that high-end machines alone are not an automatic guarantee of high-quality analysis and results. It is the combination of deep knowledge of the measurement processes, post-processing and analysis of the data. Therefore, the selection of the appropriate measurement approach and analysis method should be made carefully.

9. References

- [All00] J. M. Allen, S. K. Allen, S. W. Baertschi, *J. Pharm. Biomed.* **2000**, *24*, 167-178.
- [Alo14] S. Aloise, R. Yibin, I. Hamdi, G. Buntinx, A. Perrier, F. Maurel, D. Jacquemin, M. Takeshita, *Phys. Chem. Chem. Phys.* **2014**, *16*, 26762-26768.
- [Ame84] American Association for the Advancement "Notes and News", *Science*, **1884**, *3*, 64, 527.
- [Ans15] P. Anstaett, A. Leonidova, E. Janett, C. G. Bochet, G. Gasser, *ChemPhysChem* **2015**, *16*, 1863-1866.
- [Asa04] Y. Asano, A. Murakami, T. Kobayashi, A. Goldberg, D. Guillaumont, S. Yabushita, M. Irie, S. Nakamura, *J. Am. Chem. Soc.* **2004**, *126*, 38, 12112-12120.
- [Ass18] F. F. de Assis, X. Huang, M. Akiyama, R. A. Pilli, E. Meggers, *J. Org. Chem.* **2018**, *83*, 10922-10932.
- [Bae13] K. J. Baeg, M. Binda, D. Natali, M. Caironi, Y. Y. Noh, *Adv. Mater.* **2013**, *25*, 4267-4295.
- [Bah16] A. Bahamonde, P. Melchiorre, *J. Am. Chem. Soc.* **2016**, *138*, 8019-8030.
- [Bal19] V. Balevicius, Jr., T. Wei, D. Di Tommaso, D. Abramavicius, J. Hauer, T. Polivka, C. D. P. Duffy, *Chem. Sci.* **2019**, *10*, 4792-4804.
- [Ban09] P. Banerjee, A. Company, T. Weyhermüller, E. Bill, C. R. Hess, *Inorg. Chem.* **2009**, *48*, 2944-2955.
- [Ban12] H. M. D. Bandarab, S. C. Burdette, *Chem. Soc. Rev.* **2012**, *41*, 1809-1825.
- [Bar18] E. Barrez, G. Laurent, C. Pavageau, M. Sliwa, R. Métivier, *Phys. Chem. Chem. Phys.* **2018**, *20*, 2470-2479.
- [Bar62] S. Barr, *Infrared Physics* **1962**, *2*, 67-73.
- [Bau18] B. Baudisch, "Time resolved broadband spectroscopy from UV to NIR: Beneficial Use of the Coherent Artifact and Pyrene Dynamics" Dissertation, LMU Munich **2018**.
- [Beh11] A. A. Beharry, G. A. Wooley, *Chem. Soc. Rev.* **2011**, *40*, 4422-4437.

- [Ben98] A. T. Bens, D. Frewert, K. Kodatis, C. Kryschi, H.-D. Martin, H. P. Trommsdorff, *Eur. J. Org. Chem.* **1998**, 2333-2338.
- [Bha02] A. C. Bhasikuttan, M. Suzuki, S. Nakashima, T. Okada, *J. Am. Chem. Soc.* **2002**, *124*, 8398-8405.
- [Bir53] P. P. Birnbaum, J. H. Linford, D. W. G. Style, *Trans. Faraday Soc.* **1953**, *49*, 735-744.
- [Bor79] P. Bortolus, S. Monti, *J. Phys. Chem.* **1979**, *83*, 6, 648-652.
- [Bow76] W. D. Bowman, J. N. Demas, *J. Phys. Chem.* **1976**, *80*, 21, 2434-2435.
- [Bra07] S. E. Braslavsky, *Pure Appl. Chem.* **2007**, *79*, 293-465.
- [Bra09] M. Bradler, P. Baum, E. Riedle, *Appl. Phys. B* **2009**, *97*, 561-574.
- [Bra14] M. Bradler, E. Riedle, *J. Opt. Soc. Am. B* **2014**, *31*, 1465-1475.
- [Bra16] M. Brautzsch, C. Kerzig, M. Goez, *Green Chem.* **2016**, *18*, 4761-4771.
- [Bre03] J. Bredenbeck, P. Hamm, *Rev. Sci. Instr.* **2003**, *74*, 3188-3189.
- [Bri12a] C. Brieke, F. Rohrbach, A. Gottschalk, G. Mayer, A. Heckel, *Angew. Chem. Int. Ed.* **2012**, *51*, 8446-8476.
- [Bri12b] B. M. Briechle, Y. Kim, P. Ehrenreich, A. Erbe, D. Sysoiev, T. Huhn, U. Groth, E. Scheer, *Beilstein, J. Nanotechnol.* **2012**, *3*, 798-808.
- [Bue17] L. A. Büldt, O. S. Wenger, *Angew. Chem., Int. Ed.* **2017**, *56*, 5676-5682.
- [Bue20] S. M. Büllmann, A. Jäschke, *Chem. Commun.* **2020**, *56*, 7124-7127.
- [Bug22] L. Buglioni, F. Raymenants, A. Slattery, S. D. A. Zondag, T. Noël, *Chem. Rev.* **2022**, *122*, 2752-2906.
- [But19] F. Buth, "Beta Version of an Automated Quantum Yield and Fatigue Determination System Handling any 2-State Photoswitch", Master thesis, LMU Munich **2019**.
- [Bux88] G. V. Buxton, C. L. Greenstock, W. P. Heiman, A. B. Ross, *J. Phys. Chem. Ref. Data* **1988**, *17*, 513-886.
- [Buz19] L. Buzzetti, G. E. M. Crisenza, P. Melchiorre, *Angew. Chem. Int. Ed.* **2019**, *58*, 3730-3747.

- [Cah13] H. Cahová, A. Jäschke, *Angew. Chem. Int. Ed.* **2013**, *52*, 3186-3190.
- [Cal52] J. G. Calvert, H. J. L. Rechen, *J. Am. Chem. Soc.* **1952**, *74*, 8, 2101-2103.
- [Can22] L. Candish, K. D. Collins, G. C. Cook, J. J. Douglas, A. Gómez-Suárez, A. Jolit, S. Keess, *Chem. Rev.* **2022**, *122*, 2907-2980.
- [Cer03] G. Cerullo, S. De Silvestri, *Rev. Sci. Instrum.* **2003**, *74*, 1-18.
- [Chi96] S. Chichibu, T. Azuhata, T. Sota, S. Nakamura, *Appl. Phys. Lett.* **1996**, *69*, 4188-4190.
- [Cis15] M. A. Cismesia, T. P. Yoon, *Chem. Sci.* **2015**, *6*, 5426-5434.
- [Con10] A. G. Condie, J. C. Gonzalez-Gomez, C. R. Stephenson, *J. Am. Chem. Soc.* **2010**, *132*, 1464-1465.
- [Cor16] J. E. T. Corrie, J. H. Kaplan, B. Forbush, D. C. Ogden, D. R. Trentham, *Photochem. Photobiol. Sci.* **2016**, *15*, 604-608.
- [Coy78] J. D. Coyle, G. L. Newport, A. Harriman, *J. Chem. Soc. Perkin Trans. II* **1978**, 133-137.
- [Cri20] G. E. M. Crisenza, P. Melchiorre, *Nat. Commun.* **2020**, *11*, 803.
- [Cro76] L. C. Cross, W. Klyne, *Pure Appl. Chem.* **1976**, *45(1-B)*, 11-30.
- [Cru13] N. De la Cruz, V. Romero, R. F. Dantas, P. Marco, B. Bayarri, J. Giménez, S. Esplugas, *Catal. Today* **2013**, *209*, 209-214.
- [Dat20] D. Dattler, G. Fuks, J. Heiser, E. Moulin, A. Perrot, X. Yao, N. Giuseppone, *Chem. Rev.* **2020**, *120*, 310-433.
- [Dem76] J. N. Demas, B. H. Blumenthal, *J. Res. Natl. Bur. Stand. A Phys. Chem.* **1976**, *80A(3)*, 409-412.
- [Der17] B. Dereka, A. Rosspeintner, R. Stężycki, C. Ruckebusch, D. T. Gryko, E. Vauthey, *J. Phys. Chem. Lett.* **2017**, *8*, 6029-6034.
- [Dob10] A. Dobryakov, S. A. Kovalenko, A. Weigel, J. L. Pérez-Lustres, J. Lange, A. Müller, N. Ernsting, *Rev. Sci. Instrum.* **2010**, *81*, 113106, 1-9.
- [Dra41] J. W. Draper, *London Ed. Dublin Phil. Mag.* **1841**, *19*, 195.
- [Eck12] S. Eckel, A. O. Sushkov, S. K. Lamoreaux, *Rev. Sci. Instrum.* **2012**, *83*, 026106, 1-3.

- [Els09] C. Elsner, T. Cordes, P. Dietrich, M. Zastrow, T. T. Herzog, K. Rück-Braun, W. Zinth, *J. Phys. Chem. A* **2009**, *113*, 1033-1039.
- [Ern01] J. Ern, A. T. Bens, H.-D. Martin, S. Mukamel, S. Tretiak, K. Tsyganenko, K. Kuldova, H. P. Trommsdorff, C. Krysch, *J. Phys. Chem. A* **2001**, *105*, 1741-1749.
- [Fis60] E. Fischer, *J. Am. Chem. Soc.* **1960**, *82*, 3249-3252.
- [Fis67] E. Fischer, *J. Phys. Chem.* **1967**, *71*, 11, 3704-3706.
- [Fit06] P. Fita, E. Luzina, T. Dziembowska, C. Radzewicz, A. Grabowska, *J. Chem. Phys.* **2006**, *125*, 184508, 1-11.
- [Fle76] G. R. Fleming, J. M. Morris, G. W. Robinson, *Chem. Phys.* **1976**, *17*, 91-100.
- [Fre20] S. Fredrich, T. Morack, M. Sliwa, S. Hech, *Chem. Eur. J.* **2020**, *26*, 7672-7677.
- [Fuk14] T. Fukaminato, T. Hirose, T. Doi, M. Hazama, K. Matsuda, M. Irie, *J. Am. Chem. Soc.* **2014**, *136*, 17145-17154.
- [Gal10] E.S. Galbavy, K. Ram, C. Anastasio, *J. Photochem. Photobiol. A* **2010**, *209*, 186-192.
- [Gau76] G. Gauglitz, *Journal of Photochemistry* **1976**, *5*, 41-47.
- [Gau84] G. Gauglitz, S. Hubig, *Journal of Photochemistry* **1984**, *30*, 121-125.
- [Gau85] G. Gauglitz, S. Hubig, *J. Photochem*, **1985**, *30*, 121-125.
- [Gaw98] J. Gawronski, F. Kazmierczak, K. Gawronska, U. Rychlewska, B. Norden, A. Holmen, *J. Am. Chem. Soc.* **1998**, *120*, 12083-12091.
- [Geg68] D. Gegiou, K. A. Muszkat, E. Fischer, *J. Am. Chem. Soc.* **1968**, *90*, 12-18.
- [Gem15] M. E. Gemayel, K. Börjesson, M. Herder, D. T. Duong, J. A. Hutchison, C. Ruzi, G. Schweicher, A. Salleo, Y. Geerts, S. Hecht, E. Orgiu, P. Samor, *Nat. Commun.* **2015**, *6*, 6330.
- [Geo80] V. George, J. C. Scaiano, *J. Phys. Chem.* **1980**, *84*, 492-495.
- [Ger19] A. Gerwien, P. Mayer, H. Dube, *Nat. Commun.* **2019**, *10*, 4449.
- [Gla14] E. N. Glass, J. Fielden, A. L. Kaledin, D. G. Musaev, T. Lian, C. L. Hill, *Chem. Eur. J.* **2014**, *20*, 4297-4307.

- [Goe01] H. Görner, A. G. Griesbeck, T. Heinrich, W. Kramer, M. Oelgemöller, *Chem. Eur. J.* **2001**, *7*, 7, 1530-1538.
- [Goe14] M. Goez, C. Kerzig, R. Naumann, *Angew. Chem. Int. Ed.* **2014**, *53*, 9914-9916.
- [Gom12] M. Gombár, É. Józsa, M. Braun, K. Ösz, *Photochem. Photobiol. Sci.* **2012**, *11*(10), 1592-1595.
- [Gon19] J. Gong, C. Li, M. R. Wasielewski, *Chem. Soc. Rev.* **2019**, *48*, 1862.
- [Göp31] M. Göppert-Mayer, *Annals of Physics* **1931**, *9*, 273-295.
- [Gra20] A. Graml, T. Neveselý, R.-J. Kutta, R. Cibulka, B. König, *Nat. Commun.* **2020**, *11*, 3174, 1-11.
- [Gre21] N. J. Green, J. Xu, J. D. Sutherland, *J. Am. Chem. Soc.* **2021**, *143*, 7219-7236.
- [Gri07] A. G. Griesbeck, N. Hoffmann, K-D. Warzecha, *Acc. Chem. Res.* **2007**, *40*, 128-140.
- [Gri95] A. G. Griesbeck, A. Henz, K. Peters, E.-M. Peters, H. G. von Schnering, *Angew. Chem.* **1995**, *107*, 498-500.
- [Gri97] A. G. Griesbeck, A. Henz, W. Kramer, J. Lex, F. Nerowski, M. Oelgemöller, *Helvetica Chimica Acta* **1997**, *80*, 912-933.
- [Gri99a] A. G. Griesbeck, W. Kramer, M. Oelgemöller, *Synlett* **1999**, *7*, 1169-1178.
- [Gri99b] A. G. Griesbeck, H. Görner, *J. Photochem. Photobiol. A* **1999**, *129*, 111-119.
- [Gro19] T. Grotthuss, *Sitzungsberichte der kurlandischen Gesellschaft für Literatur und Kunst* **1819**, *I*, 119.
- [Gru18] M. Grübel, I. Bosque, P. J. Altmann, T. Bach, C. R. Hess, *Chem. Sci.* **2018**, *9*, 3313-3317.
- [Gu16] Y. Gu, W. Dong, C. Luo, T. Liu, *Environ. Sci. Technol.* **2016**, *50*, 10554-10561.
- [Gui02] D. Guillaumont, T. Kobayashi, K. Kanda, H. Miyasaka, K. Uchida, S. Kobatake, K. Shibata, S. Nakamura, M. Irie, *J. Phys. Chem. A* **2002**, *106*, 7222-7227.
- [Ham16] I. Hamdi, G. Buntinx, A. Perrier, O. Devos, N. Jaidane, S. Delbaere, A. K. Tiwari, J. Dubois, M. Takeshita, Y. Wada, S. Aloise, *Phys. Chem. Chem.*

- Phys.* **2016**, *18*, 28091-28100.
- [Han02] P. R. Hania, R. Telesca, L. N. Lucas, A. Pugzlys, J. van Esch, B. L. Feringa, J. G. Snijders, K. Duppen, *J. Phys. Chem. A* **2002**, *106*, 8498-8507.
- [Han05] P. R. Hania, A. Pugzlys, L. N. Lucas, J. J. D. de Jong, B. L. Feringa, J. H. van Esch, H. T. Jonkman, K. Duppen, *J. Phys. Chem. A* **2005**, *109*, 9437-9442.
- [Han18] A. Goulet-Hanssens, C. Rietze, E. Titov, L. Abdullahu, L. Grubert, P. Saalfrank, S. Hecht, *Chem* **2018**, *4*, 1740-1755.
- [Han92] M. Hanazawa, R. Sumiya, Y. Horikawa, M. Irie, *J. Chem. Soc., Chem. Commun.* **1992**, 206–207.
- [Hat56] C. G. Hatchard, C. A. Parker, *Proc. Roy. Soc.* **1956**, *235*, 1203, 518-536.
- [Hau14] A. F. E. Hauck, S. J. O. Hardman, R. J. Kutta, G. M. Greetham, D. J. Heyes, N. S. Scrutton, *J. Biol. Chem.* **2014**, *289*, 25, 17747-17757.
- [Her15] M. Herder, B. M. Schmidt, L. Grubert, M. Paetzel, J. Schwarz, S. Hecht, *J. Am. Chem. Soc.* **2015**, *137*, 2738-2747.
- [Her34] J. F. W. Herschel, *Explanation of the principle and construction of the actinometer. Report of the Third Meeting of the British Association for the Advancement of Science* **1834**, Vol. 379-381.
- [Her40] J. F. W. Herschel, *Instructions for making meteorological observations, Rep. Comm. Phys. Meteorol. Roy. Soc.* **1840**, 53-79.
- [Hof17] R. Hofsäß, D. Rombach, H.-A. Wagenknecht, *Synlett.* **2017**, *28*, 1422-1426.
- [Hom11] C. Homann, N. Krebs, E. Riedle, *Appl. Phys. B* **2011**, *104*, 783-791.
- [Hon20] C. R. Honick, G. M. Peters, J. D. Young, J. D. Tovar, A. E. Bragg, *Phys. Chem. Chem. Phys.* **2020**, *22*, 3314-3328.
- [Hor95] M. L. Horng, J. A. Gardecki, A. Papazyan, M. Maroncelli, *J. Phys. Chem.* **1995**, *99*, 17311-17337.
- [Hu20] Q. Hu, Photoinduced dynamics in photocatalysis: "*Mechanistic insights from time-resolved absorption spectroscopy and reaction quantum yield determination*", Dissertation, LMU Munich **2020**.
- [Hub01] R. Huber, H. Satzger, W. Zinth, J. Wachtveitl, *Opt. Commun.* **2001**, *194*, 443-

448.

- [Hui17] R. Hui, *Photo-Electro-Thermal Theory for LED Systems: Basic Theory and Applications*, Cambridge University Press, **2017**, 61.
- [Iag17] A. Iagatti, B. Patrizi, A. Basagni, A. Marcelli, A. Alessi, S. Zanardi, R. Fusco, M. Salvalaggio, L. Bussotti, P. Foggi, *Phys. Chem. Chem. Phys.* **2017**, *19*, 13604-13613.
- [Iri00] M. Irie, *Chem. Rev.* **2000**, *100*, 1685-1716.
- [Iri14] M. Irie, T. Fukaminato, K. Matsuda, S. Kobatake, *Chem. Rev.* **2014**, *114*, 24, 12174-12277.
- [Iri88] M. Irie, M. Mohri, *J. Org. Chem.* **1988**, *53*, 803-808.
- [Iri92a] M. Irie, O. Miyatake, K. Uchida, *J. Am. Chem. Soc.* **1992**, *114*, 8715-8717.
- [Iri92b] M. Irie, K. Sayo, *J. Phys. Chem.* **1992**, *96*, 7671-7674.
- [Iri95] M. Irie, K. Sakemura, M. Okinaka, K. Uchida, *J. Org. Chem.* **1995**, *60*, 8305-8309.
- [Ish09] S. Ishizaka, T. Wada, N. Kitamura, *Photochem. Photobiol. Sci.* **2009**, *8*, 562-566.
- [Ish11] Y. Ishibashi, M. Fujiwara, T. Umesato, H. Saito, S. Kobatake, M. Irie, H. Miyasaka, *J. Phys. Chem. C* **2011**, *115*, *10*, 4265-4272.
- [Ish12] Y. Ishibashi, T. Umesato, S. Kobatake, M. Irie, H. Miyasaka, *J. Phys. Chem. C* **2012**, *116*, 4862-4869.
- [Ish16] Y. Ishibashi, T. Umesato, M. Fujiwara, K. Une, Y. Yoneda, H. Sotome, T. Katayama, S. Kobatake, T. Asahi, M. Irie, H. Miyasaka, *J. Phys. Chem. C* **2016**, *120*, 1170-1177.
- [Jan17] G. S. Jang, J. Lee, J. Seo, S. K. Woo, *Org. Lett.* **2017**, *19*, 6448-6451.
- [Ji18] Y. Ji, D. A. DiRocco, C. M. Hong, M. K. Wismer, M. Reibarkh, *Org. Lett.* **2018**, *20*, 2156-2159.
- [Jia16] C. Jia, A. Migliore, N. Xin, S. Huang, J. Wang, Q. Yang, S. Wang, H. Chen, D. Wang, B. Feng, Z. Liu, G. Zhang, D. Qu, H. Tian, M. A. Ratner, H. Q. Xu, A. Nitzan, X. Guo, *Science* **2016**, *352*, 1443-1445.

- [Joh15] J. A. Johnson, J. Luo, X. Zhang, Y.-S. Chen, M. D. Morton, E. Echevería, F. E. Torres, J. Zhang, *ACS Catal.* **2015**, *5*, 5283-5291.
- [Kan95] Y. Kaneko, Y. Nishimura, T. Arai, H. Sakuragi, K. Tokumaru, D. Matsunaga, *J. Photochem. Photobiol. A* **1995**, *89*, 37-44.
- [Kaw01] T. Kawai, T. Sasaki, M. Irie, *Chem. Commun.* **2001**, 711-712.
- [Kho17] A. Khodko, V. Khomenko, O. Mamuta, S. Snegir, P. Yu, E. Lacaze, A. Marchenko, N. Kachalova, *Nano-Optics* **2017**, 521-524.
- [Kir83] A. D. Kirk, C. Namasivayam, *Anal. Chem.* **1983**, *55*, 14, 2428-2429.
- [Koe13] E. Riedle, M. Wenninger in *Chemical Photocatalysis*, Ed.: B. König, De Gruyter: Berlin, **2013**.
- [Koe15] P. Kölle, I. Pugliesi, H. Langhals, R. Wilcken, A. J. Esterbauer, R. de Vivie-Riedle, E. Riedle, *Phys. Chem. Chem. Phys.* **2015**, *17*, 25061-25072.
- [Koi14] T. Koike, M. Akita, *Inorg. Chem. Front.* **2014**, *1*, 562-576.
- [Kol21] T. Kolmar, S. M. Büllmann, C. Sarter, K. Höfer, A. Jäschke, *Angew. Chem. Int. Ed.* **2021**, *60*, 8164-8173.
- [Kov99] S. A. Kovalenko, A. L. Dobryakov, J. Ruthmann, N. P. Ernsting, *Phys. Rev. A* **1999**, *59*, 2369-2384.
- [Koz04] I. Z. Kozma, P. Baum, U. Schmidhammer, S. Lochbrunner, E. Riedle, *Rev. Sci. Instrum.* **2004**, *75*, 2323-2327.
- [Kuh04] H. J. Kuhn, S. E. Braslavsky, R. Schmidt, *Pure Appl. Chem.* **2004**, *76*(12), 2105-2146.
- [Kut13] R. J. Kutta, T. Langenbacher, U. Kesy B. Dick, *Appl. Phys. B* **2013**, *111*, 203-216.
- [Kut15] R. J. Kutta, S. J. O. Hardman, L. O. Johannissen, B. Bellina, H. L. Messiha, J. M. Ortiz-Guerrero, M. Elias-Arnanz, S. Padmanabhan, P. Barran, N. S. Scrutton, A. R. Jones, *Nat. Commun.* **2015**, *6*, 7907, 1-11.
- [Kut17] R. J. Kutta, N. Archipowa, L. O. Johannissen, A. R. Jones, N. S. Scrutton, *Sci. Rep.* **2017**, *7*, 44906, 1-11.
- [Lac19] D. Lachmann, A. Konieczny, M. Keller, B. König, *Org. Biomol. Chem.* **2019**,

17, 2467.

- [Lad17] V. Ladányi, P. Dvořák, J. Al Anshori, E. Vetráková, J. Wirz, D. Heger, *Photochem. Photobiol. Sci.* **2017**, *16*, 1757-176.
- [Lai05] S. Laimgruber, W. J. Schreier, T. Schrader, F. Koller, W. Zinth, P. Gilch, *Angew. Chem. Int. Ed.* **2005**, *44*, 7901-7904.
- [Lai08] S. Laimgruber, T. Schmierer, P. Gilch, K. Kiewisch, J. Neugebauer, *Phys. Chem. Chem. Phys.* **2008**, *10*, 3872-3882.
- [Lan13] B. Lang, S. Mosquera-Vázquez, D. Lovy, P. Sherin, V. Markovic, E. Vauthey, *Rev. Sci. Instrum.* **2013**, *84*, 073107, 1-8.
- [Lan18] B. Lang, *Rev. Sci. Instrum.* **2018**, *89*, 093112.
- [Lau21] R. Lauenstein, S. L. Mader, H. Derondeau, O. Z. Esezobor, M. Block, A. J. Romer, C. Jandl, E. Riedle, V. R. I. Kaila, J. Hauer, E. Thyraug, C. R. Hess, *Chem. Sci.* **2021**, *12*, 7521-7532.
- [Lee11] C. Hoon Lee, D. K. Dogutan, D. G. Nocera, *J. Am. Chem. Soc.* **2011**, *133*, 8775-8777.
- [Lei14] H. Lei, A. Han, F. Li, M. Zhang, Y. Han, P. Du, W. Lai, R. Cao, *Phys. Chem. Chem. Phys.* **2014**, *16*, 1883-1893.
- [Lei30] W. G. Leighton, G. S. Forbes, *J. Am. Chem. Soc.* **1930**, *52*, 8, 3139-3152.
- [Lei34] P. A. Leighton, F. A. Lucy, *J. Chem. Phys.* **1934**, *2*, 756-759.
- [Let18] R. Letrun, B. Lang, O. Yushchenko, R. Wilcken, D. Svechkarev, D. Kolodieznyi, E. Riedle, E. Vauthey, *Phys. Chem. Chem. Phys.* **2018**, *20*, 30219-30230.
- [Lev91] N. E. Levinger, A. E. Johnson, G. C. Walker, P. F. Barbara, *Chem. Phys. Lett.* **1992**, *196*, 159-165.
- [Li12a] X. Li, J. Ma, G. Liu, J. Fang, S. Yue, Y. Guan, L. Chen, X. Liu, *Environ. Sci. Technol.* **2012**, *46*, 7342-7349.
- [Li12b] X. Liu, S. Yoon, B. Batchelor, A. Abdel-Wahab, *Science of the Total Environment* **2013**, 454-455, 578-583
- [Li16] Y.-H. Li, X.-L. Liu, Z.-T. Yu, Z.-S. Li, S.-C. Yan, G.-H. Chen, Z.-G. Zou,

- Dalton Trans.* **2016**, *45*, 12400-12408.
- [Li19a] L. Li, Y. Hua, X.-N. Li, Y. Guo, H. Zhang, *Dalton Trans.* **2019**, *48*, 10683-10688.
- [Li19b] D. Li, Q. Xu, Y. Li, Y. Qiu, P. Ma, J. Niu, J. Wang, *Inorg. Chem.* **2019**, *58*, 4945-4953.
- [Li20a] Y. Li, L. Guo, L. Li, C. Yang, P. Guang, F. Huang, Z. Chen, L. Wang, J. Hu, *Front. Chem.* **2020**, *8*, 580489.
- [Li20b] X. Li, R. J. Kutta, C. Jandl, A. Bauer, P. Nuernberger, T. Bach, *Angew. Chem. Int. Ed.* **2020**, *59*, 21640-21647.
- [Lor02] M. Lorenc, M. Ziolk, R. Naskrecki, J. Karolczak, J. Kubicki, A. Maciejewski, *Appl. Phys. B.* **2002**, *74*, 19-27.
- [Lor06] V. A. Lórenz-Fonfria, H. Kandori, *Appl. Spec.* **2006**, *60*, 4, 407-417.
- [Lov19] G. H. Lovett, S. Chen, X.-S. Xue, K. N. Houk, D. W. C. MacMillan, *J. Am. Chem. Soc.* **2019**, *141*, 20031-20036.
- [Lv12] H. Lv, Y. V. Geletii, C. Zhao, J. W. Vickers, G. Zhu, Z. Luo, J. Song, T. Lian, D. G. Musaev, C. L. Hill, *Chem. Soc. Rev.* **2012**, *41*, 7572-7589.
- [Ma16] P. Ma, F. Hu, R. Wan, Y. Huo, D. Zhang, J. Niu, J. Wang, *J. Mater. Chem. C* **2016**, *4*, 5424-5433.
- [Ma21] J. Ma, S. Chen, P. Bellotti, R. Guo, F. Schäfer, A. Heusler, X. Zhang, C. Daniliuc, M. K. Brown, K. N. Houk, F. Glorius, *Science* **2021**, *371*, 1338-1345.
- [Mac14] V. G. Machado, R. I. Stock, C. Reichardt, *Chem. Rev.* **2014**, *114*, 10429-10475.
- [Mah14] A. Mahammed, B. Mondal, A. Rana, A. Dey, Z. Gross, *Chem. Commun.* **2014**, *50*, 2725-2727.
- [Mai20] M. Maiuri, M. Garavelli, G. Cerullo, *J. Am. Chem. Soc.* **2020**, *142*, 1, 3-15.
- [Maj16] M. Majek, A. J. von Wangelin, *Acc. Chem. Res.* **2016**, *49*, 2316-2327.
- [Mal12] J.-P. Malval, H. Chaumeil, W. Rettig, V. Kharlanov, V. Diemer, E. Ay, F. Morlet-Savaryd, O. Poizat, *Phys. Chem. Chem. Phys.* **2012**, *14*, 562-574.
- [Mal78] Q. G. Mulazzani, S. Emmi, P. G. Fuochi, M. Venturi, M. Z. Hoffman,

- M. G. Simic, *J. Phys. Chem.* **1979**, *83*, 1582-1590.
- [Mar14] H. Marciniak, S. Lochbrunner, *Chem. Phys. Lett.* **2014**, *609*, 184-188.
- [Mar18] L. Marzo, S. K. Pagire, O. Reiser, B. König, *Angew. Chem. Int. Ed.* **2018**, *57*, 10034-10072.
- [Mas10] T. Maschmeyer, M. Che, *Angew. Chem. Int. Ed.* **2010**, *49*, 1536-1539.
- [Mat03] K. Matsuda, Y. Shinkai, T. Yamaguchi, K. Nomiyama, M. Isayama, M. Irie, *Chem. Lett.* **2003**, *32*, 12, 1178-1179.
- [Mat13] M. M. Maturi, M. Wenninger, R. Alonso, A. Bauer, A. Pöthig, E. Riedle, T. Bach, *Chem. Eur. J.* **2013**, *19*, 7461-7472.
- [McDon98] R. S. McDonald, P. A. Wilks Jr., *Appl. Spectroscopy* **1998**, *42*, 1, 151-162.
- [McNau97] A. D. McNaught, A. Wilkinson in *IUPAC Compendium of Chemical Terminology*, IUPAC, Blackwell Scientific Publications, Oxford, **1997**.
- [Meg09] U. Megerle, I. Pugliesi, C. Schriever, C. F. Sailer, E. Riedle, *Appl. Phys. B* **2009**, *96*, 215-231.
- [Meg10] U. Megerle, R. Lechner, B. König, E. Riedle, *Photochem. Photobiol. Sci.* **2010**, *9*, 1400-1406.
- [Meg11a] U. Megerle, "Photoinduced molecular dynamics in increasingly complex systems: From ultrafast transient absorption spectroscopy to nanoscopic models." Dissertation, LMU Munich **2011**.
- [Meg11b] U. Megerle, M. Wenninger, R. J. Kutta, R. Lechner, B. König, B. Dick, E. Riedle, *Phys. Chem. Chem. Phys.* **2011**, *13*, 8869-8880.
- [Mer21] I. C. D. Merritt, D. Jacquemin, M. Vacher, *Phys. Chem. Chem. Phys.* **2021**, *23*, 19155.
- [Mue88] E. Müller, G. Bernardinelli, A. von Zelewsky, *Inorg. Chem.* **1988**, *27*, 4645-4651.
- [Mic70a] J. Michl, E. W. Thulstrup, J. H. Eggers, *J. Phys. Chem.* **1970**, *74*, 3868-3878.
- [Mic70b] J. Michl, E. W. Thulstrup, J. H. Eggers, *J. Phys. Chem.* **1970**, *74*, 3878-3884.
- [Mic87] J. Michl, E. W. Thulstrup, *Acc. Chem. Res.* **1987**, *20*, 192-199.
- [Mie82] K. Miedlar, P. K. Das, *J. Am. Chem. Soc.* **1982**, *104*, 7462-7469.

- [Miz99] Y. Mizutani, Y. Uesugi, T. Kitagawa, *J. Chem. Phys.* **1999**, *111*, 8950-8962.
- [Mon06] M. Montalti, A. Credi, L. Prodi, M. T. Gandolfi in *Handbook of Photochemistry*, 3th ed., Boca Raton, Florida USA, **2006**.
- [Mos96] G. P. Moss, *Pure & Appl. Chem.* **1996**, *68*, 12, 2193-2222.
- [Nak07] S. Nakamura, T. Kobayashi, A. Takata, K. Uchida, Y. Asano, A. Murakami, A. Goldberg, D. Guillaumont, S. Yokojima, S. Kobatake, M. Irie, *J. Phys. Org. Chem.* **2007**, *20*, 821-829.
- [Nak88] S. Nakamura, M. Irie, *J. Org. Chem.* **1988**, *53*, 6136-6138.
- [Nar17] A. Nardelli, E. Deuschle, L. D. de Azevedo, J. L. N. Pessoa, E. Ghisi, *Renew. Sustain. Energy Rev.* **2017**, *75*, 368-379.
- [Nau17] R. Naumann, C. Kerzig, Martin Goez, *Chem. Sci.* **2017**, *8*, 7510-7520.
- [Nau18a] R. Naumann, F. Lehmann, M. Goez, *Angew. Chem.* **2018**, *130*, 1090-1093.
- [Nau18b] R. Naumann, M. Goez, *Chem. Eur. J.* **2018**, *24*, 9833-9840.
- [Nau18c] R. Naumann, F. Lehmann, M. Goez, *Chem. Eur. J.* **2018**, *24*, 13259-13269.
- [Nau18d] R. Naumann, M. Goez, *Chem. Eur. J.* **2018**, *24*, 17557-17567.
- [Nic08] D. A. Nicewicz, D. W. C. MacMillan, *Science* **2008**, *322*, 77-80.
- [Nis76] N. Nishimura, T. Sueyoshi, H. Yamanaka, E. Imai, S. Yamamoto, S. Hasegawa, *Bull. Chem. Soc. Jpn.* **1976**, *49*, 1381-1387.
- [Oel01] M. Oelgemöller, A. G. Griesbeck, J. Lex, A. Haeuseler, M. Schmittel, M. Niki, D. Heseck, Y. Inoue, *Org. Lett.* **2001**, *3*, 11, 1593-1596.
- [Oel02] M. Oelgemöller, A. G. Griesbeck, *J. Photochem. Photobiol. C: Photochem. Rev.* **2002**, *3*, 109-127.
- [Omw15] S. Omwoma, C. T. Gore, Y. Ji, C. Hub, Y.-F. Song, *Coordination Chemistry Reviews* **2015**, *286*, 17-29.
- [Org14] E. Orgiu, P. Samor, *Adv. Mater.* **2014**, *26*, 1827-1845.
- [Oru20] B. Oruganti, P. P. Kalapos, V. Bhargav, G. London, B. Durbeej, *J. Am. Chem. Soc.* **2020**, *142*, 13941-13953.
- [Pai16] A. A. Paidalwar, I. P. Khedikar, *International Journal of Science Technology &*

Engineering **2016**, 2, 09, 213-219.

- [Pan20] S. Pan, C. Sun, Y. Zhou, W. Chen, R. Zhang, Y. Zheng, *Appl. Sci.* **2020**, 10, 444, 1-13.
- [Par09] H. Park, C. D. Vecitis, J. Cheng W. Choi, B. T. Mader, M. R. Hoffmann, *J. Phys. Chem. A* **2009**, 113, 690-696.
- [Par53] C. A. Parker, *Proc. Roy. Soc.* **1953**, 220, 1140, 104-116.
- [Pas03] M. Boggio-Pasqua, M. Ravaglia, M. J. Bearpark, M. Garavelli, M. A. Robb, *J. Phys. Chem. A* **2003**, 107, 11139-11152.
- [Pat18] M. P. Pattison, J. Y. Tsao, G. C. Brainard, B. Bugbee, *Nature* **2018**, 563, 493-500.
- [Pet18] C. Petermayer, H. Dube, *Acc. Chem. Res.* **2018**, 51, 1153-1163.
- [Pit15] S. P. Pitre, C. D. McTiernan, W. Vine, R. DiPucchio, M. Grenier, J. C. Scaiano, *Sci. Rep.* **2015**, 5, 16397-16407.
- [Pon14] E. Pontecorvo, C. Ferrante, C. G. Elles, T. Scopigno, *J. Phys. Chem. B* **2014**, 118, 6915-6921.
- [PQY-01] <https://www.selectscience.net/products/lightway-pqy-01-photoreaction-evaluation-system/?prodID=226877#tab-2>
- [Pri13] C. K. Prier, D. A. Rankic, D. W. C. MacMillan, *Chem. Rev.* **2013**, 113, 7, 5322-5363.
- [Put15] E. V. Puttock, P. Banerjee, M. Kaspar, L. Drennen, D. S. Yufit, E. Bill, S. Sproules, C. R. Hess, *Inorg. Chem.* **2015**, 54, 5864-5873.
- [Qui14] M. Quick, A. L. Dobryakov, M. Gerecke, C. Richter, F. Berndt, I. N. Ioffe, A. A. Granovsky, R. Mahrwald, N. P. Ernsting, S. A. Kovalenko, *J. Phys. Chem. B* **2014**, 118, 29, 8756-8771.
- [QYM-01] <https://www.shimadzu.com/an/literature/uv/jpa114005.html>
- [Rab21] J. Rabani, H. Mamane, D. Pousty, J. R. Bolton, *Photochemistry and Photobiology* **2021**, 97, 873-902.
- [Rau82] H. Rau, E. Lueddecke, *J. Am. Chem. Soc.* **1982**, 104, 1616-1620.
- [Rau84] H. Rau, *Journal of Photochemistry* **1984**, 26, 221-225.

- [Raw18] T. Rawner, E. Lutsker, C. A. Kaiser, O. Reiser, *ACS Catal.* **2018**, *8*, 3950-3956.
- [Rei19a] M. Reinfelds, V. Hermanns, T. Halbritter, J. Wachtveitl, M. Braun, T. Slanina, A. Heckel, *ChemPhotoChem* **2019**, *3(6)*, 441-449.
- [Rei19b] A. Reiffers, C. Torres Ziegenbein, L. Schubert, J. Diekmann, K. A. Thom, R. Kühnemuth, A. Griesbeck, O. Weingart, P. Gilch, *Phys. Chem. Chem. Phys.* **2019**, *21*, 4839-4853.
- [Rei21] B. Reiß, Q. Hu, E. Riedle, H.-A. Wagenknecht, *ChemPhotoChem* **2021**, *5*, 1009-1019.
- [Ret03] J. L. Retsek, C. M. Drain, C. Kirmaier, D. J. Nurco, C. J. Medforth, K. M. Smith, I. V. Sazanovich, V. S. Chirvony, J. Fajer, D. Holten, *J. Am. Chem. Soc.* **2003**, *125*, 9787-9800.
- [Rie00] E. Riedle, M. Beutter, S. Lochbrunner, J. Piel, S. Schenkl, S. Spörlein, W. Zinth, *Appl. Phys. B* **2000**, *71*, 457-465.
- [Rie13] E. Riedle, M. Bradler, M. Wenninger, Ch. F. Sailer, I. Pugliesi, *Faraday Discuss.* **2013**, *163*, 139-158.
- [Rog12] A. Rogalski, *Opto-Electronics Review* **2012**, *20(3)*, 279-308.
- [Roi18] A. Roibu, S. Fransen, M. E. Leblebici, G. Meir, T. Van Gerven, S. Kuhn, *Sci. Rep.* **2018**, *8*, 5421,1-10.
- [Rom16] N. A. Romero, D. A. Nicewicz, *Chem. Rev.* **2016**, *116*, 10075-10166.
- [Ron74] J. Ronayette, R. Arnaud, P. Lebourgeois, J. Lemaire, *Can. J. Chem.* **1974**, *52*, 1848-1857.
- [Rot16] D. M. Arias-Rotondo, J. K. McCusker, *Chem. Soc. Rev.* **2016**, *45*, 5803-5820.
- [Rou17] B. Roubinet, M. Weber, H. Shojaei, M. Bates, M. L. Bossi, V. N. Belov, M. Irie, S. W. Hell, *J. Am. Chem. Soc.* **2017**, *139*, 6611-6620.
- [Rub10] M. B. Rubin, S. E. Braslavsky, *Photochem. Photobiol. Sci.* **2010**, *9*, 670-674.
- [Ruc12] C. Ruckebusch, M. Sliwa, P. Pernot, A. de Juan, R. Tauler, *J. Photochem. Photobiol. C* **2012**, *13*, 1-27.
- [Rue11] M. Rueping, C. Vila, R. M. Koenigs, K. Poschnarny, D. C. Fabry, *Chem. Commun.* **2011**, *47*, 2360-2362.

- [Sai15] M. Saif, J. R. Widom, S. Xu, E. R. Abbey, S.-Y Liu, A. H. Marcus, *J. Phys. Chem. B* **2015**, *119*, 7985-7993.
- [San09] A. Ribeiro Santos, R. Ballardini, P. Belser, M. T. Gandolfi, V. M. Iyer, L. Moggi, *Photochem. Photobiol. Sci.* **2009**, *8*, 1734-1742.
- [Sch08] U. Schmidhammer, U. Megerle, S. Lochbrunner, E. Riedle, J. Karpiuk, *J. Phys. Chem. A* **2008**, *112*, 8487- 8496.
- [Sen17] M. Sender, D. Ziegenbalg, *Chem. Ing. Tech.* **2017**, *89*(9), 1159-1173.
- [Ser02] N. Serpone, A. V. Emeline, *Int. J. Photoenergy* **2002**, *4*, 91-131.
- [Sha13] R. C. Shallcross, P. Zacharias, A. Köhnen, P. O. Körner, E. Maibach, K. Meerholz, *Adv. Mater.* **2013**, *25*, 469-476.
- [Sha16] M. H. Shaw, J. Twilton, D. W. C. MacMillan, *J. Org. Chem.* **2016**, *81*, 6898-6926.
- [Shi07] S. Shim, I. Eom, T. Joo, E. Kim, K. S. Kim, *J. Phys. Chem. A* **2007**, *111*, 8910-8917.
- [Sia87] N. Siampiringue, G. Guyot, S. Monti, P. Bortolus, *J. Photochem.* **1987**, *37*, 185-188.
- [Sla15] C. Slavov, H. Hartmann, J. Wachtveitl, *Anal. Chem.* **2015**, *87*, 2328-2336.
- [Sny89] S. W. Snyder, S. L. Buell, J. N. Demás, B. A. DeGraff, *J. Phys. Chem.* **1989**, *93*, 5265-5271.
- [Sot17] H. Sotome, T. Nagasaka, K. Une, S. Morikawa, T. Katayama, S. Kobatake, M. Irie, H. Miyasaka, *J. Am. Chem. Soc.* **2017**, *139*, 17159-17167.
- [Sot20] H. Sotome, K. Une, T. Nagasaka, S. Kobatake, M. Irie, H. Miyasaka, *J. Chem. Phys.* **2020**, *152*, 034301, 1-9.
- [Sta18a] E. Stadler, A. Eibel, D. Fast, H. Freißmuth, C. Holly, M. Wiech, N. Moszner, N. Gescheidt, *Photochem. Photobiol. Sci.* **2018**, *17*, 660-669.
- [Sta18b] H. S. Stark, P. J. Altmann, S. Sproules, C. R. Hess, *Inorg. Chem.* **2018**, *57*, 6401-6409.
- [Sto04] I. Stokkum, D. Larsen, R. Grondelle, *Biochim. Biophys. Acta, Bioenerg.* **2004**, *1657*, 82-104.

- [Str17] K. Stranius, K. Börjesson, *Sci Rep.* **2017**, *7*, 41145.
- [Sum14] T. Sumi, Y. Takagi, A. Yagi, M. Morimoto, M. Irie, *Chem. Commun.* **2014**, *50*, 3928-3930.
- [Sys11] D. Sysoiev, A. Fedoseev, Y. Kim, T. E. Exner, J. Boneberg, T. Huhn, P. Leiderer, E. Scheer, U. Groth, U. E. Steiner, *Chem. Eur. J.* **2011**, *17*, 6663-6672.
- [Sys12] D. Sysoiev, T. Yushchenko, E. Scheer, U. Groth, U. E. Steiner, T. E. Exner, T. Huhn, *Chem. Commun.* **2012**, *48*, 11355-11357.
- [Sza22] G.-S. Szabó, R. Szabó, L. Szabó, *Energies* **2022**, *15*, 6558.
- [Tak12] Y. Takagi, T. Kunishi, T. Katayama, Y. Ishibashi, H. Miyasaka, M. Morimoto, M. Irie, *Photochem. Photobiol. Sci.* **2012**, *11*, 1661-1665.
- [Tan08] K. Tani, Y. Ishibashi, H. Miyasaka, S. Kobatake, M. Irie, *J. Phys. Chem. C* **2008**, *112*, 11150-11157.
- [The14] N. Thejokalyani, S. J. Dhoble, *Renew. Sustain. Energy Rev.* **2014**, *32*, 448-467.
- [Tia04] H. Tian, S. Yang, *J. Chem. Soc. Rev.* **2004**, *33*, 85-97.
- [Tia20] L. Tian, N. A. Till, B. Kudisch, D. W. C. MacMillan, G. D. Scholes, *J. Am. Chem. Soc.* **2020**, *142*, 10, 4555-4559.
- [Tim15] L. F. Timmermann, K. Ritter, D. Hillebrandt, T. Küpper, *Travel Medicine and Infections Disease* **2015**, *13*, 466-474.
- [Tin20] S. I. Ting, S. Garakyaraghi, C. M. Taliaferro, B. J. Shields, G. D. Scholes, F. N. Castellano, A. G. Doyle, *J. Am. Chem. Soc.* **2020**, *142*, 580-5810.
- [Tuc12a] J. Tucher, L. C. Nye, I. Ivanovic-Burmazovic, A. Notarnicola, C. Streb, *Chem. Eur. J.* **2012**, *18*, 10949-10953.
- [Tuc12b] J. W. Tucker, C. R. J. Stephenson, *J. Org. Chem.* **2012**, *77*, 1617-1622.
- [Tur91] N. J. Turro, *Modern Molecular Photochemistry*, University Science Books, Sausalito, **1991**.
- [Uch99] K. Uchida, E. Tsuchida, Y. Aoi, S. Nakamura, M. Irie, *Chem. Lett.* **1999**, *28*, 63-64.
- [Uno11] K. Uno, H. Niikura, M. Morimoto, Y. Ishibashi, H. Miyasaka, M. Irie, *J. Am.*

- Chem. Soc.* **2011**, *133*, 13558-1356.
- [Uno19] K. Uno, M. L. Bossi, M. Irie, V. N. Belov, S. W. Hell *J. Am. Chem. Soc.* **2019**, *141*, 16471-16478.
- [Van04] I. H. van Stokkum, D. S. Larsen, R. Van Grondelle, *Biochim. Biophys. Acta* **2004**, *1657*, 82-104.
- [Vet17] E. Vetráková, V. Ladányi, J. Al Anshori, P. Dvořák, J. Wirz, D. Heger, *Photochem. Photobiol. Sci.* **2017**, *16*, 1749-1756.
- [Vol19] H. Volfova, Q. Hu, E. Riedle, *Newsletter of the European Photochemical Association* June **2019**, *96*, 51-69.
- [Vos97] A. Voskuhl, *The British Journal for the History of Science* **1997**, *30*, 337.
- [Wal05] S. Wallin, J. Davidsson, J. Modin, L. Hammarstro, *J. Phys. Chem. A* **2005**, *109*, 4697-4704.
- [Wan15] S.-S. Wang, G.-Y. Yang, *Chem. Rev.* **2015**, *115*, 4893-4962.
- [War06] K.-D. Warzecha, H. Görner, A. G. Griesbeck, *J. Phys. Chem. A* **2006**, *110*, 3356-3363.
- [War12] C. L. Ward, C. G. Elles, *J. Phys. Chem. Lett.* **2012**, *3*, 2995-3000.
- [War13] E. Warburg, *Über den Energieumsatz bei photochemischen Vorgängen in Gasen*, Sitzungsber, Königlich preuss, Akademie der Wissenschaften, **1913**, XXXIV, 644-659.
- [War17] E. Warburg, *Naturwissenschaften* **1917**, *5*, 489-494.
- [Wea67] T. J. R. Weakley, S. A. Malik, *J. Inorg. Nucl. Chem.* **1967**, *29*, 2935-2944.
- [Wea73] T. J. R. Weakley, *J. Chem. Soc., Dalton Trans.* **1973**, 341-346.
- [Wid13] J. R. Widom, D. Rappoport, A. Perdomo-Ortiz, H. Thomsen, N. P. Johnson, P. H. von Hippel, A. Aspuru-Guzik, A. H. Marcus, *Nucleic Acids Research* **2013**, *41*(2), 995-1004.
- [Wie19] S. Wiegner, "Ray Tracing in complex optical systems", Masterarbeit, LMU Munich **2019**.
- [Wil18] R. Wilcken, M. Schildhauer, F. Rott, L. A. Huber, M. Guentner, S. Thumser, K. Hoffmann, S. Oesterling, R. de Vivie-Riedle, E. Riedle, H. Dube, *J. Am.*

Chem. Soc. **2018**, *140*, 5311-5318.

- [Wil22] R. Wilcken, A. Gerwien, L. A. Huber, H. Dube, E. Riedle, *ChemPhotoChem* **2022**, *6*, e202100232.
- [Wil23] R. Wilcken, *Dissertation in preparation*, **2023**.
- [Wil97] T. Wilhelm, J. Piel, E. Riedle, *Opt. Lett.* **1997**, *22*, 1494-1496.
- [Woo70] R. B. Woodward, R. Hoffmann, *The Conservation of Orbital Symmetry*, Verlag Chemie: Weinheim, Germany, **1970**.
- [Wri20] B. Wriedt, D. Ziegenbalg, *J. Flow. Chem.* **2020**, *10*, 295-306.
- [Wri21] B. Wriedt, D. Ziegenbalg, *ChemPhotoChem* **2021**, *5*, 1-11.
- [Xu17] J. Xu, B. Zhang, M. Jansen, L. Goerigk, W. W. H. Wong, C. Ritchie, *Angew. Chem. Int. Ed.* **2017**, *56*, 13882-13886.
- [Xu18] J. Xu, H. Volfova, R. J. Mulder, L. Goerigk, G. Bryant, E. Riedle, C. Ritchie, *J. Am. Chem. Soc.* **2018**, *140*, 10482-10487.
- [Yam62] S. Yamashita, H. Ono, Osamu Toyama, *Bulletin of the Chemical Society of Japan* **1962**, *35*, 11, 1849-1853.
- [Yao19] W. Yao, C. Qin, N. Xu, J. Zhou, C. Sun, L. Liu, Z. Su, *CrystEngComm* **2019**, *21*, 6423-6431.
- [Zam07] A. V. Zamyatin, A. V. Soldatova, M. A. J. Rodgers, *Inorg. Chim. Acta* **2007**, *360*, 857-868.
- [Zew00a] A. H. Zewail, *J. Phys. Chem. A* **2000**, *104*, 5660-5694.
- [Zew00b] A. H. Zewail, *Angew. Chem. Int. Ed.* **2000**, *39*, 2586-2631.
- [Zha20] W. Zhang, J. Kong, D. Hu, M. Tao, X. Niu, S. Vdović, D. Aumiler, Y. Ma, A. Xia, *J. Phys. Chem. C* **2020**, *124*, 5574-5582.
- [Zho19] Q.-Q. Zhou, Y.-Q. Zou, L.-Q. Lu, W.-J. Xiao, *Angew. Chem. Int. Ed.* **2019**, *58*, 1586-1604.
- [Zim58] G. Zimmerman, L.-Y. Chow, U.-J. Paik, *J. Am. Chem. Soc.* **1958**, *80*, 14, 3528-3531.

Acknowledgments

First of all, I would like to thank Prof. Dr. Eberhard Riedle for the opportunity to work in his group and for supervising my PhD thesis. I am grateful for all scientific discussions and also for all conversations beyond that. His trust and attitude have encouraged me to contribute my own ideas and to always aim for efficiency and optimization of all processes.

I would like to thank Prof. Dr. Jürgen Hauer for his decision to be the second supervision of this thesis.

I would like to thank PD Dr. Bert Nickel, Prof. Dr. George Craig, Prof. Dr. Dieter Braun and Prof. Dr. Jörg Schreiber for being members of my thesis committee.

Special thanks to all collaborators for their enthusiasm for photophysics, for providing samples, and for valuable scientific discussions that contributed to our understanding of the various types of photosystems: (TU München) Prof. Dr. Jürgen Hauer, Prof. Dr. Corinna Hess, Dr. Erling Thyraug, Raphael Lauenstein, Oaikhena Esezobor; (Universität zu Köln) Prof. Dr. Axel G. Griesbeck, Dr. Florian Gaida; (Monash University, Melbourne) Dr. Chris Ritchie, Dr. Jingjing Xu, Peter McDonald; (Universität Regensburg) Prof. Dr. B. König, Julia Zach; (Universität Konstanz) Dr. Thomas Huhn, Dr. Sergii Snegir, Dr. Alina Khodko; (Humboldt-Universität Berlin) Prof. Dr. Stefan Hecht and Dr. Yves Garmshausen.

I would like to thank Prof. Dr. Konstantin Karaghiosoff for making NMR measurements possible.

I am very grateful to all QYDS users for their positive feedback on QYDS. Special thanks go to Prof. Dr. Andres Jäschke's group, namely Simon M. Büllmann and Theresa Kolmar, who shared their daily experiences with QYDS and were willing to discuss all chemical topics.

Special thanks go to Dr. Roger-Jan Kutta for support in the evaluation of the Maximum entropy analysis and interpretation of the TA data.

I would like to thank my BMO colleagues for creating nice work atmosphere and for support in various types of measurements: Roland Wilcken, Dr. Qi Hu, Ferdinand Bergmeier, Matthias Block, Dr. Bastian Baudisch, Marcus Götz, Sebastian Wiegner, Philipp Neumann, Florian Buth, Valentin Weyerer and Lorenz Fischer.

I thank Dr. Karl-Heiz Mantel for the IT support and Alexandra Michaelis for her help in the administrative issues.

Hiermit erkläre ich, die vorliegende Arbeit selbstständig verfasst und keine anderen als die angegebenen Quellen und Hilfsmittel verwendet zu haben.

München, den 24. Mai 2023

Henrieta Derondeau